INVESTIGATIONS OF INITIAL STATE EFFECTS IN p+Pb COLLISIONS VIA DIJET MEASUREMENT WITH THE ATLAS DETECTOR

BY

ARIC TATE

DISSERTATION

Submitted in partial fulfillment of the requirements
for the degree of Doctor of Philosophy in Nuclear Plasma and Radiological Engineering
in the Graduate College of the
University of Illinois Urbana-Champaign, 2024

Urbana, Illinois

Doctoral Committee:

Professor Rizwan Uddin, Committee Chair
Professor Matthias Grosse Perdekamp, Co-Director of Research
Dr. Riccardo Longo, Co-Director of Research
Professor Anne Sickles
Associate Professor Angela Di Fulvio
Associate Professor Caleb Brooks

Abstract

The Large Hadron Collider (LHC) at the European Organization for Nuclear Research is the most powerful particle accelerator in the world. The ATLAS experiment, located on the LHC, is a multi-purpose detector with $\sim 4\pi$ coverage, providing tracking and calorimetry for particles generated by relativistic collisions of protons and/or nuclei. The ATLAS Collaboration uses the recorded data to test the limits of our understanding of physics, searching for new particles and investigating the fundamental structure of matter. The study of heavy ion collisions at the LHC has informed our understanding of the quark-gluon plasma (QGP), a deconfined state of matter formed at high temperature and density, in which partons collectively behave as a liquid. To disentangle initial-state effects from final-state effects originating from the QGP, proton-lead (p+Pb) collisions are studied. In such collisions, QGP formation does not occur, allowing for examination of initial-state nuclear effects. By making use of the full acceptance of the ATLAS calorimeter, dijet probes in p+Pb collisions can be used to characterize initial-state effects in terms of the hard-scattering kinematics.

This thesis represents the first measurement of the centrality dependence of the triple-differential dijet yield using 165 nb^{-1} of p+Pb data collected at $\sqrt{s_{\mathrm{NN}}} = 8.16$ TeV in 2016. In collider experiments, jets are collimated sprays of particles originating from high momentum transfer collisions. In a given event, the two jets with the largest transverse momentum are referred to as a dijet. The event centrality, which is directly related to the number of inelastic collisions between the incident proton and the nucleons bound in the Pb nucleus, is characterized by the total transverse energy measured in the Pb-going calorimeter near to the beam axis. The dijet yield is measured as a function of the average transverse momentum of the jet pair, the boost of the dijet system, and the half rapidity separation between the jets. The central-to-peripheral ratio of the dijet yields, R_{CP}, is evaluated, and the results are presented as a function of variables that reflect the kinematics of the initial hard parton-parton scattering process. The R_{CP} shows a scaling with the Bjorken-x of the parton originating from the proton, x_p, while no such trend is observed as a function of x_{Pb}. These results represent a unique input to further understand x_p-dependent color fluctuation effects, where small proton configurations are characterized by a reduced interaction strength that results in less soft proton-nucleus collisions and, therefore, a biased centrality. Results are then used to further interpret previous, less differential, p+Pb measurements that were performed at a lower center-of-mass energy.

Acknowledgments

I would like to thank my advisor, Professor Matthias Grosse Perdekamp, for providing me ample opportunities to pursue research within the fields of physics and nuclear security. I have always appreciated his ability to communicate technical topics to people with all levels of expertise. I would also like to thank Professor Anne Sickles and Dr. Riccardo Longo, without whom this analysis would not have been possible. The enthusiasm each of these individuals has for their work is something I will always admire, and I look forward to seeing what results come out of the UIUC nuclear physics group in the future. Past and current members of the group who were invaluable in helping me learn various aspects of ATLAS analysis software include Anabel Romero, Xiaoning Wang, and Virginia Bailey.

There are numerous members of the ATLAS Heavy Ion community whom I would like to acknowledge for their impact on my graduate career within ATLAS, in particular, the conveners who played instrumental roles during my Qualification Task and Analysis. These include Martin Rybar, Sebastian Tapia, Aaron Angerami, and Dominik Derendarz, as well as others who provided numerous inputs to the analysis, including Peter Steinberg and Dennis Perepelitsa. I would also like to express my gratitude to Qipeng Hu and Tim Rinn of the EdBoard, whose diligence and urgency made getting this analysis out as a conference note for Hard Probes and a paper for Quark Matter possible.

Lastly, I would like to thank my family for their unwavering support. My sister Amber set an academic example of excellence for her siblings to follow. From a young age, I only ever wanted to be as smart as my older sister. I have always looked to my brothers, Adam and Andrew, for their driven and upbeat attitudes as well as their musical influences. To my parents, Mark and Celia, thank you for everything.

Table of contents

Chapter 1

Introduction

1.1 The Standard Model

In 1897, J. J. Thompson discovered the first subatomic particle, the electron, via the cathode ray tube experiment. This elementary particle would come to be included in the Standard Model, a theory which has guided, and withstood scrutiny by, physicists for the last 70+ years by prescribing a mathematical treatment to the interaction of particles via quantum field theory. The experiments used to fill in the missing particles predicted by the model have never since been as quaint as the one used in 1897, with the Large Hadron Collider (LHC) at CERN adding the latest piece to the Standard Model with the discovery of the Higgs boson in 2012, via the ATLAS and CMS experiments [1, 2]. This thesis is based on data recorded by the ATLAS detector in 2016, with the results hopefully serving to advance our understanding of the physical world by some small margin.

The current Standard Model of particle physics is given in Figure 1.1, where the strong, electroweak, and electromagnetic fundamental forces of nature are represented by their corresponding force carriers, namely the gluon, the $W^{\pm}$ and Z bosons, and the photon, respectively. It should be noted that gravity has not yet been incorporated into this theory, which also plays no role in the measurement performed in this transcript.[1] The three generations of fermions (quarks and leptons) are shown in Figure 1.1, where moving from left to right corresponds to an increase in mass. Quarks interact via all four fundamental forces, and are bound into hadrons (e.g. neutrons and proton) by the strong force. Conversely, leptons do not interact via the strong force. Fermions are spin-$1/2$ particles, and therefore obey the Pauli-exclusion principle due to Fermi-Dirac statistics, whereas the spin-1 bosons obey Bose-Einstein statistics. All "ordinary" matter in the known universe is composed of fermions held together by the force carrying bosons, with the essential ingredients being a combination of the stable first generation up and down quarks, and electrons. For the benefit of the reader, I will briefly review some of the major contributions leading to our current understanding of the physical world, as enshrined in the Standard Model. In this way, I hope that the forces and particles which are explored in this thesis will have a more concrete underpinning.

1.1.1 Quantum Mechanics

We begin with the photon, which has the unique distinction of being the only elementary particle that can be observed with the naked eye, making it an ideal candidate for early experimental observations. In

[1] Gravity is suppressed by more than a factor of 10^{30}, when compared to the three other fundamental forces.

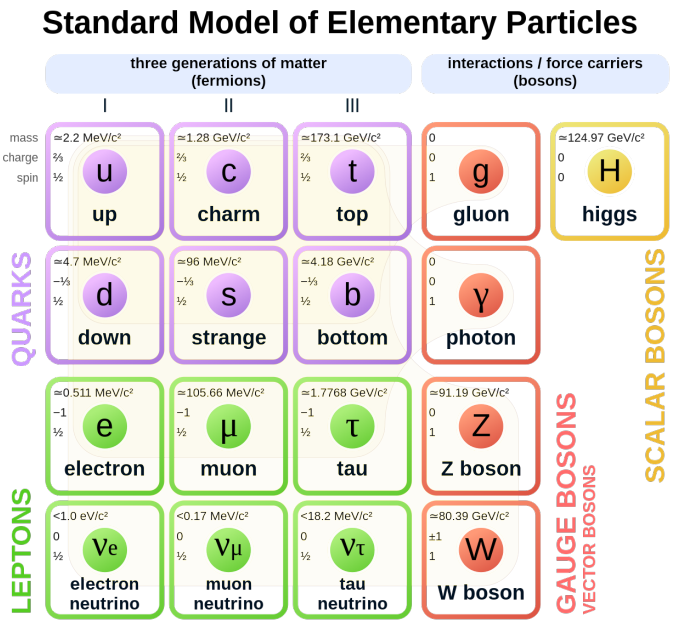

Figure 1.1: The Standard Model of particle physics. Figure taken from Ref. [3]

the mid-19$^{\text{th}}$ century, light was considered to be a wave and was mathematically described by Maxwell's equations. Through both theoretical and experimental contributions at the beginning of the 20$^{\text{th}}$ century, this perception rapidly changed, opening the door to a treatment of physics at the smallest scale, i.e., the quantum level. First came Planck's solution to the black-body radiation problem in 1900, which could not be solved classically. In his solution, energy was no longer treated as continuous, but instead as having discrete values, with energy being proportional to frequency [4, 5]. The experimental discovery in 1902 that the energy of electrons emitted via the photoelectric effect was independent of the incident light's intensity, and instead proportional to the frequency of light [6], was also incompatible with the classical wave theory put forth by Maxwell. In the years that followed, Einstein proposed the quantization of light (1905) [7] and extended Planck's work to solids (1907) [8]. In 1923, Compton confirmed experimentally that light does in fact have a particle-like nature with the scattering experiment that now bears his name [9]. Louis de Broglie followed this shortly in 1924 by attributing a wavelength to all particles. Experimentally, the scrutiny of particles using the well established double-slit experiment confirmed this so-called wave-particle duality. The final steps of the transition from classical to a "new" physics came with Schrödinger's 1926 equation describing wave functions [10] and Heisenberg's uncertainty principle, formulated in 1927 [11]. Together these contributions, as well as others of the time, laid the foundation for quantum mechanics, a framework that has since revolutionized our understanding, and mathematical treatment, of physics.

1.1.2 Quantum Electrodynamics & Chromodynamics

The major shortcoming of quantum mechanics is that it can provide predictions for interactions at the smallest distances, but not for the shortest timescales (i.e., at speeds approaching that of light). A series of developments, resulting in the theory of Quantum Electrodynamics (QED), resolved this by combining quantum mechanics with Einstein's theory of special relativity, such that the electromagnetic field was quantized and interactions between particles were treated as the exchange of virtual photons. These

interactions could be described using Feynman diagrams [12], a visual representation of a mathematical construct, which can be applied to any quantum field theory. Notable contributors to this theory include:

- Paul Dirac, whose equation combined quantum mechanics with special relativity in 1928 [13].
- Tomonaga [14], Schwinger [15], and Feynman [12], who independently developed renormalization techniques to handle infinite terms arising in perturbation theory during the 1940s, forming the basis of QED.

The strength of the electromagnetic interaction is governed by the coupling constant α, which has a dimensionless value of $1/137$ and is referred to as the *fine structure constant*. The fundamental process underlying QED is shown in Figure 1.2, where a charged particle (e) enters, emits or absorbs a photon (λ), and exits. At each vertex within a diagram, representing an interaction between particles, the conservation of charge, energy, momentum (and some lesser known quantities) must hold true. For a given process, all possible diagrams contributing can be calculated in order to determine the probability for a specific interaction to occur. For a rigorous mathematical introduction to QED, the reader is directed to Refs. [16, 17].

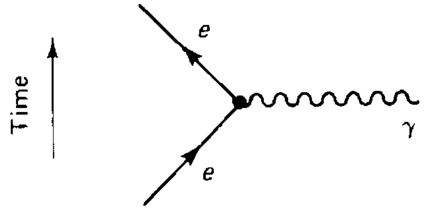

Figure 1.2: Elementary electromagnetic process, where a charged particle (electron in this case) emits or absorbs a photon. Note that this is not a valid process by itself, as energy is not conserved. Figure taken from Ref. [16], wherein the author prefers to orient time vertically.

There are many striking similarities between QED, which describes electromagnetic interactions, and the theory which describes the strong force, Quantum Chromodynamics (QCD). Here I will highlight where they diverge, and the resulting consequences. While electromagnetism has only positive and negative charges, the strong force has three charges, which are labeled using the colors red, green, and blue. A color-neutral state can be formed by combining one unit each of red, green, and blue charge (baryons), or a quark-antiquark ($q\bar{q}$) pair (mesons) such as blue-antiblue. Color charge is another quantity which must be conserved at each vertex in a Feynman diagram. The other fundamental difference between the two theories is that the force carrying boson of the strong force, gluons, carry color charge, whereas photons are electrically neutral. To be very explicit, gluons can self-interact. This fact has profound consequences that manifest as two distinct phenomena in QCD, namely *asymptotic freedom* and *confinement*, which are discussed in Section 1.2.2.

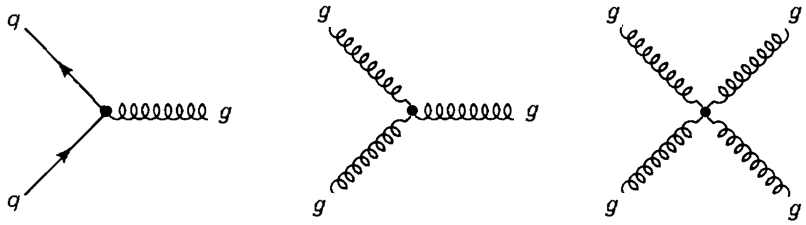

Figure 1.3: Elementary QCD vertices: quark-gluon (left), three-gluon self-interaction (middle), four-gluon self-interaction (right). Time is oriented vertically. Figure adapted from Ref. [16].

By replacing the electrons in Figure 1.2 with quarks, and the photon with a gluon, the corresponding elementary QCD process can be constructed. This is shown in the left-most diagram of Figure 1.3, along with the other two QCD vertices, which represent gluon self-interactions. A valid Feynman diagram can

then be produced by combining two such interactions, two examples of which are shown in Figure 1.4. The left process, representing the strong force mediator (gluon) acting between quarks, is responsible for the formation of protons and neutrons, and therefore all stable matter. The right diagram represents a quark and gluon scattering off one another in a high-energy collision. The results presented in this manuscript can be used to test QCD predictions for these two processes over a large kinematic phase-space.

Figure 1.4: Lowest order diagram for quark-quark interaction (left) and quark-gluon interaction (right), where a virtual gluon is exchanged. Time is oriented vertically. Figure adapted from Ref. [16].

The Standard Model is thus a predictive theory which combines QED, QCD, and Electroweak Theory, as formulated in the 1960s, and early 1970s [18–21]. This thesis will not discuss the inner-workings of the weak force, but the color and electric charge neutral Z-boson does play an important role during the calibration of the ATLAS detector. It is worth noting that at extremely high energies, present during the beginning of the universe, electromagnetism and the weak force are indistinguishable, hence the name of the theory describing the weak force being "electro"+"weak". The basics of QCD are presented in Section 1.2, while more nuanced phenomena, which are relevant to the interpretation of results presented in this thesis, are discussed in Section 2.3.

1.2 Overview of Quantum Chromodynamics

The existence of a subatomic particle within nucleons was proposed independently by Murray Gell-Mann [22] and George Zweig [23] in 1964, with both working on a theory to describe the strong fundamental force. This quantum field theory would come to be known as Quantum Chromodynamics (QCD). Experimental evidence of the existence of Gell-Mann and Zweig's point-like constituents within the proton were first reported by the MIT-SLAC *deep-inelastic scattering* (DIS) experiment in 1969 [24, 25].

1.2.1 Deep-Inelastic Scattering

In DIS measurements, a highly energetic lepton scatters off an individual parton within the target hadron, as shown in Figure 1.5, allowing for examination of its inner structure via an electromagnetic probe. The variables p_e and p_p in Figure 1.5 correspond to the momentum of the incident electron and proton, respectively, while q represents the momentum of the virtual photon.

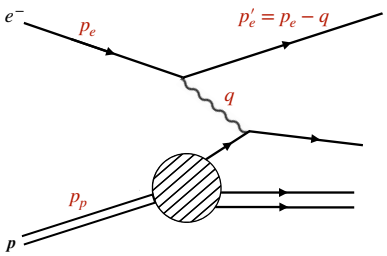

Figure 1.5: Diagram of DIS experiment, where an incident lepton (e^-) directly interacts with a constituent of the target hadron (proton) through the exchange of a virtual photon. Time is oriented horizontally.

Because DIS is performed using a fixed-target, p_p is known. By measuring the incident (p_e) and final (p'_e) electron momentum, q can be determined. This mechanism is reminiscent of the elastic scattering experiment used by Rutherford to probe the structure of the atom [26], in which alpha-particles were scattered of gold nuclei, proving the existence of a concentrated positive charge (nucleus) within the atom. Similarly, the DIS cross-section can be calculated by measuring only the angle and energy of the scattered lepton, providing evidence of charged constituents within the proton. When formulated using variables that allow for parameterizing the reaction in terms of the exchanged momenta and the configuration of the struck parton in the target, the cross-section is written as

$$\frac{d^2\sigma}{dx\,dQ^2} = \frac{2\pi\,\alpha^2}{x\,Q^4}\Big[\Big(1+(1-y)\Big)^2 F_2(x,Q^2) - y^2\Big(F_2(x,Q^2) - 2xF_1(x,Q^2)\Big)\Big], \tag{1.1}$$

where y is the fractional energy loss of the electron and x is the fraction of the proton's longitudinal momentum carried by the struck parton:

$$y = \frac{p_p \cdot q}{p_p \cdot p_e}, \quad x = \frac{Q^2}{2p_p \cdot q}, \quad \text{where} \quad Q^2 = -q^2. \tag{1.2}$$

Measuring the scattering angle θ, initial energy E, and final energy E' of the electron is crucial for the cross-section measurement as these variables are used to determine

$$y = 1 - \frac{E'}{2E}(1-\cos\theta) \quad \text{and} \quad Q^2 = 2EE'(1+\cos\theta). \tag{1.3}$$

The *structure functions* F_1 and F_2 encode the integral over the charged partonic internal structure of the hadron. The 1969 DIS experiment confirmed, for the probed energies, that the F_2 structure function only depends on x, and not on Q^2, as predicted by Bjorken [27]. This *Bjorken scaling* was the first experimental evidence of point-like particles within the proton, due to the fact that increasing the energy of the probe did not resolve any further structure within the proton. The subsequent confirmation of the Callan-Gross relation [28],

$$2x \cdot F_1 = F_2, \tag{1.4}$$

via measurements of inelastic scattering cross-sections, confirmed that quarks carry spin-½, making them fermions. This relation, derived via considerations regarding the electric and magnetic contributions to the cross-section, is shown in Figure 1.6, where the dashed line represents a ratio of unity. If quarks were spin 0 particles (bosons), $2x \cdot F_1/F_2$ would equal zero, which is not supported by data. These developments led to an acceptance of the quark parton model [29], originally introduced by Richard Feynman. In this model, parton momentum is considered to be parallel to that of a high-momentum parent nucleon, with the incident probe interacting directly with a "free" parton due to time dilation. Information related to individual quark flavors (e.g., up and down) would have to wait for the advent of *parton distribution functions*, which are discussed in Section 1.4.

From DIS experiments, it was also determined that quarks only carry approximately half of the proton's momentum, with a yet undiscovered neutral constituent contributing the remaining half. This particle, which happened to be the mediator of the strong force, would elude physicists until 1979, when multiple experiments at the Positron-Electron Tandem Ring Accelerator (PETRA) at DESY confirmed the existence of gluons, namely JADE [30], MARK–J [31], PLUTO [32] and TASSO [33]. This discovery was also accomplished using the electromagnetic force, wherein an electron and positron annihilate to form a quark, antiquark, and a gluon ($e^+e^- \to q\bar{q}g$). Using conservation laws, these experiments were able to confirm, via measurement of events with three distinct signatures, the presence of an undiscovered boson. To better understand the experimental observable, referred to as a "jet", that was measured by the experiments at PETRA, the QCD phenomena of

asymptotic freedom and confinement, resulting from gluon self-interaction, must first be explored.

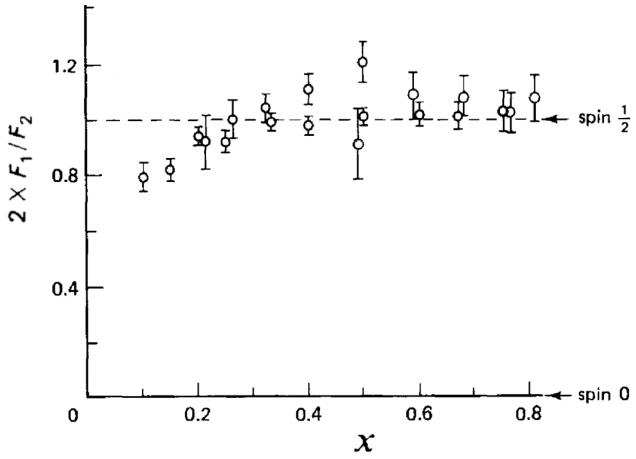

Figure 1.6: Demonstration of Callan-Gross relation, $2x \cdot F_1 = F_2$, plotted as a function of x. Figure taken from Ref [16], where the author has plotted data from Ref. [34].

1.2.2 Asymptotic Freedom and Confinement

The previously mentioned coupling constant, α, of the electromagnetic force is in reality not entirely constant. QED has an *effective coupling* due to vacuum polarization [35], and as distance increases, a weaker coupling is observed. The occurrence of gluon self-interaction results in a QCD coupling that behaves opposite to that in QED. The strong force coupling constant, α_s, depends on the momentum transferred during the interaction, Q, as shown in Figure 1.7. At low values of Q, corresponding to long length scales, the coupling grows exponentially, while at high momentum and small distances, the coupling approaches zero. These features are the true source of the QCD phenomena of asymptotic freedom (high-Q, small distance) and confinement (low-Q, large distance).

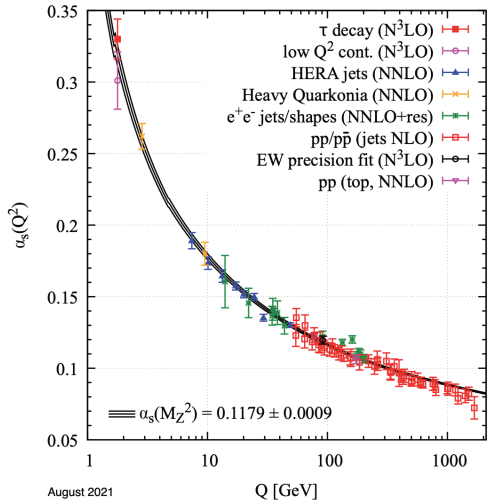

Figure 1.7: Summary of experimental measurements of the running coupling constant α_s as a function of the momentum transfer Q. Figure taken from Ref. [36].

The physical implication of α_s approaching zero is that, at small distances, quarks and gluons, referred to collectively as *partons*, move freely within the nucleus. This behavior was confirmed by the previously mentioned DIS experiments [24, 25], where asymptotic freedom allows for interacting directly with individual

partons when using a high-energy probe. On the theoretical side, asymptotic freedom allows for calculations within QCD to be approximated [37], to high accuracy, using a perturbative expansion in terms of Feynman diagrams which contribute to a given process. The interactions shown in Figure 1.4 can also be represented by infinite additional diagrams, with gluon-gluon "loops" occurring prior to the final-state. In a Feynman diagram, each additional vertex contributes a factor α_s. This allows for analytical solutions, using perturbative QCD (pQCD), due to higher order terms (loop diagrams) having a negligible impact on the result.

The phenomenon of confinement within QCD results in the behaviour shown in Figure 1.8 where: (i) a $q\bar{q}$ pair is produced in a high-momentum transfer interaction; (ii) as the pair separates, the potential energy stored in the virtual gluon field holding them together grows; (iii) eventually this energy is enough to produce new $q\bar{q}$ pairs; (iv) this process continues, along with the radiation of collinear gluons, until (v) the energy in the $q\bar{q}$ pairs is low enough to form colorless hadrons.

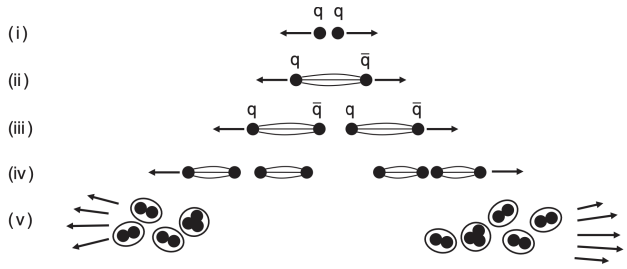

Figure 1.8: Diagram of the hadronization process resulting from QCD confinement. Figure taken from Ref. [17].

The formation of stable particles represented by Figure 1.8 is termed hadronization. This process cannot be described using pQCD, as α_s is too large, and must instead be approximated using phenomenological models [38]. As these stable particles,[2] which for the most part travel collinear to the original parton, traverse detectors built around the collision point, they deposit energy. This is the primary mechanism through which the measurement presented in this transcript is carried out, where the measured quantity is a "jet" of collimated energy contained within a cone of a given radius. At leading order, these jets correspond to single partons originating from a high-momentum transfer inelastic collision, or *hard-scattering*. In QCD, jets are interpreted as the result of the fragmentation of partons participating in a hard-scattering process. The measurement of jet cross-sections is one of the most powerful tools at the disposal of LHC experiments to explore the structure of the matter over a broad kinematic range.

1.2.3 Factorization

DIS experiments, as well numerous other cross-section measurements, rely on the QCD phenomenon of asymptotic freedom, allowing for the "factorization" of long-distance behaviour from that of perturbatively calculable short-distance behaviour [39]. In the DIS center-of-mass frame between an electron and proton, the proton is Lorentz contracted making the path-length the electron must traverse incredibly short. The constituent partons can be considered frozen during this period, i.e., not interacting with one another and each carrying a fraction of the momentum of the proton. Thus, if the momentum transfer is sufficiently high, the electron sees only individual partons with which it can interact. The subsequent process of hadronization occurs at timescales well beyond those of the hard-scatter and can therefore be considered as an entirely unique process. The same principle can also be applied to proton-proton collisions, as demonstrated by a diagram-level view of factorization in Figure 1.9 where two jets are detected in the final-state.

[2]Particles are considered *stable* if they have a lifetime longer than 30 ps and are not a muon or neutrino.

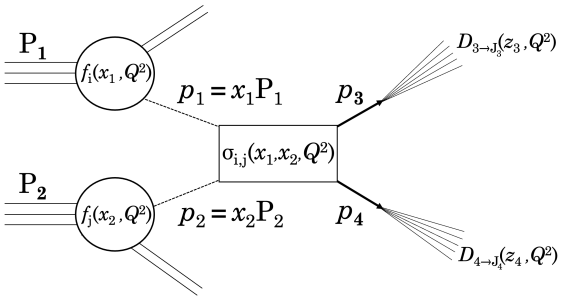

Figure 1.9: Diagram of factorization of hadronic collision between two protons. Two jets are measured in the final-state.

The protons are represented by their four-momentums, P_1 and P_2, with partons of flavor i and j participating in the hard-scattering, respectively. This long-distance, non-perturbative, behavior of the initial-state is described by parton distribution functions (PDFs) f_i and f_j, which give the probability of selecting a parton with flavor i (j) with a momentum fraction x_1 (x_2) of P_1 (P_2). The box containing the cross-section $\sigma_{i,j}$ represents the hard-scattering process, from which we can only experimentally observe the jets (J_3, J_4) produced by the resultant partons, represented by their momentums p_3 and p_4. The non-perturbative fragmentation of these partons into stable hadrons, which eventually form jets carrying a fraction z of the parton's momentum, is described by the fragmentation functions $D_{3\to\mathrm{J}_3}$ and $D_{4\to\mathrm{J}_4}$. By applying factorization, the cross-section describing the inelastic scattering of two protons, as represented by Figure 1.9, can be written as [40]:

$$\begin{aligned} d\sigma_{pp\to\mathrm{JJ}} \approx \sum_{1234} \int dx_1 \int dx_2 \int dz_3 \int dz_4 \; f_i(x_1,Q^2) \otimes f_j(x_2,Q^2) \qquad & \text{[initial-state PDFs]} \\ \otimes\, d\sigma_{i,j}(x_1,x_2,Q^2) \qquad & \text{[hard-scatter cross-section]} \\ \otimes\, D_{3\to\mathrm{J}}(z_3,Q^2) \otimes D_{4\to\mathrm{J}}(z_4,Q^2) \qquad & \text{[fragmentation functions]} \end{aligned} \tag{1.5}$$

In order to relate a cross-section to an experimental observable, physicist make use of *luminosity*. The instantaneous luminosity ($\mathcal{L}$) serves as the proportionality factor between the number of events per second, ${}^{d\mathrm{R}}/_{d\mathrm{t}}$, and the cross-section, σ_A, for a given process "A". This relationship can be written as

$$\frac{d\mathrm{R}}{d\mathrm{t}} = \mathcal{L} \cdot \sigma_\mathrm{A}, \tag{1.6}$$

where the units of luminosity are $\mathrm{cm}^{-2}\mathrm{s}^{-1}$. In particle colliders, the beams are not continuous streams of particles, but are instead composed of "bunches" of particles which have a defined size and spacing. Using these properties, the instantaneous luminosity is defined as:

$$\mathcal{L} = \frac{f \cdot N^2}{4\pi\sigma^2}, \tag{1.7}$$

where f is the bunch cross frequency, N is the number of particles per bunch, and the denominator corresponds to the cross-sectional area per bunch. The term "luminosity" in this paper will only be used to refer to the integrated luminosity, L, which has units of inverse cross-section (b^{-1})

$$\mathrm{L} = \int \mathcal{L} d\mathrm{t}. \tag{1.8}$$

A barn, b, is a unit used to express cross-sectional areas in nuclear physics and is equal to 10^{-24} cm^2. Therefore, σ_A for any process, such as the occurrence of dijets in pp collisions, can be calculated by counting the occurrences of said dijets and dividing by the luminosity.

1.3 Jets

A large number of LHC analyses make use of jets, which can be thought of as an agreement between experimentalists and theorists, providing an intermediary through which measurements and predictions can be compared to one another. In the process demonstrated by Figure 1.9, jets are produced back-to-back due to the conservation of momentum in hard-scatterings. This feature is demonstrated in Figure 1.10, where an event display from the ATLAS detector is shown in which a pair of back-to-back jets (dijet) have been produced as a result of two quarks from colliding protons scattering off one another, resulting in fragmentation of the proton, and subsequent hadronization into stable particles. In order to characterize jet properties, we first need to establish a set of coordinates with which they can be described.

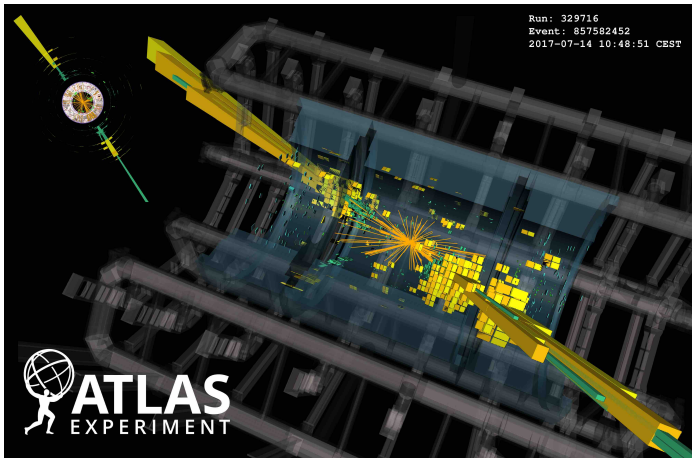

Figure 1.10: Event display from 2017 pp collision at a center-of-mass energy of 13 TeV. The orange lines denote tracks, while the green and yellow voxels represent energy deposited in the ATLAS calorimeter. A transverse view of the dijet pair is given in the top-left portion of the figure.

1.3.1 Jet Kinematics

Jets are described using four-vectors composed of the transverse momentum p_{T}, the jet mass m, a polar angle related variable termed "pseudorapidity" η, and azimuthal angle ϕ. These variables are directly related to the jet's energy and momentum (E, p_x, p_y, p_z), with the advantage that η and ϕ have a straightforward mapping to the detector being used to perform the measurement.

In collider experiments, the z–axis coincides with the beam-axis, such that the resultant sum of p_x and p_y of all the particles produced by a collision is effectively zero. The p_{T} of a jet is the magnitude of these two components: $p_{\mathrm{T}} = \sqrt{p_x^2 + p_y^2}$. Complications including detector response, inability to detect neutrinos, and QCD related phenomena result in unbalanced dijet pairs. The mass of a jet is simply the sum of the mass of each particle contained within a jet, such that $E_{\mathrm{T}} = \sqrt{p_{\mathrm{T}}^2 + m^2}$, where E_{T} is the transverse energy of the jet. The jet mass does not play a role in the measurement discussed in this thesis. Details regarding how jet constituents are defined are discussed in Section 1.3.2. The angle ϕ is defined as $\phi = \tan^{-1}\left(p_y/p_x\right)$, such that a perfectly back-to-back dijet pair would have a $\phi = \pi$. Pseudorapidity is defined as $\eta = -\ln\tan^{-1}\left(\theta/2\right)$, where θ is the polar angle. A comparison between these two variables is shown in Figure 1.11, with values of η close to zero being referred to as "central", and large values of $|\eta|$ being referred to as "forward".

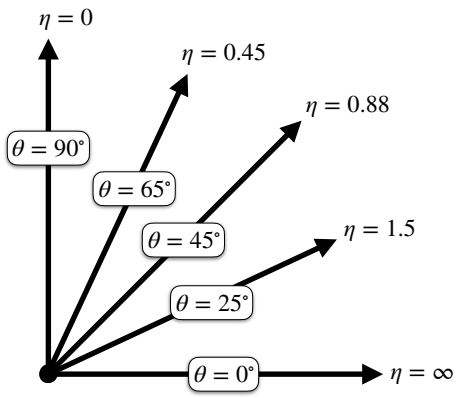

Figure 1.11: Comparison between positive η and θ values.

1.3.2 Jet Algorithms

Jets are collimated sprays of particles generated by a high-momentum transfer parton-parton collision. They are formed via the process of jet reconstruction, using clustering algorithms, whereby the momenta of fragmenting particles generated by hadronization are re-summed [41]. The resolving power of a jet is set via a radius parameter $R = \sqrt{\eta^2 + \phi^2}$, such that gluon radiation occurring inside this radius is considered part of the jet. A number of clustering algorithms have been used in the fields of high-energy and nuclear physics, which can be summarized using two broad categories: cone and sequential recombination. A successful algorithm must not only be well-defined, allowing for use by both experimentalists and theorists, but should also be computationally light. Cone algorithms represent some of the earliest attempts at providing a measureable object through which jets could be studied [42–44]. To achieve this, they iteratively cluster particles in (η-ϕ) space, with the resulting object being a cluster of particles that, in principle, corresponds to the same hard-scattered parton. Cone algorithms are no longer in standard use by experiments at the LHC, or the Relativistic Heavy Ion Collider (RHIC), as they tend to lack at least one of the two defining characteristics that all sequential recombination algorithms have: infrared and collinear safety. Together, these two features guarantee that a QCD observable is well-defined within the realm of perturbation theory.

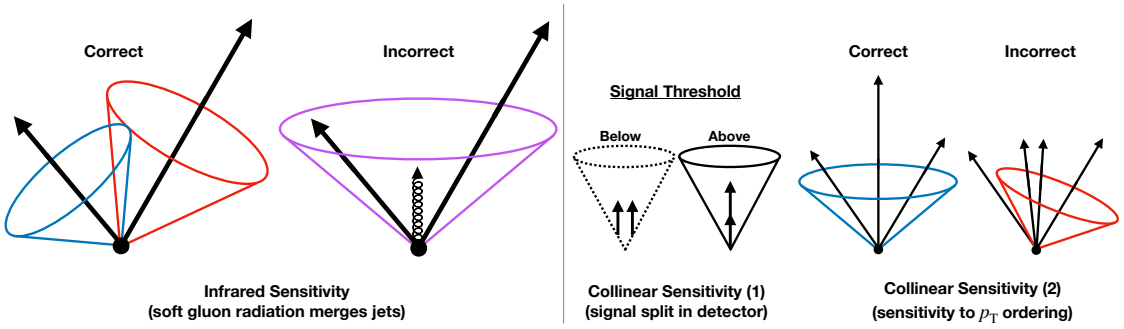

Figure 1.12: Visual representation of infrared and collinear sensitivity of jet algorithms.

Figure 1.12 presents a qualitative example of infrared (left) and collinear (right) sensitivity, i.e. what happens if an algorithm is not equipped to handle the occurrence of these phenomena. Algorithms which are not infrared safe are sensitive to low-energy (soft) gluon emissions, making them particularly problematic for theorists who rely on pQCD calculations. If an algorithm is sensitive to small angle, or collinear, splitting of the hard particle, altering either the amount of jets observed or the content of jets, then it is not collinear safe.

This aspect of the jet reconstruction has particular relevance to the work presented here, as the jets used are composed of only calorimeter towers (discussed in Section 3.3.1), and therefore no tracking information is taken into account regarding how many particles traversed the active area of our detector.

Sequential recombination algorithms cluster particles in momentum space starting from the assumption that particles close to one another in (η–ϕ) have similar p_{T}. Examples of these algorithms, in order of creation, include the k_t [45], Cambridge/Aachen [46], and anti-k_t [47], which all share the same underlying distance equations, $d_{i,j}$ and $d_{i,B}$:

$$d_{i,j} = min(p_{\mathrm{T},i}^{2a}, p_{\mathrm{T},j}^{2a}) \times \frac{\Delta_{ij}^2}{R^2}, \tag{1.9}$$

$$d_{i,B} = p_{\mathrm{T},i}^{2a}. \tag{1.10}$$

In Equation 1.9, $p_{\mathrm{T},x}$ is the transverse momentum of particle $x \in [i,j]$ and $\Delta_{ij}^2 = \sqrt{\eta_{ij}^2 + \Delta\phi_{ij}^2}$ defines the (η–ϕ) separation between particles i and j. The parameter a sets the relative weight between the geometrical (Equation 1.9) and momentum (Equation 1.10) components of the algorithm, with different values corresponding to different algorithms as follows: $p = 1$ (k_t), $p = 0$ (Cambridge/Aachen), and $p = -1$ (anti-k_t). In practice, this means that the k_t algorithm first clusters low p_{T} (soft) particles, the Cam/Aachen algorithm only depends on the geometrical factor, and the anti-k_t algorithm first clusters high-p_{T} (hard) particles.

Each algorithm first finds the smallest $d_{i,j}$ in the entire set of particles. If $d_{i,j}$ is smaller than $d_{i,B}$, the four-vectors of particles i and j are combined, replacing i and j as a new "particle" in the set. If $d_{i,j}$ is larger than $d_{i,B}$, the i^{th} particle is labelled as a jet and removed from the set. Once all particles in the set have been clustered the algorithm is complete, the results of which are shown for an example event in Figure 1.13. Here it should be noted that access to individual particles for clustering is only possible in simulation. In data, energy deposited in cells of electromagnetic and hadronic calorimeters is clustered to form jets (see Section 3.3.1).

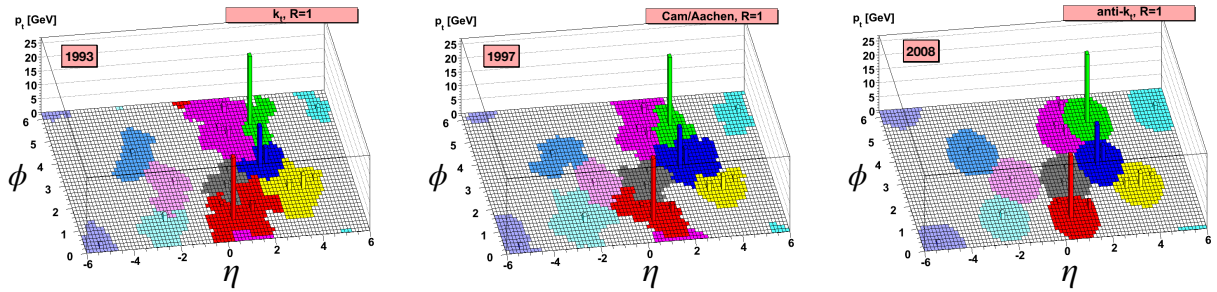

Figure 1.13: Sequential recombination jet clustering algorithms in the η-ϕ plane. Three high-p_{T} jets (red, blue, green) are visible in all algorithms. Figure adapted from Ref. [47].

Although always favored by theorists, due to them being both infrared and collinear safe, sequential clustering algorithms are more computationally expensive than cone algorithms. The creation of the FastJet software package [48] led to their widespread use within the experimental community, such that sequential recombination algorithms are now favored by both parties. In particular, the anti-k_t algorithm is the default jet clustering algorithm used by all LHC experiments.

1.4 Parton Distribution Functions

Looking to the proton structure, at low energies one can envision a simple model consisting of two up quarks, each with $+2/3$ electric charge, and one down quark with $-1/3$ electric charge, held together by the strong force via gluons. This depiction of three valence quarks is shown in the left portion of Figure 1.14. At smaller distances and shorter timescales, the picture of the proton becomes more complicated, with gluons splitting into short lived quark-antiquark pairs from the quark sea or into gluon-gluon pairs, as shown in the right portion of Figure 1.14.

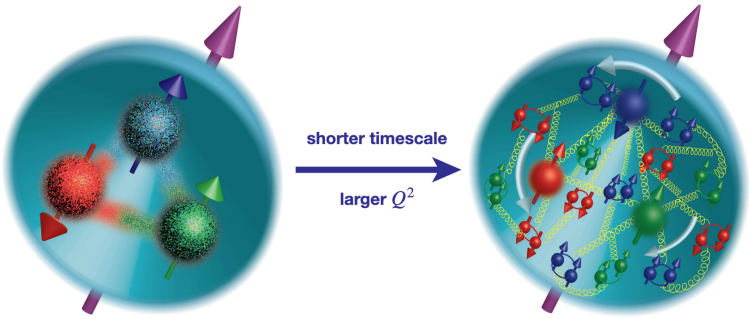

Figure 1.14: A simplified representation of the proton (left), containing two up quarks (blue and green) and a single down quark (red), held together by gluons. At shorter timescales and higher energies, quantum fluctuations can be resolved and the proton picture becomes more convoluted (right). Figure taken from Ref. [49].

The most common approach of describing the proton's structure is in terms of the momentum of its constituents through the use of PDFs, which are data driven parameterizations that provide the probability of finding a parton of a given species carrying a fraction x of the nucleon momentum. PDFs are derived by fitting available cross-section data for QCD processes at various (x,Q^2), where the PDFs are free parameters that are then extracted. The bulk of this data is comprised of precise DIS measurements, a selection of which are shown in Figure 1.16 for F_2, where the lack of dependence on Q^2 observed for $x > 10^{-2}$ is the previously mention Bjorken scaling. The F_2 structure function represents a charge-weighted sum of quark PDFs and can be defined as:

$$F_2(x, Q^2) = x \sum_i e_i^2 \cdot q_i(x, Q^2), \tag{1.11}$$

where x is the Bjorken scaling variable, e_i is the electric charge of a parton with flavor i, and q_i is the PDF of a parton with flavor i.

The H1 and ZEUS experiments at HERA provided incredible input to the extraction of PDFs with data from $e^- + p$ DIS at a center-of-mass energy of 318 GeV [50]. An example of PDFs obtained from HERA data is shown in Figure 1.15, where the y-axis represents the PDF scaled by the parton fractional momentum x. At high x ($\sim 2 \times 10^{-1}$), an approximately 2–to–1 ratio between up and down valence quarks is observed, as one would expect from the naive proton model shown in Figure 1.14. At lower x values, the gluon and sea quark distributions dominate. This is a result of the radiation of gluons, which increases with Q^2, and their subsequent splitting into quark-antiquark pairs. The behavior of the gluon PDF at low-x suggests a divergence in the low-x region, beyond $x \sim 10^{-4}$. If the distribution continued to trend towards infinity, it would violate unitarity. Therefore, at some x value less than 10^{-4}, the gluon distribution must change behaviour; this anticipated phenomenon is referred to as *gluon saturation* [51]. As the gluon density increases, gluon recombination is thought to aid in reducing the growth of the gluon PDF [52, 53].

A fundamental characteristic of PDFs is that they are universal, meaning that measurements of different

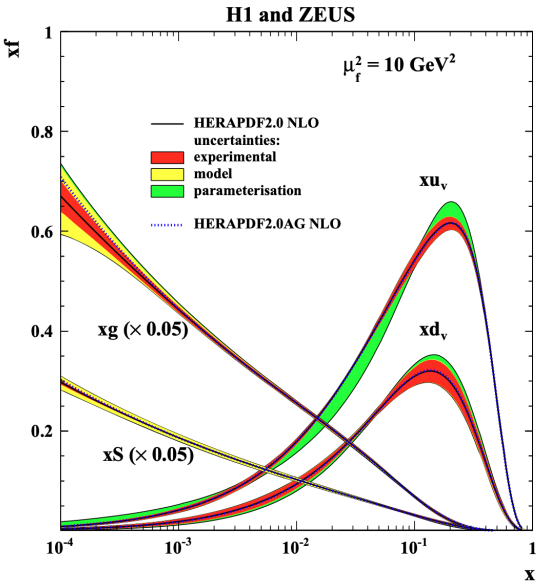

Figure 1.15: PDFs obtained by the H1 and ZEUS experiments at the HERA lepton-proton collider at a factorisation scale $\mu_f^2 = 10$ GeV^2. The sea quark and gluon distribution have been scaled down by a factor of 20. Figure taken from Ref. [54].

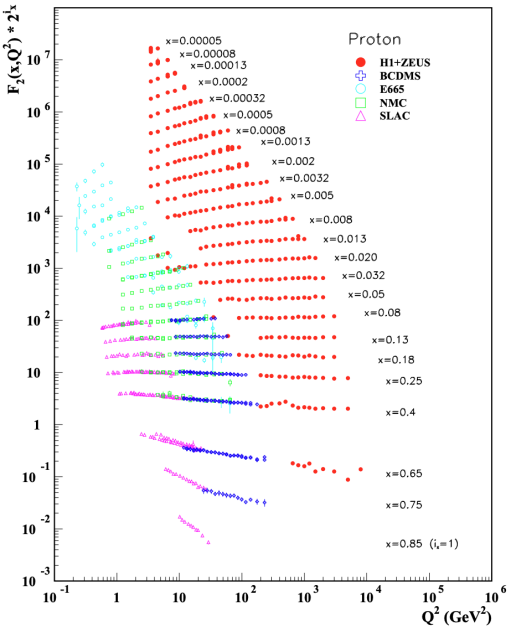

Figure 1.16: Summary of proton structure function F_2 data as a function of Q^2, as measured by DIS experiments. Figure taken from Ref. [55].

processes can be used to predict observables at (x,Q^2) not yet probed using DIS, or more recent, measurements. This phenomena is directly related to the Bjorken scaling observed for F_2, and can be described using the Dokshitzer-Gribov-Lipatov-Altarelli-Parisi (DGLAP) equations [56–58], which encode the Q^2 evolution of PDFs. The Balitsky-Fadin-Kuraev-Lipatov (BFKL) equations [59, 60] describe the x evolution of PDFs. By using the factorization approach outlined in Section 1.2.3, together with DGLAP and BFKL evolution of PDFs, theoretical predictions of jet cross-sections at LHC energies can be obtained. An ATLAS measurement [61], with pQCD predictions, of the jet cross-section in proton-proton (pp) collisions is shown in the left panel of Figure 1.17. The ratio between theory and data is presented in the right two panels, where good agreement between experimental and pQCD predictions is observed.

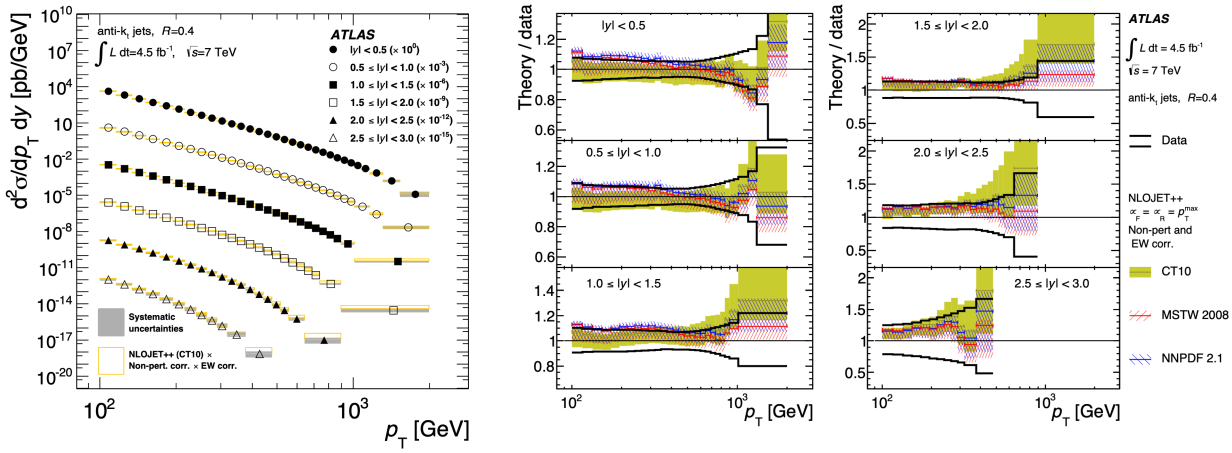

Figure 1.17: Double-differential jet cross-section as a function of the jet p_T in bins of rapidity (left) compared to pQCD predictions. Ratio of theory calculations to data (right). Figure taken from Ref. [61].

1.4.1 Nuclear Modification

All prior discussion in this thesis has assumed that the two interacting partons are extracted from protons that exist in a vacuum. This assumption is valid for a large number of analyses carried out by experiments at the LHC, where pp collisions are studied in order to further our understanding of the Standard Model, and to search for physics beyond the Standard Model. Alternatively, physicists can study the impact of the nuclear environment on QCD observables by colliding ions. At the forefront of this effort is the study of the quark-gluon plasma (QGP), a deconfined state of matter, present at the beginning of the universe, where the partonic density and energy ($\alpha_s \sim 0$) are sufficiently high such that quarks and gluons can exist in a deconfined plasma state where they move freely within the medium, constantly interacting through the strong force. This state of matter is reproduced by colliding ions, typically lead (Pb) at the LHC, at speeds approaching that of light. The study of the formation of hadronic matter from QGP is vital to our understanding of how the early universe evolved into what we observe today.

The impact of the nuclear environment on experimental observables can be classified using two categories: *cold nuclear* and *hot nuclear* matter effects. Cold nuclear matter effects are related to initial-state differences between free and bound nucleons, and are described using nuclear PDFs (nPDFs) [62]. Hot nuclear matter effects are related to the impact of the QGP on final-state observables and are probed via partons generated by the hard-scatter which must traverse the strongly interacting medium. The PDF shown in Figure 1.15 is for the free proton. When in the presence of other nucleons, *nuclear modification* of the free proton PDF results. These modifications were originally studied via fixed-target DIS experiments at the Super Proton Synchrotron[3] at CERN in the late '70s and early '80s, where the EMC collaboration observed that muon scattering rates in deuterium (scaled by a factor of 28) and iron were different [63]. The modification of the free proton PDF f_i^p with respect to the nPDF f_i^A is given by

$$R_i^A(x, Q^2) = \frac{f_i^A(x, Q^2)}{A \cdot f_i^p(x, Q^2)}, \tag{1.12}$$

where A is the mass number and i is the parton species. The nuclear modification R_i^A of the free proton PDF in four approximated x regimes, using a parameterization developed by Eskola, Paakkinen, Paukkunen, and Salgado (EPPS), is shown in Figure 1.18.

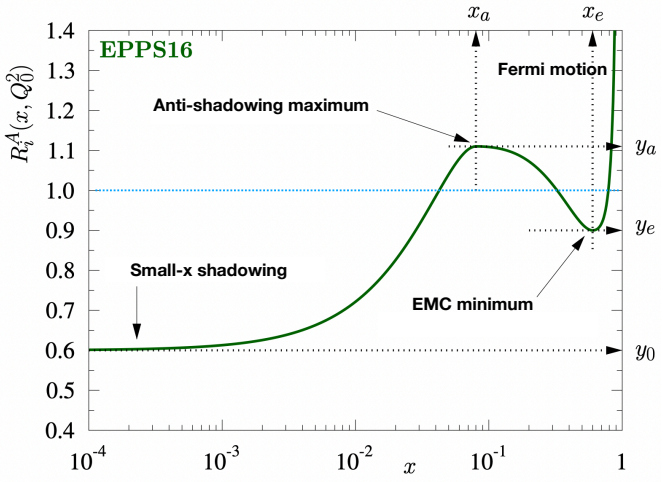

Figure 1.18: Nuclear modification of free proton PDF, resulting from cold nuclear effects. The blue line at $R_i^A = 1.0$ corresponds to no nuclear modification. See Ref. [62] for newer EPPS21 nPDFs. Figure adapted from Ref. [64].

[3]The Super Proton Synchrotron is now part of the accelerator complex which provides beam to the Large Hadron Collider.

The four approximate x regimes correspond to:

- **Shadowing:** Suppression of bound proton PDF at low-x ($x < 0.1$) relative to the geometrically scaled free proton PDF due to destructive interference arising from the partonic density [65, 66].
- **Anti-shadowing:** An enhancement ($R_i^A > 1$) in the region $0.1 < x < 0.25$ due to the momentum sum rule [67].
- **EMC effect:** The European Muon Collaboration (EMC) first measured the modification of the nucleon structure function F_2^N in 1983 [63]. The origin of this suppression of nPDFs for $0.25 < x < 0.8$ is not yet fully understood, but a proposed cause is short range correlations between nucleon pairs [68].
- **Fermi motion:** The enhancement of nPDFs for $x > 0.8$ is due to the Fermi motion of the nucleons within the nucleus [69].

A lack of experimental data from which nPDFs can be derived exists, resulting in areas of (x, Q^2) phase-space for which nPDFs are under-constrained, when compared to their PDF counterpart. Measurements performed using heavy ions, such as Xe, Au and Pb, provide a benchmark against which QCD predictions can be compared, allowing for constraint of nPDFs.

1.5 Heavy Ion Measurements

Together, hot and cold nuclear matter effects in heavy ion collisions can be described by modifying Equation 1.5:

$$\begin{aligned} d\sigma_{\mathrm{PbPb}\to \mathrm{J}'\mathrm{J}'} \approx & \sum_{1234} f_i(x_1) \otimes f_j(x_2) && \text{[initial-state nPDFs]} \\ & \otimes d\sigma_{i,j}(x_1, x_2, Q^2) && \text{[hard-scatter cross-section]} \\ & \otimes P_{\mathrm{J}_3\to \mathrm{J}'_3} \otimes P_{\mathrm{J}_4\to \mathrm{J}'_4} && \text{[medium-induced effects]} \\ & \otimes D_{3\to \mathrm{J}'_3}(z_3, Q^2) \otimes D_{4\to \mathrm{J}'_4}(z_4, Q^2) && \text{[fragmentation functions]} \end{aligned} \tag{1.13}$$

where, f_i and f_j are now nPDFs and $P_{\mathrm{J}\to \mathrm{J}'}$ describes the impact of hot nuclear matter effects on the jet formation. As the hard-scatter parton traverses the QGP, it interacts with the medium through both collisional and radiative energy loss. Together, these produce the phenomena of jet quenching [40, 70], whereby heavy ion jet observables are modified with respect to the geometrically scaled proton-proton expectation.

As previously stated, the study of heavy ion collisions is primarily directed at the understanding of QGP. Before discussing relevant measurements associated with heavy ion collisions, the concept of centrality as a means to characterize the geometry of heavy ion collisions systems must first be introduced.

1.5.1 Centrality

In a heavy ion collision, the amount of overlap between the colliding nuclei is directly related to the baryonic density, and therefore the amount of QGP produced. This overlap is quantified by the *centrality*, a fundamental concept in nearly all heavy ion measurements, which gives physicists an intuitive handle on the event geometry via measurements of the soft particle production. The overlap between nuclei is defined by the *impact parameter*, b, which is the transverse distance between the centers of the colliding nuclei. The impact parameter between two Lorentz-contracted nuclei is shown in the left portion of Figure 1.19. The overlap region is demonstrated by dashed grey lines, where QGP formation resulting from the collision of participant nucleons takes place.

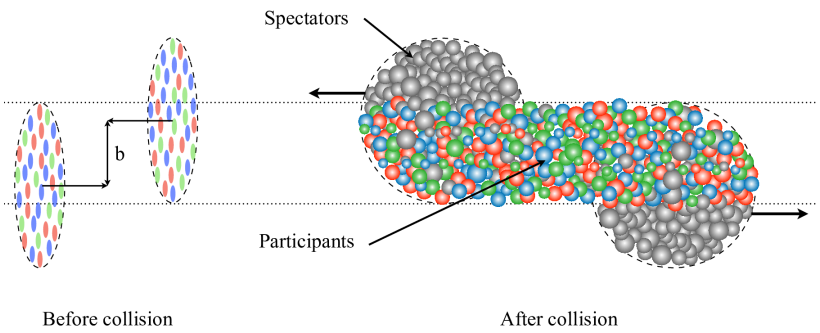

Figure 1.19: Before and after cartoon of a heavy ion collision, showing the impact parameter, b, between colliding nuclei. The overlap region is denoted by dashed lines, inside which colored participants are shown. Spectators continue on their paths toward forward detectors. Figure taken from Ref. [71].

The impact parameter cannot be directly measured. Instead, experimental observables that are measured in a region of the detector decoupled from the physics measurement, such as the energy recorded in a forward calorimeter, are used to approximate how many nucleons participated in the collision. The centrality is then determined by breaking the measured distribution into centiles, as shown in Figure 1.20 for both Pb+Pb (blue) and Xe+Xe (red) collision systems. A high centrality corresponds to low event activity, or high impact parameter, while a low centrality corresponds to a large overlap between colliding nuclei. To get from a measured observable to a geometric quantity characterizing the collision, such as the impact parameter, Glauber models are utilized [72]. An example of a heavy ion collision between two gold nuclei, using a Glauber Monte Carlo method, is shown in Figure 1.21, where N_{part} is the total number of nucleons from either nuclei that experienced more than one collision.

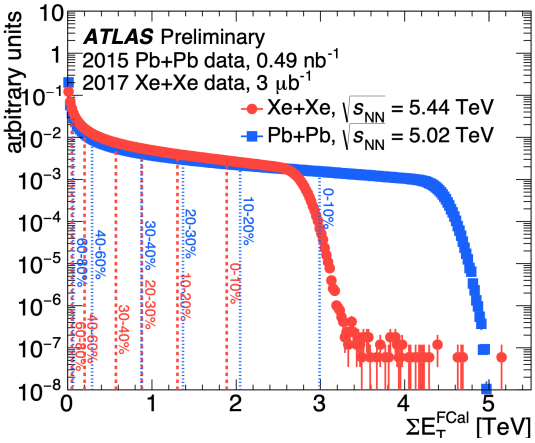

Figure 1.20: Centrality for Pb+Pb (blue) collisions at $\sqrt{s_{\text{NN}}}$= 5.44 TeV and Xe+Xe (red) at $\sqrt{s_{\text{NN}}}$= 5.02 TeV, determined using the sum of transverse energy in the forward calorimeter. Figure taken from Ref. [73].

Generally, the approach is to model a heavy ion collision by approximating the transverse shape of each nuclei using a Woods-Saxon distribution:

$$\rho(r)\,dr = \rho_0 \frac{1+\omega(r^2/R^2)}{1+e^{(r-R)/a}} dr, \tag{1.14}$$

where r and ρ_0 are the radial distance from, and density at, the nuclei's center, respectively. The nuclear radius is set by R, and a describes how quickly the nuclear density falls off with increasing r. Nuclear radii are determined from fits to experimental results [74]. Nuclei whose maximum density is at $r > 0$ are accounted for with the parameter ω. The nuclei are then generated by sampling from $\rho(r)\,dr$ to position individual

nucleons, and an impact parameter is randomly sampled from $d\sigma/db = 2\pi b$. A collision between nucleons is considered to have occurred if the distance between their centers $d < \sqrt{\sigma_{\mathrm{NN}}\,\pi}$, where σ_{NN} is the inelastic nucleon-nucleon cross-section derived from parameterizations to data.

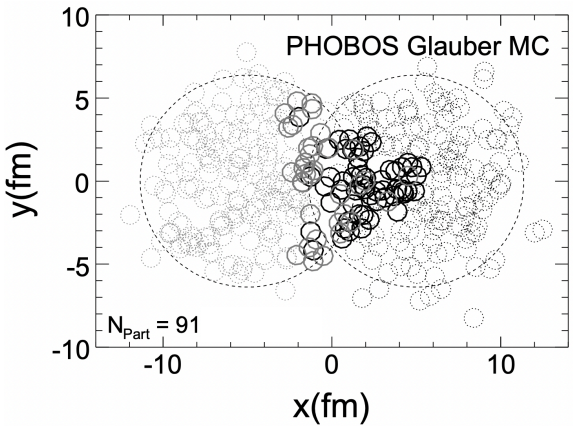

Figure 1.21: Glauber Monte Carlo simulation of a $\sqrt{s_{\mathrm{NN}}} = 200$ GeV Au+Au collision, shown in the transverse plane. Solid, dark-colored, circles represent nucleons that participated in the collision. Dashed circles represent spectators. Figure taken from Ref. [75].

1.5.2 Dijet Asymmetry

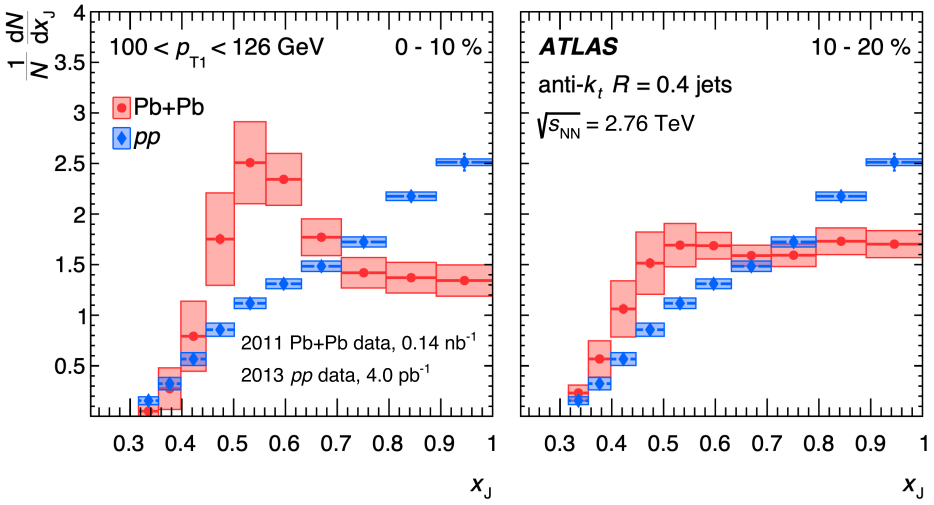

Figure 1.22: Dijet balance for pp (blue) and Pb+Pb collisions (red) for 0–10% (left panel) and 10–20% (right panel) centrality intervals, in a fixed p_{T_1} bin. The distributions have been normalized by the total number of dijet pairs. Figure taken from Ref. [76].

In a hard-scatter collision between two protons, the momentum of the two resultant partons is balanced. The jets produced by the hadronization are therefore most likely to have equal momentum, with deviations occurring primarily due to the soft radiation of gluons. Figure 1.22 demonstrates that this assumption is valid for pp collisions recorded in 2013 at $\sqrt{s_{\mathrm{NN}}} = 2.76$ TeV, where

$$x_{\mathrm{J}} = \frac{p_{\mathrm{T}_2}}{p_{\mathrm{T}_1}}, \tag{1.15}$$

is the dijet balance, and N is the total number of dijet pairs in the given p_{T_1} interval. The blue markers, representing the pp data, indicate that an x_{J} between 0.9 and 1.0 is most favored. This conclusion holds true

for all p_{T_1} intervals examined in Ref. [76]. Looking to the red markers in Figure 1.22, it is apparent that Pb+Pb collisions due not share the same preference for balanced leading and subleading jets,[4] where the most likely x_{J} is approximately 0.55 for both 0–10% and 10–20% centrality intervals. This imbalance is due to interactions of the jet's constituents with the QGP, resulting in a path length dependent loss of energy to the medium. Both higher p_{T_1} bins and more peripheral centrality intervals produce more balanced dijet pairs, due to less interaction with the medium and less QGP formation, respectively. Similar observations of dijet imbalance have been made for both different energies [77] and collision systems [78], as well as for jets of various radii [79].

1.5.3 Nuclear Modification of Jet Yield

Although the measurement of x_{J} does give incite into the role of QGP on jet formation, it in no way accounts for correlations in the loss of energy between the two leading jets. For instance, if both the leading and subleading jets are equally quenched, x_{J} will still have a value of unity. A separate observable, which is sensitive to the loss of energy by individual jets, is the ratio between the yield of jets in heavy ion and pp collisions:

$$R_{\mathrm{AA}} = \frac{\frac{1}{N_{\mathrm{evt}}}\frac{d^2N_{\mathrm{jet}}^{\mathrm{cent}}}{dp_{\mathrm{T}}dy}}{\langle T_{\mathrm{AA}}\rangle\frac{d^2\sigma_{\mathrm{jet}}^{pp}}{dp_{\mathrm{T}}dy}}, \tag{1.16}$$

where the numerator represents the per-event yield of jets in a given heavy ion centrality bin, and the denominator is the cross-section in pp collisions. The mean nuclear thickness function, $\langle T_{\mathrm{AA}}\rangle$, accounts for the geometric enhancement of heavy ion collisions in a given centrality interval relative to pp collisions and has units of inverse cross-section [72]. If nucleus-nucleus collisions were simply a superposition of the individual nucleon-nucleon collisions, R_{AA} would have a value of unity. Instead, final-state interactions between the strongly interacting parton shower and the QGP result in an R_{AA} less than one. An inclusive R_{AA}, integrated over rapidity, is shown in Figure 1.23, where four different Pb+Pb centrality intervals are reported. As expected, central events (0–10%), in which QGP formation is greatest, are most suppressed, with higher p_{T} jets being less quenched. Similar observations were also made by previous measurements at lower energies [80, 81].

The nuclear modification of jet yields can also be studied in smaller systems, such as p+Pb ($R_{p\mathrm{Pb}}$) or d+Au ($R_{d\mathrm{Au}}$). No QGP formation has been observed in these systems [83, 84], making them excellent candidates for the study of initial-state effects attributable to the behaviour of cold nuclear matter. These smaller systems will be explored further in Chapter 2. Additionally, the nuclear modification can also be constructed using jet yields in different centrality intervals, typically the most central and most peripheral. This formalism is referred to as the central-to-peripheral ratio:

$$R_{\mathrm{CP}}(\mathrm{x,y,z}) = \frac{\frac{1}{\langle T_{\mathrm{AB}}^{\mathrm{central}}\rangle}\frac{1}{N_{\mathrm{evt}}^{\mathrm{central}}}\frac{d^2N_{\mathrm{dijet}}^{\mathrm{central}}}{d\mathrm{x}dydz}}{\frac{1}{\langle T_{\mathrm{AB}}^{\mathrm{peripheral}}\rangle}\frac{1}{N_{\mathrm{evt}}^{\mathrm{peripheral}}}\frac{d^2N_{\mathrm{dijet}}^{\mathrm{peripheral}}}{d\mathrm{x}dydz}}, \tag{1.17}$$

where x, y and z represent a generic three-dimensional kinematic binning, and the subscript "AB" denotes that the collision system being studied is not symmetric. One does not have to use three dimensions when

[4] The *leading* jet is that which has the highest transverse momentum, p_{T_1}, in a given event, while the *subleading* jet has the second highest transverse momentum, p_{T_2}.

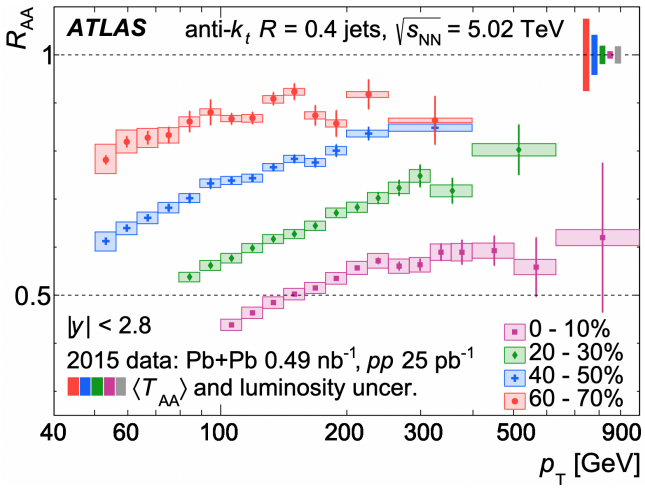

Figure 1.23: R_{AA} for anti-k_t $R = 0.4$ jets using pp and Pb+Pb data at $\sqrt{s_{\mathrm{NN}}} = 5.02$ TeV, in four centrality intervals. Figure taken from Ref. [82].

measuring a central-to-peripheral ratio, however, R_{CP}(x,y,z), constructed using data from p+Pb collisions, is the measurement on which this dissertation is based. The motivation for, and benefits of, using this observable, along with details of the measurement, are presented in Chapter 4.

1.5.4 Azimuthal Anisotropy

An alternative means by which the QGP can be studied is via a measurement of azimuthal anisotropies of final-state hadrons produced by the expansion of the medium, or *flow*. The anisotropy of the azimuthal distribution, resulting from pressure gradients generated by the initial collision geometry, is described by:

$$\frac{dN}{d\phi} \propto 1 + 2\sum_{n=1}^{\infty} v_n \cos(n(\phi - \Psi_n)), \tag{1.18}$$

where Ψ_n is the n^{th} order event plane angle and v_n are the Fourier coefficients representing the magnitude of the n^{th} order azimuthal anisotropy, referred to as flow harmonics. The event plane characterizes the orientation of the nuclear overlap between the colliding nuclei. The first three flow harmonics correspond to the directed flow, elliptical flow, and triangular flow, respectively. The elliptical flow, v_2, corresponds to pressure gradients in the transverse plane and is the most studied flow harmonic. A simplified depiction of a peripheral collision between two nuclei is shown in Figure 1.24, where a large elliptical expansion of the QGP is observed. The left diagram depicts immediately after a collision between a red and blue nucleus, with the remnant (spectators) continuing on, and the orange almond-shaped QGP beginning to expand. An anisotropic expansion is demonstrated by the right diagram. Methods used to measure flow harmonics include multi-particle correlations [85], the event-plane method [86, 87], and the cumulant method [88, 89]. These measurements can be compared to hydrodynamic models [90] in order to extract QGP properties such as the specific viscosity, from which we can deduce that the QGP behaves as a strongly-coupled fluid with a specific viscosity near the theoretical minimum [91, 92].

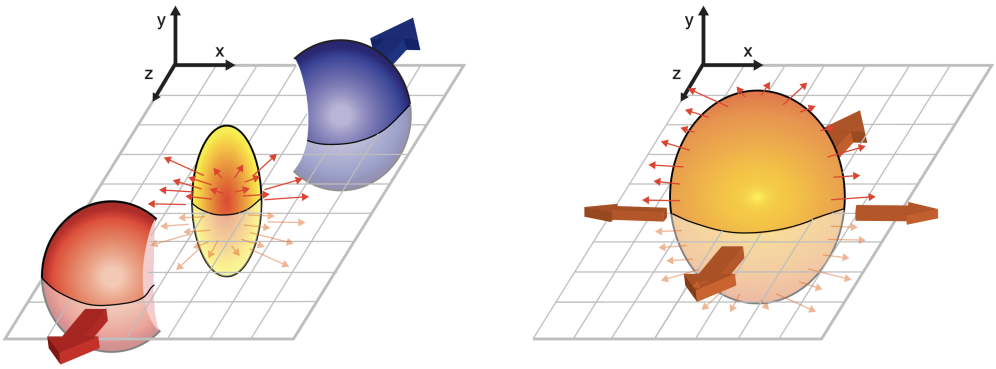

Figure 1.24: Simplified depiction of peripheral collision between two nuclei, resulting in anisotropic expansion of the QGP. Left: The blue and red nuclei remnants continue on their paths, while the orange almond-shaped QGP begins to expand due to pressure gradients, represented by red arrows. Right: The medium continues to expand anisotropically due to pressure gradients generated by the collision geometry, eventually hadronizing into final-state particle. Figure taken from Ref. [93].

Flow can be measured using different probes, including specific mesons [94], charged particles [95], and jets [87]. A jet measurement of v_2 is shown in Figure 1.25, for different centrality intervals as a function of jet p_{T}. The highest ellipticity is observed for mid-central (20–40%) collisions, decreasing with increasing jet p_{T}. A v_2 that is consistent with zero is found for most central (0–5%) collisions. These results are consistent with previous measurements at lower energies [96] and by a different collaboration [97], but are more statistically significant, also extending the measured v_2 to higher p_{T}. These results can be used to test models of the path-length dependence of jet quenching.

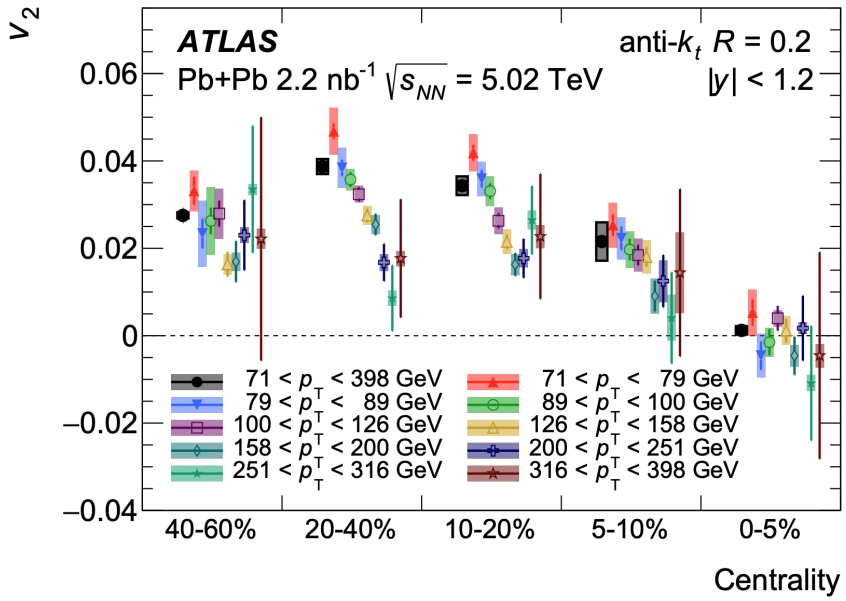

Figure 1.25: Elliptical flow harmoic, v_2, as a function of jet p_{T} in five centrality intervals for Pb+Pb collisions at $\sqrt{s_{\mathrm{NN}}} = 5.02$ TeV. Figure taken from Ref. [87].

Chapter 2

Proton Lead Collisions

The LHC at CERN represents the current frontier for investigation of nuclear structure, with proton-nucleus (p+A) collisions providing a unique opportunity to study both the proton and nucleus [98, 99]. Particle collider experiments allow for reaching much higher center-of-mass collision energies than those achievable at fixed-target experiments, such as the Common Muon and Proton Apparatus for Structure and Spectroscopy (COMPASS) experiment at CERN [100] and the HERA Measurement of Spin (HERMES) experiment at HERA [101], providing different, as well as broader, (x, Q^2) coverage. Along with higher energies, particle colliders also generate orders of magnitude more statistics than fixed-target experiments. A major drawback of hadron colliders, like RHIC and the LHC, is that they rely on strongly interacting probes which generate, together with the hard scattering, a plethora of particles commonly referred to as underlying event, which significantly increases the challenge of signal detection. This is in stark contrast to lepton-hadron colliders, including the HERA particle accelerator at DESY, where DIS measurements (see Section 1.2.1) are carried out using leptons to probe hadrons via a QED process.

One of the main goals of relativistic HI collisions is to produce droplets of QGP [102–104], a deconfined state of quarks and gluons which exists at very high temperatures and energy densities. These studies are typically carried out by analyzing changes in physics observables, such as jets and hadron spectra (see Section 1.5), when moving from pp to HI collisions. These changes can be attributed to both initial-state effects (e.g., nuclear modification of PDFs, as discussed in Section 1.4.1) and final state effects typically attributed to the formation of QGP in the collision. The former are sometimes to referred to as cold-nuclear matters effect, while the latter are termed hot-nuclear matter effects. Unravelling these contributions is a fundamental step to characterize the QGP dynamics.

To date, a major fraction of the luminosity delivered by the LHC for the HI program has used Pb nuclei with a proton probe (p+Pb) or collided among themselves (Pb+Pb). Proton-nucleus collisions offer the ability to study initial-state phenomena through various processes, providing insights on cold-nuclear effects arising in collisions involving nuclei [105–107], as well as being used to study QCD phenomena. For instance, strongly interacting particles can have dynamically reduced interactions, thanks to so-called *color transparency* (see Section 2.3). More broadly, proton-nucleus collisions allow for studying the relationship between the rate of hard processes, produced by partons scattering of one another, and the soft particle activity produced by the proton interacting with nucleons as it traverses the target nucleus.

2.1 Cold-Nuclear Matter in p+Pb Collisions

As previously stated, there are variety of measurements which can be used to study initial-state (cold-nuclear) effects in p+Pb collisions. This section presents a selection of non-jet related analyses performed at the LHC which seek to inform our understanding of these effects.

2.1.1 Multi-Particle Correlations

To date, no evidence for QGP formation has been observed in p+Pb collisions. However, results on multiparticle correlations published by ATLAS [108–111], CMS [112, 113], and ALICE [114, 115] show evidence of collective behavior in p+Pb collisions, a defining characteristic of Pb+Pb collision systems (see Section 1.5.4). This can be seen in Figure 2.1, which shows a comparison between v_2 for p+Pb collisions at 8.16 TeV and mid-central Pb+Pb collisions at 5.02 TeV. In Pb+Pb collisions, this collective behaviour produced by the expansion of the QGP, which is typically measured using the Fourier components of azimuthal particle distributions [116], is well modeled using hydrodynamics [90]. The origin of this collective behavior is not well understood in p+Pb collisions, highlighting the need for better constraints on initial conditions in p+A reactions.

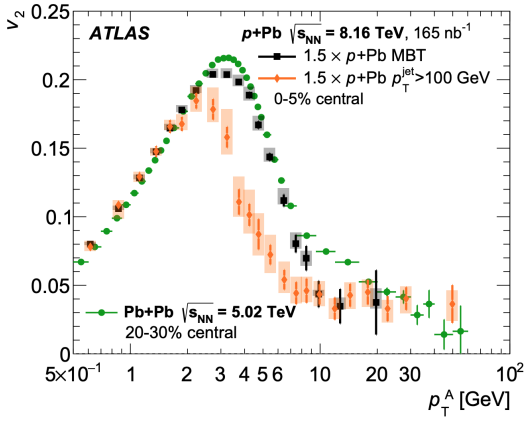

Figure 2.1: Scaled p+Pb v_2 values plotted as a function of the A-particle p_{T} overlaid with v_2 from 20–30% central Pb+Pb data at $\sqrt{s_{\mathrm{NN}}} = 5.02$ TeV [117]. Figure taken from Ref. [111].

2.1.2 Charm-Related Probes

In particle physics, quarkonium [118] refers to flavorless mesons whose constituents are a heavy quark-antiquark pair, forming a charge neutral particle that is its own antiparticle. Charmonium is a subset of quarkonium, and is concerned with the charm quark (c), which is the third most massive quark at 1.27 GeV/c^2. The discovery of the J/Ψ particle, the simplest form of charmonium ($\mathrm{c\bar{c}}$), by SLAC [119] and BNL [120] in 1974 was pivotal to confirming the existence of the charm quark, further highlighting the effectiveness of the quark model of hadrons put forth by Murray Gell-Mann [22] and George Zweig [23] ten years earlier.

J/Ψ

J/ψ production in nuclear collisions is enhanced by a factor $A^{1/3}$ with respect to pp collisions due to an increased baryon density as a result of Lorentz contraction of the nucleus, making it an ideal probe for nuclear-related effects. At forward rapidities, corresponding to large x_p and small x_{Pb}, nuclear shadowing contributes to a suppression of J/ψ production in p+Pb collisions, relative to geometrically scaled pp

collisions. Additionally, at small x_{Pb}, where the J/ψ cross-section is dominated by soft gluons, the nucleus can be described described via the Color-Glass Condensate (CGC) effective field theory [121]. The study of charmonium (J/ψ) production cross-sections at forward rapidities (low x_{Pb}) in p+Pb collisions can help to better understand these initial-state effects, allowing for constraint of gluon nPDFs and tests of CGC predictions [122].

ALICE measured the J/ψ cross-section and $R_{p\mathrm{Pb}}$ in p+Pb collisions at $\sqrt{s_{\mathrm{NN}}} = 5.02$ TeV [123], as shown in Figure 2.2. An enhancement and suppression of $R_{p\mathrm{Pb}}$ is observed at backward and forward rapidity, respectively. Several theoretical models are also shown, which generally agree with the experimental data points. These results can be used to better understand the forward rapidity suppression of J/ψ production in Pb+Pb collisions, which is due to both initial- and final-state effects.

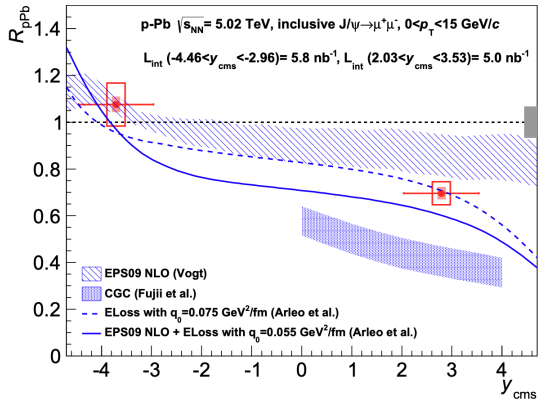

Figure 2.2: Nuclear modification factor ($R_{p\mathrm{Pb}}$) for inclusive J/ψ production in p+Pb collisions at $\sqrt{s_{\mathrm{NN}}} = 5.02$ TeV. Results from various theoretical models are also shown. Figure taken from Ref. [123].

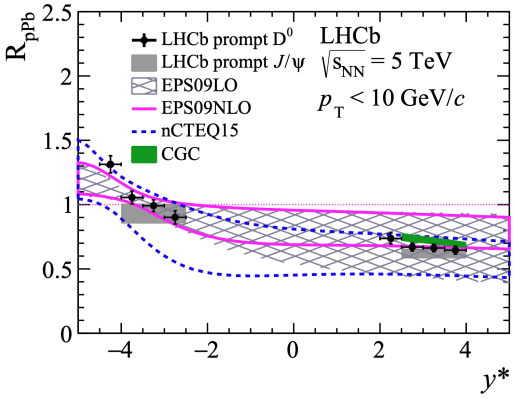

Figure 2.3: Nuclear modification factor ($R_{p\mathrm{Pb}}$) for prompt D^0 and J/ψ production in p+Pb collisions at $\sqrt{s_{\mathrm{NN}}} = 5.02$ TeV. Results from various theoretical models are also shown. Figure taken from Ref. [107].

D^0 Meson

D mesons are a bound state of a charm quark with either of an up quark, down quark, or strange quark, with the neutral D^0 being composed of a charm-antiup ($c\bar{\mathrm{u}}$) quark pair. Because of their large mass (1.27 GeV/c^2), charm quarks must be produced soon ($\sim 10^{-25}$ seconds) after the hard-scattering takes place, making them excellent probes of the QGP. To understand the role of the QGP in modifying c-quark production, charmonium studies in p+Pb collisions are needed to improve our understanding of initial-state effects, including gluon saturation [124] and parton energy loss in cold-nuclear matter [125].

LHCb measured *prompt* D^0 meson production [107], i.e., those which are generated directly by the hard scattering and not the result of b-hadron decays, as a means of investigating gluon saturation in the low-x ($x \sim 10^{-5}$) region. Figure 2.3 shows $R_{p\mathrm{Pb}}$ for both prompt D^0 and J/ψ production, as measured by LHCb. An enhancement and suppression of $R_{p\mathrm{Pb}}$ is observed at backward and forward rapidity, respectively. The results agree with theoretical predictions from various nPDF parameterizations, as well as CGC calculations at forward rapidity. Inclusion of these data in nPDF fits will help to reduce uncertainties on theoretical predictions, particularly at low-x. Refer to Figure 2.11 for a demonstration of the (x, Q^2) phase-space covered by this measurement.

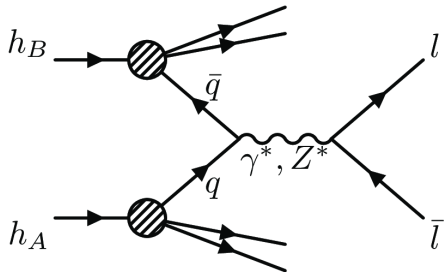

Figure 2.4: Diagram of Drell-Yan process, where a quark and antiquark from colliding hadrons annihilate to form a lepton-antilepton pair via the exchange of a virtual photon or Z-boson. Figure taken from Ref. [126].

2.1.3 Drell Yan

In 1970, Sidney Drell and Tung-Mow Yan proposed the Drell-Yan process as a means to explain the production of lepton-antilepton pairs in high energy collisions [127]. In the Drell-Yan process, a quark and antiquark from colliding nucleons annihilate, forming a virtual γ or a Z boson, which decays into a lepton pair. Because leptons do not carry color charge, they cannot interact via the strong force, making the Drell-Yan process a clean probe of cold-nuclear effects. When studying Drell-Yan production, a hadronic cross-section can be factorized (see Section 1.2.3) into a pQCD calculable partonic scattering convoluted with universal PDFs. A diagram of the Drell-Yan process is shown in Figure 2.4. One might observe a distinct similarity between the Drell-Yan process and the deep-inelastic scattering process, shown in Figure 1.5, where the DIS virtual γ is space-like, while the Drell–Yan virtual γ or Z boson is time-like. Both the Drell-Yan and DIS (see Section 1.2.1) processes play a pivotal role in the experimental constraint of PDFs.

CMS performed a Drell-Yan measurement, using the dimuon decay channel [128], in p+Pb collisions at $\sqrt{s_{\mathrm{NN}}} = 8.16$ TeV. The resultant cross-section, as well as theory predictions using two nPDF sets, are shown in Figure 2.5. The inclusion of the EPPS16 [64] nPDF set improves the agreement between the theory prediction and the measured cross-section, particularly for $\mathrm{y_{CM}} < -1$, corresponding to the antishadowing region.

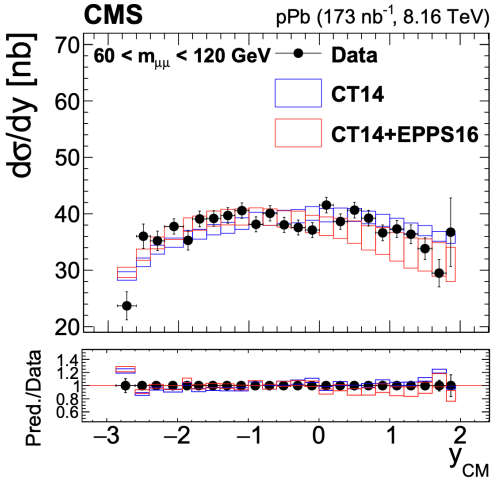

Figure 2.5: The Drell-Yan cross-section measured in the dimuon decay channel, as a function of the dimuon rapidity in the centre-of-mass frame. Theory predictions from the POWHEG next-to-leading order generator are also shown, using CT14 [129] or CT14+EPPS16 [64] nPDFs. Figure taken from Ref. [128].

2.1.4 Electroweak Bosons

In Pb+Pb collisions, measurements of prompt photons [130] and electroweak probes [131, 132] show no modification with respect to *pp* collisions, when taking into account geometrical differences. This *binary scaling* is due to these colorless probes (W, Z, and γ) not interacting with the QGP, and can be seen in Figure 2.6, where the W$\pm$ yield, scaled by the average nuclear thickness $\langle T_{\mathrm{AA}} \rangle$, is constant as a function of the average number of participating nucleons, $\langle N_{\mathrm{part}} \rangle$. Refer to Section 1.5.3 for an example of probes, namely jets, which do interact with the medium produced in heavy-ion collisions, resulting in the nuclear modification of observables. Binary scaling of electroweak probes has also been observed in p+Pb collisions, see for example Refs. [133, 134], demonstrating that the nuclear modification of jets, and other strongly interacting probes, observed in Pb+Pb collisions are a result of final-state effects.

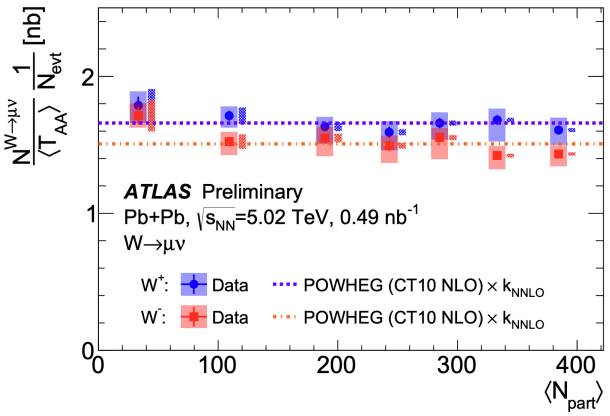

Figure 2.6: W$\pm\to\mu\nu$ yields per min-bias event, normalized by $\langle T_{\mathrm{AA}} \rangle$, as a function of pseudorapidity $\langle N_{\mathrm{part}} \rangle$ in Pb+Pb collisions. Figure taken from Ref. [132].

The analysis of W and Z boson production at LHC energies are of great interest, primarily for their use in constraining nPDFs [135]. Measurements of these bosons in p+Pb collisions have been performed by ATLAS [133, 134], CMS [106, 136, 137] and ALICE [138, 139]. Figures 2.7 and 2.8 show W and Z production, respectively, in p+Pb collisions at $\sqrt{s_{\mathrm{NN}}} = 5.02$ TeV as measured by ATLAS. Disagreements with theoretical models are observed, particularly for negative values of rapidity and pseudorapidity which correspond to the anti-shadowing region. A χ^2 goodness-of-fit test performed on the model predictions in Figure 2.7 indicates that the model which includes nuclear corrections (CT10+EPS09) performs the best.

Photon production measurements can also be used to isolate initial-state effects, including the nuclear modification of parton densities [140] and cold-nuclear effects resulting in energy loss of partons [141], due to photons not interacting strongly. A better understanding of these effects is crucial for the characterization of nuclear modification of hadronic probes in heavy-ion collisions. ATLAS measured prompt photon production in p+Pb collisions at $\sqrt{s_{\mathrm{NN}}} = 8.16$ TeV [142]. These results, presented in Figure 2.9, show an $R_{p\mathrm{Pb}}$ that is consistent with unity for forward- (left panel) and mid-pseudorapidity (middle panel), indicating that nuclear effects are not major factors in these regions. At backward pseudorapidity (right panel), a potential suppression at higher E_{T}^{γ} is observed, where the EMC effect is expected to play a role. However, the model prediction which includes nPDF corrections (red dashed line) is not always favored when compared to the free-nucleon PDF calculation (blue dashed line).

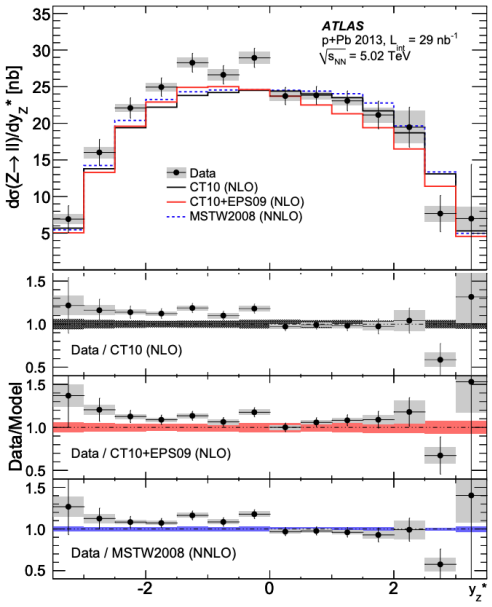

Figure 2.7: Z boson production, as a function of rapidity, in p+Pb collisions. Three nPDF model predictions, with ratios, are also shown. Figure taken from Ref. [133].

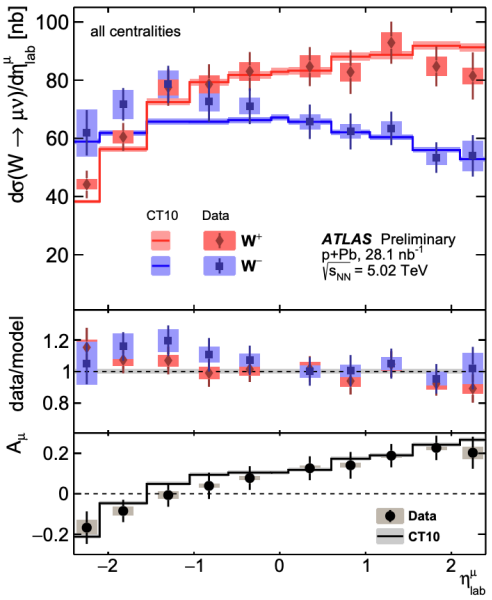

Figure 2.8: W$\pm\rightarrow\mu\nu$ production, as a function of pseudorapidity, in p+Pb collisions. Model predictions, with ratios, are also shown. Figure taken from Ref. [134].

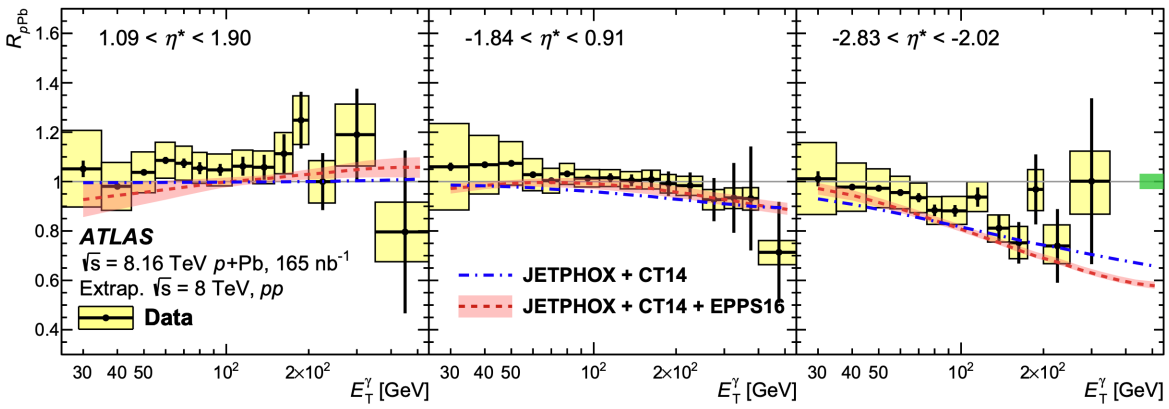

Figure 2.9: Nuclear modification factor $R_{p\mathrm{Pb}}$ for prompt photons as a function of photon transverse energy E_{T}^{γ} for three center-of-mass pseudorapidity intervals. Figure taken from Ref. [142].

2.2 Jets in p+Pb Collisions

Jets are collimated sprays a particles, originating from a high momentum transfer partonic collision (refer to Section 1.3 for an overview of jets). As discussed in Section 1.5, jets can be used to probe properties of HI collisions, in particular the QGP. Although collective effects are observed in p+Pb collisions (see Section 2.1.1), searches for evidence of QGP formation show no signs of its existence in small systems, with measurements of jet quenching playing an important role.

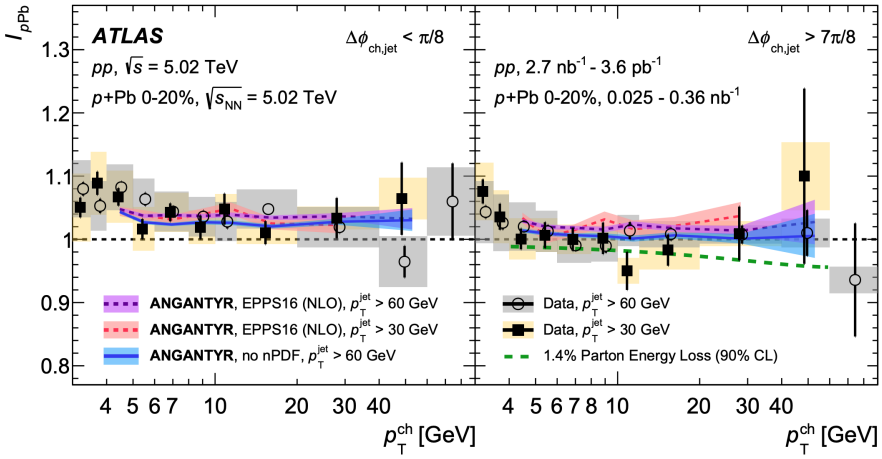

Figure 2.10: The ratio of per-jet charged-particle yields, $I_{p\mathrm{Pb}}$, on the near-side (left) and away-side (right) between p+Pb and pp are plotted for the 0–20% p+Pb centralities. Figure taken from Ref. [83].

The partonic energy loss of charged hadrons in p+Pb collisions was measured by ATLAS [83]. The per-jet yield ratio, $I_{p\mathrm{Pb}} = \langle Y_{p\mathrm{Pb}} \rangle / \langle Y_{pp} \rangle$, is the ratio of the per-jet normalized charged hadron yield in p+Pb and pp collisions. If QGP formation were present in small systems, one would expect $I_{p\mathrm{Pb}}$ to be below unity, as partons would strongly interact with the medium, reducing the measured charged hadron yield in p+Pb collisions with respect to pp collisions. The results, shown in Figure 2.10, do not support this hypothesis, severely constraining the amount of QGP-induced jet quenching which could be present in central p+Pb collisions. This lack of QGP formation is what makes p+Pb collisions such a crucial tool for understanding initial-state effects. Improvements to models can then be used to disentangle initial- and final-state effects in Pb+Pb collisions.

The study of high transverse momentum (p_{T}) probes, generated by p+A collisions, over a wide rapidity range can be used to investigate nuclear modifications of PDFs for a large range of parton fractional momenta [143–146]. The (x, Q^2) phase-space coverage of various p+A and DIS measurements, including the previously mentioned LHCb prompt D^0 [107] analysis, are shown in Figure 2.11. The orange shaded area demonstrates the excellent phase-space coverage offered by dijet measurements performed using the ATLAS detector, allowing for access to lower x values at high Q^2, where gluon saturation might contribute to initial-state effects [147]. The study of dijet azimuthal correlations has been proposed as a probe of CGC related phenomena, where broadening of the azimuthal angle distribution, $\Delta\phi$, indicates that pQCD no longer fully describes the hard-scattering cross-section [148].

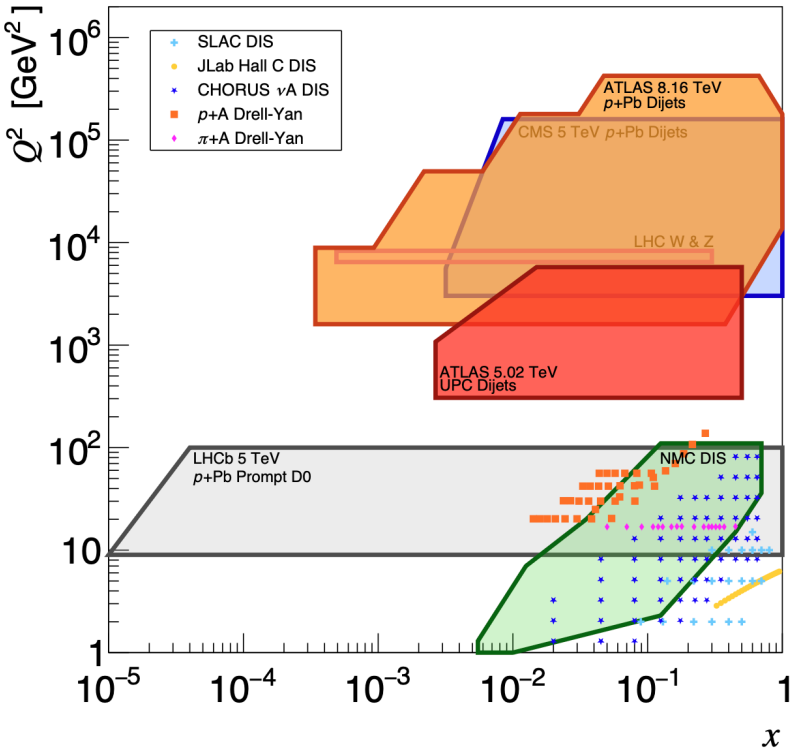

Figure 2.11: (x, Q^2) phase-space coverage of existing data from DIS and h+A measurements, which are used to better constrain nPDFs. Figure courtesy of Ben Gilbert.

To search for the onset of gluon saturation effects, ATLAS analyzed forward-forward and forward-central angular correlations for dijets in p+Pb collisions at $\sqrt{s_{\mathrm{NN}}} = 5.02$ TeV [149]. This analysis found no significant broadening of the azimuthal correlations of dijets in p+Pb compared to pp collisions. The yield of dijets was also studied as a function of the transverse momentum and center-of-mass rapidity of the two leading jets. The results, shown in Figure 2.12, indicate that forward jet pairs in p+Pb collisions are suppressed by approximately 20% compared to pp collisions. This region corresponds to the nuclear shadowing regime, where saturation effects may start to contribute, particularly at low p_{T}, to nuclear modification [150]. The observed suppression is not dependent on the transverse momentum of the leading ($p_{\mathrm{T},1}$) or subleading ($p_{\mathrm{T},2}$) jet. The dataset analyzed in Ref. [149] was statistically limited, making dijet cross-section and centrality analyses unfeasible.

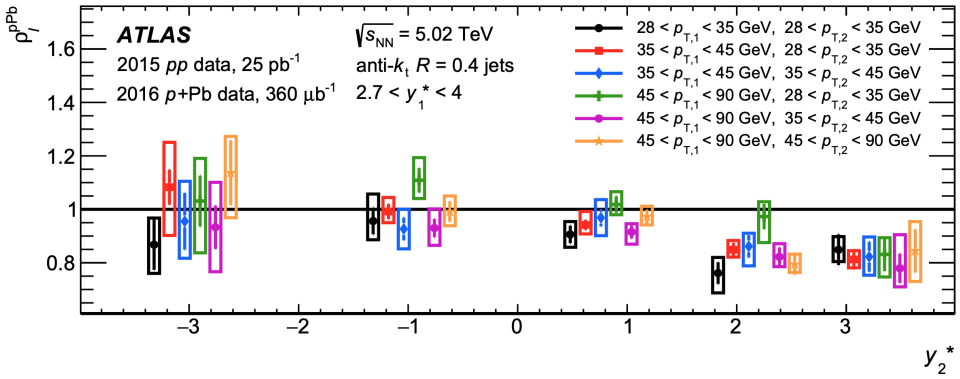

Figure 2.12: Ratio of dijet conditional yields in p+Pb and pp collisions (ρ_I^{pPb}), in different intervals of $p_{\mathrm{T},1}$ and $p_{\mathrm{T},2}$ for forward center-of-mass rapidity of the leading jet (y_1^*). The results are plotted as a function of the center-of-mass rapidity of the subleading jet (y_2^*), where a horizontal shift has been applied for visibility. Figure taken from Ref. [149].

Jets are of particular interest for constraining nPDFs, as they are a direct representation of the partons generated by the 2→2 hard-scattering process. The dijet cross-section depends on both the non-perturbative probability of finding a particular parton inside the parent hadrons and on the elementary cross-section describing the parton-parton interaction, which can be well understood using pQCD techniques. The inclusive yields of jets measured in p+Pb collisions at the LHC [84, 105, 151, 152] and d+Au collisions at RHIC [153] are consistent with pp yields scaled up by the expected nuclear thickness, i.e. for p+A, scaling with the atomic mass number A: $\sigma^{p+\mathrm{A}} \simeq A\sigma^{p+p}$. This can be seen in Figure 2.13, where $R_{p\mathrm{Pb}}$ for 0–90% p+Pb collisions at $\sqrt{s_{\mathrm{NN}}} = 5.02$ TeV is compatible with unity within the experimental uncertainties for all values of p_{T}.

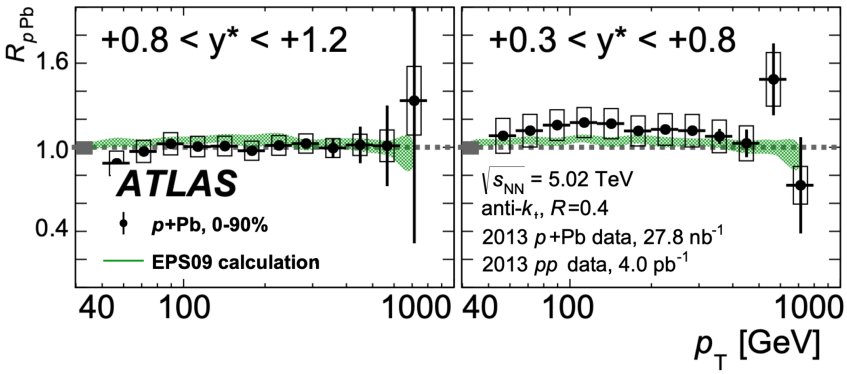

Figure 2.13: Measured $R_{p\mathrm{Pb}}$ values for $R = 0.4$ jets in 0–90% p+Pb collisions at 5.02 TeV in two different rapidity intervals. Figure taken from Ref. [152].

The centrality dependence[1] of the jet production in p/d+A was analyzed by both ATLAS [152] and PHENIX [153]. In small systems, centrality is no longer correlated with the overlap between the two colliding nuclei, and is instead a quantification of the multiple interactions between the projectile (p or d) and the nucleons (Pb or Au) in the nucleus. More central (peripheral) events are characterized by a higher (lower) average number of nucleon-nucleon (NN) collisions. A suppression of the jet yield in central events, and an enhancement in peripheral events, was observed by both Refs. [152] and [153], as shown in Figure 2.14 for the PHENIX measurement and Figure 2.15 for the ATLAS measurement, respectively.

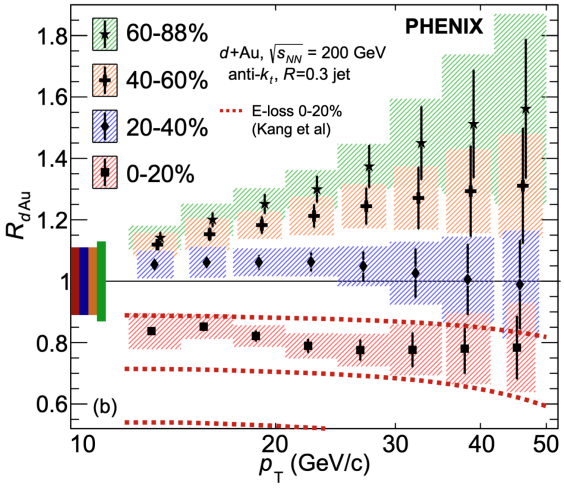

Figure 2.14: Measured $R_{d\mathrm{Au}}$ values as a function of p_{T} for $R = 0.3$ jets in four centrality intervals in $\sqrt{s_{\mathrm{NN}}} = 200$ GeV d+Au collisions. Figure taken from Ref. [153].

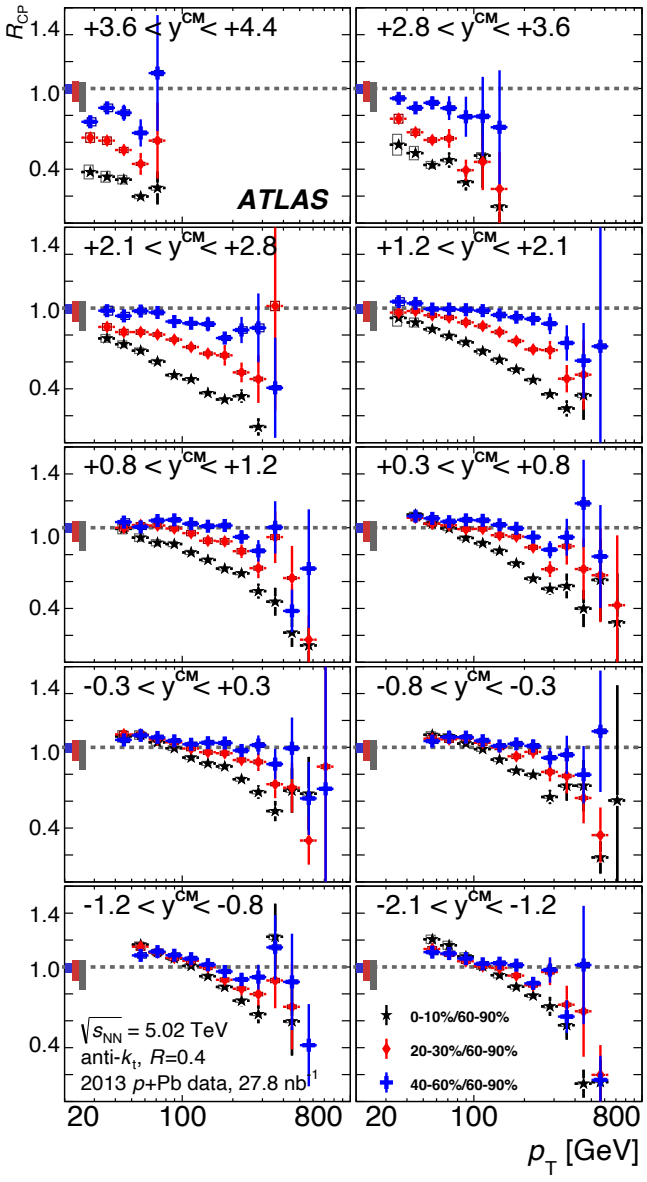

Figure 2.15: Measured R_{CP} values for $R = 0.4$ jets in p+Pb collisions as a function of p_{T} in central (black stars), mid-central (red diamonds) and mid-peripheral (blue crosses) centrality intervals. Each panel represents a different center-of-mass rapidity (y^{CM}) interval. Figure taken from Ref. [152].

[1]Refer to Section 1.5.1 for a review of centrality in HI collisions.

The $R_{d\mathrm{Au}}$ results shown in Figure 2.14 are presented in four centrality intervals, with the most central (0–20%) interval having a suppression of ∼20% for all values of p_{T}. Figure 2.15 shows the R_{CP}(see Equation 1.17) in ten different rapidity intervals, constructed using the most peripheral (60–90%) events in p+Pb collisions as the reference. A suppression, increasing with jet p_{T}, is observed for all centrality and rapidity intervals, with respect to the most peripheral events. Together, these results suggest that a nuclear-related mechanism is responsible for a reduction of jet production in events characterized by a higher soft-particle multiplicity in the nucleon (Pb or Au) going direction.

The ATLAS analysis went on to further characterize the relationship between the suppression and the enhancement as being only a function of the total jet energy. In relativistic kinematics, the energy (E) of a particle, i.e. jet, is given by

$$E = m_{\mathrm{T}} \times \cosh(y^{\mathrm{CM}}) \ , \quad m_{\mathrm{T}} = \sqrt{m^2 + p_{\mathrm{T}}^2}, \tag{2.1}$$

where m_{T} is the transverse mass of the jet. In jets characterized by a transverse momentum at the ∼GeV scale, the mass of the jet can be considered negligible, such that the approximation $m_{\mathrm{T}} \approx p_{\mathrm{T}}$ is valid. The jet energy can therefore be approximated as

$$p_{\mathrm{T}} \times \cosh(\langle y^{\mathrm{CM}} \rangle), \tag{2.2}$$

where $\langle y^{\mathrm{CM}} \rangle$ indicates that the average center-of-mass rapidity value in a given rapidity interval has been used to calculate the jet energy. These results are shown in Figure 2.16 for different intervals of rapidity, where the R_{CP} is constructed using the most central (0–10%) and most peripheral (60–90%) centrality intervals. Note that the results are the exact same data points displayed in Figure 2.15, but are now shown on only two panels with the x-axis being a function of $p_{\mathrm{T}} \times \cosh(\langle y^{\mathrm{CM}} \rangle)$. The left panel of Figure 2.16 shows a remarkable level of scaling between the results in five positive rapidity intervals, corresponding to the proton-going direction. For all rapidity intervals, suppression of central jet yields increases with total jet energy. These results suggest that the observed phenomena is related to the initial kinematics of the hard parton-parton scattering, and in particular to the parton originating from the incident proton due to the observed scaling at forward rapidities.

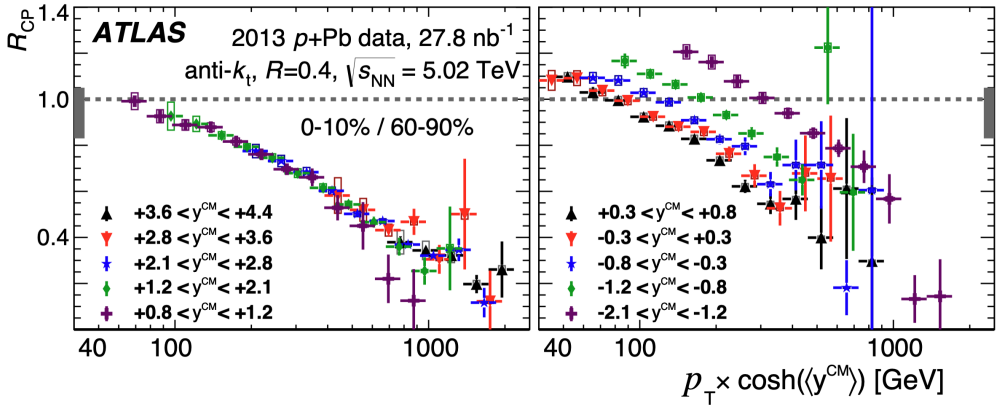

Figure 2.16: Measured R_{CP} values for $R = 0.4$ jets in 0–10% p+Pb collisions at 5.02 TeV, plotted as a function of the approximated total jet energy. The panel on the left shows the five rapidity ranges that are the most forward-going, while the panel on the right shows the remaining five. Figure taken from Ref. [152].

Several theoretical papers [154–156] were published attempting to explain the ATLAS [152] and PHENIX [153] results. Refs. [154] and [155] suggested that in nucleon-nucleon collisions, energy production at backward rapidities decreases with increasing x in the proton-going direction, either via suppression of soft gluons due to high p_{T} jets [154] or from an energy-momentum conservation between the hard process and the production

of soft particles [155]. The results of the latter are shown in Figure 2.17, where the authors have used PYTHIA8+HIJING to simulate p+Pb collisions in which the minimum-bias event is generated using a proton that is missing the energy from the hard-scattering. Their findings reproduce the general trend of the ATLAS $R_{p\mathrm{Pb}}$ results for central (0–10%) events. Because they did not also enforce conservation of energy for the Pb nuclei,[2] their results entirely fail to reproduce the experimental values for peripheral (60–90%) collisions.

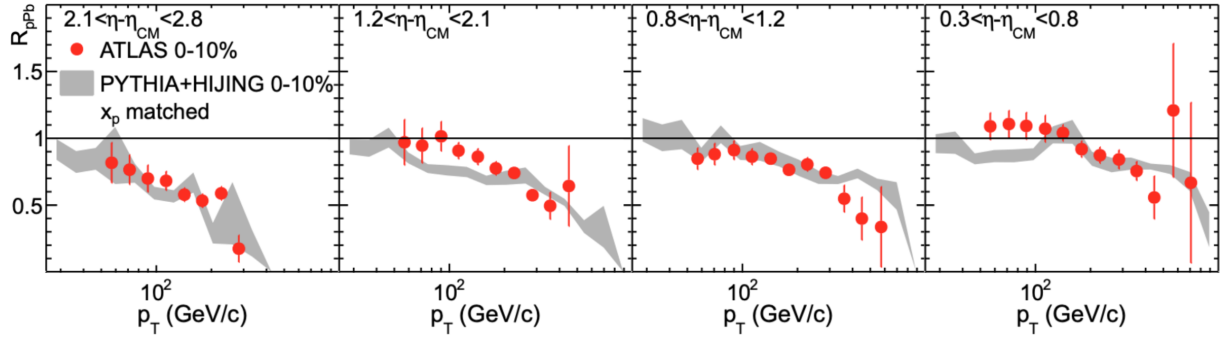

Figure 2.17: $R_{p\mathrm{Pb}}$ calculation in PYTHIA8+HIJING with x_p matching (grey bands) and the measured values by ATLAS [152] (red circles) are shown for the 0–10% centrality class in bins of pseudorapidity in the center-of-mass frame. Figure taken from Ref. [152].

To test the arguments presented by Refs. [154] and [155], ATLAS measured the forward transverse momentum E_{T} using their FCal in pp dijet events at $\sqrt{s} = 2.76$ TeV in order to investigate the relationship between hard-process kinematics (x of the projectile and target) and transverse energy production (ΣE_{T}) at large pseudorapidity [157]. By measuring the transverse momentum and pseudorapidity of the two leading jets in each event, the authors were able to approximate the momentum fractions carried by the partons which participated in the hard-scattering via

$$x_{\mathrm{proj}} = p_{\mathrm{T,Avg}}(e^{+\eta_1} + e^{+\eta_2})/\sqrt{s}\ , \quad x_{\mathrm{targ}} = p_{\mathrm{T,Avg}}(e^{-\eta_1} + e^{-\eta_2})/\sqrt{s}, \tag{2.3}$$

where $p_{\mathrm{T,Avg}}$ is the average transverse momentum of the two leading jets, x_{proj} corresponds to the parton originating from the proton travelling towards positive rapidity, and x_{targ} corresponds to the parton originating from the proton travelling towards negative rapidity, where the FCal used to measure ΣE_{T} is located. The equivalences in Equation 2.3 hold true for pQCD calculations of 2→2 hard-scatterings at leading order. The experimental results, shown in Figure 2.18, show that the production of transverse forward energy strongly depends on the x of the target (left panel, which corresponds to the Pb-going direction in p+Pb collisions), but is nearly independent of the x of the projectile (right panel, which corresponds to the proton-going direction in p+Pb collisions). As noted by the authors of Ref. [157], the findings directly contradict the theoretical interpretations put forth by Refs. [154] and [155] of the centrality-dependence of the jet rate in p+Pb collisions measured in Ref. [152]. If the observed scaling in p+Pb collisions was simply due to a suppression of ΣE_{T} at backward rapidities in events characterized by partons from the incident proton having a large momentum fraction, ΣE_{T} should strongly decrease with increasing x_{proj}, which is not the case, as shown in the right panel of Figure 2.18.

[2]The authors of Ref. [155] do not state why this choice was made, only that they plan to address it in a future work, which has yet to be published after 8 years.

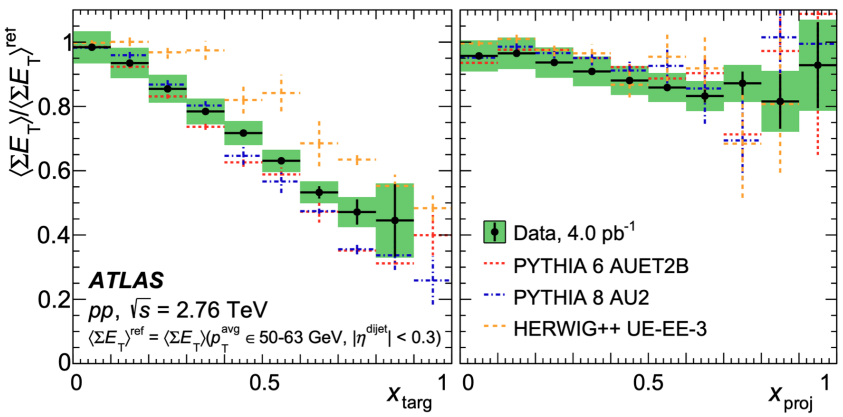

Figure 2.18: Measured ratio $\langle \Sigma E_{\mathrm{T}} \rangle / \langle \Sigma E_{\mathrm{T}} \rangle^{\mathrm{ref}}$ in pp collisions at $\sqrt{s_{\mathrm{NN}}} = 2.76$ TeV, as a function of x_{targ} (left) and x_{proj} (right). See the left panel for the definition of $\langle \Sigma E_{\mathrm{T}} \rangle^{\mathrm{ref}}$. Figure taken from Ref. [157].

A third theoretical paper [156] sought to explain the results in Ref. [152] in terms of color transparency effects (see Section 2.3), where an x_p-dependent shrinking of the proton results in less nucleon-nucleon interactions for collisions involving a high-x_p parton. This manifests as a centrality-bias in p+Pb collisions, due to a reduction of the underlying-event. To model this effect, the authors introduce a variable $\lambda(x_p)$, which is the x_p-dependent shrinking of the average interaction strength at a given collision energy. They then extract this parameter from fits to the results by both ATLAS [152] and PHENIX [153], and find that their model is able to capture the general trend in both cases, as shown in Figure 2.19.

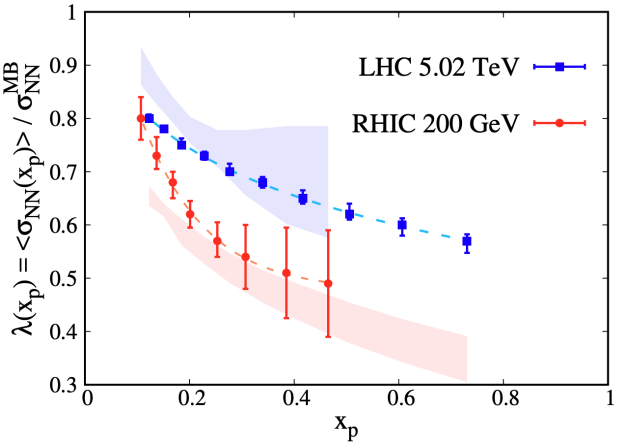

Figure 2.19: Extracted values of $\lambda(x_p)$ as a function of x_p at RHIC (2.76 TeV) and LHC (5.02 TeV) energies (solid points), with fits to an exponential function in x_p shown as dashed lines. The shaded bands are a prediction for $\lambda(x_p)$ at each energy using the results at the other energy as input. Figure taken from Ref. [156].

The same 2013 LHC p+Pb run at 5.02 TeV in which ATLAS recorded the data that was used in Ref. [152], was also utilized by the CMS experiment to study dijets. CMS measured a shift in the Pb beam direction of the mean dijet pseudorapidity as a function of the total forward transverse energy [84] in the Pb-going direction. The results, shown in Figure 2.20, demonstrate a correlation between increasing η_{dijet} and decreasing $\mathrm{E}_{\mathrm{T}}^{4<|\eta|<5.2}$, which corresponds to more peripheral collisions. The inclusive measurement was observed to be consistent with predictions based on nPDFs, but the relative changes with $\mathrm{E}_{\mathrm{T}}^{4<|\eta|<5.2}$ were found to be much larger than those available from nPDF predictions [158]. While this result had qualitative similarities to those reported by ATLAS [152], it covered a more limited kinematic range in only a single dijet p_{T} interval, and did not unfold for detector effects, making it difficult to assess more quantitatively.

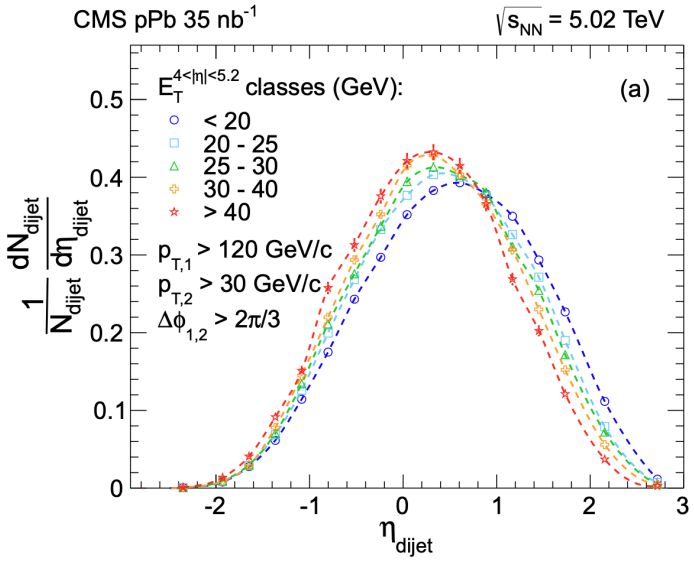

Figure 2.20: Normalized dijet pseudorapidity distributions in the five hadron-forward calorimeter activity classes. Figure taken from Ref. [84].

2.3 Color Transparency in in p+Pb Collisions

As discussed in Section 1.2, QCD has proven to be a remarkably successful theory, allowing physicists to make accurate predictions of phenomena related to the strong force, including DIS, which led to acceptance of the quark-parton model. Unfortunately, it is hard to be certain that these successes are actually testing QCD, and not higher-level principles related to the quark-parton model or perturbative calculations. Additionally, even for the simplest processes, one must account for the convolution of QCD mechanisms including non-perturbative initial-state and final-state effects, as well as uncertainties on perturbative QCD calculations arising from non-perturbative dynamics, along with other effects [159].

An interesting, and more direct, prediction of QCD is that of color transparency in the nuclear environment, which does not explicitly rely on the probe used. The concept of color transparency was first introduced more than four decades ago by Mueller and Brodsky [159–162] and is related to the presence of color degrees of freedom underlying strongly interacting matter. The basic idea is that configurations in which a large fraction of the hadron's momentum (x), typical of the valence region, is carried by a single parton are spatially compact, resulting in a reduced interaction strength. To understand how smaller spatial configurations in QCD can produce a lower number of collisions with the nucleus, we will first look to QED for a less complex example, where confinement does not prevent one from direct observation.

2.3.1 Charge Transparency in QED

Just as Cherenkov light, a QED phenomena, has a classical counterpart in sonic booms, so to does color transparency have a QED analog, referred to as charge transparency. Note that charge transparency was well known to the originators of color transparency theory, who used the following example as a basis from which to explore color transparency in QCD [163]. Positronium (e^+e^-) is a hydrogen-like bound state of an electron and a positron. At high energies, positronium can fluctuate to have transverse separations that approach zero. These spatially compact configurations can then pass through a thin foil without interacting, as explored theoretically by two groups in 1981 [164, 165].

Unbeknownst to him at the time, this same phenomena was observed by Perkins in 1955, in an ionization experiment observing the decay of neutral pions (π^0) in emulsions [166]. Neutral pions are generated in cosmic ray particle showers originating in the upper atmosphere. The two most common decay modes for π^0 are [36]:

$$\begin{aligned} &\pi^0 \to 2\gamma && \text{Branching Ratio: } 98.8\% \\ &\pi^0 \to e^+ + e^- + \gamma && \text{Branching Ratio: } 1.2\% \end{aligned} \tag{2.4}$$

with the second process, resulting in an electron positron pair and a photon, being the process of interest for Perkins. In his experiment, Perkins observed a distinct lack of ionization at the intersection of the e^+e^- tracks, corresponding to the vertex of the π^0 decay. Only after reaching a separation greater than that of the atomic scale did the observed ionization correspond to a naive superposition of an individual electron and positron. The explanation for the lack of ionization in the emulsion experiment and the passage of spatially compact positronium states through a thin foil are the same, at small distances the interactions of the electron and positron with the medium cancel [167]. It should be noted that in the emulsion experiment, the generated photon, which is charge neutral, does not ionize the emulsion until after undergoing pair production, which dominates over Compton and photoelectric contributions at high energies (> 10 MeV).

We have not yet addressed how such small configuration exist long enough to have observable (macroscopic) consequences in the context of a quantum system, where fluctuations are constantly occurring. In the case of the positronium passing through foil, much larger distances are able to be traversed than the average interaction cross-section would imply, with the foil appearing transparent to specific configurations. In Perkins' study of π^0 decay, the e^+e^- pair is generated with essentially zero spatial separation, and remains close enough over a macroscopic distance that a lack of ionization can be observed in the emulsion. Both of these processes are made possible due to an interplay between Heisenberg's uncertainty principle and relativistic time dilation. From the uncertainty principle, one can calculate that the fluctuation time (Δt) for positronium to change configurations is on the order of

$$\Delta t \sim \frac{\hbar}{\Delta E}, \tag{2.5}$$

where the excitation energy ΔE is approximately 5 eV for positronium in the ground state, and Planck's constant $\hbar$ has a value of 6.58×10^{-16} eV $\cdot$ s, giving a value of $\Delta t \sim 0.1$ fs. This timescale is far too short to result in macroscopically observable phenomena. However, due to relativistic time dilation, a positronium with energy $E_{+-} = 1$ GeV experiences a time dilation given by the Lorentz factor, γ, as

$$\Delta t' = \gamma \cdot \Delta t, \quad \gamma = \frac{E_{+-}}{2m_e \cdot c^2} \quad \to \quad \Delta t' = 10^{-13} \text{ s}\,, \tag{2.6}$$

where the electron mass, m_e, is 0.511 MeV/c^2. Therefore, in the lab frame, a relativistic positronium remains in a given configuration for 3 orders of magnitude longer than in its own rest frame. This extended time allows for positronium to traverse a few microns of metal foil while remaining in the same configuration. Charge transparency also has other QED consequences, including the suppression of bremsstrahlung radiation and pair production at high energies [168], which will not be explored here.

2.3.2 Color Transparency in QCD

In QCD, CT is the prediction that QCD color fields cancel for physically small color-singlet systems of quarks and gluons. Such an effect can lead to the suppression of initial- or final-state interactions involving small-sized hadronic systems, depending on the collision system and the type of reactions considered. CT can

manifest in final-state interactions when a hadron is formed in a scattering in the nuclear environment and is produced with sufficient energy such that its configuration remains frozen when emerging from the nucleus. If the hadron is produced in a small-size configuration, its interact tion with the nucleus is suppressed, enhancing its probability of emerging from the nucleus intact. These final-state CT effects are usually investigated using a weak-interacting probe, e.g. a lepton, scattering off a nucleus, such that CT effects can be due only to the final-state. The typical signature expected in these effects is an increase of the medium nuclear transparency, T_A, as a function of the momentum transferred in the scattering. At intermediate center of mass energies, these effects have been studied by the Fermilab E791 Collaboration [169], by HERMES at DESY [170], and by the CEBAF[3] Large Acceptance Spectrometer at Jefferson Lab [171], with potential to investigate this phenomena using μ+A data recorded by COMPASS [172]. The results of the aforementioned analyses provide well established evidence for the onset of a CT regime at a Q^2 of a few GeV^2. Further characterization of final-state CT will be possible at the future Electron-Ion Collider (EIC) at BNL [173], exploring a much broader range of Q^2 for e+A reactions, see Figure 2.11.

CT effects can also arise in collisions between a hadron and a nucleus. In this type of reaction, the relevant small configuration becomes that of the projectile, a p if one considers the p+Pb collisions studied in this thesis. Recall the internal structure of the proton from Figure 1.14, where at short timescales, the proton is a dynamic system consisting of valence and sea quarks, surrounded by gluons. A given instantaneous internal configuration of these partons is akin to a specific separation distance between an e^+e^- pair from our QED example, with the interaction cross-section now depending on how spatially compact the color charge inside the proton is. When a proton is in a small configuration, its internal configuration takes on a simpler configuration, where valence quarks carry the majority of the longitudinal momentum of the proton. The probability of this occurring is described by PDFs (refer to Section 1.4 for a review of PDFs), where for large values of x, sea quark and gluon PDFs are highly suppressed.

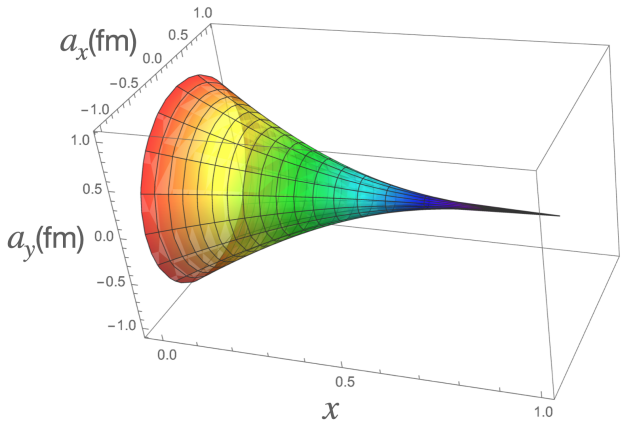

Figure 2.21: The x-dependence of the proton transverse-size, $\langle a_\perp^2(x)\rangle$. At large values of x, corresponding to high-Q^2, the reduced transverse size of the hadron results in a point-like color-neutral object. Figure taken from Ref. [174].

As with positronium, for a sufficiently high energy, and therefore time dilation, the proton will remain frozen in a given configuration. Instead of traversing a thin foil ($\sim 10^{-6}$ m), the proton must remain in its configuration as it passes through a nucleus ($\sim 10^{-15}$ m). This mechanism is analogous to the one which allows DIS (see Section 1.2.1) to probe individual partons, where the probe is a high energy lepton that directly interacts with a parton inside a frozen proton. At the LHC, protons carry energy (E_p) at the TeV scale, making their passage through the nucleus shorter than quantum fluctuations of their constituent

[3]Continuous Electron Beam Accelerator Facility

partons. No direct calculations presently exist for determining the energy associated with the quantum fluctuations associated with hadrons, as was possible for the electron in the QED case. However, limits can be derived from considerations related to the constituent mass, providing the relation: $E_p \gg 50\,A^{1/3}$ GeV, which guarantees that the proton will remain in the same configuration while interacting with the nucleus [163].

If the frozen configuration includes a high-x_p parton, one can expect a suppression of non-valence partons ($q\bar{q}$ pairs), as observed in pion-nucleus scattering [169], and an associated decrease in transverse size. The transverse separation ($a_\perp$) between quark constituents is inversely proportional to the hard-scale, $a_\perp \sim 1/Q$, with an x dependence that is demonstrated in Figure 2.21. Therefore, hard-scatterings involving high-x_p partons, typically valence quarks (refer to the free proton PDF in Figure 1.15), are expected to be more spatially compact with respect to small-x_p scatterings involving primarily gluons [175]. In this way, spatially compact proton configurations propagate as a small color-neutral state due to the cancellation of color fields emitted by the constituent quarks and gluons, termed *color screening*, resulting in minimal strong interactions with the nuclear medium [163], as depicted in Figure 2.22.

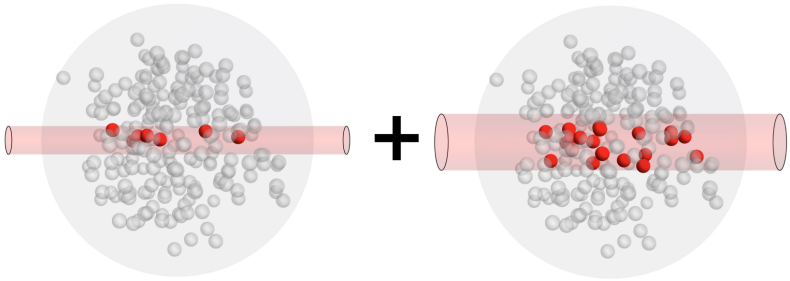

Figure 2.22: Schematic representation of a proton–nucleus collision, where both the left and right configurations contribute to the average cross-section. The red cylinder represents the transverse size of the incident proton, with wounded nucleons depicted as red spheres. The left depiction is representative of large x_p configurations, resulting in a reduced interaction between the proton and nucleus. Figure taken from Ref. [156].

In order to directly connect the observed scaling as a function of total jet energy that was observed in Ref. [152] with the color transparency, a triple differential dijet analysis would need to be performed as a function of centrality, allowing for full constraint of the 2→2 hard-scattering kinematics (x_p and x_{Pb}). This would allow for an analysis of the soft particle multiplicity to be studied as a function of the configuration of the colliding nucleons in the hard scattering, i.e. the beam proton and the one in the target nucleus. Such a measurement would provide crucial input to the understanding of small proton configurations and their relation to the suppression of the overall interaction strength in p+A collisions. The dijet measurement could then be mapped back to the less differential inclusive jet measurement, allowing for a qualitative comparison of the results.

Chapter 3

The LHC and ATLAS

3.1 The Large Hadron Collider

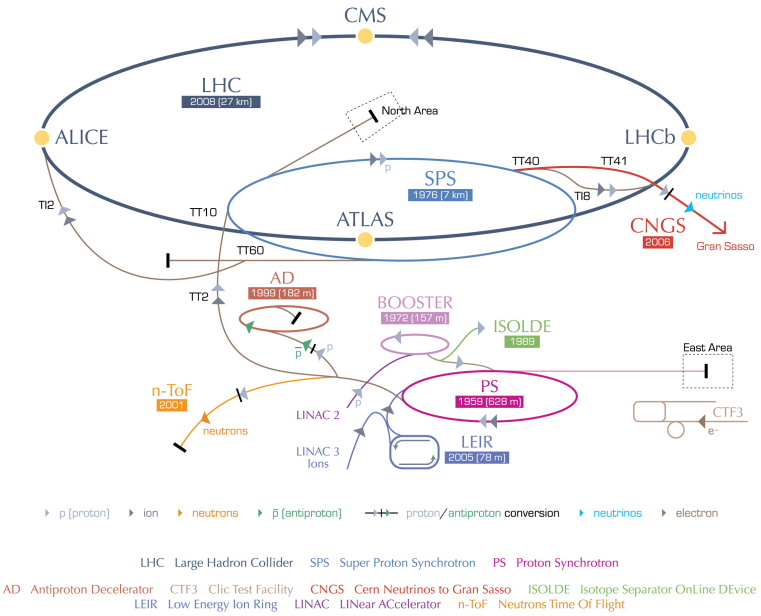

Figure 3.1: The CERN accelerator complex, with dates of commissioning for each subsystem. This facility is capable of bringing protons and ions to within fractions of a percent of the speed of light. Four interaction points upon which detectors have been built, denoted by yellow circles, are located around the LHC ring.

The Large Hadron Collider (LHC), built by the European Organization for Nuclear Research (CERN), is located on the Franco-Swiss border near Geneva, Switzerland and Meyrin, France. The full accelerator complex of CERN is shown in Figure 3.1. To date, the LHC is the world's highest energy accelerator, with the Tevatron at Fermilab shutting down in 2011 after colliding protons and anti-protons at ∼1 TeV. This energy was not high enough to produce the Higgs particle, which was one of the major thrusts of the LHC program, along with the search for physics beyond the Standard Model. Although primarily designed for colliding protons, the LHC is also capable of colliding stripped ions, with Pb being the most commonly used. After two years of planned maintenance and upgrades, Run 2 of the LHC begin in 2015. Different data were taken during Run 2, including proton-proton (p+p) collisions at 13 TeV, Pb+Pb collisions at a center-of-mass

energy of 5.02 TeV, and p+Pb collisions at both 5.02 TeV and 8.16 TeV center-of-mass energies. The 8.16 TeV p+Pb dataset is what the analysis presented in this thesis is based on.

Prior to commissioning of the LHC in 2009, the tunnel which houses the beam pipes was used by the the Large Electron-Proton Collider from 1989–2000. The 27 km long LHC tunnel is approximately 100 m underground and hosts two high vacuum counter-rotating beam pipes. Steering of positively charged particles is achieved using superconducting electromagnets operating at 1.9 K, which are cooled using liquid helium. Generally, dipole magnets are used for steering beams around the rings, with quadrupoles used for beam focusing. At four points along the LHC, the beams cross at intersections in which a shared pipe allows for collisions between the two beams. The four major experiments of the LHC, each built around one such interaction point, are A Toroidal LHC Apparatus (ATLAS), Compact Muon Solenoid (CMS), A Large Ion Collider Experiment (ALICE), and Large Hadron Collider - Beauty (LHCb).

ATLAS and CMS are both multi-purpose detectors capable of taking data during both p+p and heavy-ion (HI) running. The author of this thesis is a member of the ATLAS HI collaboration. ALICE was specifically designed as a HI detector and does not prioritize running during p+p operations. Its distinguishing feature is its charged hadron identification. LHCb is aimed at the study of beauty and anti-beauty quarks, which were last seen in abundance in the aftermath of the Big Bang. By studying the decay of these particles, physicists hope to better understand why the visible universe is composed of matter, when anti-matter should have been produced in equal amounts.

To accelerate protons, hydrogen gas is ionized removing all electrons. The protons are then accelerated by the Linac2 before entering the proton synchroton (PS) via a booster. Pb^{+29} atoms begin their journey in Linac3 where some electrons are stripped as the ions pass through a carbon foil on their way to the Low Energy Ion Ring (LEIR). From LEIR, the Pb ions enter the PS. Both protons and ions travel from the PS to the Super Proton Synchroton (SPS) before finally being injected into the LHC. Pb ions are fully stripped of electrons by a final aluminum foil at the exit of the PS. It is in the LHC where particles are accelerated to their final collision energies.

3.2 The ATLAS Detector

The ATLAS detector[1] is located at Interaction Point 1 of the LHC, inside of the SPS ring. The subsystems of ATLAS include an inner detector, electromagnetic and hadronic calorimeter, muon spectrometer, and trigger system. The inner detector is encompassed by a superconducting solenoid magnet, which produces a 2T magnetic field, allowing for charged particle momentum determination. A schematic of the ATLAS detector is shown in Figure 3.2.

3.2.1 Inner Detector

The inner detector measures charged particle tracks, with full azimuthal and pseudorapidity coverage of $|\eta| < 2.5$. The three systems which make up the inner detector are silicon pixel detectors, the semiconductor tracker (SCT), and the transitional radiation tracker (TRT), as shown in Figure 3.3.

[1]ATLAS uses a right-handed coordinate system with its origin at the nominal interaction point (IP) in the center of the detector, and the z-axis along the beam pipe. The x-axis points from the IP to the center of the LHC ring, and the y-axis points upward. Cylindrical coordinates (r, ϕ) are used in the transverse plane, ϕ being the azimuthal angle around the z-axis. The pseudorapidity is defined in terms of the polar angle θ as $\eta = -\ln\tan(\theta/2)$. The rapidity is defined as $y = 0.5\ln[(E+p_z)/(E-p_z)]$ where E and p_z are the energy and z-component of the momentum along the beam direction, respectively. Transverse momentum and transverse energy are defined as $p_{\mathrm{T}} = p\sin\theta$ and $E_{\mathrm{T}} = E\sin\theta$, respectively. The angular distance between two objects with relative differences $\Delta\eta$ in pseudorapidity and $\Delta\phi$ in azimuth is given by $\Delta R = \sqrt{(\Delta\eta)^2 + (\Delta\phi)^2}$.

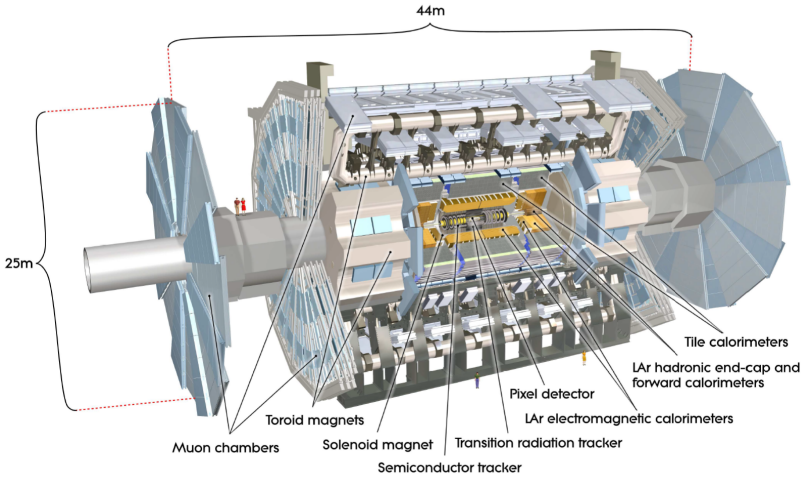

Figure 3.2: The ATLAS detector, with subsystems labelled. Figure taken from Ref. [176].

The pixel detector is the innermost of the tracking detectors, and has the highest granularity at 50×400 μm^2 [177, 178]. The barrel portion of the pixel detector, which has three concentric layers, is encompassed by the barrel SCT. Both the pixel detector and SCT have endcaps on each side of the interaction point. Endcaps are detectors which form discs that are perpendicular to the beam axis, and are used to detect particles at high pseudorapidities [176]. The TRT is a drift tube detector, made up of "straws" that are 4 mm in diameter and 144 cm long in the barrel region. The straws in the endcap of the of TRT are 37 cm long, and fan radially outward from the beam axis. Together, the barrel and endcap of the TRT provide coverage of $|\eta| < 2.0$ [176]. The pixel detector, SCT, and TRT are fully encompassed by the 2T magnetic field produced by a solenoid magnet, allowing for reconstruction of charged particle trajectories as they bend in the field. Collision vertices are also reconstructed using the inner detector. Together, these systems provide precise tracking of charged particles with p_{T} greater than 0.5 GeV.

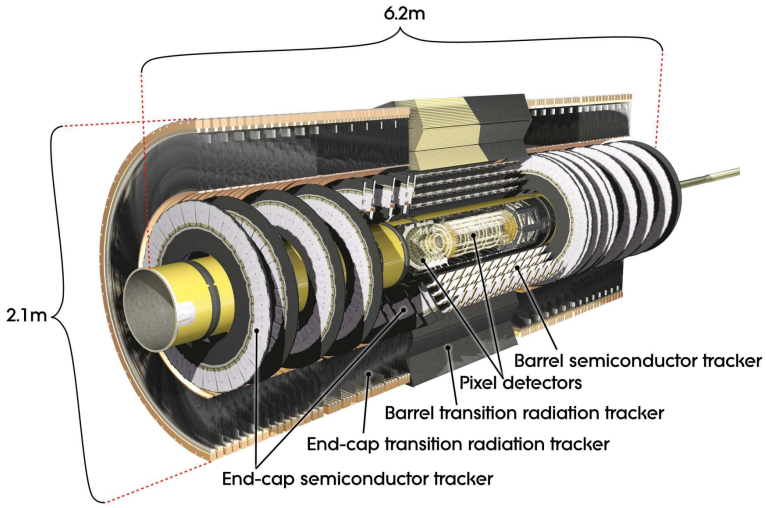

Figure 3.3: A schematic of the ATLAS inner detector. Figure taken from Ref. [176].

3.2.2 Calorimeter

The ATLAS calorimeter system has a coverage of $|\eta| < 4.9$. Both the hadronic and electromagnetic portions are sampling calorimeters, meaning that they have alternating layers of dense "passive" absorber material and "active" sampling material. As incident particles traverse the absorber, they lose energy and produce secondary particles, creating a shower of lower energy particles. As the shower travels through the active material, charged particles produce electrons and photons that are measured using various particle detection mechanisms, depending on the calorimeter system. Using calibrations and tracking information, these energy deposits can be used to reconstruct the energy of the initial particle responsible for the shower formation. The individual subsystems of the ATLAS calorimeter are labelled in Figure 3.4, with the previously discussed inner detector greyed out in the center.

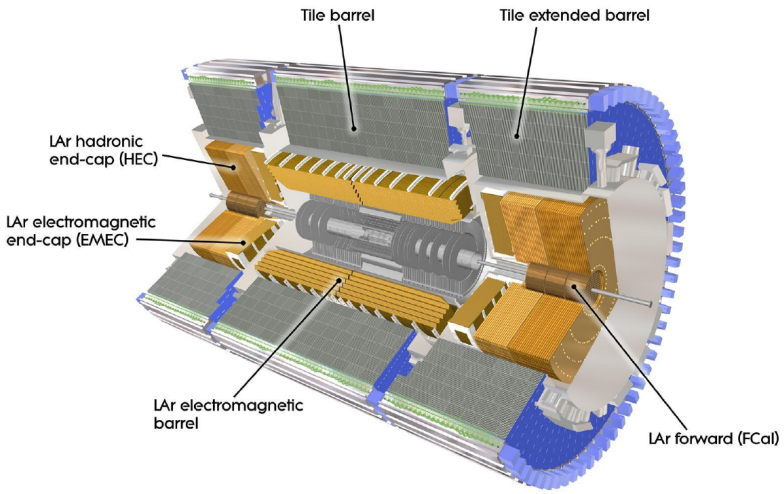

Figure 3.4: A schematic of the ATLAS calorimeter system. Figure taken from Ref. [176].

The electromagnetic calorimeter of ATLAS in both the barrel and endcap regions use liquid argon (LAr) as the active medium, with Pb absorbers. As charged particles pass through the LAr, ionization results in the production of electrons which drift to copper electrodes due to an electric field gradient within the active region. The primary purpose of the electromagnetic calorimeter is to measure the energy of photons and electrons. The thickness of calorimeters is measured in units of radiation length ($X_\circ$) for electromagnetic calorimeters and interaction length (λ) for hadronic calorimeters. One radiation length is equal to the average distance an electron will travel in a given medium before its energy is reduced to $1/e$ of its initial energy due to Bremsstrahlung radiation [179]. One interaction length is equal to the average distance a hadron will travel in a given medium before participating in a nuclear interaction. Particles which survive the electromagnetic calorimeter are typically hadrons, including neutrons, protons and pions. The barrel portion of the hadronic calorimeter is composed of steel absorber and scintillating tiles which detect photons generated by hadronic showers. Wavelength shifting fibers within the scintillating tiles redirect light to photomultiplier tubes, where the photons are converted to an electronic signal. The hadronic endcap calorimeter uses LAr with copper absorbers and covers $1.5 < |\eta| < 3.2$. The electromagnetic and hadronic calorimeters both have full coverage in azimuth and for $|\eta| < 3.2$. The forward calorimeter (FCal) of ATLAS uses copper and tungsten with LAr. The FCal plays a prominent role in the measurement presented in this thesis, as discussed in Section 4.5. It has coverage of $3.2 < |\eta| < 4.9$, made possible by its close proximity to the beam pipe. Refer to Table 3.1 for a summary of the relevant parameters for each of the subsystems within the ATLAS calorimeter.

Subsystem	Sampling Medium	Absorber Material	η Coverage	Depth
EM Barrel	LAr	Lead	$\|\eta\| < 1.475$	$> 22X_0$
EM Endcap	LAr	Lead	$1.375 < \|\eta\| < 3.2$	$> 24X_0$
Hadronic Barrel	Scintillating Tiles	Steel	$\|\eta\| < 1.0$	7.4 λ
Hadronic Extended Barrel	Scintillating Tiles	Steel	$0.8 < \|\eta\| < 1.7$	7.4 λ
Hadronic Endcap	LAr	Copper	$1.5 < \|\eta\| < 3.2$	10 λ
FCal	LAr	Copper/Tungsten	$3.2 < \|\eta\| < 4.9$	10 λ

Table 3.1: Summary of ATLAS calorimeter subsystems [176].

Muons are weakly interacting particles and require an additional muon spectrometer beyond the hadronic calorimeter. The spectrometer is surrounded by a torroid magnet, allowing for a momentum determination of the particles. The muon spectrometer is located outside of the calorimeter system and is used to measure muons which do not stop within the calorimeter. The toroid magnets provide a magnetic field for the muons to bend in order to measure their momenta. Precision tracking chambers are used to measure muons in the region of $|\eta| < 2.7$.

3.2.3 ZDC

The Zero-Degree Calorimeters (ZDC) of ATLAS are placed in the Target Absorber for Neutrals (TAN) during HI running at $z = \pm 140$ m from the interaction point. The ZDCs are tungsten/quartz sampling calorimeters which only see far forward ($|\eta| > 8.3$) neutral particles, referred to as spectators. The energy resolution in these detectors is good enough to resolve both the one neutron and two neutron peeks, allowing for use as a trigger on specific event topologies. Two such topologies are shown in Figure 3.5, where the left plot represents Ultra-Peripheral Collisions (UPC) in which a photon generated by the electromagnetic field of one nuclei interacts with a colliding nuclei, breaking it apart. The result of this interaction is one completely intact nuclei, which is swept away by the beam magnets before reaching the ZDC, and a broken nuclei whose liberated neutrons deposit their energy in the ZDC. The right plot represent collisions in which both colliding nuclei break apart, sending forward neutrons to both ZDC arms. The ZDC can also be used as an alternative to the FCal for measuring the event centrality.

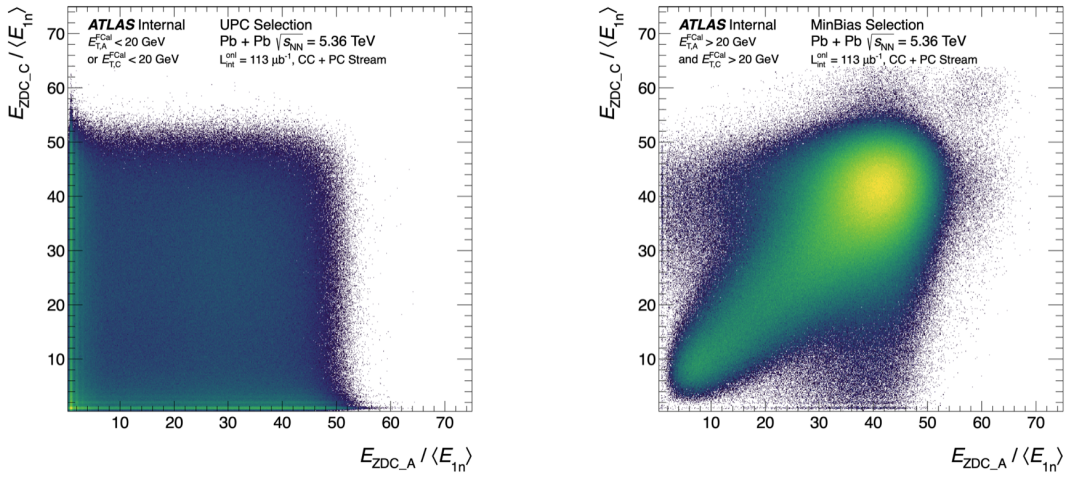

Figure 3.5: Demonstration of UPC (left) and hadronic (right) event topolgies, as seen in the energy recorded by the ZDCs on each side of ATLAS.

3.2.4 Trigger

Only a fraction of the interactions which occur within the detector can be saved for later analysis. In order to decide which events are of interest, ATLAS uses a two-level trigger system. The first level is hardware-based, meaning that the decision of whether or not to record an event is made via parameters set on custom electronics close to where the signals are read-out, allowing for fast decision making. The second level of the trigger is software-based, and is referred to as the High-Level Trigger (HLT). Together, this system aims to record events which are of high interest for physicists. The full trigger strategy used in this analysis is discussed at length in Section 4.4.

3.3 ATLAS Heavy-ion Jet Reconstruction and Calibration

3.3.1 Jet Reconstruction

When studying HI collisions with the ATLAS detector, jets are reconstructed using the anti-k_t jet clustering algorithm [47]. Refer to Section 1.3.2 for a review of clustering algorithms. The anti-k_t algorithm uses collections of four-vectors corresponding to a set of tracks of charged particles in the inner tracking system (track jets), massless calorimeter towers with size $\Delta\eta \times \Delta\phi = 0.1 \times 0.1$ (HI jets), or sets of simulated particles at the generator level (truth jets). The measurement presented in this thesis makes use of HI jets reconstructed using the anti-k_t algorithm with a radius of $R = 0.4$. A detailed review of the performance of HI jet reconstruction can be found in Ref. [180].

To reconstruct jets in HI collisions, a large background arising from the underlying event (UE) must be subtracted from each tower to avoid large rates of fake jets [181], giving access the kinematics of the initiating parton. The energy registered in each calorimeter cell can be decomposed into contributions from a jet and from the UE as

$$\frac{d^2E_{\mathrm{T}}^{\mathrm{total}}}{d\eta d\phi} = \frac{d^2E_{\mathrm{T}}^{\mathrm{jet}}}{d\eta d\phi} + \frac{d^2E_{\mathrm{T}}^{\mathrm{UE}}}{d\eta d\phi}. \tag{3.1}$$

Only the first contribution should be used to reconstruct jets. Therefore, the UE contribution to the transverse energy must be estimated and subtracted. The UE subtraction procedure makes use of the UE average transverse energy density, $\rho(\eta, \phi)$. The ϕ dependence in ρ arises from global azimuthal correlations in the particle production, usually referred to as flow, that arises from the hydrodynamic response of the medium to the geometry of the initial collision [117]. One can describe the UE contribution to the transverse energy of the calorimeter towers by using the amplitudes (ν_n) and the phases (Ψ_n) of the Fourier components of the azimuthal angle distributions (see Section 1.5.4):

$$\rho(\eta, \phi) = \frac{1}{2\pi}\frac{\langle dE_T\rangle}{d\eta}\big(1 + 2\sum_{n=2}^{N}\nu_n \cos(n(\phi - \Psi_n))\big), \tag{3.2}$$

where ϕ and n represent the azimuthal angle of the tower and the order of the flow harmonic, respectively. Although ν_2 dominates, the third and the fourth harmonics are used to further improve the ρ evaluation. A value of $N = 4$ was used to reconstruct Run 2 Pb+Pb data, while for p+Pb data used for the analysis presented in this thesis, no anisotropic component was allowed in the fit, *i.e.* $N = 0$. This choice was made due to the relatively low multiplicity characterizing p+Pb collisions compared to Pb+Pb. Additional information on the subtraction of elliptic flow during the HI jet reconstruction used for ATLAS Run 2 data can be found in Refs. [182, 183] and in the references therein. A summary of the underlying event subtraction procedure is shown in Figure 3.6. In short, "seed" jets are identified by running the anti-k_t algorithm with

$R = 0.2$ over the raw calorimeter clusters, which are shown in the left portion of Figure 3.7. Any towers used to form candidate seed jets, which exceed a threshold determined using the mean tower energy, are excluded from the following $\rho(\eta, \phi)$ subtraction procedure. Next, $R = 0.4$ track jets with $p_{\mathrm{T}} > 4$ GeV are identified, using the subtracted seed jets. Another iteration of subtraction is then performed to determine the final value of $\rho(\eta, \phi)$, after which the final jets can be reconstructed.

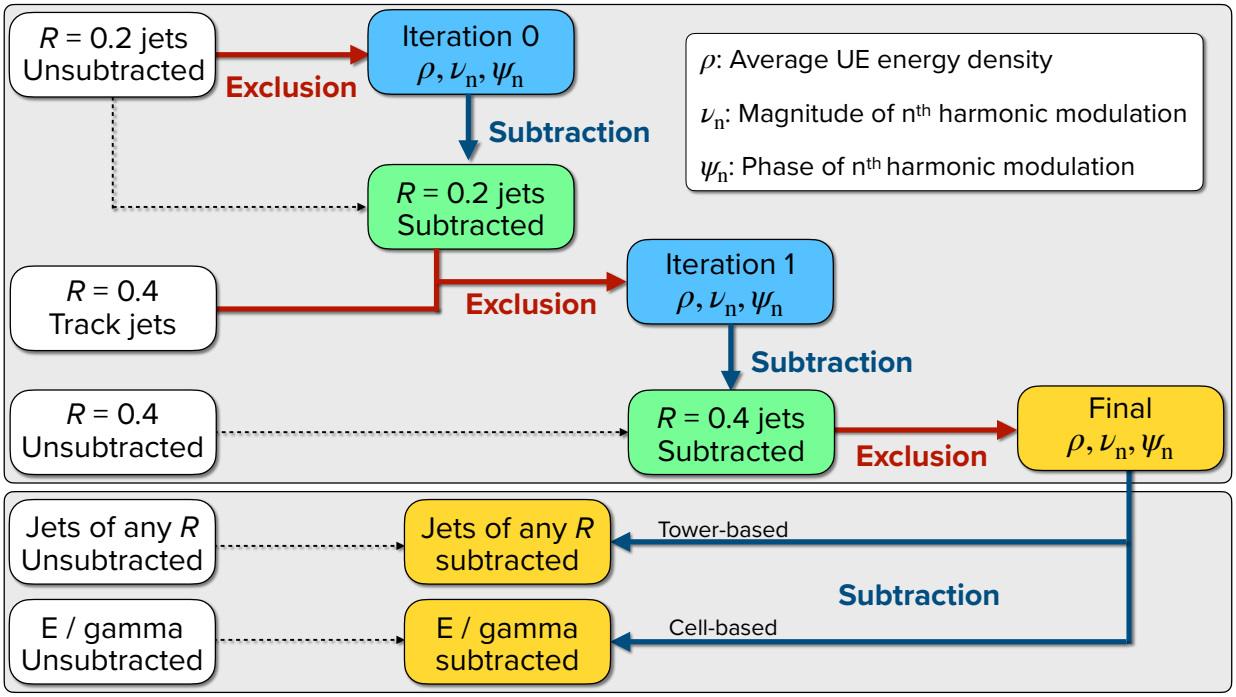

Figure 3.6: Diagram of underlying event subtraction procedure for heavy-ion jets in ATLAS.

The result of this procedure on minimum-bias Pb+Pb data at $\sqrt{s_{\mathrm{NN}}} = 5.36$ TeV recorded in October 2023 is shown in the right portion of Figure 3.7. The single noisy tower at $\eta \approx -1$ and $\phi \approx 2$ does not negatively impact the procedure. The average subtracted transverse energy from jets in Pb+Pb data in different centrality classes is shown in Figure 3.8. The subtracted energy is independent of the transverse energy of the jet, depending only on the centrality of the collision and the pseudorapidity of the jet, showing that the background subtraction works as expected, removing the underlying event without being biased by the jet itself.

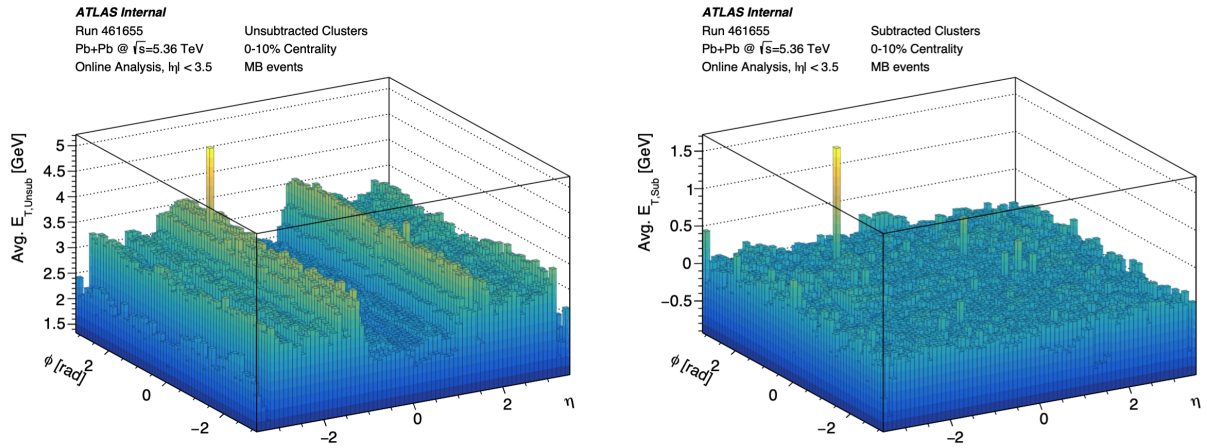

Figure 3.7: Demonstration of underlying event subtraction for calorimeter towers in central collisions. A single noisy calorimeter tower is observed after subtraction.

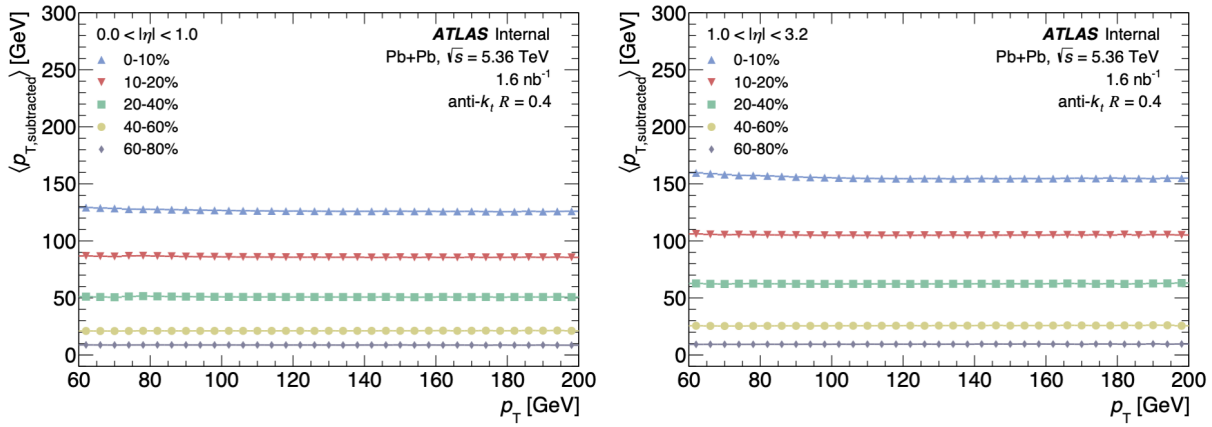

Figure 3.8: Average underlying event subtraction for jets in different centrality classes for $|\eta| < 1.0$ (left) and $1.0 < |\eta| < 3.2$ (right).

3.3.2 Jet Calibration

Individual calorimeter cells are themselves calibrated, but there is a variety of factors (*e.g.* passive material in the detector, gaps between cells, signal losses, etc.) that allow only for a partial measurement of the energy deposited by a single jet in the detector [184]. To compensate for these experimental effects, the energy scale of reconstructed jets needs to be calibrated to the truth energy scale. The HI jet calibration procedure is similar to the standard *pp* reconstruction performed in ATLAS, which uses topological clusters of energy deposited in the calorimeter as constituents. The calibration sequence for HI jets is presented in Ref. [185]. After the UE subtraction, two different types of calibrations are applied, namely:

1. EtaJES MC-based calibration, to recover the truth energy scale in MC.
2. HI/EMTopo cross-calibration and *in situ* / η-intercalibration, to account for differences between MC and data.

The EtaJES calibration is typically the larger between the two and is derived from Pythia8 simulated dijet events. The scope of this calibration is to correct for the energy scale component that is common to both data and MC. The per-jet energy correction factor is computed using a numerical inversion procedure [186, 187], see Ref. [188] for a review of the math used to perform this procedure. A typical jet energy scale correction, $E_{\mathrm{T}}^{\mathrm{true}}/E_{\mathrm{T}}^{\mathrm{reco}}$, ranges from $\sim$ 1.2 to 2.0. Within this step of the calibration procedure a small pseudorapidity correction is also applied to the jet's reconstructed η, to counteract the implicit assumption that the z-vertex = 0 made during the reconstruction of the data. The z-vertex corresponds to the position of the vertex associated to the jet along the beam axis. For this reason, this procedure is called "origin correction".

The second calibration component is only applied to data to account for discrepancies between MC and data. The *in situ* and η-intercalibrations implement residual corrections to the jet energy scale based on the p_{T} balance in vector boson (γ, Z^0) - jet events (the *in situ* correction) and dijet events where mid-rapity jets are used to calibrate the forward rapidity jets (the η-intercalibration). Both factors have been investigated in detail for EMTopo jets in *pp* within the JetEtMiss group, but they cannot be directly applied to HI jets because of the different type of constituents used in the two cases. The cross-calibration, derived using the direct balance method in events containing a Z boson or photon opposite to a jet, is used to bridge between HI and fully calibrated EMTopo jets by accounting for additional differences in response between them [187]. Thanks to the cross-calibration, it is possible to characterize the performance of the HI jets within the EMTopo jet framework. This procedure makes it possible to use the baseline component as recommended by JetEtMiss group. It is worth noting that this procedure also has an associated uncertainty that has to be accounted for when evaluating systematics (see Section 4.7).

Chapter 4

Centrality Dependence of Dijets in p+Pb Collisions

4.1 Overview

The measurement presented in this thesis capitalizes on the substantially increased statistics collected in p+Pb collisions at $\sqrt{s_{\mathrm{NN}}} = 8.16$ TeV ($\sim$165 nb^{-1}) and the superior kinematic reach of fully reconstructed dijets over a wide range of transverse momentum (p_{T}) and rapidity (y) in this dataset to carry out a detailed measurement of the per-event dijet yield as a function of the collision geometry, which is usually defined through the event centrality observable. The dijet per-event yield of central (0–10%) and peripheral (60–90%) events are compared by constructing a central-to-peripheral ratio, R_{CP}. In this way, it is possible to quantify the deviation of dijet production in different p+Pb geometric configurations. The R_{CP} results are then compared to ATLAS results obtained analyzing p+Pb data at 5.02 TeV [152], providing evidence for a direct link between these two jet measurements. The results provide unprecedented input to characterize the onset of color transparency effects in p+A collisions in terms of the initial partonic system kinematics and study the dependence of the interaction strength as a function of the momentum fraction carried by the colliding partons [156].

4.2 Analysis Strategy

The analysis seeding this thesis aims at studying dijet production in proton-lead collisions using the ATLAS detector, and was initially proposed to achieve two main goals:

1. Measure the dijet production cross-section in p+Pb, and compare it to a constructed pp reference, to constrain nPDFs over a wide kinematic range.

2. Analyze the centrality dependence of the dijet production by measuring dijet per-event yields, to then construct a central-to-peripheral ratio (R_{CP}) in order to provide insights on initial state effects due to the nuclear environment.

These two goals have substantial common ground, but require different analysis techniques. For example, the cross-section analysis necessitates construction of a pp reference which involves dedicated NLO Monte Carlo

production and associated studies. Both of these physics goals are of high interest to the physics community on their own. For this reason, the two analyses were separated, with this thesis only concerning ②. The cross-section analysis will be carried out in the near-future, as the framework for calculating the p+Pb cross-section already exists, and only the pp reference and associated uncertainties remain to be produced.

4.2.1 Binning

The per-event dijet yield was measured as a function of

$$p_{\mathrm{T,Avg}} = \frac{p_{\mathrm{T},1} + p_{\mathrm{T},2}}{2}, \quad y_{\mathrm{b}} = \frac{y_1^{\mathrm{CM}} + y_2^{\mathrm{CM}}}{2}, \quad \text{and} \quad y^* = \frac{|y_1^{\mathrm{CM}} - y_2^{\mathrm{CM}}|}{2}, \tag{4.1}$$

where the superscript 'CM' denotes variables translated in the center-of-mass frame of the collision, while the subscripts '1' and '2' refer to the jets with the highest (leading) and second-highest (sub-leading) p_{T} in a given event, respectively. $p_{\mathrm{T,Avg}}$ is the average transverse momentum, and y_{b} and y^* are the boost, and the half rapidity separation of the dijet system, respectively. Note that y^* is directly related to the 2→2 scattering angle.

In the case of p+Pb collisions, the CM value for the rapidity can be obtained by adding/subtracting $\Delta y = \pm 0.465$, as discussed in Section 4.3.1. This value is obtained using

$$\Delta y \approx \frac{1}{2} \log \frac{Z_p A_{\mathrm{Pb}}}{Z_{\mathrm{Pb}} A_p}, \tag{4.2}$$

where Z and A represent the atomic number and mass of the participants, respectively [98]. The atomic mass and atomic number of a proton are both 1, while that of the Pb nuclei are 82 and 208, respectively.

The chosen kinematic variables allow for full access to the parton level kinematics:

$$x_p = \frac{p_{\mathrm{T},1} e^{y_1^{\mathrm{CM}}} + p_{\mathrm{T},2} e^{y_2^{\mathrm{CM}}}}{\sqrt{s}} \simeq \frac{2 p_{\mathrm{T,Avg}}}{\sqrt{s}} e^{y_{\mathrm{b}}} \cosh(y^*), \tag{4.3}$$

$$x_{\mathrm{Pb}} = \frac{p_{\mathrm{T},1} e^{-y_1^{\mathrm{CM}}} + p_{\mathrm{T},2} e^{-y_2^{\mathrm{CM}}}}{\sqrt{s}} \simeq \frac{2 p_{\mathrm{T,Avg}}}{\sqrt{s}} e^{-y_{\mathrm{b}}} \cosh(y^*), \tag{4.4}$$

$$m_{12} = x_p x_{\mathrm{Pb}} s = 4 p_{\mathrm{T,Avg}}^2 \cosh^2(y^*), \tag{4.5}$$

where m_{12} represents the mass of the dijet system, and x_p and x_{Pb} are the momentum fractions carried by the partons participating in the hard scattering, which originate from the colliding proton and the lead nucleus, respectively. The implications of the $\simeq$ symbol in these formulas were studied by analyzing dijet events generated with Pythia8. Note that the measurement is not performed directly in these variables, but bins defined for the analysis can be approximately mapped to them using average kinematic values, as detailed in Section 4.8.

In order to improve the statistics of forward bins and to avoid large bin migrations, allowing for a 1D unfolding, large y_{b} and y^* bins were utilized for the per-event dijet yield measurement (see Figure 4.1). In the preliminary version of this analysis, reported in Ref. [189], a variable y^* binning in different y_{b} intervals was chosen to maximize the phase space coverage of the analysis. This approach was revisited for the final analysis, reported in this thesis, trying to maximize the statistics in the kinematic bins located at the edges of the phase space, and to tailor each kinematic bin to its effective coverage, e.g. not extending edge bins over their effective kinematic coverage. The binning chosen for $p_{\mathrm{T,Avg}}$ is logarithmic such that the measurement can be carried out over approximately two orders of magnitude (40–1000 GeV). Underflow and overflow bins are utilized to allow for migration between bins at the edges of the measurement during unfolding (particularly at low $p_{\mathrm{T,Avg}}$).

The binning for the three kinematic variables is as follows:

- $p_{\mathbf{T,Avg}}$ **binning** [Logarithmic: 40 – 1000 GeV]
  - underflow (3 bins): 22.0 27.0 33.0 40.0 GeV
  - measurement (16 bins): 40.0 49.57 61.44 76.15 94.37 116.96 144.96 179.65 222.65 275.95 341.99 423.85 525.31 651.04 806.87 1000 GeV
  - overflow (1 bin): 1000.0 1200.0 GeV
- $y_{\mathbf{b}}$ **binning** [Linear: -3.0 – 4.0]
  - measurement (8 bins): -3.0 -2.0 -1.0 0.0 1.0 2.0 3.0 4.0
- y^* **binning** [Linear: 0 – 4.0, depending on y_{b}]
  - measurement for $-3.0 < y_{\mathrm{b}} < -2.0$ (1 bins): 0.0 1.0
  - measurement for $-2.0 < y_{\mathrm{b}} < -1.0$ (2 bins): 0.0 1.0 2.0
  - measurement for $-2.0 < y_{\mathrm{b}} < -1.0$ (3 bins): 0.0 1.0 2.0 3.0
  - measurement for $0.0 < y_{\mathrm{b}} < 1.0$ (3 bins): 0.0 1.0 2.0 4.0
  - measurement for $1.0 < y_{\mathrm{b}} < 2.0$ (3 bins): 0.0 1.0 2.0 3.0
  - measurement for $2.0 < y_{\mathrm{b}} < 3.0$ (2 bins): 0.0 1.0 2.0
  - measurement for $3.0 < y_{\mathrm{b}} < 4.0$ (1 bins): 0.0 1.0

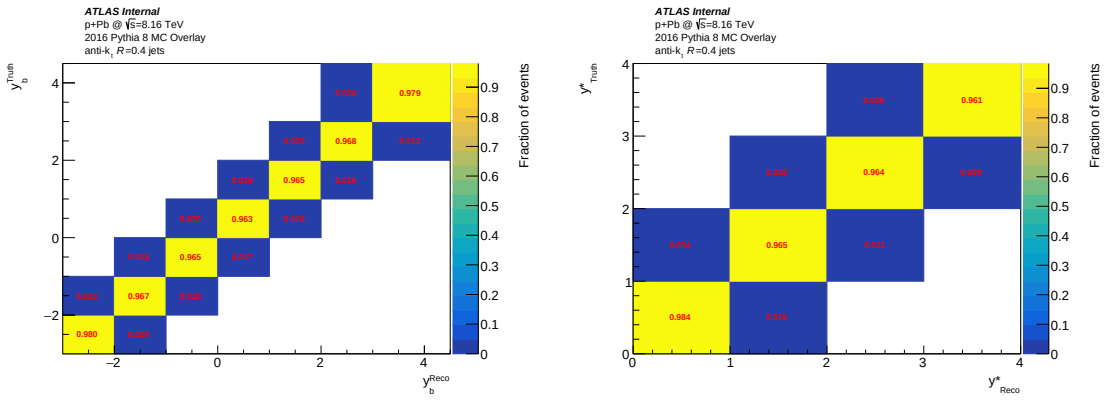

(a) Bin migration for y_{b}.

(b) Bin migration for y^*.

Figure 4.1: Bin migration for y_{b} and y^* variables. Each row (*e.g.* each series of bin at the same truth value) is normalized to the total number of entries in that row. Minimal migration is observed for both y_{b} and y^*, allowing for 1D Bayesian unfolding in $p_{\mathrm{T,Avg}}$ to be utilized.

Pythia x Approximation Study

Accessing the parton level kinematics using jets involves approximations built in to the definition of the probe, which has a finite precision due to the radius characterizing it. If, in a given event, particles are emitted outside of the cone considered in the analysis, set by the jet radius ($R = 0.4$ in this analysis), the corresponding jet momentum will be intrinsically lower than that of the parton initiating the jet. Such a discrepancy can be easily accounted for by evaluating the accuracy of the initial state kinematics description achieved by using a certain jet radius via Monte Carlo generators. Another similar factor is introduced by the approximation applied to evaluate the initial parton momentum fraction using the right side of Equations 4.3 and 4.4, starting from the dijet kinematic variables constructed in this analysis. The assumption that allows one to write the following relation:

$$\frac{p_{\mathrm{T},1}e^{y_1^{\mathrm{CM}}} + p_{\mathrm{T},2}e^{y_2^{\mathrm{CM}}}}{\sqrt{s}} = \frac{2p_{\mathrm{T,Avg}}}{\sqrt{s}}e^{y_b}\cosh(y^*), \tag{4.6}$$

is that $p_{\mathrm{T},1} = p_{\mathrm{T},2}$. Equations 4.3 and 4.4 contain a $\simeq$ symbol instead of equality because, once three parton events are included at next-to-leading order, the two leading jets are no longer exactly balanced [190]. The equality in Equation 4.6 is approached in events containing two hard partons while the third parton is soft. No additional approximations are introduced by the use of y_{b} and y^* as an alternative to y_1^{CM} and y_2^{CM}.

To test the quality of the $p_{\mathrm{T,Avg}}$ approximation, dedicated studies, based on Pythia8 dijet Monte Carlo, were carried out and are reported below. The mean values for x_p, obtained using the left (nominal) and right (approximate) side of Equation 4.6, are given in Figure 4.2 for each (y_{b}, y^*) bin. The corresponding values for x_{Pb} are given in Figure 4.3. The mean value for the original parton momentum fraction, i.e., of the parton before the fragmentation into a jet, directly accessible in the information provided by the generator, is also reported for completeness in both cases. As expected from the considerations made above, a hierarchy $x_{\mathrm{pythia}} > x_{\mathrm{nominal}} > x_{\mathrm{approx}}$ is observed in all the kinematic bins.

ATLAS Internal Simulation $\sqrt{s_{\mathrm{NN}}}$ = 8.16 TeV anti-k_t R=0.4, Pythia 8		$-1.0 < y_b < 0.0$ $2.0 < y^* < 3.0$ $\mu_{x_p,\,\mathrm{pythia}} = 0.0572$ $\mu_{x_p,\,\mathrm{nominal}} = 0.0469$ $\mu_{x_p,\,\mathrm{approx}} = 0.0389$	$0.0 < y_b < 1.0$ $2.0 < y^* < 4.0$ $\mu_{x_p,\,\mathrm{pythia}} = 0.1572$ $\mu_{x_p,\,\mathrm{nominal}} = 0.1381$ $\mu_{x_p,\,\mathrm{approx}} = 0.1159$	$1.0 < y_b < 2.0$ $2.0 < y^* < 3.0$ $\mu_{x_p,\,\mathrm{pythia}} = 0.2443$ $\mu_{x_p,\,\mathrm{nominal}} = 0.2177$ $\mu_{x_p,\,\mathrm{approx}} = 0.1897$		
	$-2.0 < y_b < -1.0$ $1.0 < y^* < 2.0$ $\mu_{x_p,\,\mathrm{pythia}} = 0.0091$ $\mu_{x_p,\,\mathrm{nominal}} = 0.0069$ $\mu_{x_p,\,\mathrm{approx}} = 0.0058$	$-1.0 < y_b < 0.0$ $1.0 < y^* < 2.0$ $\mu_{x_p,\,\mathrm{pythia}} = 0.0222$ $\mu_{x_p,\,\mathrm{nominal}} = 0.0177$ $\mu_{x_p,\,\mathrm{approx}} = 0.0149$	$0.0 < y_b < 1.0$ $1.0 < y^* < 2.0$ $\mu_{x_p,\,\mathrm{pythia}} = 0.0603$ $\mu_{x_p,\,\mathrm{nominal}} = 0.0511$ $\mu_{x_p,\,\mathrm{approx}} = 0.0432$	$1.0 < y_b < 2.0$ $1.0 < y^* < 2.0$ $\mu_{x_p,\,\mathrm{pythia}} = 0.1548$ $\mu_{x_p,\,\mathrm{nominal}} = 0.1362$ $\mu_{x_p,\,\mathrm{approx}} = 0.1175$	$2.0 < y_b < 3.0$ $1.0 < y^* < 2.0$ $\mu_{x_p,\,\mathrm{pythia}} = 0.2633$ $\mu_{x_p,\,\mathrm{nominal}} = 0.2333$ $\mu_{x_p,\,\mathrm{approx}} = 0.2074$	
$-3.0 < y_b < -2.0$ $0.0 < y^* < 1.0$ $\mu_{x_p,\,\mathrm{pythia}} = 0.0030$ $\mu_{x_p,\,\mathrm{nominal}} = 0.0014$ $\mu_{x_p,\,\mathrm{approx}} = 0.0012$	$-2.0 < y_b < -1.0$ $0.0 < y^* < 1.0$ $\mu_{x_p,\,\mathrm{pythia}} = 0.0063$ $\mu_{x_p,\,\mathrm{nominal}} = 0.0035$ $\mu_{x_p,\,\mathrm{approx}} = 0.0031$	$-1.0 < y_b < 0.0$ $0.0 < y^* < 1.0$ $\mu_{x_p,\,\mathrm{pythia}} = 0.0129$ $\mu_{x_p,\,\mathrm{nominal}} = 0.0094$ $\mu_{x_p,\,\mathrm{approx}} = 0.0082$	$0.0 < y_b < 1.0$ $0.0 < y^* < 1.0$ $\mu_{x_p,\,\mathrm{pythia}} = 0.0319$ $\mu_{x_p,\,\mathrm{nominal}} = 0.0250$ $\mu_{x_p,\,\mathrm{approx}} = 0.0218$	$1.0 < y_b < 2.0$ $0.0 < y^* < 1.0$ $\mu_{x_p,\,\mathrm{pythia}} = 0.0803$ $\mu_{x_p,\,\mathrm{nominal}} = 0.0691$ $\mu_{x_p,\,\mathrm{approx}} = 0.0600$	$2.0 < y_b < 3.0$ $0.0 < y^* < 1.0$ $\mu_{x_p,\,\mathrm{pythia}} = 0.2114$ $\mu_{x_p,\,\mathrm{nominal}} = 0.1886$ $\mu_{x_p,\,\mathrm{approx}} = 0.1670$	$3.0 < y_b < 4.0$ $0.0 < y^* < 1.0$ $\mu_{x_p,\,\mathrm{pythia}} = 0.3558$ $\mu_{x_p,\,\mathrm{nominal}} = 0.3212$ $\mu_{x_p,\,\mathrm{approx}} = 0.2873$

Figure 4.2: Comparison of average values of x_p computed in each kinematic bin using values directly provided by Pythia8 in the event generator truth ($\mu_{\mathrm{x_p,pyhtia}}$), by the nominal formula using the truth values of $p_{\mathrm{T},1}$ and $p_{\mathrm{T},2}$ ($\mu_{\mathrm{x_p,nominal}}$) and by the approximation using $p_{\mathrm{T,Avg}}$ ($\mu_{\mathrm{x_p,approx}}$).

It is important to note how the discrepancy between x_{nominal} and x_{approx} reaches at maximum an absolute 3.5% in the valence region, and 0.02% in the low-x region. These values do not change at all the attribution of the kinematic regime of the initial state parton in the corresponding bins. All the discrepancies are

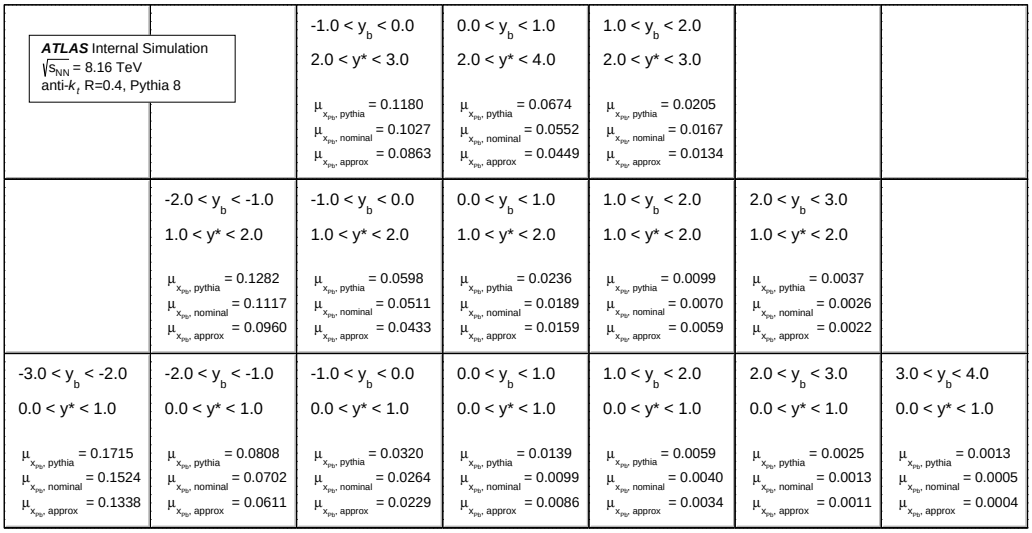

Figure 4.3: Comparison of average values of x_{Pb} computed in each kinematic bin using values directly provided by PYTHIA8 in the event generator truth ($\mu_{x_{\mathrm{Pb,pyhtia}}}$), by the nominal formula using the truth values of $p_{\mathrm{T},1}$ and $p_{\mathrm{T},2}$ ($\mu_{x_{\mathrm{Pb,nominal}}}$) and by the approximation using $p_{\mathrm{T,Avg}}$ ($\mu_{x_{\mathrm{Pb,approx}}}$).

well contained within the horizontal bin width, directly related to the initial $p_{\mathrm{T,Avg}}$ binning, and are more prominent in the forward/backward regions compared to the central one.

This analysis includes data collected with two opposite beam orientations. To provide results that properly account for this feature of the data taking, the per-event dijet yield analysis is first carried out using the variables in Equation 4.1 computed starting from the reference frame of the data taking. After unfolding, the results are combined by flipping them in terms of y_{b}, which is directly affected by the beam orientation.

The convention chosen for the final results has the proton travelling from negative to positive rapidities.

4.2.2 Measured Observables

The fundamental quantity measured in this analysis is the inclusive triple-differential per-event dijet yield

$$\frac{1}{N_{\mathrm{evt}}^{\mathrm{cent}}} \frac{d^3 N_{\mathrm{dijet}}^{\mathrm{cent}}}{dp_{\mathrm{T,Avg}} dy_{\mathrm{b}} dy^*}(p_{\mathrm{T,Avg}}, y_{\mathrm{b}}, y^*) \tag{4.7}$$

where $N_{\mathrm{evt}}^{\mathrm{cent}}$ and $N_{\mathrm{dijet}}^{\mathrm{cent}}$ represent the number of prescale-corrected minimum bias (MB) events and the number of dijet events passing the selection criteria applied in the analysis in the given centrality class, respectively. The measurement is carried out as a function of $p_{\mathrm{T,Avg}}$, y_{b}, and y^*. The results are also presented in three centrality selections, 0–10%, 10–60% and 60–90% (see Section 4.5). A bayesian unfolding procedure is used to correct the measurement for experimental effects back to the ideal "particle" final state of a p+Pb collision, consisting of stable particles, excluding muons and neutrinos, with a lifetime longer than 30 ps. The kinematic boundaries of the measurement are defined in Section 4.2.1. The leading and sub-leading jets are required to have p_{T}>40 GeV and >30 GeV, respectively. A detailed analysis of the trigger efficiencies and of the jet reconstruction performance was carried out in order to keep these kinematic cuts as low as possible, allowing for access to very low x_{Pb} (see Equation 4.4). All three kinematic variables used to scan the phase space are defined in the center-of-mass reference system of the p+Pb collisions.

The centrality-dependent physics observable constructed making use of the central (0–10%) and peripheral (60–90%) bins is the $R_{\mathrm{CP}}{}^{\frac{0-10\%}{60-90\%}}$, defined as

$$R_{\mathrm{CP}}^{\frac{0-10\%}{60-90\%}}(p_{\mathrm{T,Avg}}, y_{\mathrm{b}}, y^*) = \frac{\frac{1}{\langle T_{\mathrm{AB}}^{0-10\%}\rangle}\frac{1}{N_{\mathrm{evt}}^{0-10\%}}\frac{d^3N_{\mathrm{dijet}}^{0-10\%}}{dp_{\mathrm{T,Avg}}dy_{\mathrm{b}}dy^*}(p_{\mathrm{T,Avg}}, y_{\mathrm{b}}, y^*)}{\frac{1}{\langle T_{\mathrm{AB}}^{60-90\%}\rangle}\frac{1}{N_{\mathrm{evt}}^{60-90\%}}\frac{d^3N_{\mathrm{dijet}}^{60-90\%}}{dp_{\mathrm{T,Avg}}dy_{\mathrm{b}}dy^*}(p_{\mathrm{T,Avg}}, y_{\mathrm{b}}, y^*)} \tag{4.8}$$

This observable quantifies the deviation of dijet production between the geometric configuration of p+Pb collisions relative to the ratio assumed from geometric scaling arguments. Since the centrality classification of the data is carried out using the overall event activity, the R_{CP} is sensitive to eventual color transparency (CT) effects that would reduce the number of nucleon-nucleon interactions between the projectile proton and the nucleus. An interesting explanation of this mechanism can be found in Ref. [156] (see Chapter 2.3). In addition, the R_{CP} offers relevant advantages in the evaluation of the systematic uncertainty, allowing for the partial or full cancellation of large systematic uncertainties from the model-dependent determination of $\langle T_{\mathrm{AB}}\rangle$, and other uncertainties related to jet reconstruction and trigger efficiencies. Equation 4.8 can be re-written in a way that accounts for partial cancellation of systematic uncertainties on $\langle T_{\mathrm{AB}}\rangle$ as

$$R_{\mathrm{CP}}^{\frac{0-10\%}{60-90\%}}(p_{\mathrm{T,Avg}}, y_{\mathrm{b}}, y^*) = \frac{\frac{1}{R_{\mathrm{coll}}^{0-10\%}}\frac{1}{N_{\mathrm{evt}}^{0-10\%}}\frac{d^3N^{0-10\%}}{dp_{\mathrm{T,Avg}}dy_{\mathrm{b}}dy^*}(p_{\mathrm{T,Avg}}, y_{\mathrm{b}}, y^*)}{\frac{1}{N_{\mathrm{evt}}^{60-90\%}}\frac{d^3N^{60-90\%}}{dp_{\mathrm{T,Avg}}dy_{\mathrm{b}}dy^*}(p_{\mathrm{T,Avg}}, y_{\mathrm{b}}, y^*)}. \tag{4.9}$$

Where now $R_{\mathrm{coll}}^{0-10\%}$ is defined as [191]

$$R_{\mathrm{coll}}^{0-10\%} = \frac{\langle N_{\mathrm{part}} - 1\rangle^{0-10\%}}{\langle N_{\mathrm{part}} - 1\rangle^{60-90\%}}, \tag{4.10}$$

where N_{part} represents the number of participating nucleons in the collision (e.g. the proton beam and the participants in the Pb nucleus). For this analysis, it will not be possible to take advantage of the partial uncertainties cancellation while building $R_{\mathrm{coll}}^{0-10\%}$ [192], since the values of N_{part} reported in the centrality analysis for this dataset only have a total uncertainty associated (e.g. no breakdown in separate contributions), and $R_{\mathrm{coll}}^{0-10\%}$ was not evaluated at that time. For this reason, Equation 4.8 will be used to compute $R_{\mathrm{CP}}^{\frac{0-10\%}{60-90\%}}$ in this thesis.

4.3 Datasets and Event Selection

4.3.1 p+Pb Data

The p+Pb data at $\sqrt{s_{\mathrm{NN}}} = 8.16$ TeV used for this analysis were delivered by the LHC to ATLAS in November and December of 2016. In p+Pb collisions at 8.16 TeV the colliding beams have different energies per nucleon (6.5 TeV protons colliding with (Z/A) $\times$ 6.5 TeV $\sim$ 2.65 TeV per nucleon in a lead nucleus), resulting in a collision system with $\sqrt{s_{\mathrm{NN}}} = 8.16$ TeV per nucleon pair. In these conditions, the center-of-mass frame is shifted in rapidity, y, by $\Delta y = 0.465$ in the direction of the proton beam. Data were collected in two different periods, characterized by opposite beam orientations. All the datasets used in this analysis, listed in Table 4.1, were processed using ATHENA release 21. The runs in these periods are organized as follows:

- **Period B:** 59.1 nb^{-1} of total luminosity collected. Beam 1: protons. Beam 2: Pb ions. Protons travels towards negative rapidities, "A→C" direction, corresponding to clockwise motion in the accelerator

(according to ATLAS conventions). In the following, this will be denoted as the p+Pb configuration.

- **Period C:** 110.6 nb^{-1} of total luminosity collected. Beam 1: Pb ions. Beam 2: protons. Protons travels towards positive rapidities, "C→A" direction, corresponding to counterclockwise motion in the accelerator (according to ATLAS conventions). In the following, this will be denoted as the Pb+p configuration.

2016 $\sqrt{s_{\text{NN}}}$ = 8.16 TeV Data Samples	**Period**	**Luminosity [nb^{-1}]**
data16_hip8TeV.00313063.physics_Main.merge.AOD.r11416_p3868	B	0.022
data16_hip8TeV.00313067.physics_Main.merge.AOD.r11416_p3868	B	0.947
data16_hip8TeV.00313100.physics_Main.merge.AOD.r11416_p3868	B	8.829
data16_hip8TeV.00313107.physics_Main.merge.AOD.r11416_p3868	B	11.053
data16_hip8TeV.00313136.physics_Main.merge.AOD.r11416_p3868	B	9.602
data16_hip8TeV.00313187.physics_Main.merge.AOD.r11416_p3868	B	3.298
data16_hip8TeV.00313259.physics_Main.merge.AOD.r11416_p3868	B	4.724
data16_hip8TeV.00313285.physics_Main.merge.AOD.r11416_p3868	B	4.272
data16_hip8TeV.00313295.physics_Main.merge.AOD.r11416_p3868	B	9.923
data16_hip8TeV.00313333.physics_Main.merge.AOD.r11416_p3868	B	3.791
data16_hip8TeV.00313435.physics_Main.merge.AOD.r11416_p3868	B	0.303
data16_hip8TeV.00313572.physics_Main.merge.AOD.r11416_p3868	C	0.005
data16_hip8TeV.00313574.physics_Main.merge.AOD.r11416_p3868	C	1.218
data16_hip8TeV.00313575.physics_Main.merge.AOD.r11416_p3868	C	7.168
data16_hip8TeV.00313603.physics_Main.merge.AOD.r11416_p3868	C	8.283
data16_hip8TeV.00313629.physics_Main.merge.AOD.r11416_p3868	C	6.347
data16_hip8TeV.00313630.physics_Main.merge.AOD.r11416_p3868	C	6.734
data16_hip8TeV.00313688.physics_Main.merge.AOD.r11416_p3868	C	7.475
data16_hip8TeV.00313695.physics_Main.merge.AOD.r11416_p3868	C	4.203
data16_hip8TeV.00313833.physics_Main.merge.AOD.r11416_p3868	C	4.769
data16_hip8TeV.00313878.physics_Main.merge.AOD.r11416_p3868	C	1.811
data16_hip8TeV.00313929.physics_Main.merge.AOD.r11416_p3868	C	0.514
data16_hip8TeV.00313935.physics_Main.merge.AOD.r11416_p3868	C	10.368
data16_hip8TeV.00313984.physics_Main.merge.AOD.r11416_p3868	C	2.232
data16_hip8TeV.00314014.physics_Main.merge.AOD.r11416_p3868	C	6.960
data16_hip8TeV.00314077.physics_Main.merge.AOD.r11416_p3868	C	9.642
data16_hip8TeV.00314105.physics_Main.merge.AOD.r11416_p3868	C	6.157
data16_hip8TeV.00314112.physics_Main.merge.AOD.r11416_p3868	C	9.947
data16_hip8TeV.00314157.physics_Main.merge.AOD.r11416_p3868	C	9.294
data16_hip8TeV.00314170.physics_Main.merge.AOD.r11416_p3868	C	4.665

Table 4.1: Data samples from $\sqrt{s_{\text{NN}}}$ = 8.16 TeV p+Pb collisions collected during the 2016 Heavy Ion Run. The luminosity collected for each run is reported, along with the corresponding data taking period that indicates the beam orientation.

To be included in the analysis, events must be pass the relevant good run list (GRL) selection. The GRL for the 2016 8.16 TeV p+Pb data is:

`GoodRunsLists/data16_hip/20190708/data16_hip8TeV.periodAllYear_DetStatus-v105-pro22-13_Unknown_PHYS_HeavyIonP_All_Good.xml`.

Refer to Section 4.4 for details related to the construction of jet spectra for the three unique p+Pb data taking periods used in this analysis. Jets are reconstructed using the anti-k_t jet algorithm with a radius parameter of $R = 0.4$.

Fiducial Cuts

This analysis considers the measured leading dijet pair constructed from the two highest p_{T} jets in the event with reconstructed $p_{\mathrm{T},1} > 40$ GeV, $p_{\mathrm{T},2} > 30$ GeV. Both jets are required to pass the LooseBad jet cleaning cut and the event is required to have a primary vertex. A dijet event is considered if the leading jet fired the lowest prescale, fully-efficient (i.e. with efficiency $> 99\%$) trigger corresponding to the jet η and p_{T} (see Section 4.4.3). The measured leading dijet pair is considered if both jets are within $-4.5 < \eta < 2.8$ ($-2.8 < \eta < 4.5$) for the p+Pb (Pb+p) beam orientation. The forward η cut is set to avoid considering jets which may have some constituents inside of the FCal acceptance. The backward η cut is imposed by the absence of jet triggers in the backward region during the measurement and is selected to avoid jets biasing the centrality determination in the Pb-going arm of the FCal. This choice effectively reduced the fiducial acceptance of the measurement at backward y_{b}.

Originally, the analysis fiducial region in the backward region was set according to the coverage provided by central trigger, reaching up to $\eta = \pm 3.1$ ($-$ for Pb+p, + for for p+Pb). This approach leaves room for events characterized by the leading and/or sub-leading jet partially detected in the backward arm of the FCal (acceptance starting at $\eta \pm 3.2$). This part of the detector is used to determine centrality (See Section 4.5). To remove this contribution, ensuring the selection of a data sample not biased in the centrality determination, the fiducial region of the measurement was restricted in the backwards (Pb-going) η. Requiring that $\eta >$ -2.8 introduces a buffer region in η wide enough to contain $R = 0.4$ jets detected on the edge of the acceptance. The impact of this cut on the statistics of each kinematic bin is displayed in Figure 4.4 and 4.5 for Period B and C, respectively. From these results, it is evident how this selection strongly impacts the backward most y_{b} in each range of y^*, with statistics reduced by approximately 70%. To ensure that both centrality and the measurement are independent from one another, the fiducial region of the measurement was reduced, discarding the most backward y_{b} bins. A more moderate impact can be observed for other bins, of the order of $\sim$10%. In these bins, an efficiency correction at the level of unfolding is applied in order to account for the acceptance reduction imposed by the fiducial cut. Events with either the leading or the sub-leading jet reconstructed in the HEC issue region (see Section 4.3.2) are not considered in the analysis. Events entering the analysis must have at least two such jets which pass all of the above criteria, allowing for construction of the kinematic variables defined by Equation 4.1.

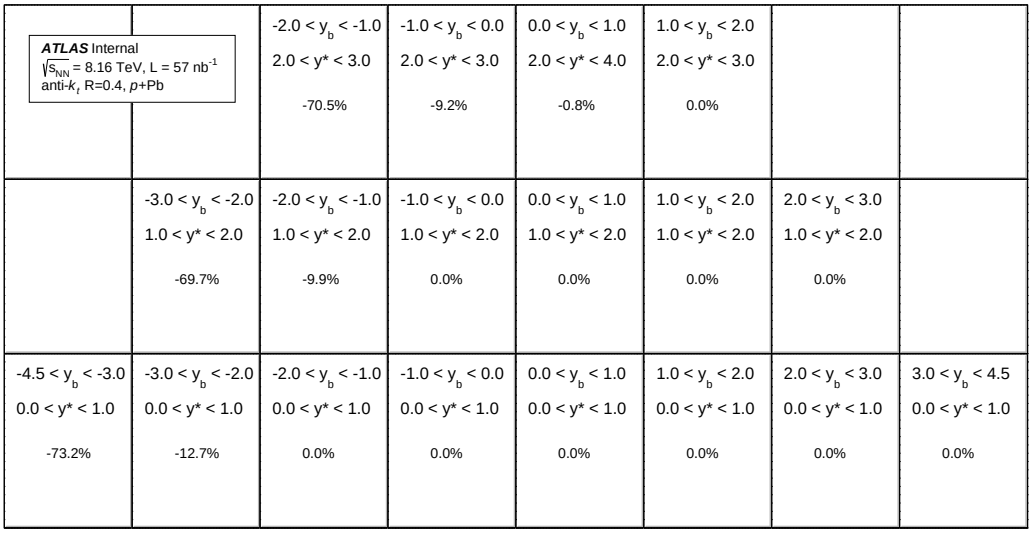

Figure 4.4: The impact of the $\eta <$ 2.8 cut for the p+Pb (Period B) data collected in 2016, in bins of y_{b} and y^*. The value shown corresponds to the percentage of events rejected in a given bin.

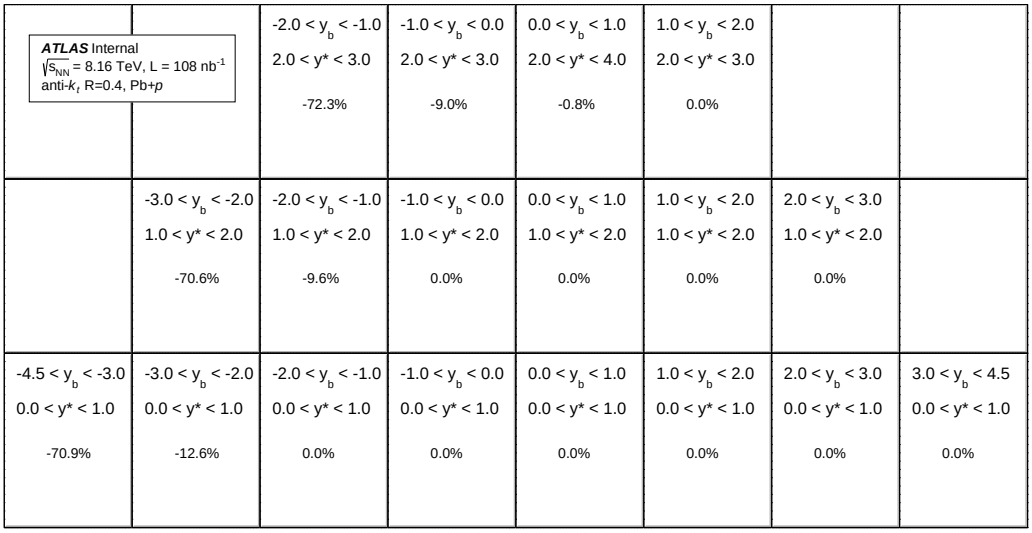

Figure 4.5: The impact of the $\eta >$ -2.8 cut for the Pb+p (Period C) data collected in 2016, in bins of y_{b} and y^*. The value shown corresponds to the percentage of events rejected in a given bin.

Pileup Removal

To have a meaningful determination of per-event centrality, it is essential to analyze events where only one hadronic p+Pb collision occurred. To meet this requirement, an effective pile-up rejection strategy is needed, in particular for data with non-trivial average number of interactions per bunch-crossing (μ) like those analyzed in this thesis (μ ranging from 0.15 to 0.3 in most of the runs), as shown in Figure 4.6.

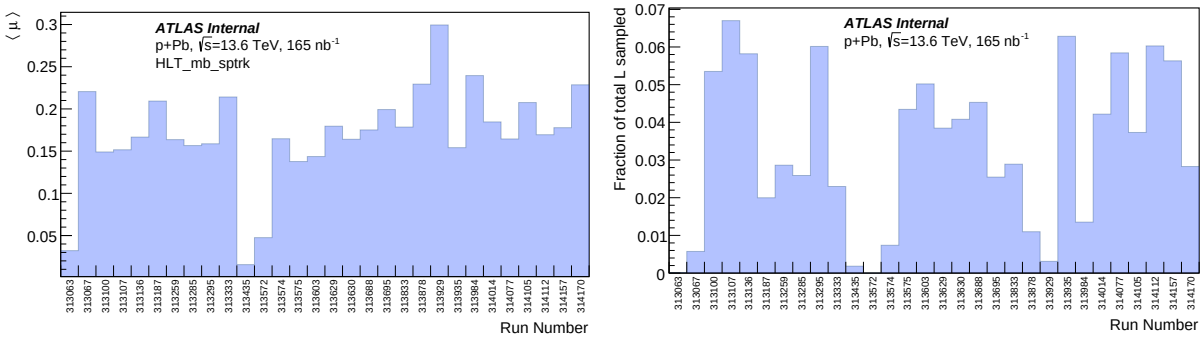

Figure 4.6: Left: average μ per each of the 2016 p+Pb runs, calculated from events with the `HLT_mb_sptrk` trigger fired. Right: relative luminosity fraction sampled per each run.

The expected level of pile-up in this dataset can be evaluated analytically using a Poissonian statistical distribution. The Poisson distribution for a mean μ is given by $P(n) = \mu^n \exp(-\mu/n!)$. Using this formula, the pile-up level can be calculated as the zero-suppressed mean of this distribution as $\mu/(1-P(0)) = \mu/(1-\exp(\mu))$. This relation estimates a pile-up of 10.3% (13%) for μ=0.2 (μ=0.25).

In order to remove pileup, the same type of cut applied in the centrality analysis (see Ref. [193]) was chosen, rejecting all the events with more than one vertex with 7 or more outgoing tracks. The resulting pile-up rejection rate, per data-taking period and centrality bin, is reported in Table 4.2. A clear (and expected) centrality dependence can be observed. The mild period dependence reflects the average μ characterizing the different phases of the data-taking. The overall rejection for the 0–90% centrality class is 13%. When integrated over all the events, without centrality selection, the value drops to ∼11%.

	p+Pb	Pb+p ion	Pb+p pp	Total
0-20%	20.4%	20.1%	23.7%	22.4%
20-60%	5.9%	6.3%	7.3%	6.8%
60-90%	2.3%	2.1%	3.0%	2.7%
0-90%	11.4%	11.2%	14.4%	13.0%

Table 4.2: Pile-up rejection in each running period per centrality bin.

Ultra-Peripheral Event Rejection

Due to the difference in Z between the Pb ion (82) and the proton (1), most of the events from this type of process are expected to involve the emission of a virtual photon from the Pb ion to the p, with subsequent low activity on the Pb-going side of the FCal. By applying a 0–90% selection for the per-event dijet yield analysis, one can expect a substantial fraction of these events to be effectively rejected. To further enforce the rejection of ultra-peripheral collision (UPC) events, a cut based on rapidity gaps, similar to the one utilized in the centrality analysis [193], where events with $\Delta\eta^{\mathrm{Pb}}_{\mathrm{gaps}} > 1.8$ were rejected. In this analysis, such a cut rejects only a handful of events in the 0–90% centrality class, as demonstrated by Figure 4.7.

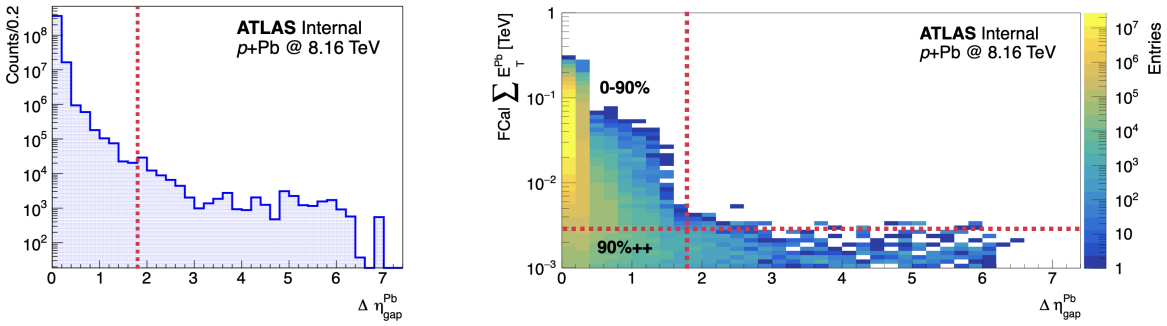

Figure 4.7: (left) 1-dimensional nucleus-going rapidity gap distribution. The red dotted line shows the cut applied in the analysis. (right) Correlation between $\Sigma E_{\mathrm{T}}^{\mathrm{Pb}}$ and $\Delta\eta_{\mathrm{gaps}}^{\mathrm{Pb}}$. The vertical (horizontal) red dotted line represents the cut applied in the analysis for the rapidity gap (centrality) selection.

Beam Orientation Considerations

Refer to Section 4.2.1 for details related to the binning used for the measurement. Recall that the data were collected with opposite beam orientations and, due to higher boost of the p beam, the products of the collision are preferentially emitted toward the p-going direction (and therefore detected by different halves of the ATLAS detector). To properly unfold for the detector effects, the data from each period were analyzed separately using dedicated simulations for each beam orientation (see Section 4.3.3). To be able to combine the two beam orientations, the p+Pb results were flipped in y_{b} to obtain a reference system compatible with the Pb+p one, where the p is travelling toward positive rapidities. After this step, the results were combined to obtain the final results. The procedures applied to combine the yield and the R_{CP} results are described in Section 4.8.

4.3.2 Disabled HEC Sector

2016 p+Pb data were affected by an issue in the hadronic calorimeter endcap, colloquially referred to as the "disabled HEC" or "HEC issue". The issue affected a set of channels in the 4^{th} quadrant of the A-side (positive η) of the HEC, that were disabled during the data taking operations because of a faulty low-voltage power supply [194]. The region of phase space affected was roughly $[\eta,\phi] \in [1.5,3.2]\times[-\pi,-\pi/2]$, see Figure 4.8, central panel. Jets reconstructed in this part of the detector are likely to have a mischaracterized response, since only the electromagnetic portion of the calorimeter was fully operational during the Run in this region (see Section 4.7.3 for a quantification of this impact on the jet ordering). Therefore, this fraction of the phase space was removed from the analysis of p+Pb data (both beam orientations) by rejecting events where at least one of the two leading jets was detected in the HEC problematic region, padded with a contour of thickness equal to $R = 0.4$, *i.e.* $[\eta,\phi] \in [1.1,3.6]\times([-\pi,-\pi/2+0.4] \cup [\pi-0.4,\pi])$.

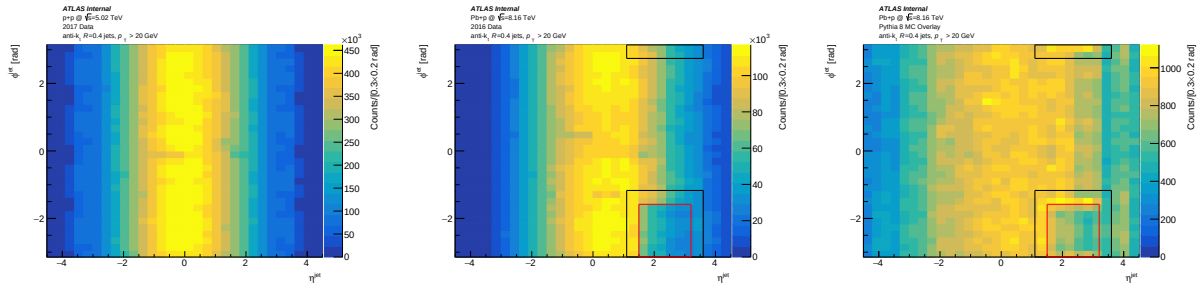

Figure 4.8: ϕ vs η distribution for 2017 pp data, 2016 Pb+p data and 2016 Pb+p PYTHIA8 MC overlay. The Pb+p orientation was chosen because of the boost ($\Delta y = +0.465$) towards positive η that helps in highlighting the dip due to the HEC issue. No (η,ϕ) cut is applied in any of the three distributions, in order to illustrate how the issue is not present in pp data (left), present in Pb+p data (center) and reproduced in Pb+p reconstructed MC (right). In the latter two distributions, the red (black) lines show the region corresponding to the (cut to reject events affected by the) HEC issue. All the distributions are obtained using jets with $R = 0.4$ and $p_{\text{T}} > 20$ GeV.

These cuts, illustrated by the black lines in Figure 4.8 central and right panels, carve out a rectangular shaped region in the $[\eta,\phi]$ of the jets. This cut creates a bias in the η acceptance that is corrected for at the level of unfolding. Figures 4.9 and 4.10 show η_1 vs ϕ_1 distributions for each (y_{b}, y^*) bin in Periods B & C, respectively, allowing for visualization of the HEC issue and its impact on a given bin's statistics. A depletion in the distribution opposite of the HEC issue in ϕ is observed, due to the rejection of subleading jets and the preference for back-to-back dijets.

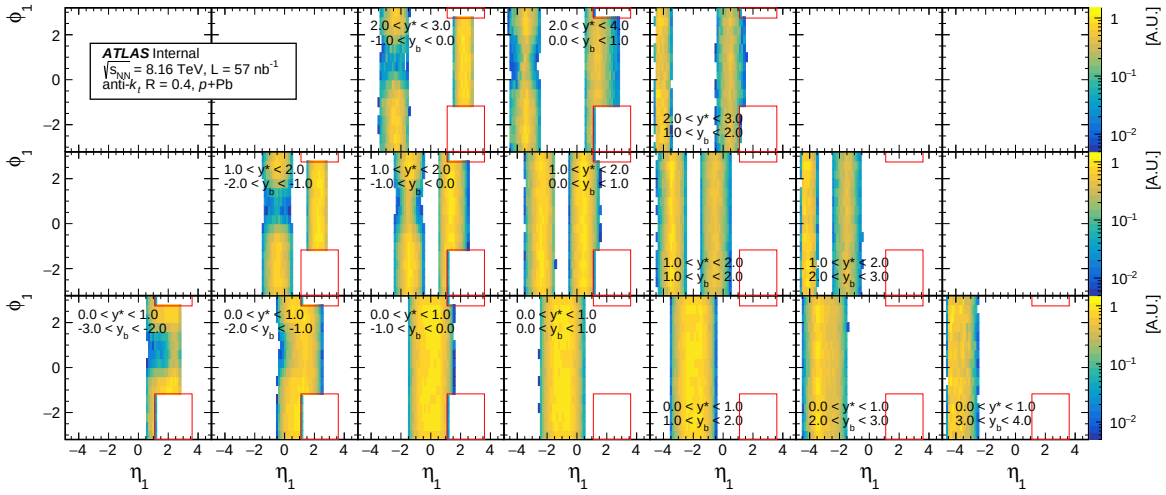

Figure 4.9: Distribution of η_1 vs ϕ_1 for p+Pb (Period B) data collected in 2016. The proton is traveling towards **negative** η. The HEC issue can be observed in negative y_b bins, particularly at low y^* values.

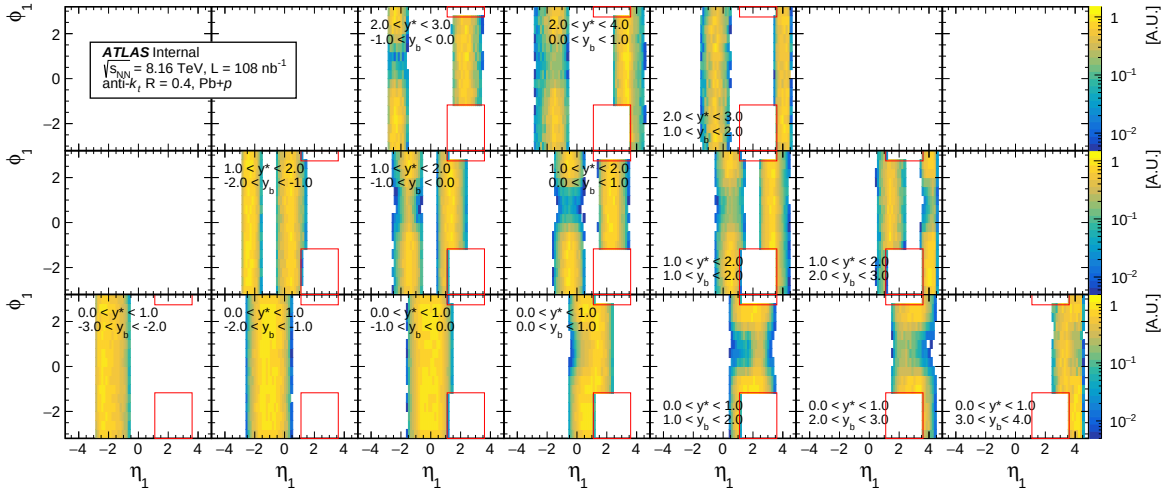

Figure 4.10: Distribution of η_1 vs ϕ_1 for Pb+p (Period C) data collected in 2016. The proton is traveling towards **positive** η. The HEC issue can be observed in positive y_b bins, particularly at low y^* values.

4.3.3 Monte Carlo Samples

In order to evaluate the performance of jet reconstruction and the jet response within ATLAS, dijet Monte Carlo samples generated using PYTHIA8 [195] with the A14 tune and the NNPDF2.3LO PDFs [196] were produced. Dijet events are filtered using the JZ∗R04 filters, which select events containing an anti-k_t $R = 0.4$ jet in specific truth p_{T} ranges, referred to using the prefix 'JZ' and an integer ranging from 1-5 in this analysis. The detector response was simulated using the full ATLAS detector simulation based on the GEANT4 toolkit [197]. For p+Pb collisions, PYTHIA8 truth events are overlaid with real minimum-bias p+Pb data, with separate MC samples for Period B and Period C. For each event, the PYTHIA8 generation and subsequent simulations were run with conditions matching the collected data, allowing for the simulation to account for underlying event effects in the jet reconstruction.

Tables 4.3 and 4.4 list the $p_{\mathrm{T}}^{\mathrm{truth}}$ range, PYTHIA8 cross-section and filter efficiency, and the number of events for the inclusive and forward-filtered p+Pb and Pb+p Monte Carlo samples, respectively. For forward-filtered samples a specific filter, characterized by its own efficiency, is applied in order to preferentially select events in which a jet exists at forward η, where the cross-section is lower compared to central jets. This allows for smaller MC productions to provide increased statistics in the region of phase space most interesting to the analysis, i.e. low x_{Pb} and high x_p. For the forward-filtered samples generated for this analysis, only jets in the proton-going direction are considered forward.

JZ	$p_{\mathrm{T}}^{\mathrm{truth}}$ [GeV]	σ [nb]	ϵ	N_{evt}
1	20 - 60	7.3070x10^{7}	5.8782x10^{-3}	4M
2	60 - 160	1.2916x10^{6}	5.6911x10^{-3}	4M
3	160 - 400	1.1775x10^{4}	7.4572x10^{-3}	4M
4	400 - 800	8.9941x10^{1}	8.1320x10^{-3}	4M
5	800+	1.1951x10^{0}	7.1577x10^{-3}	4M

Table 4.3: Summary of inclusive $\sqrt{s_{\mathrm{NN}}} = 8.16$ TeV p+Pb and Pb+p PYTHIA8 MC samples.

JZ	$p_{\mathrm{T}}^{\mathrm{truth}}$ [GeV]	σ [nb]	ϵ	N_{evt}
1	20 - 60	7.3070x10^{7}	9.0671x10^{-4}	4M
2	60 - 160	1.2916x10^{6}	5.3628x10^{-4}	2M

Table 4.4: Summary of forward-filtered $\sqrt{s_{\mathrm{NN}}} = 8.16$ TeV p+Pb and Pb+p PYTHIA8 MC samples.

The ATLAS dataset names for the Monte Carlo samples used in this analysis are listed below.

$\sqrt{s_{\mathrm{NN}}}$ = 8.16 TeV Pb+p Inclusive

mc16_pPb8TeV.420011.Pythia8EvtGen_A14NNPDF23LO_jetjet_JZ1R04.merge.AOD.e6519_d1604*

mc16_pPb8TeV.420012.Pythia8EvtGen_A14NNPDF23LO_jetjet_JZ2R04.merge.AOD.e6395_d1604*

mc16_pPb8TeV.420013.Pythia8EvtGen_A14NNPDF23LO_jetjet_JZ3R04.merge.AOD.e6519_d1604*

mc16_pPb8TeV.420014.Pythia8EvtGen_A14NNPDF23LO_jetjet_JZ4R04.merge.AOD.e6519_d1604*

mc16_pPb8TeV.420015.Pythia8EvtGen_A14NNPDF23LO_jetjet_JZ5R04.merge.AOD.e6519_d1604*

$\sqrt{s_{\mathrm{NN}}}$ = 8.16 TeV Pb+p Forward-filtered

mc15_pPb8TeV.420048.Pythia8EvtGen_A14NNPDF23LO_jetjet_JZ1R04_MaxEta_3p0.merge.AOD.e8310_d1604*

mc16_pPb8TeV.420049.Pythia8EvtGen_A14NNPDF23LO_jetjet_JZ2R04_MaxEta_3p0.merge.AOD.e8310_d1604*

$\sqrt{s_{\mathrm{NN}}}$ = 8.16 TeV p+Pb Inclusive

mc16_pPb8TeV.420011.Pythia8EvtGen_A14NNPDF23LO_jetjet_JZ1R04.merge.AOD.e6518_d1603*

mc16_pPb8TeV.420012.Pythia8EvtGen_A14NNPDF23LO_jetjet_JZ2R04.merge.AOD.e6394_d1603*

mc16_pPb8TeV.420013.Pythia8EvtGen_A14NNPDF23LO_jetjet_JZ3R04.merge.AOD.e6518_d1603*

mc16_pPb8TeV.420014.Pythia8EvtGen_A14NNPDF23LO_jetjet_JZ4R04.merge.AOD.e6518_d1603*

mc16_pPb8TeV.420015.Pythia8EvtGen_A14NNPDF23LO_jetjet_JZ5R04.merge.AOD.e6518_d1603*

$\sqrt{s_{\mathrm{NN}}}$ = 8.16 TeV p+Pb Forward-filtered

mc16_pPb8TeV.420018.Pythia8EvtGen_A14NNPDF23LO_jetjet_JZ1R04_MaxEta_m3p0.merge.AOD.e8288_d1603*

mc16_pPb8TeV.420019.Pythia8EvtGen_A14NNPDF23LO_jetjet_JZ2R04_MaxEta_m3p0.merge.AOD.e8288_d1603*

1D distributions of leading truth jet p_{T} and η are shown in Figure 4.11 for the p+Pb inclusive MC sample (grey), and the combined inclusive and forward-filtered MC samples (red). Particular attention should be given to $p_{\mathrm{T},1}^{\mathrm{truth}} = 160$ GeV in the left figure and $\eta_1^{\mathrm{truth}} = -3.0$ in the right figure. This $p_{\mathrm{T},1}^{\mathrm{truth}}$ value corresponds to the transition between JZ2 and JZ3, where there is no forward-filtered MC sample. Therefore, no matter the value of η_1^{truth}, any event with $p_{\mathrm{T},1}^{\mathrm{truth}} > 160$ GeV will only be used if it comes from the inclusive MC sample. In the region where $\eta_1^{\mathrm{truth}} < -3.0$ and $p_{\mathrm{T},1}^{\mathrm{truth}} < 160$ GeV, only events from the forward-filtered MC sample are used. The bottom panels in Figure 4.11 show that this strategy leads to a smooth transition, where the inclusive sample has been divided by the combined inclusive and forward-filtered sample, using the strategy outlined above. The same strategy is employed for the combination of the Pb+p inclusive and forward-filtered MC samples, with the η_1^{truth} transition taking place at +3.0.

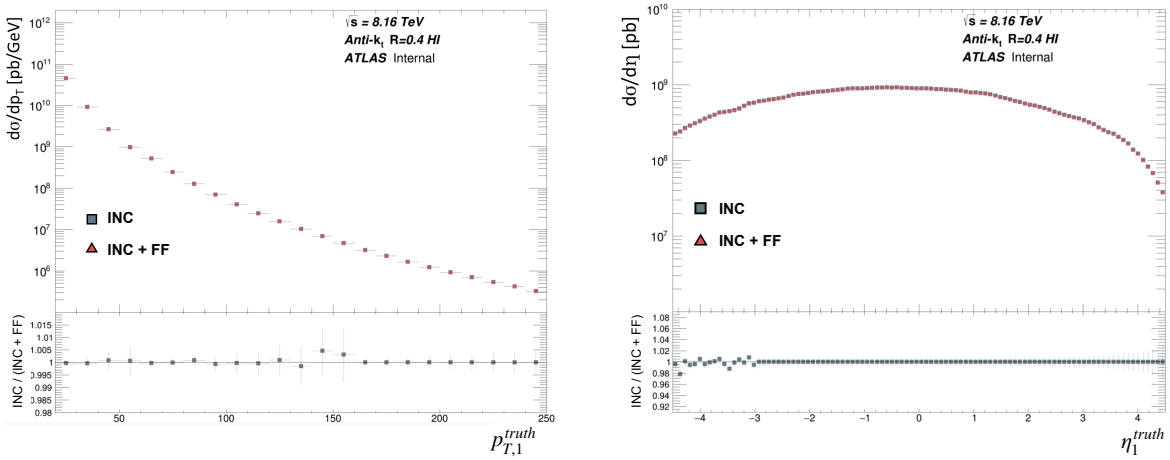

Figure 4.11: 1D distributions of leading truth jet p_{T} (left) and η (right) for both the p+Pb inclusive (INC) MC sample, denoted by grey squares, and the combined inclusive and forward-filtered (INC+FF) MC samples, denoted by red triangles. The bottom panels show the ratio of the inclusive sample to the combined inclusive and forward-filtered samples.

4.3.4 Jet Reconstruction Performance

Criteria used to select jets in this analysis are discussed in Section 4.3.1. All the jet performance studies were carried out for both the beam orientations of p+Pb data taking. All the jet performance studies presented in this thesis were carried out using the `HIJetValTools` package [198] modified to accommodate peculiarities of the p+Pb data taking [199] (beam dependent configuration, centrality determination using only one side of the FCal, triggers etc.).

The analysis of jet reconstructed performance is carried out segmenting the detector into 6 different η regions, characterized by the following limits: -4.5, -3.2, -1.5, 0, 1.5, 3.2, 4.5. In the case of p+Pb collisions, the backward (Pb going) η bin is excluded from the analysis (*e.g.* [-4.5, -3.2] for Pb+p data, and [3.2, 4.5] for p+Pb collisions. In addition to this choice, determined by the lack of triggers covering this region and by the intention of avoiding contamination from jets in the portion of the FCal used for centrality determination, an additional reduction of $\eta = 0.1$ is applied to the outermost surviving backward bin, to avoid the trigger *transition* region discussed in Section 4.4, resulting in the following η binning:

- p+Pb: -4.5, -3.2, -1.5, 0, 1.5, 3.1;
- Pb+p: -3.1, -1.5, 0, 1.5, 3.2, 4.5;

This binning was adopted only for the sake of the jet performance studies reported in this section. The centrality dependence of the jet reconstruction performance was also investigated. Three centrality bins, namely 0–10%, 10–60% and 60–90%, were defined for the sake of these studies.

The jet reconstruction efficiency was evaluated using the PYTHIA8 MC samples listed in Section 4.3.3 by determining how often a reconstructed jet is associated with a truth one. The results, binned in terms of event centrality, were obtained for both p+Pb and Pb+p data taking periods and are reported in Figures 4.12 and 4.13, respectively. In both cases, a mild dependence on η and centrality can be noted, with the 99% efficiency threshold varying by a few GeV between the forward-backward region and central and peripheral collisions.

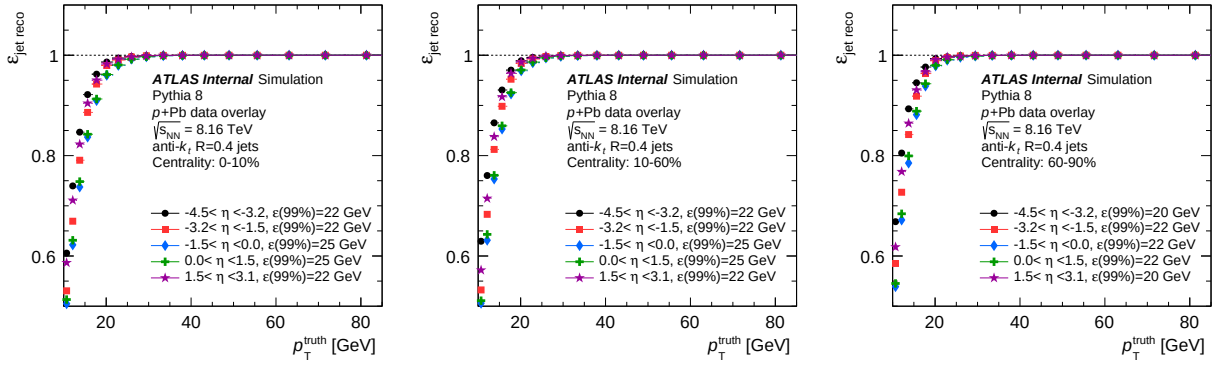

Figure 4.12: Jet reconstruction efficiency in p+Pb data-taking configuration, evaluated in different η regions of the ATLAS detector for central (0–10%, left), mid-central (10–60%, center) and peripheral (60–90%, right) collisions. Corresponding 99% efficiency $p_{\mathrm{T}}^{\mathrm{truth}}$ thresholds are also reported for each region and centrality interval.

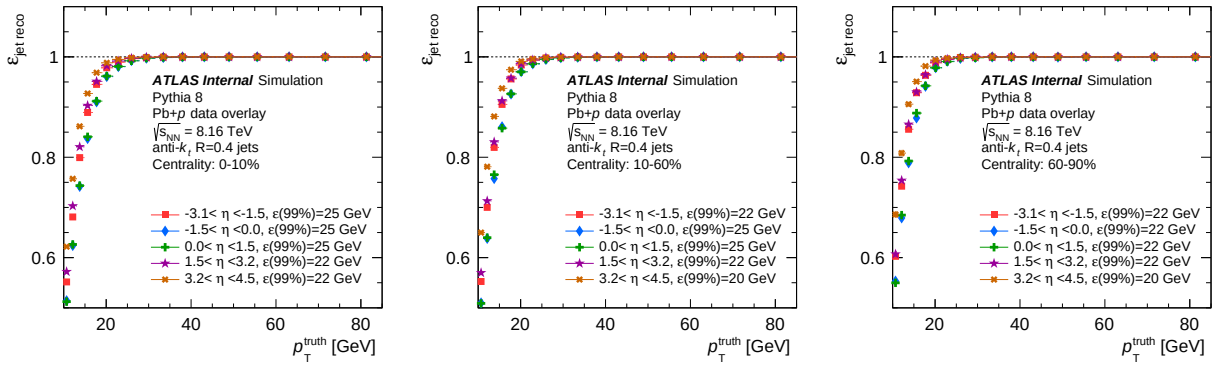

Figure 4.13: Jet reconstruction efficiency in Pb+p data-taking configuration, evaluated in different η regions of the ATLAS detector for central (0–10%, left), mid-central (10–60%, center) and peripheral (60–90%, right) collisions. Corresponding 99% efficiency $p_{\mathrm{T}}^{\mathrm{truth}}$ thresholds are also reported for each region and centrality interval.

The post-calibration jet energy scale (JES), calculated as $\langle p_{\mathrm{T}}^{\mathrm{reco}}/p_{\mathrm{T}}^{\mathrm{truth}}\rangle$ was studied as a function of truth jet p_{T}, centrality, and collision type. Closure is achieved when the ratio is equal to 1, meaning that, on average, $p_{\mathrm{T}}^{\mathrm{reco}}$ matches $p_{\mathrm{T}}^{\mathrm{truth}}$. To quantitatively evaluate the closure, the distribution of $\langle p_{\mathrm{T}}^{\mathrm{reco}}/p_{\mathrm{T}}^{\mathrm{truth}}\rangle$ is constructed in each $p_{\mathrm{T}}^{\mathrm{truth}}$ bin and then fit using a gaussian function. The fit is carried out in two iterations, with the second one restricted to $\mu \pm 1.5\sigma$, with μ and σ being in this case the mean and the standard deviation obtained from the first iteration of the fit, respectively. The jet energy resolution (JER) is evaluated as the ratio σ/μ constructed using the parameters obtained from the second fit iteration.

The JES and JER for jets detected in p+Pb and Pb+p collisions are reported in Figures 4.14 and 4.15, respectively. The top panel shows the JER, while the bottom one displays the JES closure. It should be noted

that the fit procedure suffers from instability due to some asymmetry in the $p_{\mathrm{T}}^{\mathrm{reco}}/p_{\mathrm{T}}^{\mathrm{truth}}$ distribution at low $p_{\mathrm{T}}^{\mathrm{truth}}$. In regions where good convergence of the fit can be achieved (*e.g.* above $p_{\mathrm{T}}^{\mathrm{truth}}$∼28–30 GeV), the JES closure is found to be within 3%, with the most forward bin showing the largest non-closure values. A mild JER dependence on centrality can be noticed for jets with $p_{\mathrm{T}}^{\mathrm{truth}}$ below 80 GeV. The two beam orientations show compatible results when compared within same the η region of the detector. For the Pb+p orientation, the statistics entering the studies in the semi-forward ($1.5 < \eta < 3.2$) and forward ($3.2 < \eta < 4.5$) regions are lower compared to p+Pb because of the rejection of the (η, ϕ) region corresponding to the HEC issue in 2016, discussed in Section 4.3.2.

A worsening of the JER can be observed in both forward directions for $p_{\mathrm{T}}^{\mathrm{truth}} > 40$ GeV. This behavior was observed also in other analyses including jets in the forward region, see for instance the dijet analysis in pp at 7 TeV [200, 201]. An illustration of the JES and JER from this analysis in reported is Figure 4.16 for completeness. The observed worsening of the detector response in this region is due to a transition between two calorimeter systems with different energy responses determined by different calorimeter geometry and/or technology. This artificially increases the energy of one side of the jet with respect to the other, altering the reconstructed four-momentum [202].

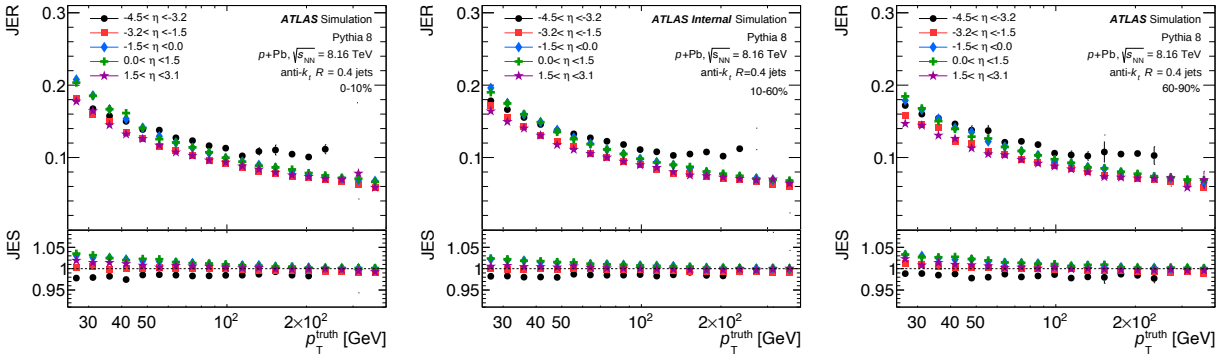

Figure 4.14: Post-calibration jet energy resolution (top) and jet energy scale (bottom) evaluated in p+Pb collisions (p traveling towards negative η) as a function of different η of the leading jet and of different centrality values characterizing the p+Pb reaction. The JES and JER values were obtained using the mean (μ) and standard deviation (σ) of the $\langle p_{\mathrm{T}}^{\mathrm{reco}}/p_{\mathrm{T}}^{\mathrm{truth}}\rangle$ distribution evaluated by applying a gaussian fit to it. The error bars displayed corresponds to the uncertainty resulting from the fit on each parameter. Some issue with the convergence of the fit can be noticed at high p_{T} in the forward region ($\eta < -3.2$), near to the edges of the detector acceptance, where statistics start to be low.

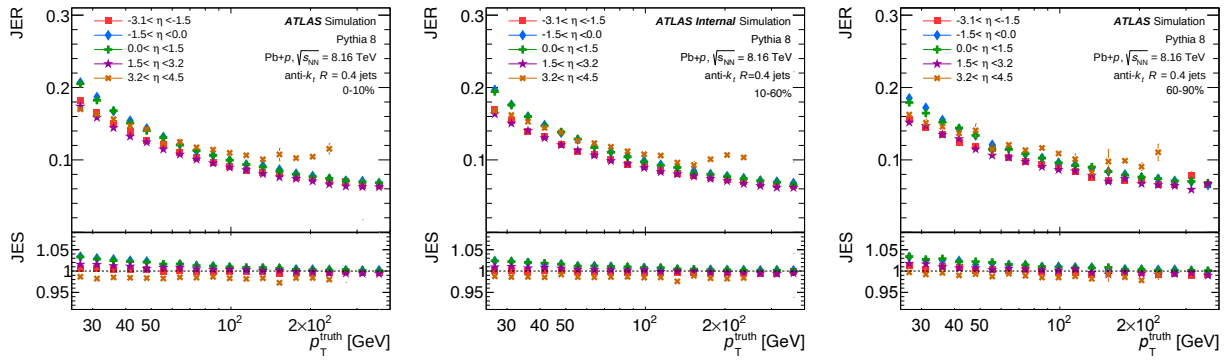

Figure 4.15: Post-calibration jet energy resolution (top) and jet energy scale (bottom) evaluated in Pb+p collisions (p traveling towards positive η) as a function of different η of the leading jet and of different centrality values characterizing the Pb+p reaction. The JES and JER values were obtained using the mean (μ) and standard deviation (σ) of the $\langle p_{\mathrm{T}}^{\mathrm{reco}}/p_{\mathrm{T}}^{\mathrm{truth}}\rangle$ distribution evaluated by applying a gaussian fit to it. The error bars displayed corresponds to the uncertainty resulting from the fit on each parameter. Some issue with the convergence of the fit can be noticed at high p_{T} in the forward region ($\eta > 3.2$), near to the edges of the detector acceptance, where statistics start to be low.

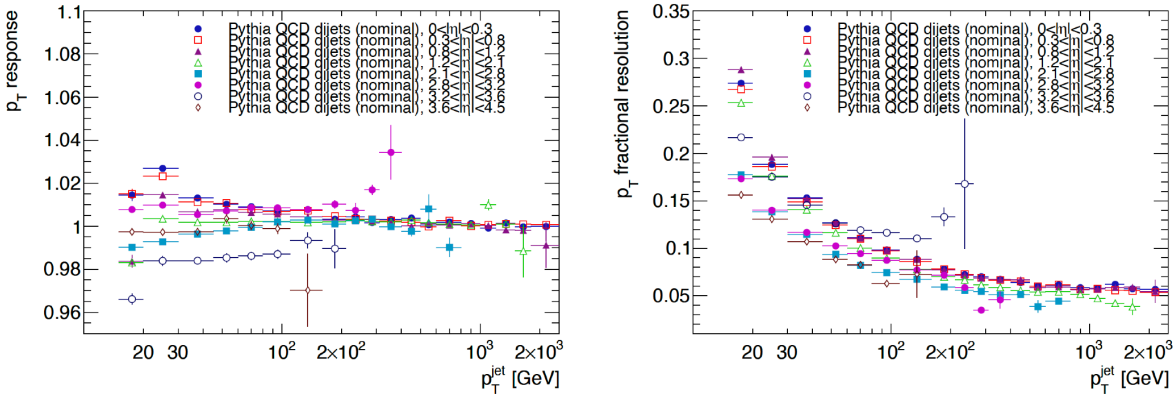

Figure 4.16: JES (left) and JER (right) in function of $p_{\mathrm{T}}^{\mathrm{truth}}$ for 7 TeV pp data. The plots show results in seven different rapidity ranges. Worse performance is observed for $3.2 < |\eta| < 3.6$. Figures taken from Ref. [201].

4.4 ATLAS Trigger Selection

The ATLAS trigger system consists of a hardware-based component, the Level-1 (L1) trigger, and a software-based trigger system, the higher-level trigger (HLT). The HLT runs a simplified version of the ATLAS reconstruction software. At the HLT level, calibrated jets defined by the anti-k_t algorithm with $R = 0.4$ are used. Each trigger item is composed of an L1 trigger and an HLT trigger. The L1 system first evaluates each given trigger if it is passed. To keep the trigger rate at an acceptable level, and to not saturate the available bandwidth, triggers with a high rate are only read out for a fraction of all events by setting a prescale value, characteristic of each trigger item. The prescale is a number applied online by the ATLAS trigger system. If an event satisfies the requirements of a given trigger, the prescales for the L1 and HLT triggers are determined. If the L1 or the HLT trigger is prescaled, the HLT trigger decision is not evaluated to optimize the computing time. Prescales for the L1 trigger and the HLT trigger are decided independently.

Single-jet triggers are designed to fire with events characterized by large transverse energy depositions in the ATLAS calorimeter system. The HLT trigger name encodes the nominal threshold value (expressed in GeV) set for the HLT jet. Central and forward jets are constructed in two separate systems. The transition between central and forward jets occurs at $|\eta| = 3.1$ and at $|\eta| = 3.2$ for the L1-Calo system and HLT, respectively. As the name suggests, central jet triggers cover the pseudorapidity region $|\eta| < 3.2$, while forward jet triggers cover the range $3.2 < |\eta| < 4.9$. The forward jet triggers are denoted with a suffix `320eta490`, highlighting their acceptance. In p+Pb data taking, where the collision system is asymmetric, the forward triggers are separated by being either positive or negative as a function of their η coverage. The two orientations are distinguished by a letter `p` or `n` before `320eta490`, respectively. It is worth noting that a set of semi-forward triggers were enabled during the 2016 data-taking. These triggers cover $2.0 < |\eta| < 3.2$ and are denoted with a suffix `p200eta320` (`n200eta320`) if they cover the positive (negative) pseudorapidity region. All the triggers scrutinized for use in the analysis are listed in Table 4.5, where the HLT and the L1-Calo components for each trigger item are listed. This measurement will use only the central and forward jet triggers. The studies that led to this choice are presented in the following sections. Originally, this set of triggers was complemented by a minimum bias trigger, used to cover the lowest part of the jet p_{T} spectrum (20–40 GeV). Given the high level of prescale of this trigger and the granularity of this measurement in both kinematics and centrality, as well as the limited additional impact of this kinematic region for the measurement presented in this thesis, it was agreed to drop events with $p_{\mathrm{T},1} < 40$ GeV to avoid the use of the minimum bias trigger. Such a trigger will be re-considered for a subsequent dijet cross-section analysis, where the results will have no binning in centrality.

4.4.1 Triggers for p+Pb Data Analysis

As discussed in Section 4.3.1, the 2016 p+Pb dataset is characterized by two different beam orientations. Trigger recommendations for this data-taking are available on the Heavy Ion Trigger Menu Forum [203]. Two different trigger menus were deployed during the Run, with `ion` and `pp` triggers used as primary triggers, respectively. The switch between the two configurations did not happen in between Period B (p+Pb) and C (Pb+p) but after a few runs of Period C. In addition, given the asymmetric collision system, trigger configurations are different for forward (p-going) and backward (Pb-going) arms of the detector. Forward triggers in the backward part of the detector were turned off for most of the data taking and therefore are not considered in this analysis.

MB triggers were the same for the entire data-taking period, but are not utilized in this analysis due

HLT Tag	L1-Calo
HLT_mb_sptrk	L1_RD0_FILLED
HLT_j30(_ion)_0eta490	L1_TE10
HLT_j40(_ion)	L1J5
HLT_j50(_ion)	L1J10
HLT_j60(_ion)	L1J20
HLT_j75(_ion)	L1J20
HLT_j90(_ion)	L1J20
HLT_j100(_ion)	L1J20
HLT_j45(_ion)_(n,p)200eta320	L1_J10
HLT_j55(_ion)_(n,p)200eta320	L1_J10
HLT_j65(_ion)_(n,p)200eta320	L1_J15
HLT_j75(_ion)_(n,p)200eta320	L1_J20
HLT_j15(_ion)_(n,p)320eta490	L1MBTS_1_1
HLT_j25(_ion)_(n,p)320eta490	L1TE5
HLT_j35(_ion)_(n,p)320eta490	L1TE10
HLT_j45(_ion)_(n,p)320eta490	L1_J15.31ETA49
HLT_j55(_ion)_(n,p)320eta490	L1_J15.31ETA49
HLT_j65(_ion)_(n,p)320eta490	L1_J20.31ETA49

Table 4.5: L1-Calo trigger items used for each trigger scrutinized for use in the analysis. The _ion component for the HLT tag applies for ion triggers only. (n,p) denotes that a given HLT has both negative and positive η variations, respectively.

to the high prescale of the HLT_mb_sptrk trigger. Each of the HLT ion triggers has a corresponding pp equivalent. An overview of the central, semi-forward, and forward triggers examined at the beginning of this analysis is shown in Figure 4.17. The results presented in this figure were obtained by analyzing the output of the ATLAS Luminosity Calculator [204]. From this analysis, it was possible to identify a few issues with specific triggers, in particular:

- HLT_j90_ion_L1J20 was off for the entirety of the data taking, even when ion triggers were set to be primary. Conversely, HLT_j90_L1J20 was regularly working during the period when pp triggers were primary.
- All semi-forward triggers were turned off during the first three runs of the p+Pb period.

Within the same analysis of the LumiCalc output, it was possible to evaluate the full luminosity sampled by each trigger, reported in Figure 4.18, left panel. The right panel of the same picture shows the number of good lumi blocks collected per run.

4.4.2 Trigger Efficiencies

All the triggers listed in Table 4.5 were scrutinized to determine the efficiency of the full trigger chain, meaning both the L1-Calo and HLT components. The number of triggers in the Main data stream is reported in Figure 4.19 for both p+Pb and Pb+p samples.

The trigger efficiency of a given signal trigger can be calculated using a data-set triggered by a fully efficient monitor trigger:

$$\epsilon_{\text{Trigger}} = \frac{N_{\text{Signal}} \wedge N_{\text{Monitor}}}{N_{\text{Monitor}}}. \tag{4.11}$$

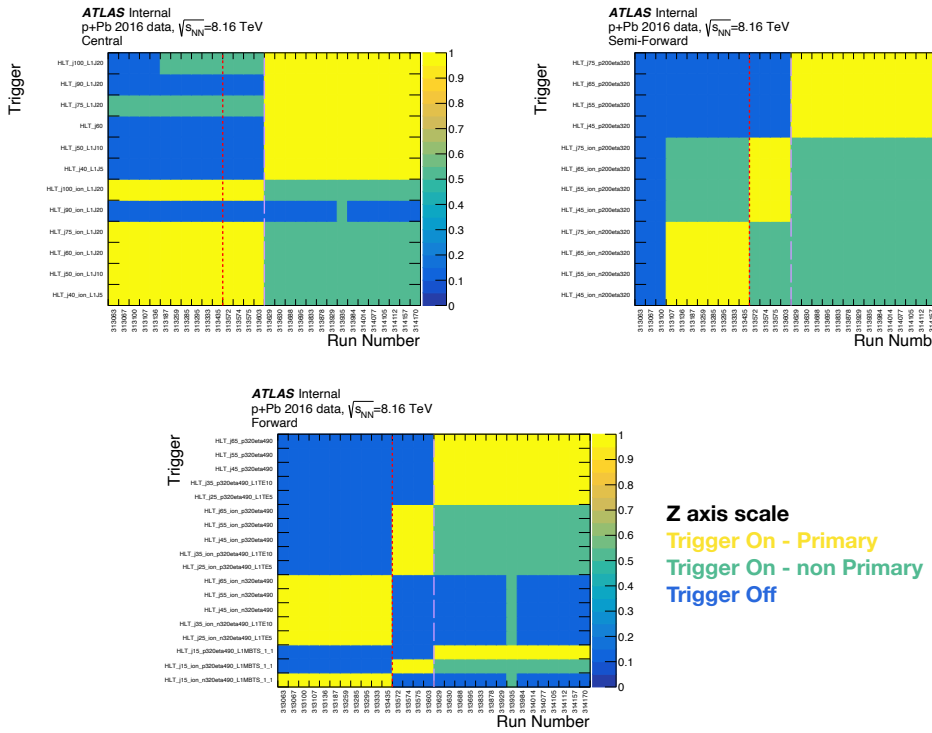

Figure 4.17: Summary of central (top left panel), semi-forward (top right panel) and forward (bottom panel) triggers across the entire 2016 p+Pb run. The color scale identifies the status of each trigger in a specific run. The dashed red (violet) line denotes the separation between p+Pb and Pb+p beam orientations (Pb+p data taking with `ion` and `pp` set as primary triggers).

Different choices can be made to select suitable monitor triggers. The work carried out for this analysis was informed by very detailed studies carried out to support jet and dijet measurements in pp data, summarized in Ref. [205]. In an ideal case, the monitor trigger should be independent of the signal trigger, should provide good statistical precision, and should have a large overlap with the data-set selected by the signal trigger. Listed below are the methods that were considered for this analysis:

- **Minimum Bias (MB) Method**: This method uses the MB trigger as the monitor trigger. Since it uses a reference trigger that is completely independent from the signal trigger, this technique is the most unbiased one. The MB trigger does not depend at all on the calorimeter trigger system. Therefore it can be used to evaluate the performance of both the L1-Calo system and the jet triggers. This trigger selects the same events as the jet trigger, but has only a limited jet p_{T} reach, since only a small number of minimum bias events are saved. Moreover, the probability that a low-p_{T} jet trigger and a MB trigger fired at the same time is very small, since the two are (heavily) prescaled independently. Therefore, the biggest downside of this method is the limited statistical precision.

- **Boostrap method**: This method relies on the evaluation of the jet trigger with the lowest threshold with an independent trigger, e.g. the MB trigger. Once the full-efficiency threshold (p_{T}^{99}, defined as the p_{T} where the efficiency curve reaches a value greater or equal to 99%) for this trigger is determined, one can use it in the region beyond this value as the monitor trigger and evaluate the efficiency of jet triggers with the higher thresholds with respect to it. In order to maximize the event sample triggered by the monitor trigger, one can also use the closest lower threshold jet trigger to evaluate the efficiency

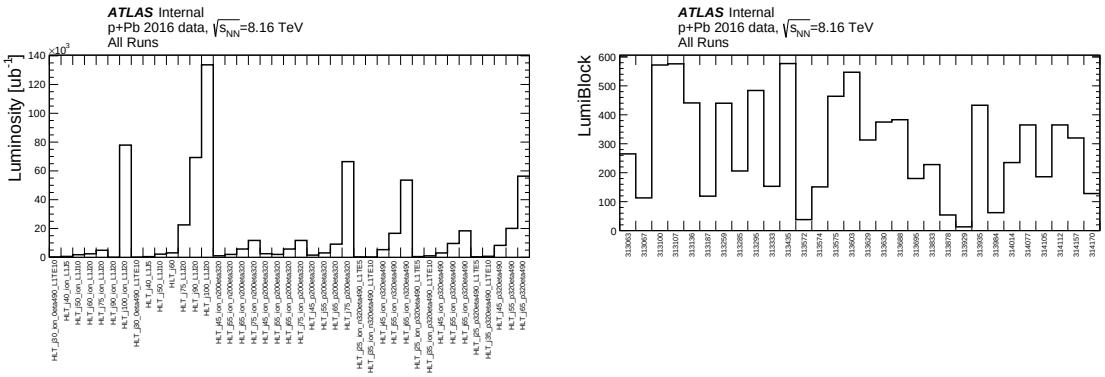

Figure 4.18: Left panel: Luminosity collected by each HLT jet trigger during 2016 p+Pb data taking. Right panel: number of good lumi blocks recorded per each good run in 2016 p+Pb data taking.

of each trigger. In this analysis, if not stated otherwise, the lower p_{T} HLT item is used as the monitor in the bootstrap method.

- **Emulation method**: The above methods are implemented using the actual trigger bits, accessible in the offline analysis. However, for the low-p_{T} triggers the prescale factors can be very large. Since the triggers are prescaled independently, the signal and the monitor trigger fire simultaneously only for a few events. An alternative way is to use the information of the L1 trigger before prescale together with the information provided by the HLT jets in the event record. By scanning the HLT jets array, it is possible to emulate the HLT decision by requiring that at least one jet satisfies the firing conditions of the trigger under consideration, *i.e.* in the HLT jets array there is at least one jet in the η acceptance of the trigger and passing the nominal trigger threshold. If used together with the L1 information before prescale available in the event record, this method is only limited by the number of event passing the monitor trigger and is not affected by the trigger prescale. Depending on the analysis, the emulation method can be used by requiring at least one HLT-jet in the event to pass the nominal jet trigger threshold (per-event trigger strategy) or by associating an HLT-jet to each offline jet and cutting on the matched jet (per-jet efficiency). This second method, referred to in this analysis as "enforced emulation", was used to determine the efficiency of the HLT part of each trigger chain considered for this analysis. This choice was made to avoid artificial inefficiencies around $\eta = \pm 3.2$, due to events where the same jet was reconstructed on the two sides of this boundary in HLT jets and offline AntiKt4HI calibrated jets, respectively. How to handle the pre-scaling correction in events falling in the transition region will be discussed in Section 4.4.4.

Among these three methods, there is no clearly preferred one. All of them were used to scrutinize the jet trigger system for this analysis. After these preliminary studies, the MB method was used to evaluate the trigger efficiencies of the L1-Calo system. The enforced emulation method, together with the boostrap method was used to evaluate the trigger efficiency of the HLT part of the trigger chain.

4.4.3 Full Trigger Chain Efficiencies

For each trigger chain considered for the analysis, the L1-Calo and HLT efficiencies were determined separately using different methods, namely:

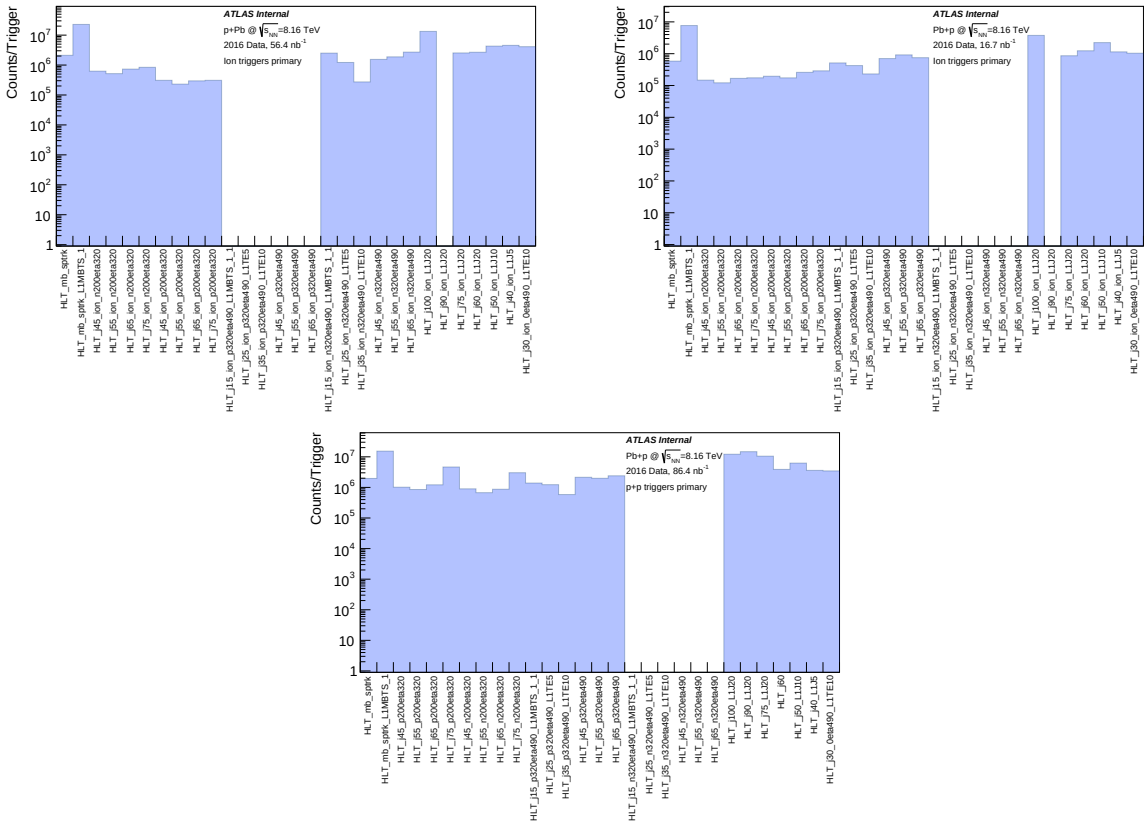

Figure 4.19: Trigger rates registered in each of the three data taking period characterized by different beam orientation or trigger configuration (p+Pb, Pb+p `ion` triggers primary and Pb+p `pp` triggers primary).

- **L1-Calo trigger:** the trigger efficiency for the L1-Calo system was calculated with the MB method. The `HLT_mb_sptrk` was used as the monitor trigger for these studies. The L1-Calo trigger information before prescale was used in order maximize statistics.

- **HLT:** the HLT efficiency was calculated using the enforced emulation method, in combination with a bootstrapped approach when statistical precision of the efficiency was too loose if the MB triggers were used as monitor.

Both the efficiencies were determined first as a function of both p_{T} and η, to search for eventual topologies corresponding to particular regions of the detector, and then integrated over η to obtain the p_{T} efficiency profile over the full angular acceptance of the trigger. Once L1-Calo and HLT efficiencies were determined, the highest p_{T}^{99} threshold between the two was chosen as the fully-efficient working point for the chain. The centrality dependence of the triggers was also investigated, to identify potential centrality-related effects that may be relevant for the centrality-binned analysis and the construction of a central-to-peripheral ratio.

Summarizing, the considerations outlined above lead to three different trigger configurations for the 2016 p+Pb run:

- Runs $\in$ [313063, 313435]: p+Pb beam orientation (p traveling from arm A to C, towards negative η). `ion` triggers primary. The list of triggers considered for the analysis in this period is reported in Table 4.6. Corresponding trigger efficiency plots are shown in Figures 4.20 and 4.21.

- Runs ∈ [313572, 313603]: Pb+p beam orientation (p traveling from arm C to A, towards positive η). `ion` triggers primary. The list of triggers considered for the analysis in this period is reported in Table 4.7.

- Runs ∈ [313629, 314170]: Pb+p beam orientation (p traveling from arm C to A, towards positive η). `pp` triggers primary. The list of triggers considered for the analysis in this period is reported in Table 4.8.

Trigger Chain	p_{T}^{99} **[GeV]**	η	$\mathcal{L}$ **[ub**$^{-1}$**]**	p_{T}^{99} **Monitor**
HLT_j30_ion_0eta490_L1TE10	36	0 - 4.9	113.76	HLT_mb_sptrk
HLT_j40_ion_L1J5	44	0 - 3.2	468.1	HLT_mb_sptrk
HLT_j50_ion_L1J10	57	0 - 3.2	1120	HLT_mb_sptrk
HLT_j60_ion_L1J20	70	0 - 3.2	1562	HLT_mb_sptrk
HLT_j75_ion_L1J20	80	0 - 3.2	3468	HLT_mb_sptrk
HLT_j100_ion_L1J20	111	0 - 3.2	56671	HLT_mb_sptrk
HLT_j15_ion_n320eta490_L1MBTS_1_1	44	3.2 - 4.9	77.5	HLT_mb_sptrk
HLT_j25_ion_n320eta490_L1TE5	40	3.2 - 4.9	247.7	HLT_mb_sptrk
HLT_j35_ion_n320eta490_L1TE10	57	3.2 - 4.9	179.9	HLT_j25_ion_n320eta490_L1TE5
HLT_j45_ion_n320eta490	65	3.2 - 4.9	5288	HLT_j25_ion_n320eta490_L1TE5
HLT_j55_ion_n320eta490	80	3.2 - 4.9	16635	HLT_j25_ion_n320eta490_L1TE5
HLT_j65_ion_n320eta490	85	3.2 - 4.9	53571	HLT_j25_ion_n320eta490_L1TE5

Table 4.6: Overview of p+Pb `ion` triggers used in the analysis. The sampled luminosity, $\mathcal{L}$, is prescale corrected. The L1 for triggers that do not specify this detail in the chain name are: `L1_J15.31ETA49` for `HLT_j45_ion_n320eta490` and `HLT_j55_ion_n320eta490`, and `L1_J20.31ETA49` for `HLT_j65_ion_n320eta490`.

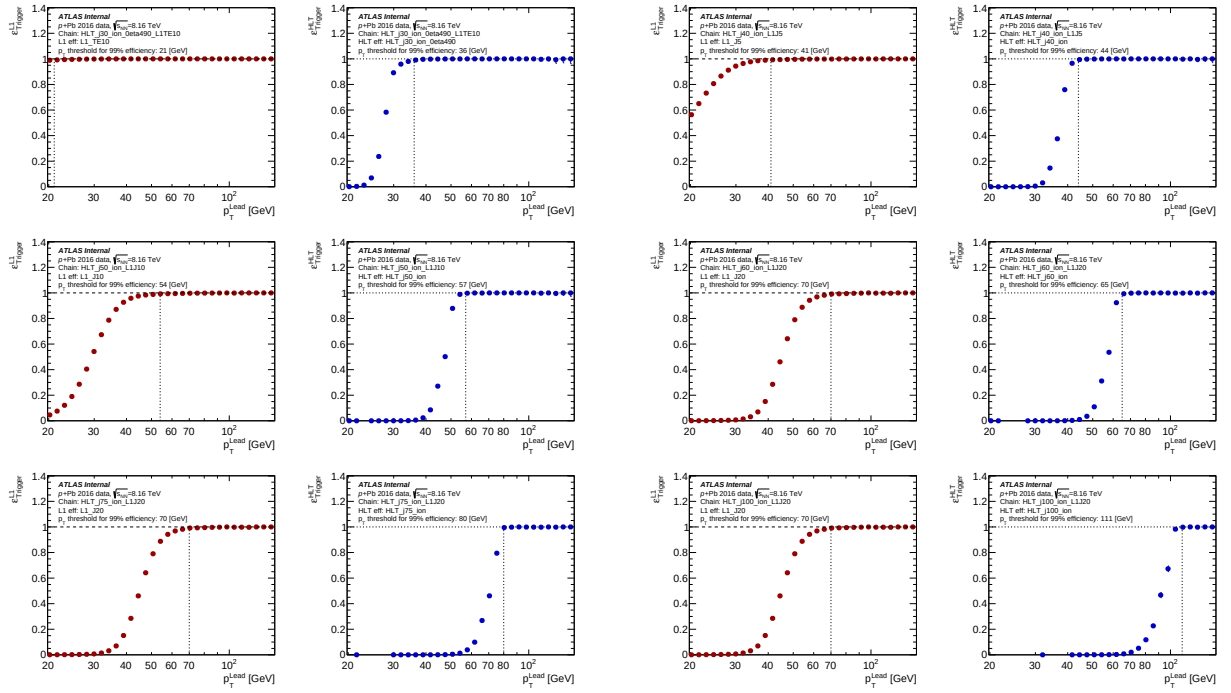

Figure 4.20: L1 and HLT trigger efficiencies (denoted by dark red and blue curves, respectively) for central triggers used in the analysis of the p+Pb data sample, where `ion` triggers were primary. The p_{T}^{99} value, determined as explained in the text, is reported for each efficiency curve. For a given trigger, the maximum value between p_{T}^{99} of L1 and HLT is chosen as fully efficient p_{T} threshold.

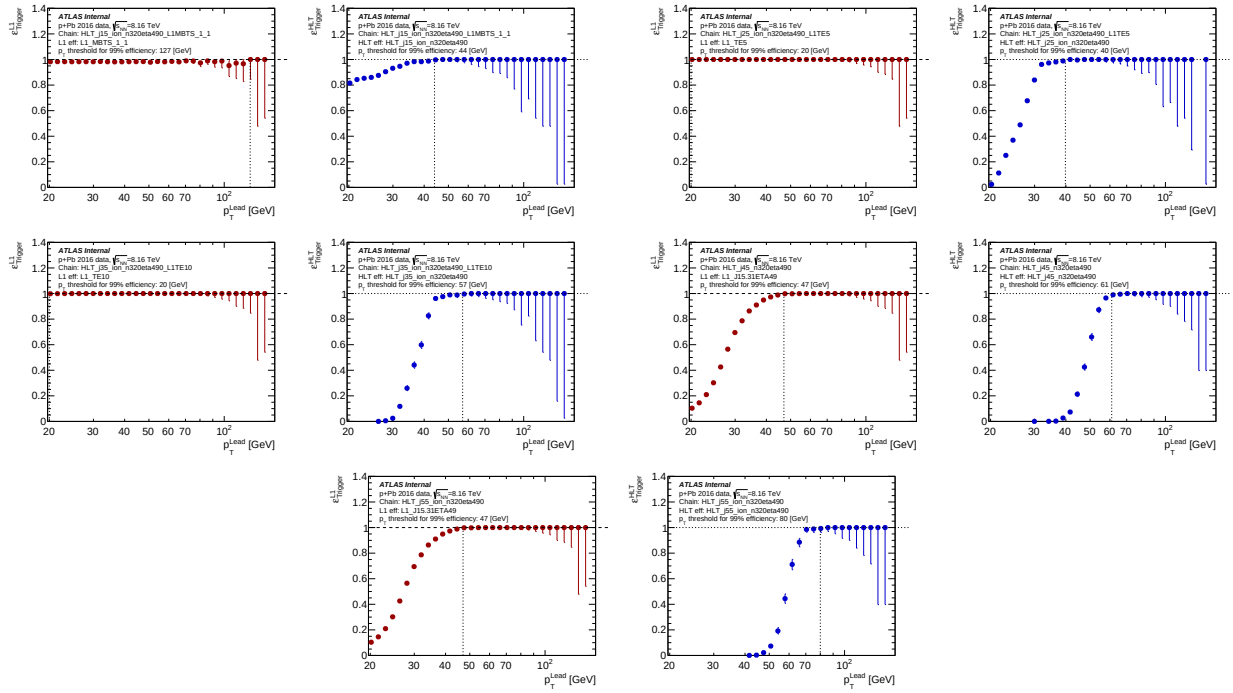

Figure 4.21: L1 and HLT trigger efficiencies (denoted by dark red and blue curves, respectively) for forward triggers used in the analysis of the p+Pb data sample, where `ion` triggers were primary. The p_{T}^{99} value, determined as explained in the text, is reported for each efficiency curve. For a given trigger, the maximum value between p_{T}^{99} of L1 and HLT is chosen as fully efficient p_{T} threshold.

Trigger Chain	p_{T}^{99} [GeV]	η	$\mathcal{L}$ [ub^{-1}]	p_{T}^{99} Monitor
HLT_j30_ion_0eta490_L1TE10	38	0 - 4.9	30.13	HLT_mb_sptrk
HLT_j40_ion_L1J5	50	0 - 3.2	120.9	HLT_mb_sptrk
HLT_j50_ion_L1J10	57	0 - 3.2	599.6	HLT_mb_sptrk
HLT_j60_ion_L1J20	75	0 - 3.2	745.3	HLT_mb_sptrk
HLT_j75_ion_L1J20	85	0 - 3.2	1223	HLT_mb_sptrk
HLT_j100_ion_L1J20	111	0 - 3.2	16674	HLT_mb_sptrk
HLT_j15_ion_p320eta490_L1MBTS_1_1	44	3.2 - 4.9	27.6	HLT_mb_sptrk
HLT_j25_ion_p320eta490_L1TE5	31	3.2 - 4.9	115.4	HLT_mb_sptrk
HLT_j35_ion_p320eta490_L1TE10	44	3.2 - 4.9	277.2	HLT_j25_ion_p320eta490_L1TE5
HLT_j45_ion_p320eta490	57	3.2 - 4.9	2628	HLT_j25_ion_p320eta490_L1TE5
HLT_j55_ion_p320eta490	61	3.2 - 4.9	8612	HLT_j25_ion_p320eta490_L1TE5
HLT_j65_ion_p320eta490	75	3.2 - 4.9	15559	HLT_j25_ion_p320eta490_L1TE5

Table 4.7: Overview of Pb+p ion triggers used in the analysis. The sampled luminosity, $\mathcal{L}$, is prescale corrected. The L1 for triggers that do not specify this detail in the chain name are: L1_J15.31ETA49 for HLT_j45_ion_p320eta490 and HLT_j55_ion_p320eta490, and L1_J20.31ETA49 for HLT_j65_ion_p320eta490.

Trigger Chain	p_{T}^{99} [GeV]	η	$\mathcal{L}$ [ub^{-1}]	p_{T}^{99} Monitor
HLT_j30_0eta490_L1TE10	40	0 - 4.9	108.48	HLT_mb_sptrk
HLT_j40_L1J5	54	0 - 3.2	463.8	HLT_mb_sptrk
HLT_j50_L1J10	61	0 - 3.2	2169	HLT_mb_sptrk
HLT_j60	75	0 - 3.2	3036	HLT_mb_sptrk
HLT_j75_L1J20	85	0 - 3.2	21717	HLT_mb_sptrk
HLT_j90_L1J20	104	0 - 3.2	68464	HLT_mb_sptrk
HLT_j100_L1J20	111	0 - 3.2	86453	HLT_mb_sptrk
HLT_j15_p320eta490_L1MBTS_1_1	24	3.2 - 4.9	61.75	HLT_mb_sptrk
HLT_j25_p320eta490_L1TE5	34	3.2 - 4.9	310.9	HLT_mb_sptrk
HLT_j35_p320eta490_L1TE10	47	3.2 - 4.9	685.2	HLT_j25_p320eta490_L1TE5
HLT_j45_p320eta490	65	3.2 - 4.9	8274	HLT_j25_p320eta490_L1TE5
HLT_j55_p320eta490	80	3.2 - 4.9	20076	HLT_j25_p320eta490_L1TE5
HLT_j65_p320eta490	91	3.2 - 4.9	56342	HLT_j25_p320eta490_L1TE5

Table 4.8: Overview of Pb+p pp triggers used in the analysis. The sampled luminosity, $\mathcal{L}$, is prescale corrected. The L1 for triggers that do not specify this detail in the chain name are: L1_J15.31ETA49 for HLT_j45_p320eta490 and HLT_j55_p320eta490, and L1_J20.31ETA49 for HLT_j65_p320eta490.

Notes On Efficiencies Of Certain Trigger Chains

While scrutinizing all the different triggers, a number of relevant features were discovered and studied in detail, to properly evaluate the final trigger strategy. This section is a summary of relevant topologies identified for specific chains.

- **Inefficiencies in forward `ion` triggers at low p_{T}:** low p_{T} triggers covering the forward p-going region of the detector (in particular `HLT_j15_ion_n320eta490_L1TE5` for p+Pb data taking, and `HLT_j15_ion_p320eta490_L1TE5` for Pb+p beam orientation) were found to be affected by widespread inefficiencies, see Figure 4.21 for the `HLT_j15_ion_n320eta490_L1TE5` example. By analyzing the centrality dependence of this issue, it was determined that it arises from peripheral events, see Figure 4.22. The full efficiency point for this trigger is way beyond that of the `j25` covering this area (*i.e.*, 41 GeV). Therefore, a dedicated approach was needed to include the forward low p_{T} region in the analysis (and explore the lowest reachable x_{Pb} values, see Equations 4.3 and 4.4, and avoid a centrality dependent bias in the R_{CP} analysis.

- **Inefficiencies of semi-forward triggers:** as previously mentioned and also evident from Tables 4.5, 4.6, and 4.7, semi-forward triggers were not considered in this analysis. This choice was made ① to reduce the complexity of the trigger schemes for the p+Pb data, and ② because semi-forward triggers were showing widespread L1 inefficiencies below 80 GeV, that would have strongly limited the region of phase space available for analysis, see Figure 4.23. These inefficiencies were later tracked down to the transition region between central and forward L1-calo, at $|\eta| = 3.1$.

- **Efficiency of HLT MB triggers:** in the preliminary analysis, significant help to cover the low-p_{T} regions (up to 40 GeV) was obtained by using MB triggers, namely `HLT_mb_sptrk` and `HLT_mb_sptrk_L1MBTS_1`. The performance of these triggers in p+Pb was examined in detail in Ref. [206]. The `HLT_mb_sptrk` is fully efficient if there is at least one primary vertex in the event, since this requirement ensures enough tracks to achieve the best performance of this trigger. The situation for the `HLT_mb_sptrk_L1MBTS_1` is more complex, see Figure 4.24. Due to radiation damage, the `L1_MBTS_1` is not fully efficient below $N_{\mathrm{ch}} = 120$. For these reasons, only the `HLT_mb_sptrk` was considered in the preliminary analysis when the MB was used to complement physics triggers. This trigger was heavily prescaled, and was only sufficient to provide coverage for central events considered at that stage of the analysis (0–20%). The final centrality binning adopted for this analysis, selecting central events as done in Ref. [152](0–10%), has further impacted the available statistics coming from this trigger, which was used to cover mostly the low p_{T} region between 20 and 50 GeV. Given the very limited impact in terms of phase space coverage gained by using this trigger, and the partial recovery of it that can be done by using the `HLT_j30` trigger, it was decided to drop the usage of MB triggers for the final analysis. These triggers will be considered again for the cross-section analysis, where the absence of centrality binning will allow for meaningful statistics at lower p_{T} values.

4.4.4 Final Trigger Strategy

Using the information outlined above, a well-defined (η, p_{T}) map of triggers to be considered in this analysis was constructed for each of the three trigger schemes used in the p+Pb data taking. Events are considered only if the leading jet in the trigger has fired the corresponding trigger chosen for the (η, p_{T}) region where the jet

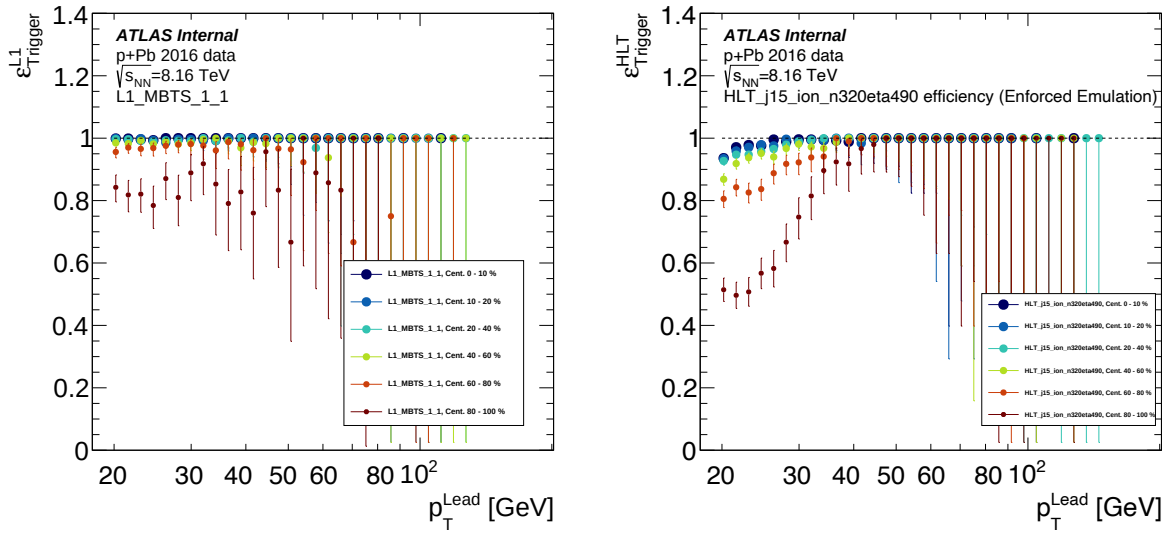

Figure 4.22: L1 and HLT efficiencies (left and right panel, respectively) for `HLT_j15_ion_n320eta490_L1_MBTS_1`, analyzed as a function of centrality. One can notice that L1 inefficiencies come distinctively from the most peripheral class of events, while for HLT there are widespread inefficiencies at low p_{T} that extends over different centrality classes (also mid-central).

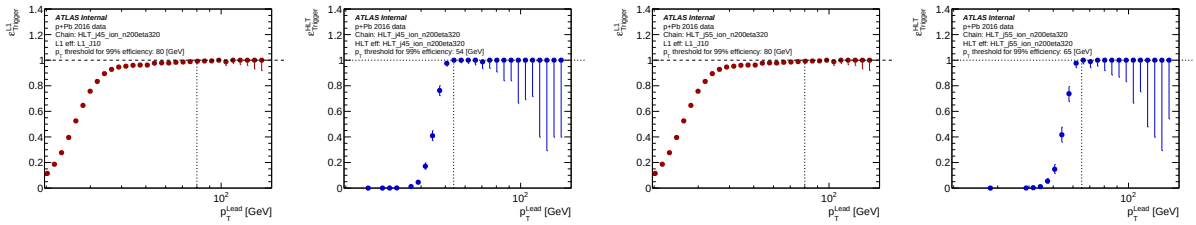

Figure 4.23: L1 (dark red curves) and HLT (blue curves) efficiencies for `HLT_j45_ion_n200eta320_L1_J10` and `HLT_j55_ion_n200eta320_L1_J10` (left and right panel, respectively). Widespread inefficiencies can be noticed at L1 for both triggers.

is reconstructed. The trigger selection for $|\eta| < 3.0$ and for $|\eta| > 3.5$above a p_{T} of 40 GeV is straightforward. In these regions, the fully efficient trigger associated with the lowest prescale value is chosen. Efficiency values used to determine what trigger to choose in each (η, p_{T}) region are reported in Tables 4.6, 4.7, and 4.8. For triggers covering the same η region, prescale values decrease as the p_{T} threshold increases.

A different treatment is required in the η region corresponding to the transition between central and forward triggers, i.e. around $\eta = \pm 3.2$.[1] To handle the trigger analysis in this region, an inclusive approach (see Ref. [207] and references therein), hereafter referred to as the Fully Efficient Trigger Combination (FETC) method, was chosen. In the FETC approach, a combined weight based on all the considered trigger items for the given kinematic region is determined for the entire event sample. For each event, at least one actual trigger item bit from the set of considered items is required to be set. The weight ($w_{j,k}$) calculation for an event j in a given run k is based on the probability to accept the event after the application of the prescale to all the i-th trigger items considered. If $r_{i,j}$ is the bit for the trigger item i in the event j, and the same trigger item is prescaled by a factor $p_{i,k}$ during the run k, the probability that the event j in the run k is

[1]The sign is determined by the beam orientation, since this analysis covers only central and forward regions, discarding the backward η region where the energy accumulated in the FCal is used for centrality determination.

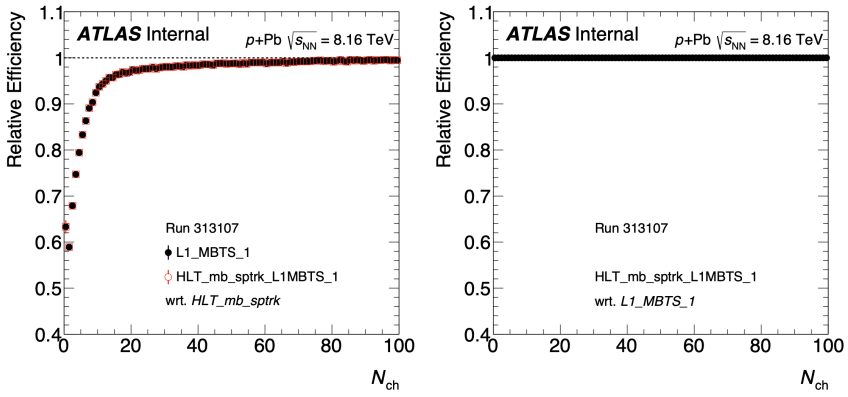

Figure 4.24: Left: `L1_MBTS_1` trigger efficiency as a function of `L1_MBTS_1` multiplicity in 2016 p+Pb collisions, measured as the relative efficiencies of `L1_MBTS_1` and `HLT_mb_sptrk_L1MBTS_1` with respect to `HLT_mb_sptrk`. Due to radiation damage in 2015 and 2016, the `MBTS` is not fully efficient until $N_{\text{ch}} > 120$. Right: `HLT_mb_sptrk_L1MBTS_1` efficiency with respect to `L1_MBTS_1` as a function of multiplicity in 2016 p+Pb collisions. No inefficiency is observed for the HLT requirement `HLT_mb_sptrk` with respect to `L1_MBTS_1` since the relative efficiency is always 100%. Figure taken from Ref. [206].

accepted by the trigger item i after the prescale can be expressed as

$$q_{i,j,k} = \frac{r_{i,j}}{p_{i,k}}. \tag{4.12}$$

Assuming the prescale decisions for each trigger item are independent from one another, the probability that at least one of the N_{items} trigger items accepts the event is given by

$$q_{j,k} = 1 - \prod_{i=1}^{N_{\text{items}}} \left(1 - \frac{r_{i,j}}{p_{i,k}}\right). \tag{4.13}$$

Starting from this, one can define the run dependent weight for event j as

$$w_{j,k} = \frac{1}{q_{j,k}}. \tag{4.14}$$

When combining all the considerations outlined above, one obtains a (η, p_{T}) map that provides, per each jet with $p_{\text{T}}>$ 40 GeV and -4.5 $< \eta <$ 3.1 (-3.1 $< \eta <$ 4.5), the jet triggers considered for the analysis of the p+Pb (Pb+p) data. The three maps corresponding to the trigger configurations used in this analysis are shown in Figure 4.25. The analysis reported in this thesis uses dijet events with a leading jet $p_{\text{T}}>$ 40 GeV and a sub-leading jet $p_{\text{T}}>$ 30 GeV.

Note on HEC issue implication for the trigger: The area related to the HEC issue (see Section 4.3.2) is excluded from the analysis, including a buffer region of $R = 0.4$ around it, therefore no correction to the trigger efficiency for this hardware issue is needed.

4.5 Centrality Determination

In Pb+Pb collisions, the volume of the QGP droplet created is related to the impact parameter, or *centrality*, of the collision. For this reason, many observables sensitive to QGP effects are usually studied in different centrality intervals to infer the property of the medium and understand its evolution. Centrality still plays an important role even in small systems such as p+A collisions. Here it can be seen as an experimental classification of the collision geometry generally based on a measurement of the overall event activity in a rapidity region separated from the hard process of interest [192]. The centrality determination for the 2016

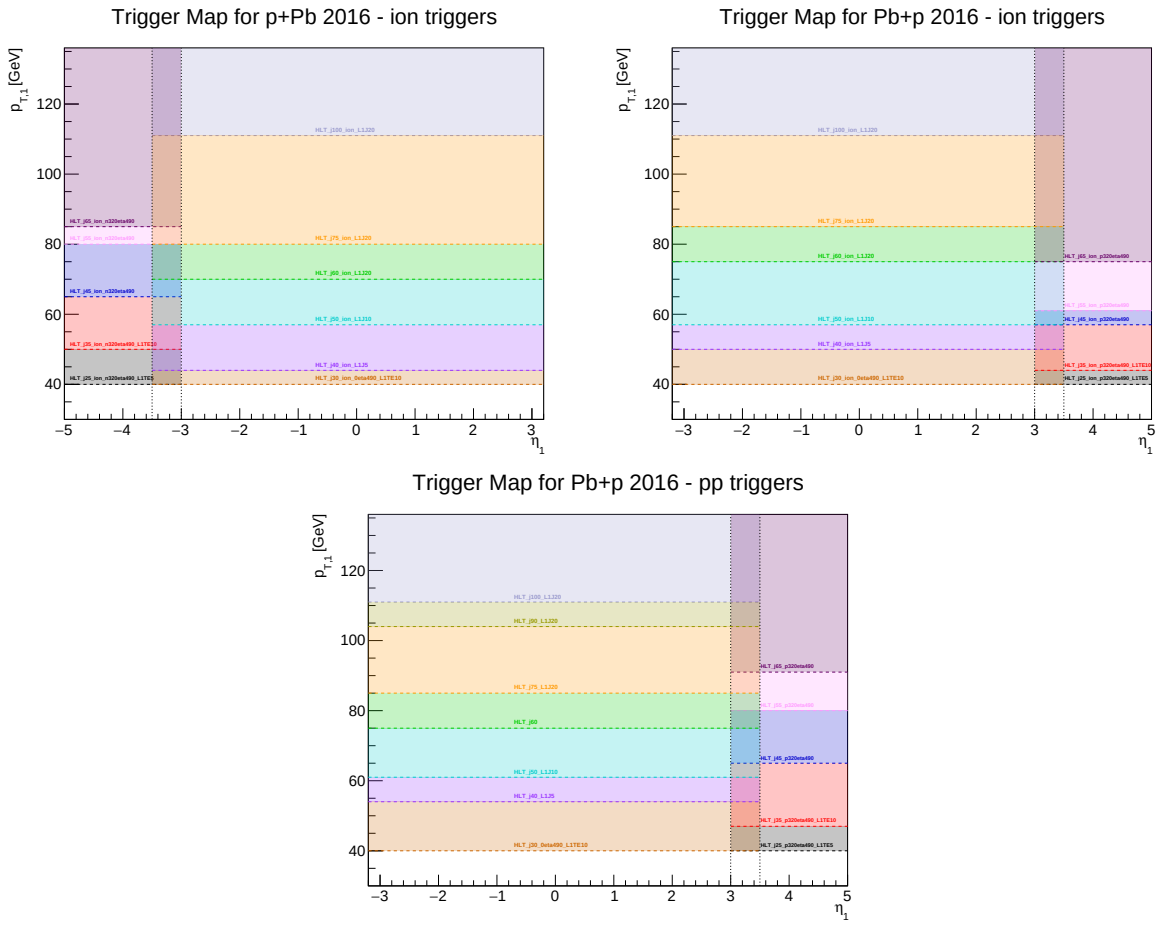

Figure 4.25: (η, p_{T}) maps identifying the trigger selected for analysis of an event where the leading jet is characterized by a given η and p_{T}. Different colors correspond to different triggers. Overlapping colors represent regions where the FETC method is applied. The three panels correspond to the three trigger configurations of the 2016 p+Pb data: p+Pb (top left), Pb+p `ion` triggers (top right), Pb+p `pp` triggers (bottom). The lower p_{T} boundary corresponds to the minimum p_{T} cut set for the leading jet in the analysis.

p+Pb dataset was carried out by K.Hill and D.Perepelitsa in 2018. All the details of these studies, used to define centrality in the analysis presented in this thesis, are available in Ref. [193]. Main aspects relevant for the 8.16 TeV dijet analysis are summarized in this section.

4.5.1 Centrality Selections

In p+Pb collisions, the momentum asymmetry of the projectiles, resulting in a boost of the center-of-mass frame relative to the detector, resulted in a corresponding shift in the rapidity distribution of soft particles. This shift corresponds to $\Delta y = \pm 0.465$ for Pb+p and p+Pb data taking, respectively. The correlation between the two arms of the FCal for p+Pb data is shown in Figure 4.26.

At low total energy in both FCals the correlation is roughly one-to-one, but as the energy in the Pb-going direction increases, the energy in the p-going direction seems to saturate. This implies a lack of sensitivity of the p-going direction to the overall soft particle production and, therefore, to the event centrality. For this reason, centrality was determined using solely the transverse energy registered in the Pb-going arm of the FCal (side A for p+Pb data, side C for Pb+p data, respectively). The latter was correlated with the

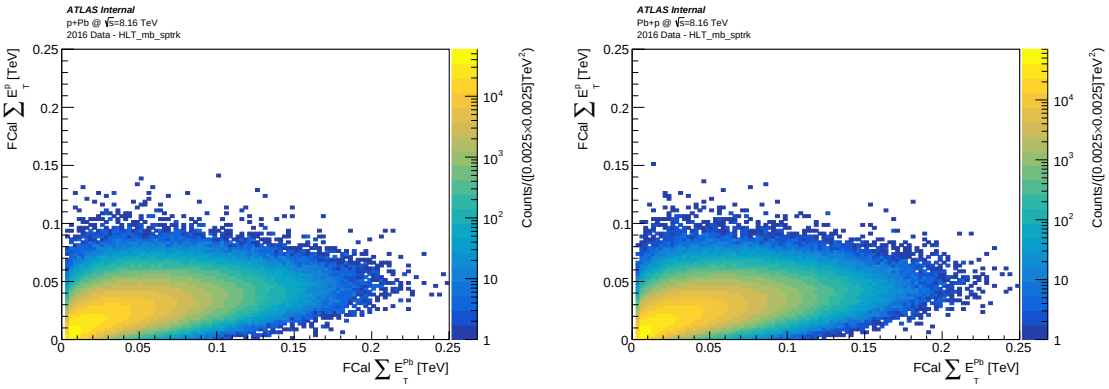

Figure 4.26: Correlation between the transverse energy accumulated in the two FCal arms: p-going (side C for p+Pb and A for Pb+p) and Pb-going (side A for p+Pb and C for Pb+p). Distributions obtained using the `HLT_mb_sptrk` trigger only and event selection analogous to the centrality analysis.

collision geometry thanks to Monte Carlo Glauber models (see Section 1.5.1). In particular, traditional MC Glauber and Glauber-Gribov models were considered in the analysis. By using the Pb-going arm of the FCal, centrality is determined in a kinematic region totally separated from the region considered for the analysis presented in this thesis since, as discussed in Section 4.4, the jet triggers in the backward region (e.g. the Pb going side of the experiment) were not active for most of the data taking. Centrality selections taken from Ref. [193], and used for this analysis, are reported in Table 4.9.

Centrality	$\Sigma E_{\mathrm{T}}^{\mathrm{Pb}}$ [TeV]
0–10 %	0.06518 - 6.00
10–20 %	0.04916 - 0.06518
20–30 %	0.03866 - 0.04916
30–40 %	0.03046 - 0.03866
40–60 %	0.01769 - 0.03046
60–90 %	0.00360 - 0.01769

Table 4.9: Definition of centrality binning based on the distribution of transverse energy in the Pb-going FCal ($\Sigma E_{\mathrm{T}}^{\mathrm{Pb}}$) for a nominal efficiency value of 98%. Values taken from Ref. [193].

Three main sources of systematic uncertainty were identified while carrying out this analysis, namely:

- **Uncertainty due to the event selection efficiency:** the event selection filter efficiency was studied by making use of PYTHIA8 MC simulations, and found to be about 98% for non-diffractive events, with an asymmetric variation of +2% and -1%. These numbers already account for additional model dependent uncertainty related to the model used to describe the individual nucleus-nucleus interactions. In the case of this analysis, both Glauber and Glauber-Gribov models were used, see Ref. [193] for more details.

- **Uncertainty due to Glauber parameters:** this source of systematics was inspected by varying the nucleon-nucleon cross-section (σ_{NN}), the Wood-Saxon radius and skin depth parameters (R,a), and the hard-core radius ($d_{min} \pm 0.2$ fm from the nominal value of 0.4 fm).

- **Fit model:** to correlate the observed energy distribution in the FCal on the Pb-going side with the $\langle N_{\mathrm{part}} \rangle$ derived from the Glauber model, the observed data FCal $\Sigma E_{\mathrm{T}}^{\mathrm{Pb}}$ is fit with gamma distributions with parameters k and θ and directly dependent from $\langle N_{\mathrm{part}} \rangle$. These parameters are characteristics of the two different models, and are used to determine the uncertainty on the centrality determination related to the fit procedure.

For the most peripheral and central collisions, the dominant uncertainty is the one related to the model parameters, whereas for mid-central collisions the main source of variations is related to σ_{NN}. For all details related to the determination of the centrality in the 2016 p+Pb data-set, and the associated uncertainties, see Ref. [193].

Centrality is determined in this analysis to construct a central-to-peripheral ratio for per-event dijet yields. For this purpose, three centrality intervals are defined:

- 0–10%, Central events, $0.06518 < \Sigma E_{\mathrm{T}}^{\mathrm{Pb}}$ / [TeV]< 6.00
- 20–40%, Mid-central events, $0.03046 < \Sigma E_{\mathrm{T}}^{\mathrm{Pb}}$ / [TeV]< 0.04916
- 60–90%, Peripheral events, $0.00360 < \Sigma E_{\mathrm{T}}^{\mathrm{Pb}}$ / [TeV]< 0.01769

An example of FCal transverse energy distribution obtained from minimum-bias events and divided in different centrality intervals is shown in Figure 4.27. A comparison between the FCal distribution in minimum-bias events and in dijet events selected for the analysis is reported in Figure 4.28.

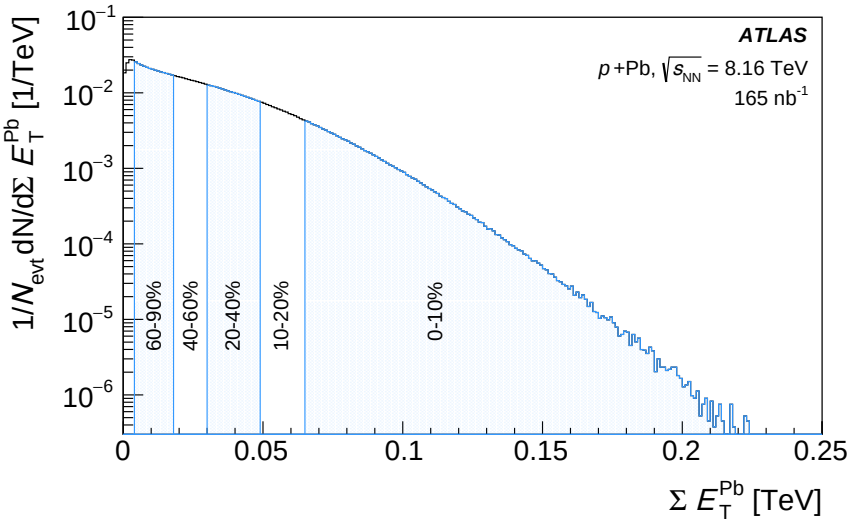

Figure 4.27: Distribution of $\Sigma E_{\mathrm{T}}^{\mathrm{Pb}}$ in the FCal for p+Pb data taking, extracted from minimum-bias events. The three centrality bins defined for the analysis are denoted by blue-shaded areas, namely 0–10% (central), 20–40% (mid-central) and 60–90% (peripheral).

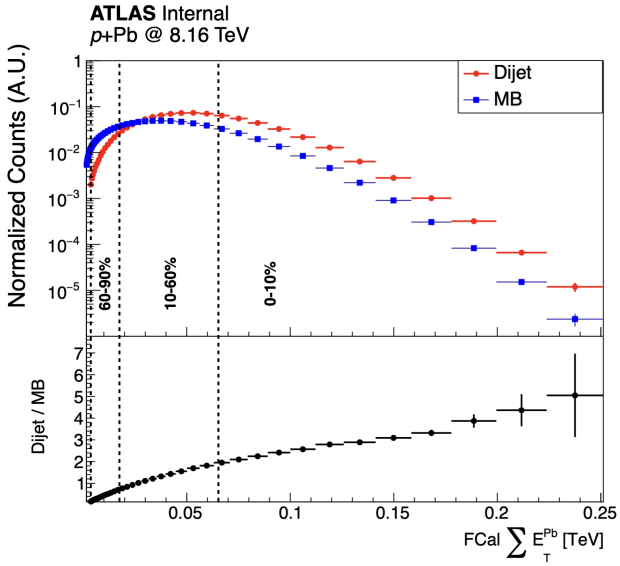

Figure 4.28: Distributions of $\Sigma E_{\mathrm{T}}^{\mathrm{Pb}}$ in the FCal for p+Pb data taking, extracted from minimum-bias (blue) and dijet (red) events. The `HLT_mb_sptrk` trigger was used to obtain the minimum-bias distribution. The dijet distribution was obtained using the same event selections applied in the analysis.

4.5.2 Nuclear Thickness and Number of Participating Nucleons

Within the centrality analysis reported in Ref. [193], the number of participating nucleons, $\langle N_{\text{part}} \rangle$, and the nuclear thickness seen by the proton projectile, $\langle T_{\text{AB}} \rangle$, were also estimated in the same centrality intervals. They are reported in Tables 4.10 and 4.11 for two different MC Glauber models. The standard Glauber model uses a fixed nucleon-nucleon cross-section, while the Glauber-Gribov model allows the nucleon-nucleon cross-section to fluctuate on an event by event basis. For more details, refer to Chapter 5 of Ref. [193]. The approach chosen to adapt $\langle N_{\text{part}} \rangle$ and $\langle T_{\text{AB}} \rangle$ to the centrality binning used in this analysis was to build a weighted average, where the weights are set to the width of the centrality interval associated to $\langle N_{\text{part}} \rangle$ and $\langle T_{\text{AB}} \rangle$. It is worth noting that the fine values of $\langle N_{\text{part}} \rangle$ and $\langle T_{\text{AB}} \rangle$ are characterized by asymmetric uncertainties, while their weighted average [208] returns a symmetrized uncertainty. By making use of Equation 4.10 and the $\langle N_{\text{part}} \rangle$ values reported in Table 4.10, it is possible to calculate $R_{\text{coll}}^{0\text{–}10\%}$. The different contributions to the systematic error were not reported explicitly for the results in Ref. [193]; therefore, it was not possible to profit from the cancellation of part of them while constructing the $R_{\text{coll}}^{0\text{–}10\%}$ ratio. For this reason, $R_{\text{coll}}^{0\text{–}10\%}$ will not be constructed in this analysis.

Centrality	$\langle N_{\mathbf{part}} \rangle$			
	Standard Glauber		Glauber-Gribov	
0–1%	$19.10^{+0.61}_{-1.28}$	16.37±1.00	$25.60^{+0.55}_{-1.61}$	19.49±2.17
1–5%	$16.94^{+0.52}_{-0.90}$		$20.60^{+0.47}_{-0.98}$	
5–10%	$15.37^{+0.45}_{0.69}$		$17.37^{+0.42}_{-0.62}$	
10–20%	$13.76^{+0.37}_{0.51}$	10.41±1.18	$14.52^{+0.38}_{0.37}$	10.07±1.46
20–30%	$12.03^{+0.28}_{-0.36}$		$11.87^{+0.34}_{-0.21}$	
30–40%	$10.41^{+0.21}_{-0.24}$		$9.77^{+0.32}_{-0.15}$	
40–50%	$8.76^{+0.20}_{0.18}$		$7.92^{+0.31}_{-0.11}$	
50–60%	$7.08^{+0.36}_{0.14}$		$6.25^{+0.32}_{0.10}$	
60–70%	$5.46^{+0.55}_{-0.13}$	4.21±0.69	$4.81^{+0.31}_{-0.09}$	3.75±0.58
70–80%	$4.08^{+0.64}_{-0.10}$		$3.64^{+0.30}_{-0.07}$	
80–90%	$3.09^{+0.54}_{0.07}$		$2.81^{+0.24}_{-0.06}$	
0–90%	$8.80^{+0.33}_{-0.18}$		$8.86^{+0.22}_{-0.18}$	

Table 4.10: Values of $\langle N_{\text{part}} \rangle$ calculated using standard Glauber and Glauber-Gribov models for different centrality classes, taken from Ref. [193]. The weighted mean of the values corresponding to the centrality classes used in this analysis, computed as described in the text, is also reported. These values currently represent a conservative estimate of $\langle N_{\text{part}} \rangle$.

4.6 Unfolding

To correct for detector effects, the per-event dijet yields are unfolded in $p_{\text{T,Avg}}$ using a one-dimensional Bayesian procedure [209] implemented within the RooUnfold package [210]. For each y_{b} and y^* bin, a response matrix is filled using truth-reconstructed pairs of jets from the Pythia8 MC overlay sample. Note that the jet yields are also separated using centrality intervals (see Section 4.5). The response binning includes 3 underflow bins and 1 overflow bin to allow for reconstructed jet pairs with truth $p_{\text{T,Avg}}$ below the kinematic selection to migrate out of the measurement region. An efficiency correction is included in the unfolding, which accounts for reconstructed jets that are outside of the measurement region, including the disabled HEC.

Centrality	$\langle T_{\mathbf{AB}} \rangle$ [mb^{-1}]			
	Standard Glauber		Glauber-Gribov	
0–1%	$0.241^{+0.0109}_{-0.0143}$	0.205±0.013	$0.328^{+0.0170}_{-1.61}$	0.247±0.029
1–5%	$0.213^{+0.0096}_{-0.0123}$		$0.261^{+0.0136}_{-0.0123}$	
5–10%	$0.192^{+0.0087}_{-0.0113}$		$0.218^{+0.0114}_{0.0103}$	
10–20%	$0.170^{+0.0077}_{0.0100}$	$0.170^{+0.0077}_{0.0100}$	$0.180^{+0.0094}_{0.0085}$	$0.180^{+0.0094}_{0.0085}$
20–30%	$0.147^{+0.0067}_{-0.0087}$	0.136±0.011	$0.145^{+0.0075}_{-0.0068}$	0.131±0.014
30–40%	$0.125^{+0.0057}_{-0.0074}$		$0.117^{+0.0061}_{-0.0055}$	
40–50%	$0.103^{+0.0047}_{0.0061}$	0.092±0.011	$0.092^{+0.0048}_{-0.0043}$	0.081±0.011
50–60%	$0.081^{+0.0037}_{0.0048}$		$0.070^{+0.0036}_{0.0033}$	
60–70%	$0.060^{+0.0027}_{-0.0035}$	0.043±0.009	$0.051^{+0.0026}_{-0.0024}$	0.037±0.008
70–80%	$0.041^{+0.0019}_{-0.0024}$		$0.035^{+0.0018}_{-0.0017}$	
80–90%	$0.028^{+0.0013}_{0.0016}$		$0.024^{+0.0013}_{-0.0011}$	
0–90%	$0.104^{+0.0047}_{-0.0061}$		$0.105^{+0.0055}_{-0.0049}$	

Table 4.11: Values of $\langle T_{\mathrm{AB}} \rangle$ calculated using standard Glauber and Glauber-Gribov models for different centrality classes, taken from [193]. The weighted mean of the values corresponding to the centrality classes used in this analysis, computed as described in the text, is also reported. These values currently represent a conservative estimate of $\langle T_{\mathrm{AB}} \rangle$.

Additionally, an efficiency correction is applied to account for bin migration in y_{b} and y^*, using the `Fake` and `Miss` functionality within RooUnfold.

4.6.1 Efficiency Correction

This analysis utilizes large (y_{b}, y^*) bins in order to increase the statistical significance of the results, particularly at high y_{b}, and to minimize the impact of y_{b} and y^* bin migration on the results. Figure 4.29 shows the amount of migration into and out of a given (y_{b}, y^*) bin, evaluated using truth and reco level Pythia8 MC. To ensure that this migration is being accounted for, the RooUnfold `Fake` and `Miss` functions were used to produce an efficiency correction accounting for the bin migration. Truth-matched reco dijets with a y_{b} or y^* which belongs to a different reco bin than that at the truth-level are counted as fakes in the response matrix corresponding to the reco (y_{b}, y^*) bin. A miss is then recorded in the response matrix corresponding to the truth level (y_{b}, y^*) bin.

The impact of the efficiency correction is shown for two example central (y_{b}, y^*) bins of the Pb+p per-event dijet yield in Figure 4.30. The correction is largest at low $p_{\mathrm{T,Avg}}$, where the jet energy resolution is responsible for truth jets being matched to reconstructed jets which do not pass the p_{T} threshold, and in y_{b} bins impacted by the HEC issue. The term "Miss" in the efficiency correction plots refers to the `RooUnfoldResponse::Miss` function used to produce the efficiency correction. This is done by recording unmatched truth jets which pass the selection criteria while filling the response matrices, which are shown for each centrality, y_{b} and y^* bin of the measurement in Section A.1. Section A.2 shows the response matrices with each reconstructed bin normalized to unity, allowing for visualization of the $p_{\mathrm{T,Avg}}$ bin migration.

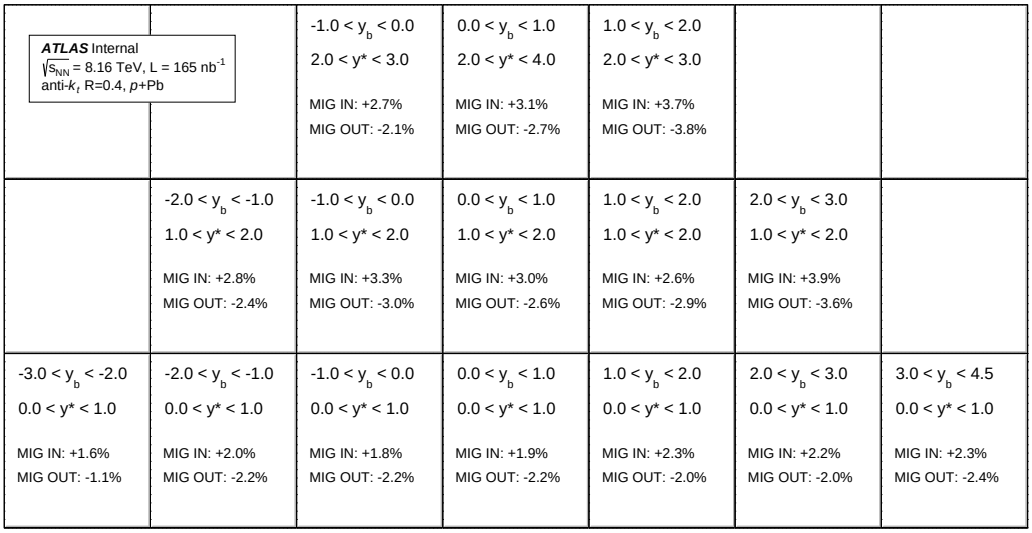

Figure 4.29: The amount of migration in the full p+Pb MC is shown in bins of y_{b} and y^*. The value shown corresponds to the percentage of events which migrate into"MIG IN" and out of "MIG OUT" a given (y_{b}, y^*) bin.

4.6.2 Reweighting

Each response matrix is reweighted at the event level such that the MC spectrum better matches the shape of the data. The reconstructed MC spectrum is first produced using an FCal weight in order to have better agreement between the underlying events in data and overlay MC, which is derived by calculating the ratio of away-side (Pb-going direction) sum FCal tranverse energy, $\Sigma E_{\mathrm{T}}^{\mathrm{Pb}}$, shown in the bottom portion of Figure 4.31 for both p+Pb and Pb+p periods. In order to avoid contributions from the hard-scatter, a jet cut of $\eta > -2.8$ ($\eta < 2.8$) is imposed for Period B (Period C) when filling the FCal distribution. The value of the FCal ratio for a given overlay MC event is then retrieved and used as an additional weight when producing an FCal-weighted reconstructed MC spectrum.

The Data-to-MC reweighting factors are derived by calculating the ratio of the reconstructed data spectra to that of the FCal-weighted reconstructed MC. The Data-to-MC ratios are fit using a function that is linear in the logarithm of $p_{\mathrm{T,Avg}}$,

$$f(p_{\mathrm{T,Avg}}) = c_0 + c_1 \log(p_{\mathrm{T,Avg}}), \tag{4.15}$$

and is demonstrated by the red dashed line in Figure 4.32. The blue lines are used to determine the systematic uncertainty on the reweighting, as described in Section 4.7.2. When filling the response matrices, the Data-to-MC factors are used as an additional weight and are retrieved from the fit using the truth kinematics of the dijet.

4.6.3 Unfolding Iterations

Bayesian unfolding is an iterative procedure [209], and therefore, the optimal number of iterations must be decided. The two contributing factors to this decision are the convergence of the unfolding (σ_{conv}), and the growth of the statistical uncertainty (σ_{stat}). The convergence is quantified as the sum over all $p_{\mathrm{T,Avg}}$ bins of

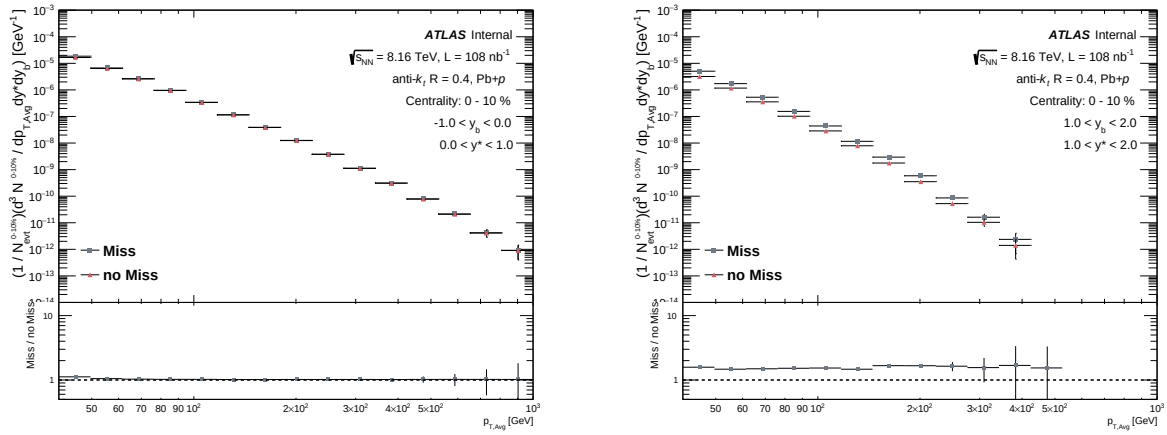

Figure 4.30: Non-efficiency corrected (red) and efficiency corrected (grey) Pb+p dijet yield in two central (y_b, y^*) bins. The impact of the efficiency correction on the yield is demonstrated by the ratio. As one moves closer to the forward HEC region, a larger correction for the HEC issue is seen.

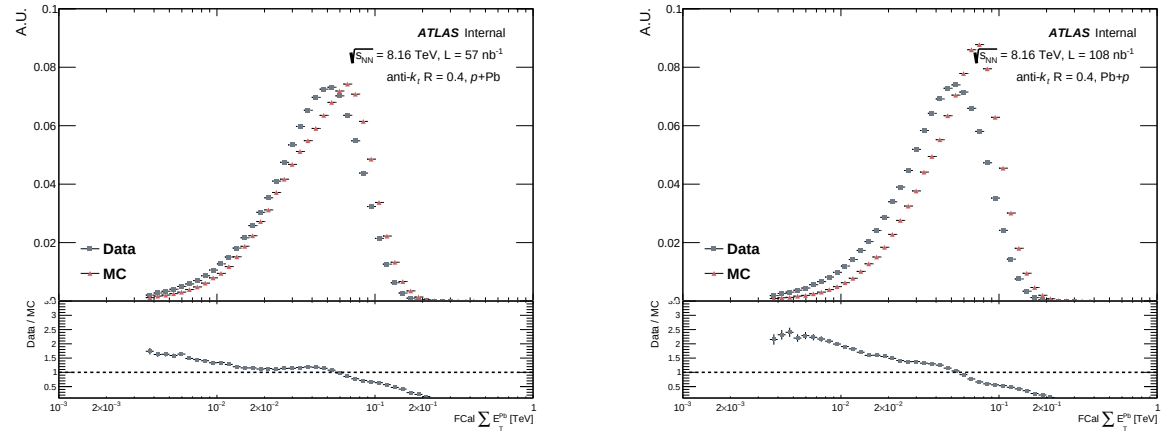

Figure 4.31: The away-side (Pb-going direction) FCal distributions for data (red) and MC (grey) in both the p+Pb (left) and Pb+p (right) periods. The ratio of data to MC used to produced the Data-to-MC weight for response matrix construction is shown in the bottom portion of each figure. Both distributions have been normalized to the same integral.

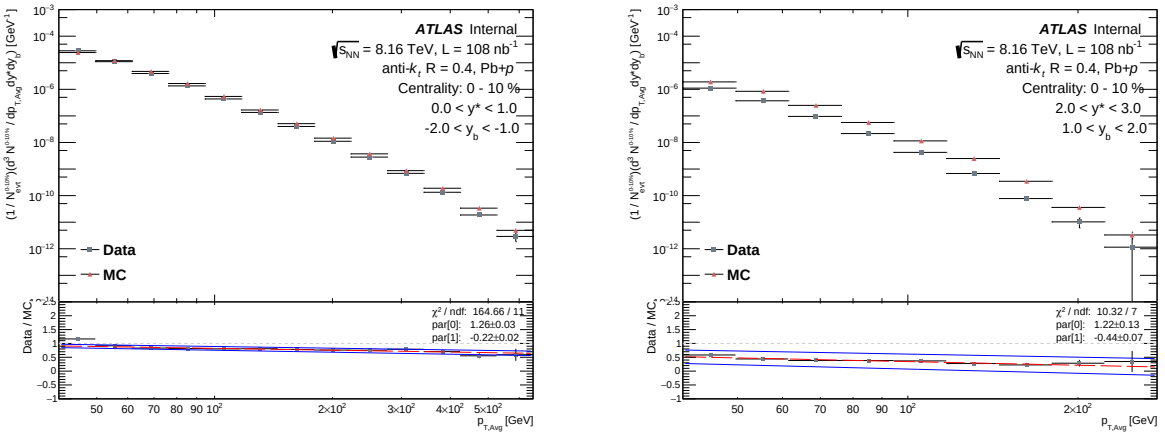

Figure 4.32: Reconstructed level data (grey) and reconstructed MC (red) jet spectra (top panel), with ratio (bottom panel), for Pb+p collisions in two central (y_b, y^*) bins. The ratio has been fit (red-dashed line) using Equation 4.15, and the resulting function has been shifted up and down by the uncertainty on the slope and intercept, shown by the solid blue lines.

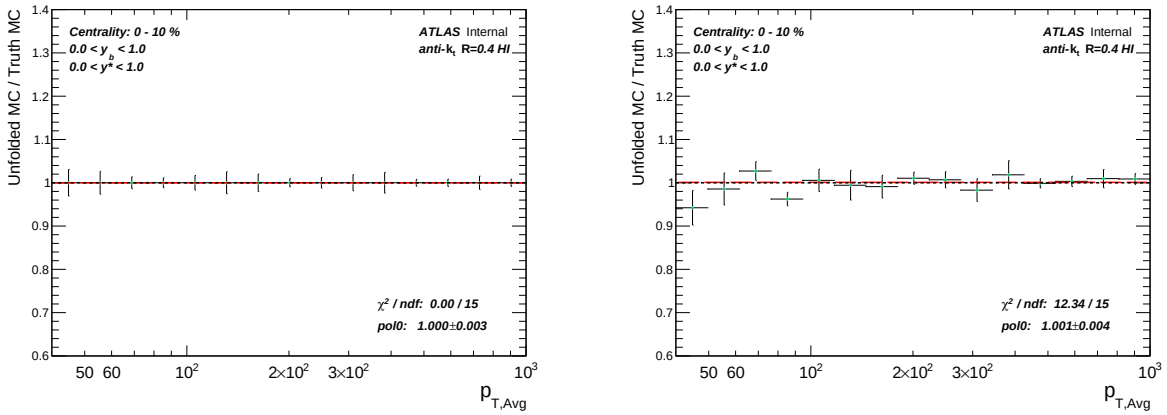

Figure 4.33: The technical-closure test in a single (centrality, y_{b}, y^*) bin of the Pb+p R_{CP} measurement (left). The half-closure test in the same (centrality, y_{b}, y^*) bin of the p+Pb R_{CP} measurement (right). A pol0 fit (red-dashed line) is shown in both plots, indicating that closure is achieved.

the difference between a bin's value at iteration, i, and the value at the previous iteration, $i-1$:

$$\sigma_i^{\mathrm{conv}} = \sqrt{\sum_k^{N_{\mathrm{bins}}} \left(N_{i,k} - N_{i-1,k}\right)^2} \tag{4.16}$$

where $N_{i,k}$ is the value of a given $p_{\mathrm{T,Avg}}$ bin k, at iteration i. Contrary to the statistical component, this contribution will decrease as a function of iterations, as successive unfoldings converge to the "truth" distribution. The statistical uncertainty for the i^{th} iteration is summed over all $p_{\mathrm{T,Avg}}$ bins,

$$\sigma_i^{\mathrm{stat}} = \sqrt{\sum_k^{N_{\mathrm{bins}}} \left(\sigma_{i,k}^{\mathrm{stat}}\right)}. \tag{4.17}$$

The quadrature sum of the two components at each iteration ($\sigma_i^{\mathrm{total}}$) is computed,

$$\sigma_i^{\mathrm{total}} = \sqrt{(\sigma_i^{\mathrm{conv}})^2 + (\sigma_i^{\mathrm{stat}})^2}, \tag{4.18}$$

and the iteration that produces the minimum value across the most (centrality, y_{b}, y^*) bins is chosen. Three unfolding iterations are used in this analysis.

4.6.4 Closure Test

In order to verify that the unfolding is able to correct for detector effects and extract the underlying truth information, two unfolding closure tests were performed. First, the unfolding closure was examined by applying the full unfolding procedure to the reweighted reconstructed MC and comparing to the truth distributions. This check, referred to as the "technical-closure" test, is used to ensure that no significant flaws exist within the unfolding portion of the analysis procedure. The results of this study for one (y_{b}, y^*) bin of the 0–10% Pb+p test are shown in the left plot of Figure 4.33. As expected, the closure is found to be exactly unity, and is found to be the same for all bins in the p+Pb and Pb+p technical-closure tests for the per-event dijet yield unfolding.

The second closure test, termed "half-closure", consists of dividing the Pythia8 overlay MC sample into two statistically independent halves, with the first being used to construct the response matrices used for unfolding, and the second serving as pseudo-data to be unfolded. The result of this study for one (y_{b}, y^*) bin

of the 0–10% Pb+p test is shown in the right plot of Figure 4.33. It is expected for the closure to be unity, within statistical uncertainties. For all (centrality, y_{b}, y^*) bins in the p+Pb and Pb+p analyses, the unfolded to truth ratio is consistent with unity within statistical uncertainties, indicating that sufficient closure exists between the unfolded and truth results.

4.6.5 Statistical Uncertainties

Statistical uncertainties for the unfolding come from both the reconstructed data and the response matrices. A bootstrapping method with 100 toys is used in order to ensure statistical significance of the results. See Ref. [211] for a detailed description of both the method and the ROOT `TH1Bootstrap` class. The weights for each event in a given toy are sampled from a Poisson distribution with a mean of one, producing statistically correlated samples.

The data contribution to the statistical uncertainty in a given (centrality, y_{b}, y^*) bin is evaluated as follows:

1. Nominal data spectrum is smeared, using Poisson weights, producing 100 toy distributions.
2. RMS of the toy distributions is calculated and is taken as the error of the nominal data spectrum.
3. Nominal data spectrum is unfolded using the nominal response matrix.
4. Error on the unfolded result is taken as the data contribution to the statistical uncertainty.

The MC contribution to the statistical uncertainty in a given (centrality, y_{b}, y^*) bin is evaluated as follows:

1. 100 response matrices are produced with weights obtained by sampling from a Poisson distribution with a mean of one.
2. Nominal data spectrum is unfolded 100 times, using the smeared response matrices.
3. RMS of the 100 unfolded data spectra is taken as the MC contribution to the statistical uncertainty.

The final statistical uncertainty is calculated by taking the quadrature sum of the bootstrapped data and MC statistical uncertainties.

4.7 Systematic Uncertainties

Systematic uncertainties are evaluated as a function of $p_{\mathrm{T,Avg}}$ for the dijet yield and R_{CP} measurements. For each systematic variation, the full analysis procedure is performed and the difference from the nominal result is taken as the uncertainty. The variations for each systematic are then added in quadrature to produce the individual systematic uncertainties.

The sources of systematic uncertainty are summarized in Table 4.12. Sources which are "symmetrized" have only an upper variation, which is then used to determine the negative relative uncertainty for the systematic. The total systematic uncertainty is calculated as the quadratic sum of all the listed systematic uncertainties.

In the case where the R_{CP} systematic uncertainties are correlated, the uncertainty is evaluated by comparing the R_{CP} for the various systematic variations and the nominal R_{CP}. For uncorrelated systematic uncertainties, the uncertainty on the R_{CP} distribution is evaluated by adding the uncertainties on the central

Uncertainty	Correlated	two-sided or symmetrized
JES(baseline, cross-calib, flavor)	yes	two-sided
JER	yes	symmetrized
Unfolding Prior	no	two-sided
HEC	yes	symmetrized
T_{AB}	yes	two-sided
Statistical	no	symmetrized

Table 4.12: Summary of systematic uncertainties.

and peripheral dijet yields in quadrature. Thus for correlated uncertainties the corresponding uncertainty on the ratio, $r = A/B$ was taken as:

$$\pm\delta r|_C \equiv \frac{A \pm \delta A}{B \pm \delta B} - \frac{A}{B}. \tag{4.19}$$

For uncorrelated uncertainties, the uncertainty was propagated using the usual method:

$$\delta r|_U \equiv \frac{A}{B}\sqrt{\left(\frac{\delta A}{A}\right)^2 + \left(\frac{\delta B}{B}\right)^2}. \tag{4.20}$$

A statistically weighted average was then used to combine the systematic uncertainties from Period B and Period C. To compute the uncertainties in each kinematic bin, Equation 4.21 was used:

$$\bar{\mu} = \frac{\Sigma x_i/\sigma_i^2}{\Sigma 1/\sigma_i^2}\ , \quad \sigma_i^2(\bar{\mu}) = \frac{1}{\Sigma 1/\sigma_i^2}, \tag{4.21}$$

where $i = \{\text{Period B, Period C}\}$, x_i represents the systematic uncertainty in a given period, and σ_i represents the statistical uncertainty in a given period.

4.7.1 Jet Related Uncertainties

Jet Energy Scale

The JES uncertainty for this analysis has two components. The first component is taken from 13 TeV *pp* JES uncertainties for EMTopo jets, as recommended by the JetEtMiss group. HI jets are first calibrated with respect to jets reconstructed using the nominal *pp* algorithm (EMTopo), referred to as cross-calibration. This calibrated JES is then adapted to the center-of-mass energy used in the HI analysis [212]. These uncertainties are retrieved using the JetUncertainties package with the following configuration file:

`R4_GlobalReduction_SimpleJER.config` ,

which corresponds to ∼20 JES and 8 JER nuisance parameters [213]. Variations which are not related to the analysis have been left out of their respective systemic uncertainty and are listed below:

`JET_EtaIntercalibration_NonClosure_2018data`: Only applicable to 2018 data

The second JES component is specific to heavy ion jets and collision energies (for flavor-related uncertainties) and is evaluated using the Heavy Ion Jet recommendation [214]. The jet flavor uncertainty has both an energy-independent (flavour response) and energy-dependent term (flavour fraction). The uncertainties are used to produce variations by shifting the jet p_{T} according to

$$p_{\mathrm{T}}^{*,\mathrm{reco}} = p_{\mathrm{T}}^{\mathrm{reco}}\big(1 \pm U^{\mathrm{JES}}(p_{\mathrm{T}}, \eta)\big), \tag{4.22}$$

where η accounts for the boost of the p+Pb system in the case of the flavor fraction. The flavor response represents a property of the detector and therefore does not require boosting. It is the dominant systematic,

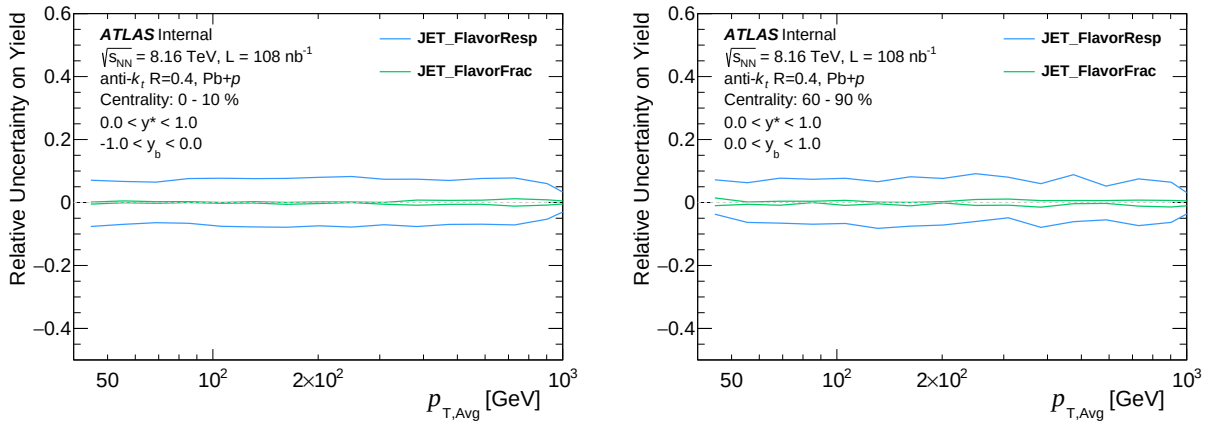

Figure 4.34: Flavor portion of the JES systematic uncertainty in two (centrality, y_{b}, y^*) bins of the Pb+p per-event dijet yield. The flavor response uncertainty is shown by a blue line and the flavor fraction uncertainty by a green line.

with a value of ∼8% in all bins of the per-event dijet yield, as shown in Figure 4.34.

Jet Energy Resolution

The JER systematic accounts for differences between the jet energy resolution in data and MC, where the fractional resolution, $\sigma_{\mathrm{JER}}^{\mathrm{syst}}$, is retrieved as a function of reco jet p_T and η using the JetUncertainties tool [215]. Unfolding is repeated with a modified response matrix for each JER uncertainty component, where the jet p_{T} has been smeared by

$$p_{\mathrm{T}}^{*,\mathrm{reco}} = p_{\mathrm{T}}^{\mathrm{reco}} \times \mathcal{N}\left(1, \sigma_{\mathrm{JER}}^{\mathrm{eff}}\right), \tag{4.23}$$

where $\mathcal{N}\left(1, \sigma_{\mathrm{JER}}^{\mathrm{eff}}\right)$ is the normal distribution with the effective resolution

$$\sigma_{\mathrm{JER}}^{\mathrm{eff}} = \sqrt{\left(\sigma_{\mathrm{JER}} + \sigma_{\mathrm{JER}}^{\mathrm{syst}}\right)^2 - \sigma_{\mathrm{JER}}^2}. \tag{4.24}$$

In addition to the 8 JER nuissance parameters produced using the SimpleJER configuration, a heavy ion specific JER uncertainty corresponding to HI jet collections and the cross-calibration was added to the uncertainties in p+Pb collisions. The JER uncertainty is sub-dominant, reaching up to ∼10% only for the highest y^* values.

4.7.2 Systematic Uncertainty Due to the Unfolding Procedure

The systematic uncertainty on the unfolding is related to the sensitivity of the unfolding procedure to the choice of the input distributions, referred to as "prior". To determine the uncertainty on how much reweighting should be done, the data/MC fits are varied by the uncertainty on their slope and intercept, similarly to the approach used in Ref. [152]. A set of correction factors are then generated using these upper and lower functions (solid blue lines in bottom panel of Figure 4.32), and the analysis procedure is carried out for the two variations. The difference from the nominal result is taken as a systematic uncertainty. This uncertainty is at the sub-percent level for all bins.

4.7.3 Systematic Uncertainty due to Disabled HEC Quadrant

Reconstructed level jets that fall within the region covered by the disabled $+\eta$ HEC have been removed from the p+Pb and Pb+p portion of this analysis (see Section 4.3.2). Two systematic components related to this removal are included in the analysis, with the first being evaluated by increasing the exclusion region by 0.1 in all directions in azimuth and pseudorapidity, and repeating the analysis procedure. The difference between the nominal exclusion and increased exclusion is taken as a systematic uncertainty and is symmetrized. The resultant uncertainty was found to be on the order of 1–2% in the majority of the measurement's phase space, with a few exceptions in η intervals which are impacted by the HEC exclusion.

The second component accounts for a specific topology in which the true sub-leading jet is within the acceptance of the disabled HEC quadrant, causing a subsequent loss of energy at the reconstructed level, resulting in a third-leading truth jet having the second-highest p_{T} at the reconstructed level. The Pythia8 Monte Carlo sample was used to study the occurrence of events which meet the criteria listed below.

- The leading jet is NOT within the disabled HEC
- The subleading jet is within the forward HEC (either a nominal or disabled quadrant)
- A third jet exists within the phase-space of the measurement (not in disabled HEC)
- At the reco-level, the third jet has a higher p_{T} than the subleading jet

The rate of occurence of this "flipping" of the subleading and third jet was then separated between the two cases where the subleading jet is in the disabled HEC ("BAD" in Figure 4.35) and where the subleading jet is in the nominal HEC ("NOM" in Figure 4.35). The flipping of the subleading and third jet in the nominal HEC can be attributed to JES and JER. The impact of the disabled HEC on the flipping is quantified in Figure 4.36, where the rate of occurrence is normalized by the area of two HEC regions and the ratio of BAD to NOM is shown. The systematic is evaluated by, in addition to the nominal HEC rejection, also rejecting events in which a third reco-level jet is present in the disabled HEC and is within 25 GeV of the sub-leading p_{T}, and repeating the analysis procedure. The difference between the nominal exclusion and third jet rejection is taken as a systematic uncertainty and is symmetrized. The resultant uncertainty is found to be at, or below, the one percent level in all bins.

ATLAS Internal $\sqrt{s_{NN}}$ = 8.16 TeV, anti-k_t R=0.4, Pythia 8		$-1.0 < y_b < 0.0$ $2.0 < y^* < 3.0$ NOM = 0.98%±0.03 BAD = 1.27%±0.03 TOT EVT = 91086	$0.0 < y_b < 1.0$ $2.0 < y^* < 4.0$ NOM = 1.20%±0.03 BAD = 1.19%±0.03 TOT EVT = 108005	$1.0 < y_b < 2.0$ $2.0 < y^* < 3.0$ NOM = 0.05%±0.27 BAD = 0.04%±0.30 TOT EVT = 28297		
	$-2.0 < y_b < -1.0$ $1.0 < y^* < 2.0$ NOM = 0.03%±0.10 BAD = 0.02%±0.13 TOT EVT = 331835	$-1.0 < y_b < 0.0$ $1.0 < y^* < 2.0$ NOM = 0.54%±0.01 BAD = 0.57%±0.01 TOT EVT = 1067202	$0.0 < y_b < 1.0$ $1.0 < y^* < 2.0$ NOM = 0.97%±0.01 BAD = 1.91%±0.01 TOT EVT = 1056033	$1.0 < y_b < 2.0$ $1.0 < y^* < 2.0$ NOM = 1.19%±0.02 BAD = 1.37%±0.01 TOT EVT = 364447	$2.0 < y_b < 3.0$ $1.0 < y^* < 2.0$ NOM = 0.43%±0.06 BAD = 0.26%±0.08 TOT EVT = 61714	
$-3.0 < y_b < -2.0$ $0.0 < y^* < 1.0$ NOM = 0.00%±nan BAD = 0.00%±nan TOT EVT = 252238	$-2.0 < y_b < -1.0$ $0.0 < y^* < 1.0$ NOM = 0.00%±nan BAD = 0.00%±nan TOT EVT = 1254976	$-1.0 < y_b < 0.0$ $0.0 < y^* < 1.0$ NOM = 0.04%±0.02 BAD = 0.02%±0.04 TOT EVT = 4490152	$0.0 < y_b < 1.0$ $0.0 < y^* < 1.0$ NOM = 0.46%±0.01 BAD = 0.60%±0.01 TOT EVT = 4485341	$1.0 < y_b < 2.0$ $0.0 < y^* < 1.0$ NOM = 0.76%±0.01 BAD = 2.14%±0.01 TOT EVT = 1226767	$2.0 < y_b < 3.0$ $0.0 < y^* < 1.0$ NOM = 0.76%±0.02 BAD = 1.42%±0.02 TOT EVT = 277659	$3.0 < y_b < 4.0$ $0.0 < y^* < 1.0$ NOM = 0.45%±0.10 BAD = 0.27%±0.12 TOT EVT = 24037

Figure 4.35: The occurrence rate of third jet p_{T} flipping in the nominal and disabled HEC is shown for each (y_{b}, y^*) bin.

ATLAS Internal $\sqrt{s_{NN}}$ = 8.16 TeV, anti-k_t R=0.4, Pythia 8		$-1.0 < y_b < 0.0$ $2.0 < y^* < 3.0$ $\frac{BAD}{NOM}$ = 2.13x	$0.0 < y_b < 1.0$ $2.0 < y^* < 4.0$ $\frac{BAD}{NOM}$ = 1.63x	$1.0 < y_b < 2.0$ $2.0 < y^* < 3.0$ $\frac{BAD}{NOM}$ = 1.30x		
	$-2.0 < y_b < -1.0$ $1.0 < y^* < 2.0$ $\frac{BAD}{NOM}$ = 0.99x	$-1.0 < y_b < 0.0$ $1.0 < y^* < 2.0$ $\frac{BAD}{NOM}$ = 1.75x	$0.0 < y_b < 1.0$ $1.0 < y^* < 2.0$ $\frac{BAD}{NOM}$ = 3.25x	$1.0 < y_b < 2.0$ $1.0 < y^* < 2.0$ $\frac{BAD}{NOM}$ = 1.90x	$2.0 < y_b < 3.0$ $1.0 < y^* < 2.0$ $\frac{BAD}{NOM}$ = 1.01x	
$-3.0 < y_b < -2.0$ $0.0 < y^* < 1.0$ $\frac{BAD}{NOM}$ = nanx	$-2.0 < y_b < -1.0$ $0.0 < y^* < 1.0$ $\frac{BAD}{NOM}$ = nanx	$-1.0 < y_b < 0.0$ $0.0 < y^* < 1.0$ $\frac{BAD}{NOM}$ = 0.83x	$0.0 < y_b < 1.0$ $0.0 < y^* < 1.0$ $\frac{BAD}{NOM}$ = 2.15x	$1.0 < y_b < 2.0$ $0.0 < y^* < 1.0$ $\frac{BAD}{NOM}$ = 4.66x	$2.0 < y_b < 3.0$ $0.0 < y^* < 1.0$ $\frac{BAD}{NOM}$ = 3.08x	$3.0 < y_b < 4.0$ $0.0 < y^* < 1.0$ $\frac{BAD}{NOM}$ = 0.99x

Figure 4.36: The ratio of the occurrence rate of third jet p_{T} flipping in the nominal and disabled HEC, normalized by the corresponding areas, is shown for each (y_{b}, y^*) bin.

4.7.4 Systematic Uncertainty on T_{AB}

The uncertainty on the T_{AB} arises from the geometric modeling and the efficiency of the minimum-bias trigger. The values of these uncertainties along with T_{AB} are tabulated in Table 4.11 taken from Ref. [193]. For the standard Glauber model, the T_{AB} uncertainty has a value of $+12\%$ and -19% in all kinematic bins used in the analysis. For the Glauber-Gribov model, the T_{AB} uncertainty has a value of $+7.7\%$ and -12% in all kinematic bins used in the analysis.

4.7.5 Systematics Summary

The individual and total systematic uncertainties on the 0–10% and 60–90% p+Pb per-event dijet yields are shown in Figures 4.37 and 4.38, respectively. The individual and total systematic uncertainties for the R_{CP} measurement are shown in Figure 4.39. Refer to Equations 4.19 and 4.20 for equations governing treatment of the correlated and uncorrelated uncertainties in Table 4.12, respectively. A Gaussian smoothing ($\sigma = 0.15$) has been applied to minimize statistical fluctuations.

0–10% Per-Event Dijet Yield Systematics

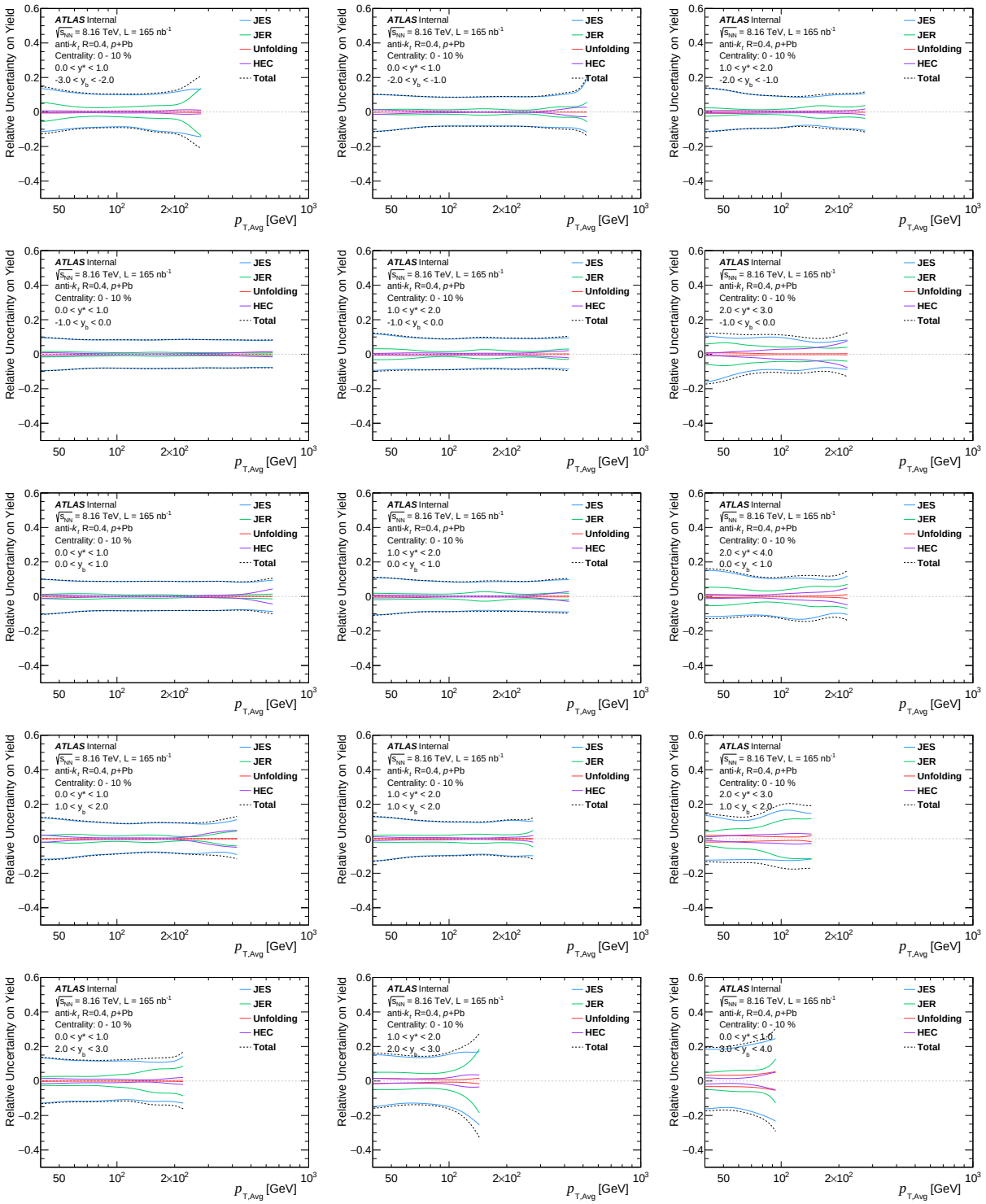

Figure 4.37: The systematic uncertainties on the 0–10% per-event dijet yield measurement as a function of $p_{\mathrm{T,Avg}}$ for $\sqrt{s_{\mathrm{NN}}} = 8.16$ TeV p+Pb collisions. Each panel shows the total systematic uncertainty (black dashed line), as well as the contributions from each source, namely the JES, JER, unfolding and disabled HEC sector.

60–90% Per-Event Dijet Yield Systematics

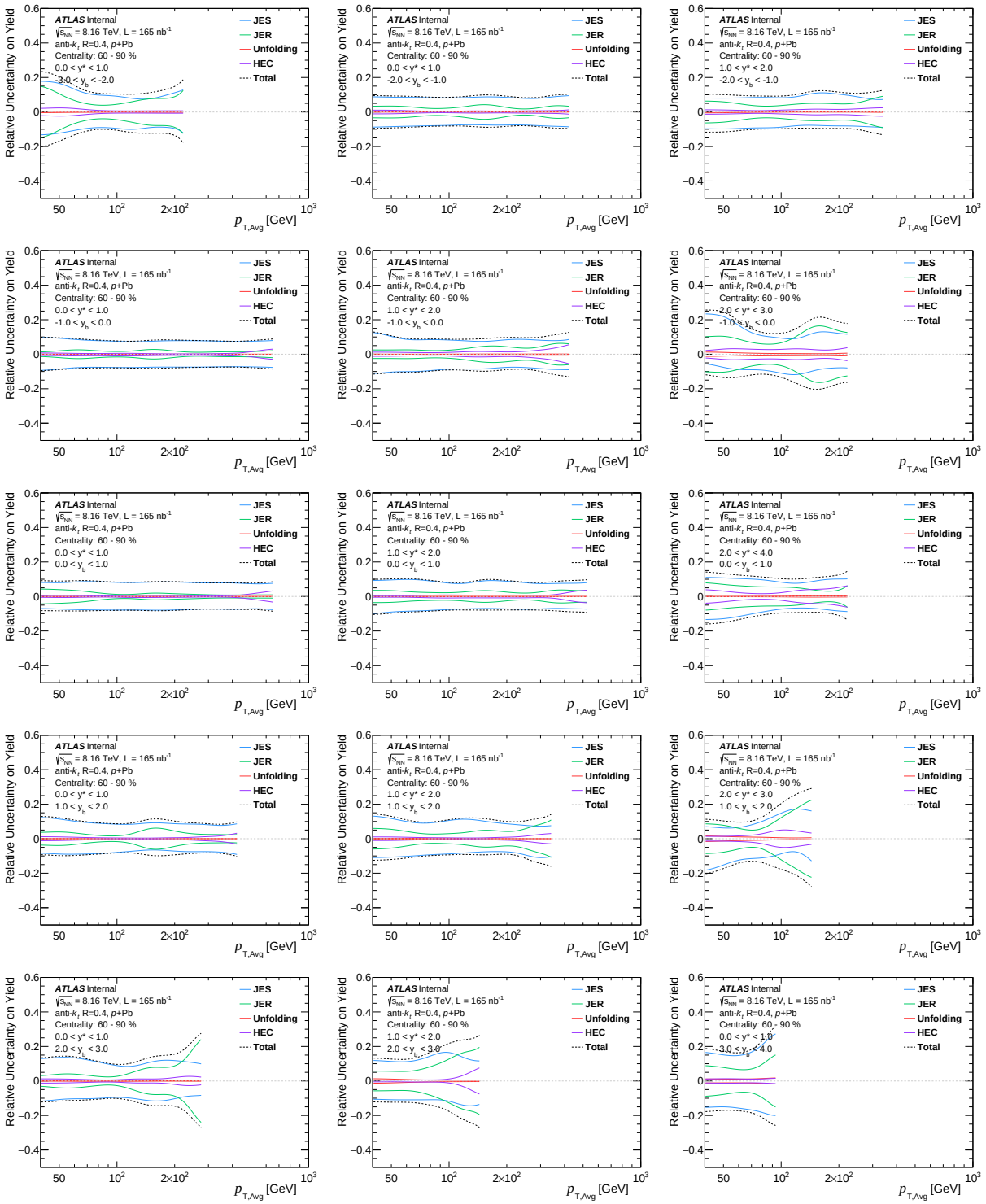

Figure 4.38: The systematic uncertainties on the 60–90% per-event dijet yield measurement as a function of $p_{\mathrm{T,Avg}}$ for $\sqrt{s_{\mathrm{NN}}} = 8.16$ TeV p+Pb collisions. Each panel shows the total systematic uncertainty (black dashed line), as well as the contributions from each source, namely the JES, JER, unfolding and disabled HEC sector.

R_{CP} Systematics

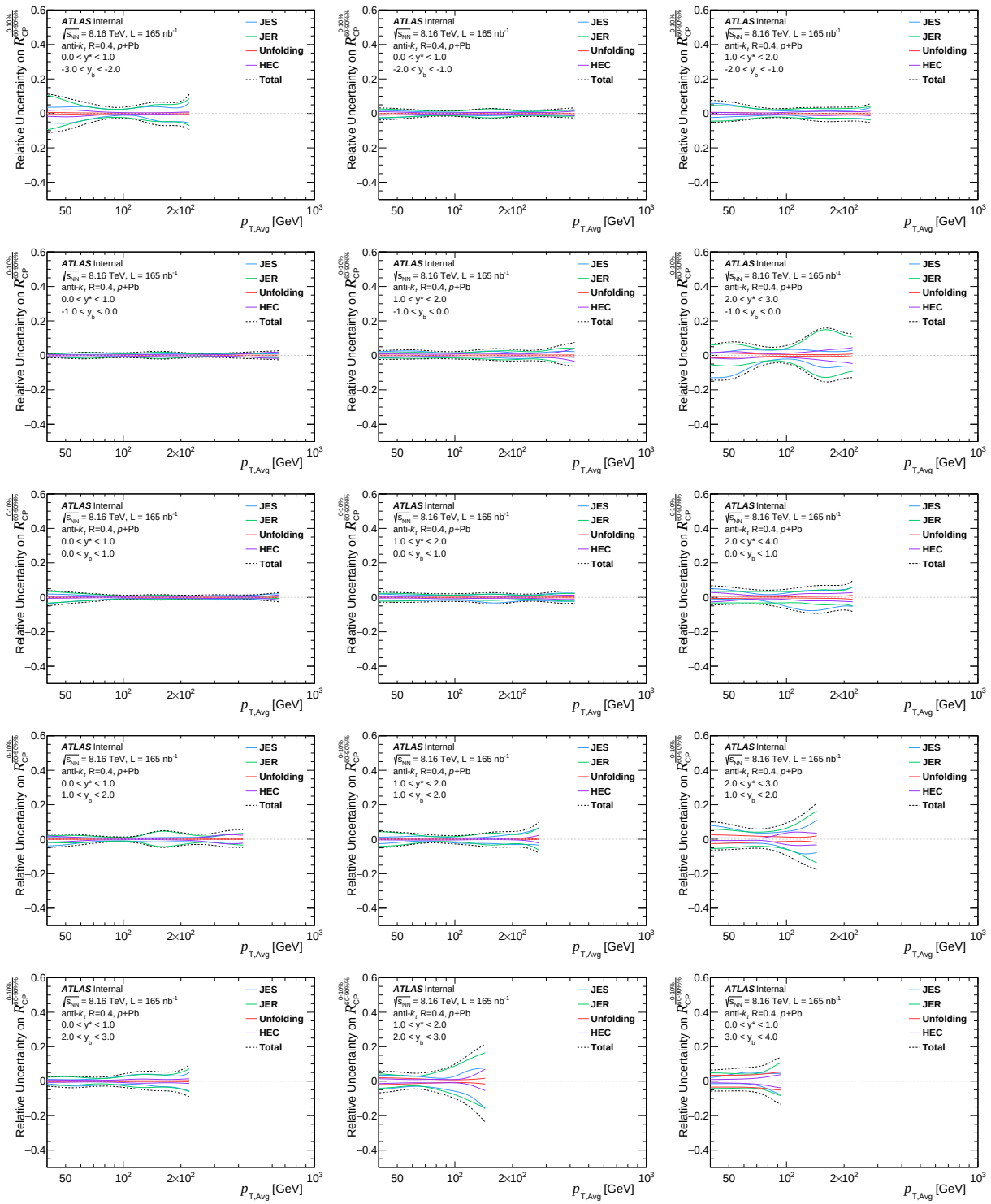

Figure 4.39: The systematic uncertainties on the R_{CP} measurement. Each panel shows the total systematic uncertainty (black dashed line), as well as the contributions from each source, namely the JES, JER, unfolding, and HEC sector exclusion. The T_{AB} uncertainty (not displayed) has a value of +12% and −19% in all bins for the standard Glauber model.

4.8 Results

This section presents results for the per-event dijet yield and R_{CP} in bins of $p_{\mathrm{T,Avg}}$, y_{b}, and y^* for $\sqrt{s_{\mathrm{NN}}} = 8.16$ TeV p+Pb collisions. These distributions are measured for pairs of leading and sub-leading jets in the average transverse momentum range of $40 < p_{\mathrm{T,Avg}} < 1000$ GeV. The boost of the dijet system and half rapidity separation are measured in the range [-3.0,4.0] and [0.0,4.0], respectively. A statistically weighted average was used to combine results from Period B and Period C. To compute the mean value and associated uncertainties in each kinematic bin, Equation 4.21 was used, where now x_i represents the per-event dijet yield in a given period. All results presented in this thesis, which make use of T_{AB} for geomtric scaling, are produced using the standard Glauber model.

4.8.1 Dijet Yield as a Function of $p_{\mathrm{T,Avg}}$

The measured 0–10% per-event dijet yield for negative and positive y_{b} is shown in Figure 4.40. The measured 60–90% per-event dijet yield for negative and positive y_{b} is shown in Figure 4.41. A scaling by powers of 10^{-2}, for each successive y_{b} bin, has been applied to the yields in order to improve the readability of the plots. The dijet yield decreases with increasing $p_{\mathrm{T,Avg}}$, y^*, and centrality,[2] with the highest yield observed for $0.0 < y_{\mathrm{b}} < 1.0$ and $0.0 < y^* < 1.0$ events. This topology corresponds to a dijet pair with minimal rapidity separation, such that $y_1^{\mathrm{CM}} \sim y_2^{\mathrm{CM}}$, with both tending to be slightly positive. Recall that there is a rapidity shift of $\Delta y = 0.465$ in the direction of the proton beam, due to the kinematics of the collision system, which is responsible for the observed asymmetry of the dijet yield between negative and positive y_{b} bins. This can be seen in Figure 4.42, where the distribution of y_1^{CM} vs y_2^{CM} is presented for each (y_{b}, y^*) bin.

[2] Central dijet yields are always higher than peripheral dijet yields only before geometric consideration are taken into account.

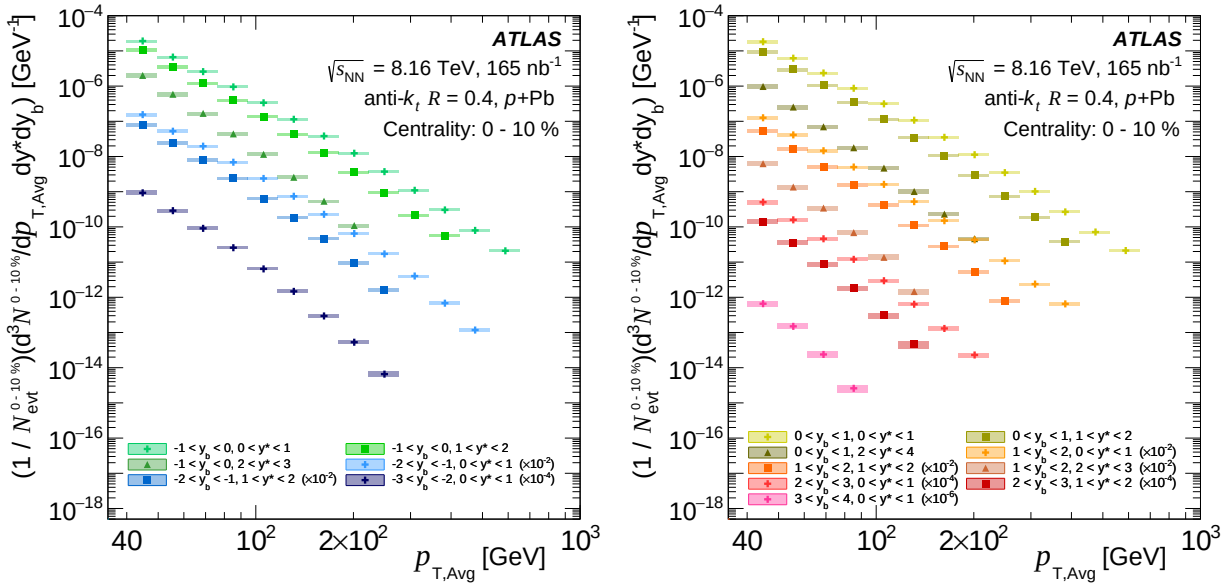

Figure 4.40: Triple differential per-event dijet yield in 0–10% p+Pb collisions as a function of $p_{\mathrm{T,Avg}}$ in different intervals of y^* for negative (left) and positive (right) y_{b} bins, scaled by successive powers of 10^{-2}. The proton-going direction is defined by $y_{\mathrm{b}} > 0$. Shaded rectangles represent the total systematic uncertainty, while the vertical error bars represent the statistical uncertainty.

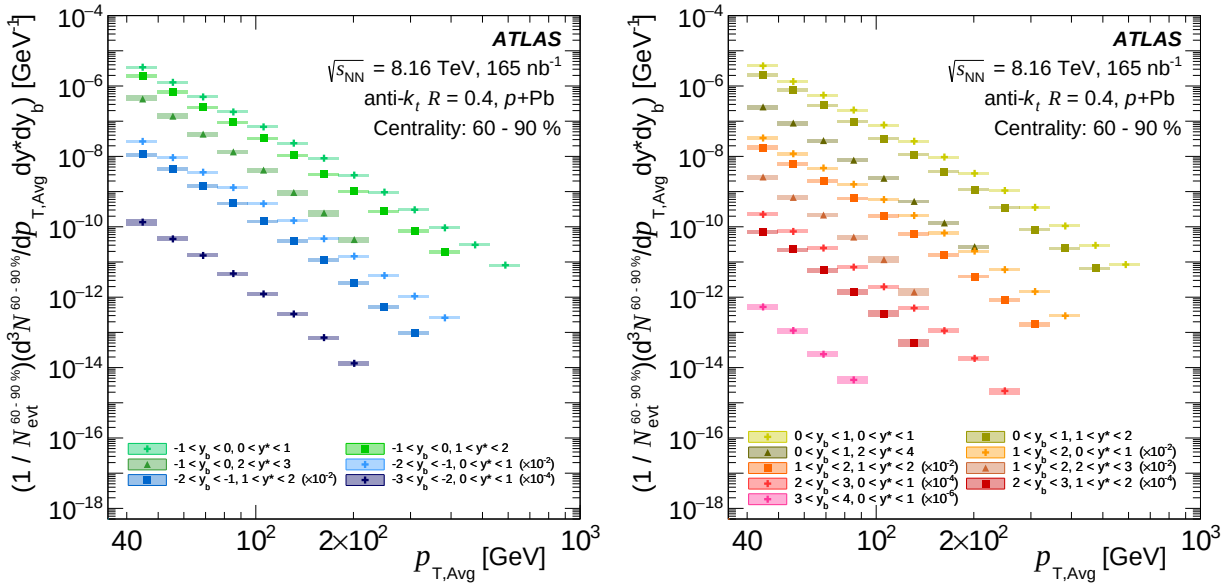

Figure 4.41: Triple differential per-event dijet yield in 60–90% p+Pb collisions as a function of $p_{\mathrm{T,Avg}}$ in different intervals of y^* for negative (left) and positive (right) y_{b} bins, scaled by successive powers of 10^{-2}. The proton-going direction is defined by $y_{\mathrm{b}} > 0$. Shaded rectangles represent the total systematic uncertainty, while the vertical error bars represent the statistical uncertainty.

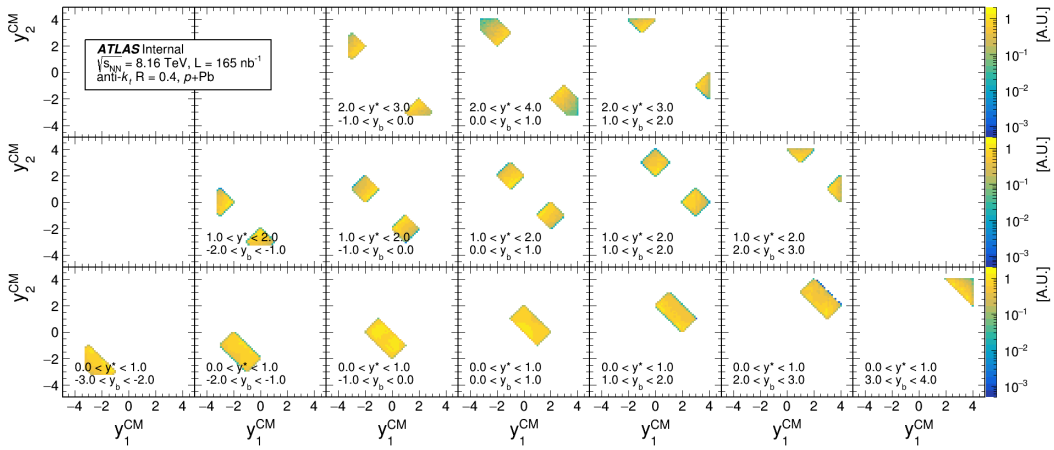

Figure 4.42: Distribution of y_1^{CM} vs y_2^{CM} for p+Pb data collected in 2016 prior to unfolding. The proton-going direction is defined by $y_{\mathrm{b}} > 0$. The sharp cuts observed in the y_1^{CM}-y_2^{CM} phase space are directly related to the fiducial requirements in y_{b} and y^* for each bin.

For completeness, the $\langle T_{\mathrm{AB}} \rangle$ normalized per-event dijet yield was also constructed integrating over the 0–90% centrality interval, defined as:

$$\rho^{0\text{–}90\%}(p_{\mathrm{T,Avg}}, y_{\mathrm{b}}, y^*) = \frac{1}{\langle T_{\mathrm{AB}}^{0\text{–}90\%} \rangle} \frac{1}{N_{\mathrm{evt}}^{0\text{–}90\%}} \frac{d^3 N^{0\text{–}90\%}}{dp_{\mathrm{T,Avg}} dy_{\mathrm{b}} dy^*}(p_{\mathrm{T,Avg}}, y_{\mathrm{b}}, y^*). \tag{4.25}$$

In this case, the normalization of the results, $N_{\mathrm{evt}}^{0\text{–}90\%}$, was computed by counting the number of minimum bias events sampled in each sub-period. This number is determined by the prescale-corrected set of recorded events which fire the `HLT_mb_sptrk` minimum bias trigger and that have a centrality classification within 0–90%. Formally,

$$N_{\mathrm{evt}}^{0\text{–}90\%} = \sum_{i \in (\mathrm{HLT\_mb\_sptrk}\ \&\ 0\text{–}90\%)} C_i, \tag{4.26}$$

where the sum is over recorded events meeting the conditions above and C_i is the `HLT_mb_sptrk` prescale set for the event. Events are also requested to pass the same non-jet related event selection applied for the analysis, see Section 4.3.1. With this method, the prescale-corrected number of `HLT_mb_sptrk` minimum bias p+Pb crossings was found to be $N_{evt}^{0\text{–}90\%} = 88.65 \times 10^9$ for Period B and $N_{evt}^{0\text{–}90\%} = 163.82 \times 10^9$ for Period C. The resulting 0–90% $\langle T_{\mathrm{AB}} \rangle$ normalized per-event dijet yield for negative and positive y_{b} is shown in Figure 4.43.

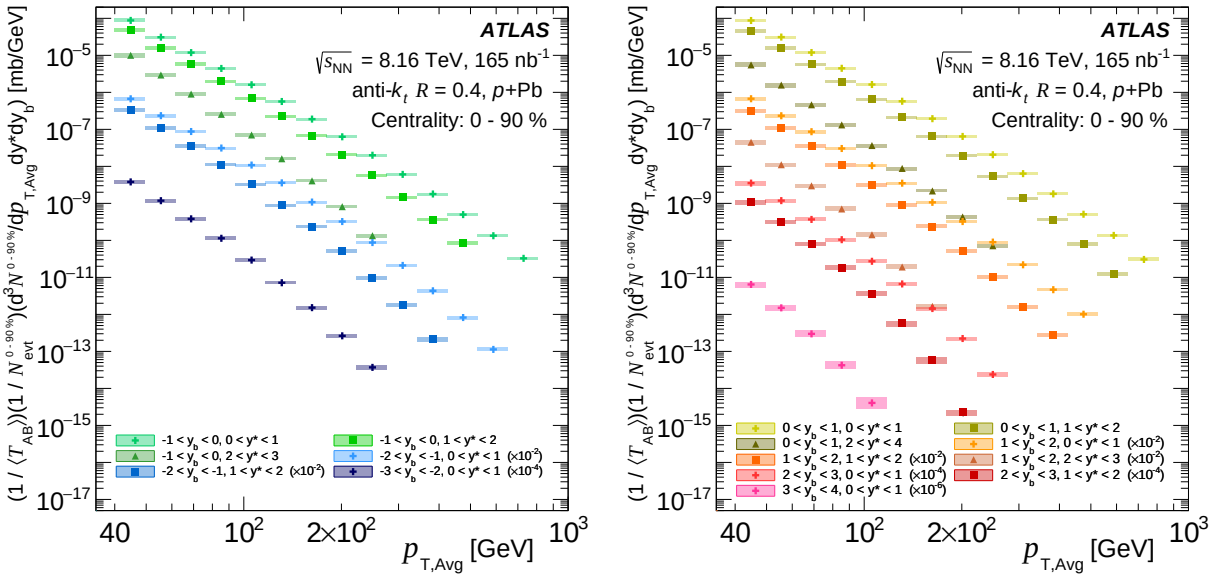

Figure 4.43: $\langle T_{\mathrm{AB}}\rangle$ normalized triple differential per-event dijet yield in 0–90% p+Pb collisions as a function of $p_{\mathrm{T,Avg}}$ in different intervals of y^* for negative (left) and positive (right) y_{b} bins, scaled by successive powers of 10^{-2}. The proton-going direction is defined by $y_{\mathrm{b}} > 0$. Shaded rectangles represent the total systematic uncertainty, while the vertical error bars represent the statistical uncertainty.

4.8.2 Dijet Yield as a Function of y_{b}

The unfolded per-event dijet yield, shown in Figures 4.40 and 4.41, can also be displayed as a function of y_{b} for individual $p_{\mathrm{T,Avg}}$ and y^* bins. Representative plots of the dijet yield, plotted as a function of $\langle y_{\mathrm{b}} \rangle$, are presented in Figure 4.44. Note that the yields are now normalised by $\langle T_{\mathrm{AB}} \rangle$ in order to facilitate a comparison between the central and peripheral results.

The mean y_{b} ($\mu_{y_{\mathrm{b}}}$) of the yields can then be calculated, for both central and peripheral results. In order to determine the uncertainty on the mean, the following steps are carried out separately for each centrality interval, y^* bin, and $p_{\mathrm{T,Avg}}$ bin:

1. Yields are shifted by 1σ for each systematic and $\mu_{y_{\mathrm{b}}}^{\mathrm{syst}}$ is determined
2. Difference between nominal and systematically shifted mean ($|\mu_{y_{\mathrm{b}}}$ - $\mu_{y_{\mathrm{b}}}^{\mathrm{syst}}|$) is taken as sytematic uncertainty on $\mu_{y_{\mathrm{b}}}$ for the given systematic
3. Separate systematics are added in quadrature to obtain the total systematic uncertainty on $\mu_{y_{\mathrm{b}}}$
4. A Gaussian with width equal to the statistical uncertainty on a given y_{b} bin is sampled and applied as a shift the yield
5. A new $\mu_{y_{\mathrm{b}}}^{\mathrm{stat}}$ is determined after all bins have been smeared
6. Steps 4 and 5 are repeated 1000 times, and the resulting $\mu_{y_{\mathrm{b}}}^{\mathrm{stat}}$ distribution is fit with a Gaussian, with the σ of the fit being taken as the statistical uncertainty on $\mu_{y_{\mathrm{b}}}$

Next, the difference between the $\mu_{y_{\mathrm{b}}}$ for the central and peripheral yields ($\mu_{y_{\mathrm{b}}}^{0-10\%}$ - $\mu_{y_{\mathrm{b}}}^{60-90\%}$) was taken. The individual systematics were treated as correlated or uncorrelated (see Table 4.12) when propagating them to the difference. The statistical uncertainty was taken as the quadratic sum of the statistical uncertainty on the central and peripheral $\mu_{y_{\mathrm{b}}}$. The results of this exercise are shown in Figure 4.45 for different y^* intervals. A shift from zero of the two distributions is observed in all the kinematic bins. This deviation is found to be monotonically decreasing as a function of $p_{\mathrm{T,Avg}}$ for peripheral yields in all the y^* ranges. Conversely, central yields show a shift from zero decreasing in magnitude with increasing $p_{\mathrm{T,Avg}}$ only in $0.0 < y^* < 1.0$. A moderate increase with $p_{\mathrm{T,Avg}}$ is observed in $1.0 < y^* < 2.0$, while in $2.0 < y^* < 4.0$ the shift goes from positive (low $p_{\mathrm{T,Avg}}$) to negative (high $p_{\mathrm{T,Avg}}$).

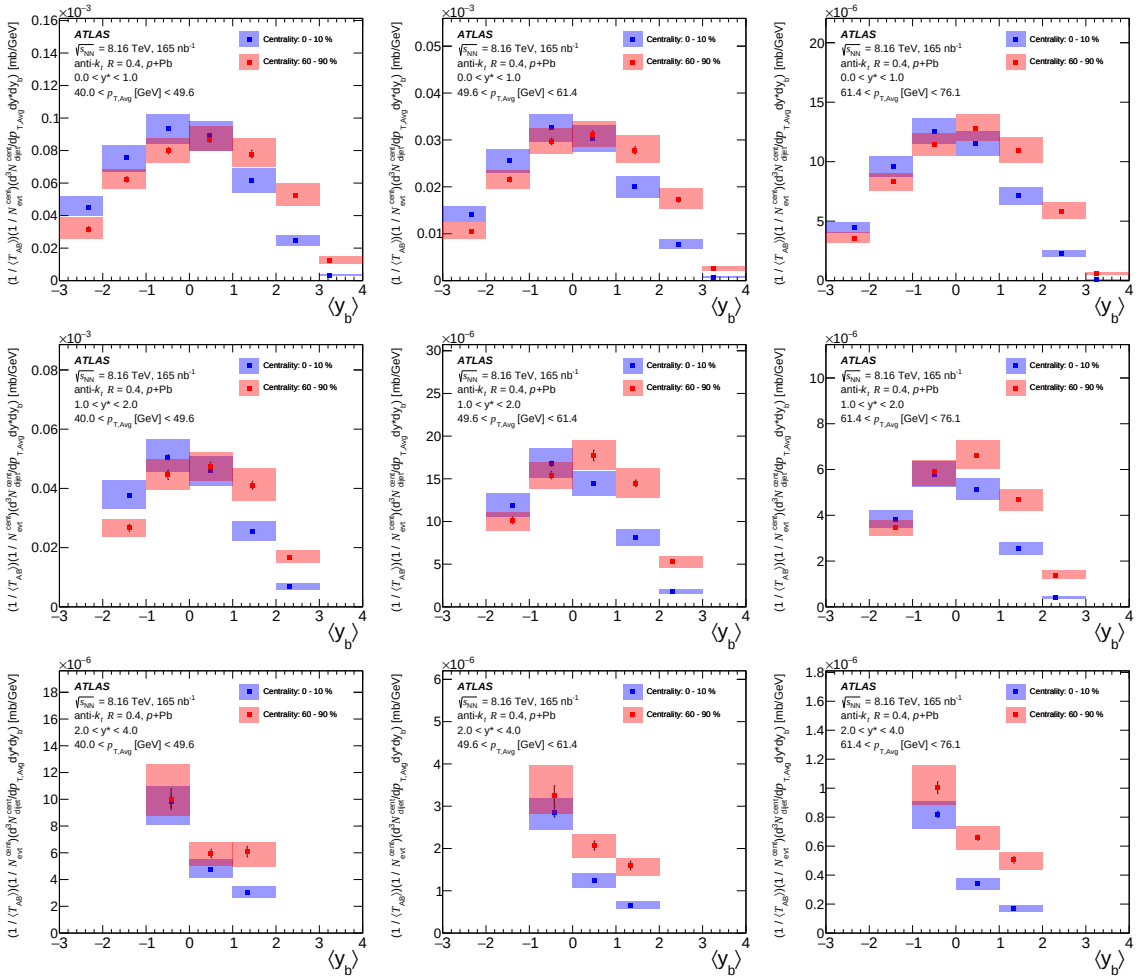

Figure 4.44: $\langle T_{\mathrm{AB}} \rangle$ normalized per-event dijet yields in 0–10% (blue) and 60–90% (red) collisions as a function of $\langle y_{\mathrm{b}} \rangle$ in three representative $p_{\mathrm{T,Avg}}$ bins for $0.0 < y^* < 1.0$ (top row), $1.0 < y^* < 2.0$ (middle row), $2.0 < y^* < 4.0$ (bottom row). Shaded rectangles represent the total systematic uncertainty, while the vertical error bars represent the statistical uncertainty. The systematic uncertainties for the two distributions are highly correlated.

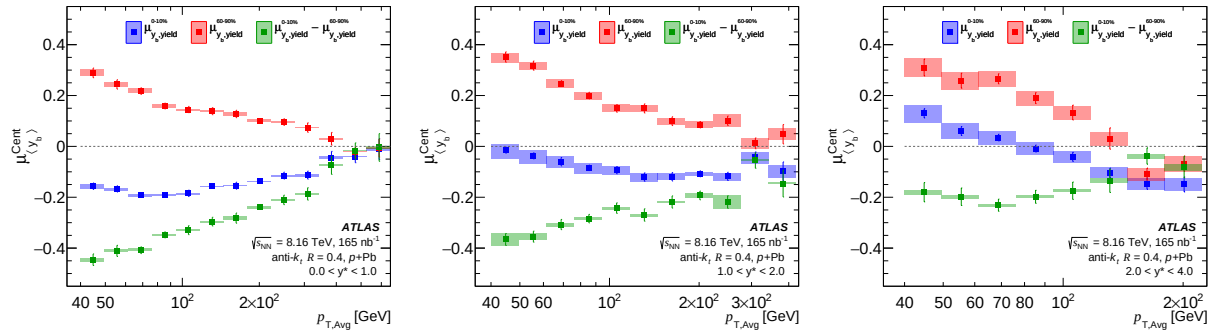

Figure 4.45: Mean of $\langle y_{\mathrm{b}} \rangle$ distribution of $\langle T_{\mathrm{AB}} \rangle$ normalized per-event dijet yields in 0–10% (blue) and 60–90% (red) collisions as a function of $p_{\mathrm{T,Avg}}$. The three panels represent different y^* bins. The difference between the blue and the red distribution is reported in green. Shaded rectangles represent the total systematic uncertainty, while the vertical error bars represent the statistical uncertainty.

4.8.3 Central-to-Peripheral Ratio as a Function of $p_{\mathrm{T,Avg}}$

An R_{CP} was constructed using Equation 4.8, to provide insights about the initial-state effects on the dijet production. As was previously noted, per-event dijet yields are used to construct the R_{CP} since there is no centrality-dependent measurement of the luminosity delivered and recorded by ATLAS. For this analysis, the per-event dijet yield, normalized to the number of minimum bias events, was used to construct the R_{CP}. This choice is particularly convenient, since the number of events is expected to scale with the centrality interval size, i.e. $N_{\mathrm{evt}}^{0-10\%} \simeq \frac{1}{3} N_{\mathrm{evt}}^{60-90\%}$. This expectation is directly derived from the definition of centrality. The nuclear thickness function T_{AB} was evaluated as discussed in Section 4.5.2. The two data-taking periods are combined after removing the dependence introduced by the different beam orientations in Periods B & C. In order to achieve this goal, the unfolded central and peripheral per-event dijet yield obtained in p+Pb (proton traveling towards negative rapidities) were first flipped in y_{b} (e.g. -4.0 $< y_{\mathrm{b}} <$ -3.0 became 3.0 $< y_{\mathrm{b}} <$ 4.0), and then combined with the corresponding centrality-dependent yield obtained from the Pb+p sample.

After this step, it was possible to construct the R_{CP}, making use of the full 2016 p+Pb dataset at 8.16 TeV. Bins with a relative statistical uncertainty greater than 40% have been removed from the per-event dijet yield result, and are therefore not present in the R_{CP} result. This was done in order to reject points at the edge of the phase space where limited statistics lead to less meaningful results. The combined R_{CP} results for the full 2016 p+Pb dataset at 8.16 TeV, obtained taking the ratio of central (0–10%) and peripheral (60–90%) dijet yield, are presented in successive y^* intervals in Figures 4.46, 4.47, and 4.48 as a function of $p_{\mathrm{T,Avg}}$, using the standard Glauber T_{AB} model. The R_{CP} shows a suppression in the dijet yield measured in central p+Pb collisions compared to peripheral ones. The suppression is dependent on $p_{\mathrm{T,Avg}}$, y_{b}, and y^*. In all the y^* intervals studied, the R_{CP} decreases with increasing $p_{\mathrm{T,Avg}}$. Furthermore, in a given $p_{\mathrm{T,Avg}}$ and y_{b} interval, the R_{CP} decreases with y^*. In addition, the R_{CP} is found to decrease while moving from backward to forward y_{b} intervals in a given y^* region.

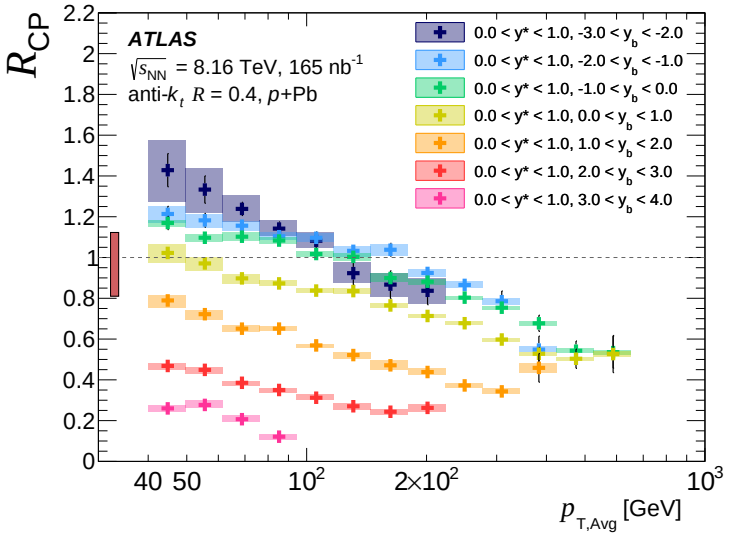

Figure 4.46: R_{CP} plotted as a function of the $p_{\mathrm{T,Avg}}$ in y^* bin [0.0,1.0], for different y_{b} bins. The proton-going direction is defined by $y_{\mathrm{b}} > 0$. Shaded rectangles represent the total systematic uncertainty, while the vertical error bars represent the statistical uncertainty. The solid rectangle on the left side of the panel represents the uncertainty on the T_{AB}.

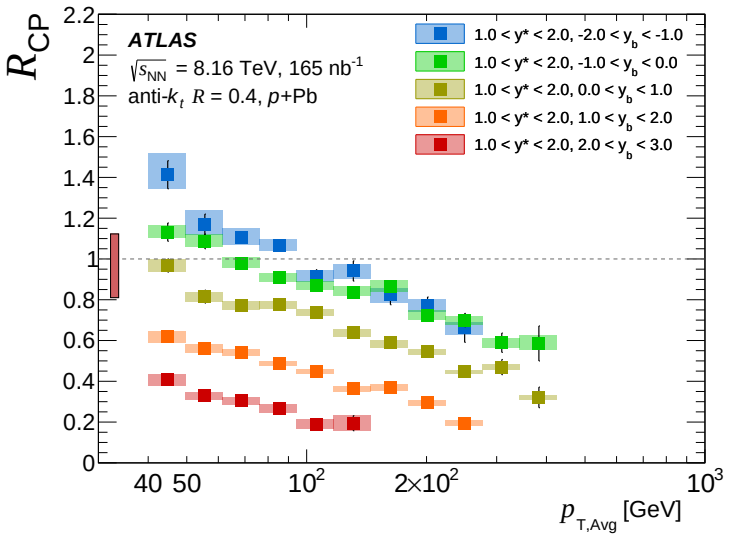

Figure 4.47: R_{CP} plotted as a function of the $p_{\mathrm{T,Avg}}$ in y^* bin [1.0,2.0], for different y_{b} bins. The proton-going direction is defined by $y_{\mathrm{b}} > 0$. Shaded rectangles represent the total systematic uncertainty, while the vertical error bars represent the statistical uncertainty. The solid rectangle on the left side of the panel represents the uncertainty on the T_{AB}.

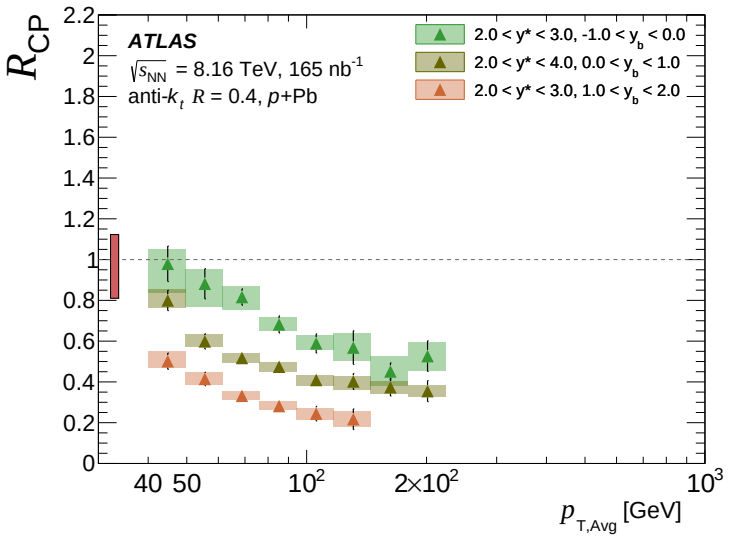

Figure 4.48: R_{CP} plotted as a function of the $p_{\mathrm{T,Avg}}$ in y^* bins [2.0,3.0] and [2.0,4.0], for different y_{b} bins. The proton-going direction is defined by $y_{\mathrm{b}} > 0$. Shaded rectangles represent the total systematic uncertainty, while the vertical error bars represent the statistical uncertainty. The solid rectangle on the left side of the panel represents the uncertainty on the T_{AB}.

4.8.4 Central-to-Peripheral Ratio as a Function of x_p and x_{Pb}

The triple-differential binning of this analysis allows for constraining the full kinematics of the partonic collision system using Equations 4.3, 4.4 and 4.5. An illustration of the x_p and x_{Pb} phase space probed in each kinematic bin defined in the analysis is reported in Figure 4.49. The approximation of the two partonic fractional momenta are constructed by re-scaling the central value of the $p_{\mathrm{T,Avg}}$ bin of each experimental point in Figures 4.46, 4.47, and 4.48 according to Equations 4.3 and 4.4, using the average $\langle y^* \rangle$ and $\langle y_{\mathrm{b}} \rangle$ values in the given kinematic bin. The values of $\langle y_{\mathrm{b}} \rangle$ and $\langle y^* \rangle$, used to rescale the x-axis, are taken as the mean of the y_{b} and y^* distributions in a given (y_{b}, y^*) bin, and are reported in Table 4.13. Figure 4.50 shows the results as a function of $\langle x_p \rangle$ (left) and $\langle x_{\mathrm{Pb}} \rangle$ (right). An inlay legend is included in both figures, indicating the color and marker used for each (y_{b}, y^*) bin. A distinct x_p-scaling of $R_{\mathrm{CP}}(x_p)$ is observed in the valence quark dominance region, characterized by a log-linear decreasing trend. No similar scaling is observed for smaller values of x_p, or for any region when R_{CP} is plotted as a function of x_{Pb}.

The results can also be plotted by segmenting the phase space in terms of x_{Pb}, allowing for one to display the dependence of the results as a function of x_p, as shown in Figure 4.51. A log-linear decreasing behavior with increasing x_p for low values of x_{Pb} is observed. This trend appears to be broken when approaching the valence region in the Pb ion.

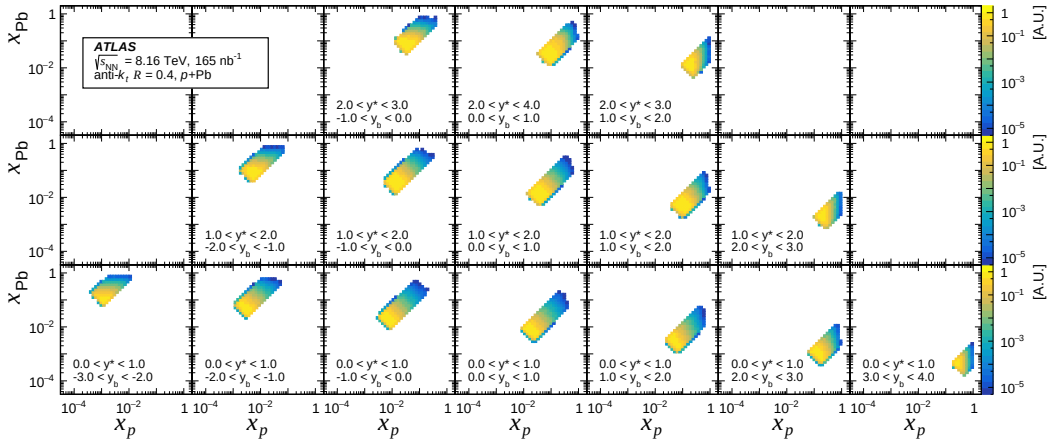

Figure 4.49: Distribution of x_{Pb} vs x_p for p+Pb data collected in 2016 prior to unfolding. The proton-going direction is defined by $y_{\mathrm{b}} > 0$. The sharp cuts observed in the x_p-x_{Pb} phase space are directly related to the fiducial requirements in y_{b} and y^* for each bin.

y^* \ y_{b}	**[-3.0:-2.0]**	**[-2.0:-1.0]**	**[-1.0:0.0]**	**[0.0:1.0]**	**[1.0:2.0]**	**[2.0:3.0]**	**[3.0:4.0]**
[2.0:3.0]	-	-	(-0.42,2.29)	(0.50,2.42)†	(1.33,2.26)	-	-
[1.0:2.0]	-	(-1.39,1.32)	(-0.50,1.37)	(0.48,1.40)	(1.45,1.41)	(2.30,1.30)	-
[0.0:1.0]	(-2.33,0.43)	(-1.45,0.49)	(-0.49,0.49)	(0.46,0.49)	(1.44,0.52)	(2.44,0.0.51)	(3.24,0.37)

Table 4.13: The average value of the dijet boost, $\langle y_{\mathrm{b}} \rangle$, and the half rapidity separation, $\langle y^* \rangle$, in each bin of (y_{b}, y^*). The values are used to rescale the $p_{\mathrm{T,Avg}}$ axis, according to Equations 4.3 and 4.4 to display the R_{CP} results as a function of x_p and x_{Pb}, respectively. The bin denoted by "†" has a maximum y^* of 4.0.

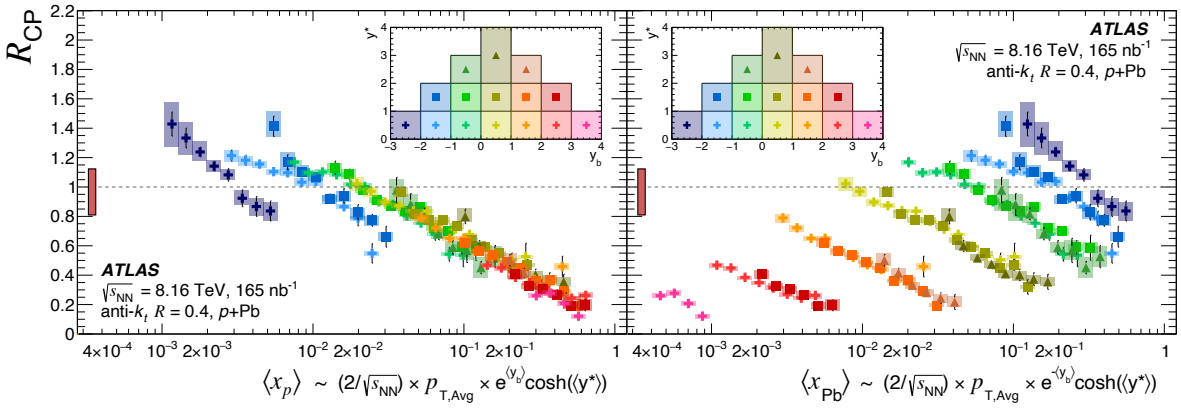

Figure 4.50: R_{CP} plotted as a function of approximated x_p (left panel) and x_{Pb} (right panel), constructed using $\langle y_{\mathrm{b}} \rangle$ and $\langle y^* \rangle$. An inset legend is included, showing the (y_{b}, y^*) bins, and their corresponding markers. The proton-going direction is defined by $y_{\mathrm{b}} > 0$. Shaded rectangles represent the total systematic uncertainty, while the vertical error bars represent the statistical uncertainty. The solid rectangle on the left-side of each panel represents the uncertainty on the T_{AB}.

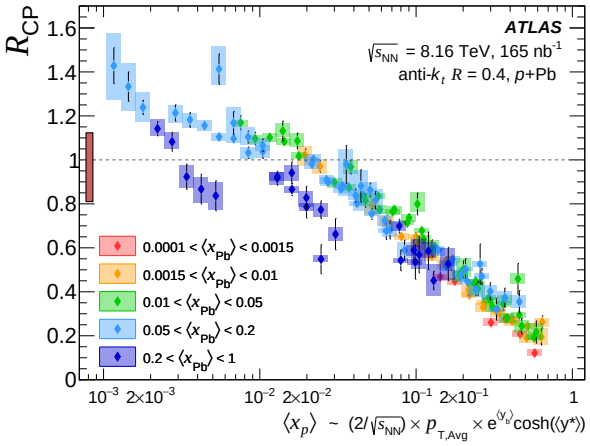

Figure 4.51: R_{CP} plotted as a function of approximated x_p, in different ranges of approximated x_{Pb}, both constructed using $\langle y_{\mathrm{b}} \rangle$ and $\langle y^* \rangle$. The proton-going direction is defined by $y_{\mathrm{b}} > 0$. Shaded rectangles represent the total systematic uncertainty, while the vertical error bars represent the statistical uncertainty. The solid rectangle on the left-side of the panel represents the uncertainty on the T_{AB}.

It is also possible to make use of the 20–40% centrality interval, defined in Figure 4.27 and Table 4.11, to construct a mid-central R_{CP}, as shown in Figure 4.52. As a result of centrality being defined using the minimum-bias FCal distribution, larger statistical uncertainties are present in the 20–40% centrality interval compared to the 0–10% interval, due to there being less statistics in the corresponding region of the dijet FCal distribution. A comparison between the 0–10%/60–90% and the 20–40%/60–90% R_{CP} is reported in Figure 4.53, for approximated x_p. Results are displayed only for the positive y_{b} region, where the parton originating from the proton has a momentum fraction typical of the valence region. Both R_{CP} distributions show a log-linear suppression with increasing x_p. As one would expect, the suppression observed for the 20–40% R_{CP} is milder compared to 0–10%.

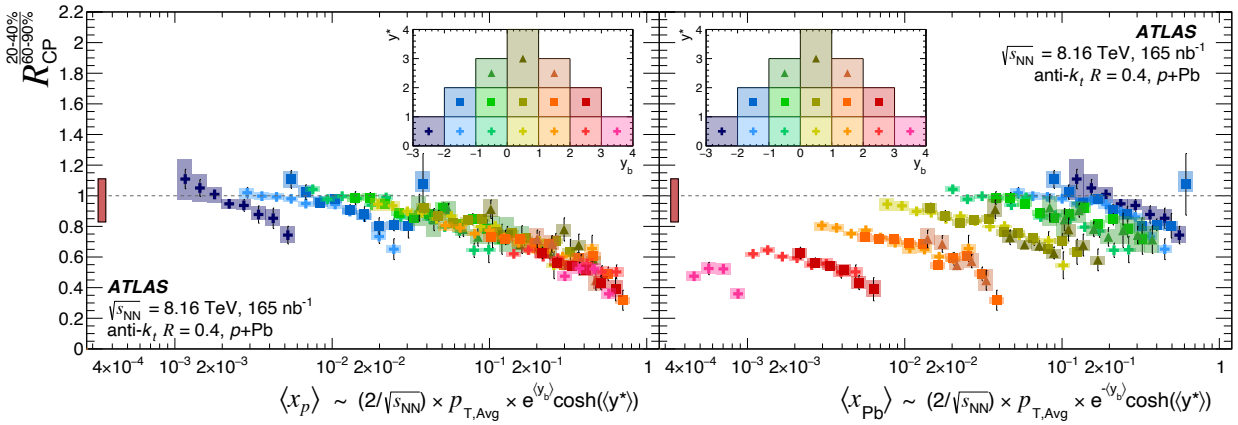

Figure 4.52: R_{CP} for mid-central collisions (20–40%/60–90%) plotted as a function of approximated x_p (left panel) and x_{Pb} (right panel), constructed using $\langle y_{\mathrm{b}} \rangle$ and $\langle y^* \rangle$. An inset legend is included, showing the (y_{b}, y^*) bins, and their corresponding markers. The proton-going direction is defined by $y_{\mathrm{b}} > 0$. Shaded rectangles represent the total systematic uncertainty, while the vertical error bars represent the statistical uncertainty. The solid rectangle on the left-side of each panel represents the uncertainty on the T_{AB}.

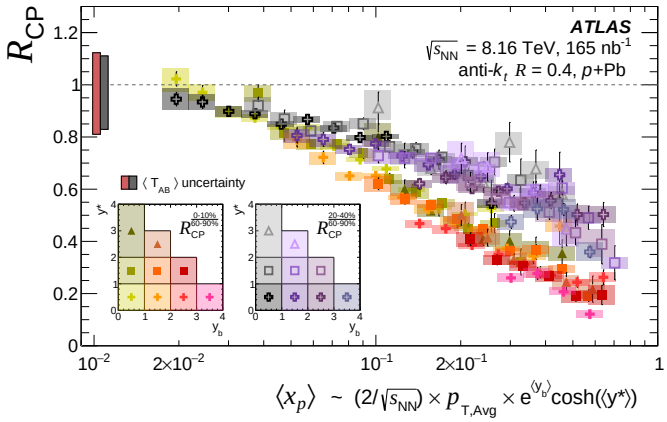

Figure 4.53: Positive y_{b} R_{CP} plotted as a function of approximated x_p for 0–10% (closed markers) and 20–40% (open markers) events, constructed using $\langle y_{\mathrm{b}} \rangle$ and $\langle y^* \rangle$. An inset legend is included for each R_{CP} showing the (y_{b}, y^*) bins, and their corresponding markers. The proton-going direction is defined by $y_{\mathrm{b}} > 0$. Shaded rectangles represent the total systematic uncertainty, while the vertical error bars represent the statistical uncertainty. The solid red (gray) rectangle on the left-side of the panel represents the uncertainty on the T_{AB} for the 0–10% (20–40%) R_{CP}.

4.8.5 Central-to-Peripheral Ratio as a Function of y_b

The R_{CP} can also be displayed as a function of $\langle y_b \rangle$ for different intervals of $p_{T,Avg}$. A selection of $\langle T_{AB} \rangle$ normalized per-event dijet yields in 0–10% and 60–90% collisions, plotted as a function of $\langle T_{AB} \rangle$, are shown in Figure 4.44. Using the full set of these distributions, Figures 4.54–4.58 can be constructed, which show $R_{CP}(\langle y_b \rangle)$ for increasing bins of $p_{T,Avg}$. As was observed for $R_{CP}(p_{T,Avg})$, but now plotted in a way that makes the behavior more prominent, the R_{CP} decreases with increasing y_b and y^* in all $p_{T,Avg}$ bins studied.

Analyzing the rapidity dependence of the results in Figure 4.50, a more substantial R_{CP} suppression is associated with larger values of y_b, corresponding to higher values of x_p. This observation is directly linked to a shift in the $\langle y_b \rangle$ dependence of the dijet yield measured in central and peripheral events. These results, as well as Figure 4.44, provide further interpretation to the dijet pseudorapidity measurement by CMS [84] (shown in Figure 2.20), where a shift in η_{dijet} distributions in different classes of forward transverse energy was observed.

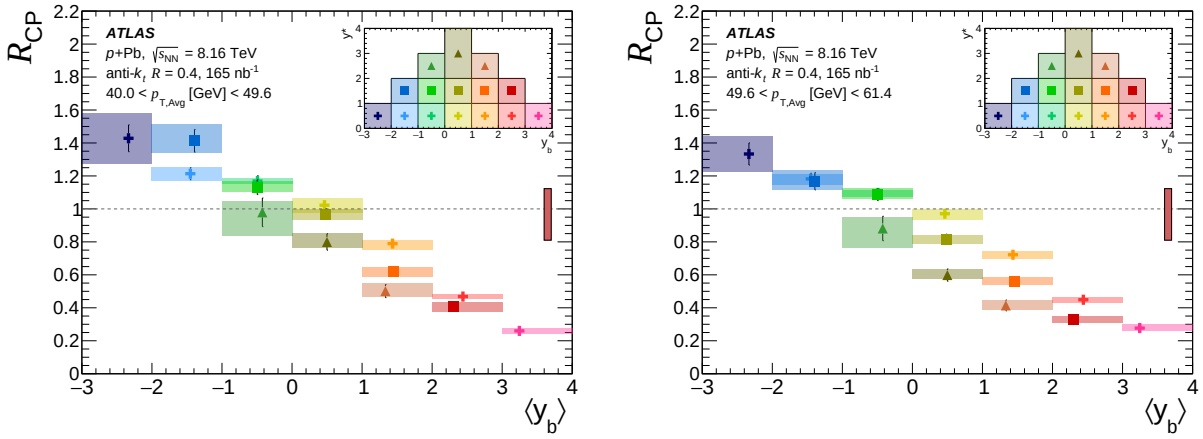

Figure 4.54: R_{CP} plotted as a function of the $\langle y_b \rangle$ for different values of y^*, and 40 GeV $< p_{T,Avg} <$ 49.6 GeV (left) and 49.6 GeV $< p_{T,Avg} <$ 61.4 GeV (right). An inset legend is included, showing the (y_b, y^*) bins, and their corresponding markers. This representation is analogous to the one used to display the results as a function of approximated x_p and x_{Pb}, and allows for direct interpretation of the $\langle y_b \rangle$ dependence in terms of the kinematics of the hard-scattering. The proton-going direction is defined by $y_b > 0$. Shaded rectangles represent the total systematic uncertainty, while the vertical error bars represent the statistical uncertainty. The solid rectangle on the right-side of the plot represents the uncertainty on the T_{AB}.

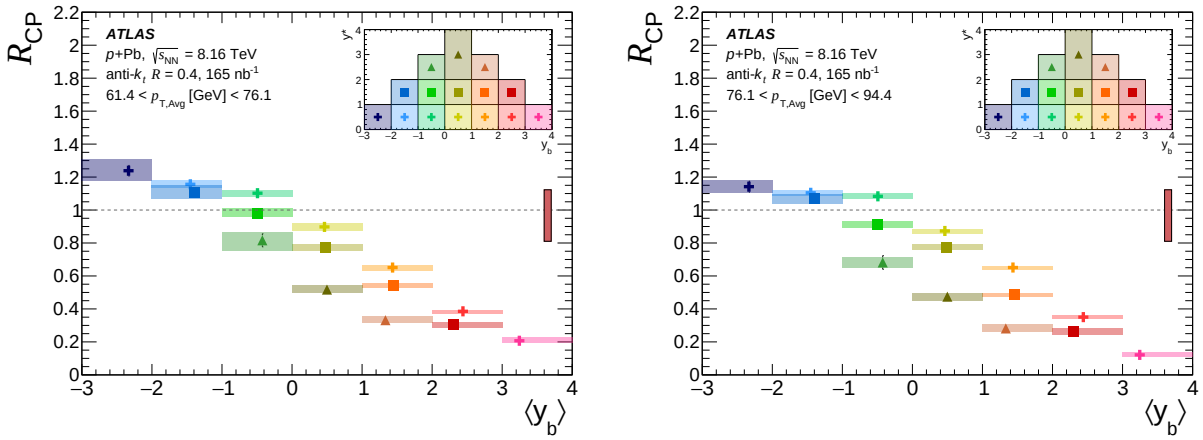

Figure 4.55: R_{CP} plotted as a function of the $\langle y_{\mathrm{b}} \rangle$ for different values of y^*, and 61.4 GeV $< p_{\mathrm{T,Avg}} <$ 76.1 GeV (left) and 76.1 GeV $< p_{\mathrm{T,Avg}} <$ 94.4 GeV (right). An inset legend is included, showing the (y_{b}, y^*) bins, and their corresponding markers. This representation is analogous to the one used to display the results as a function of approximated x_p and x_{Pb}, and allows for direct interpretation of the $\langle y_{\mathrm{b}} \rangle$ dependence in terms of the kinematics of the hard-scattering. The proton-going direction is defined by $y_{\mathrm{b}} > 0$. Shaded rectangles represent the total systematic uncertainty, while the vertical error bars represent the statistical uncertainty. The solid rectangle on the right-side of the plot represents the uncertainty on the T_{AB}.

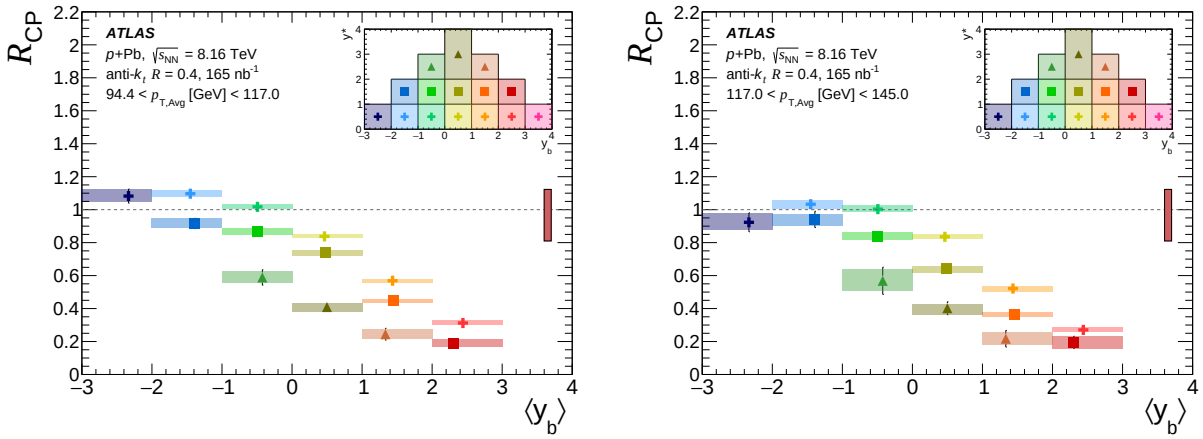

Figure 4.56: R_{CP} plotted as a function of the $\langle y_{\mathrm{b}} \rangle$ for different values of y^*, and 94.4 GeV $< p_{\mathrm{T,Avg}} <$ 117 GeV (left) and 117 GeV $< p_{\mathrm{T,Avg}} <$ 145 GeV (right). An inset legend is included, showing the (y_{b}, y^*) bins, and their corresponding markers. This representation is analogous to the one used to display the results as a function of approximated x_p and x_{Pb}, and allows for direct interpretation of the $\langle y_{\mathrm{b}} \rangle$ dependence in terms of the kinematics of the hard-scattering. The proton-going direction is defined by $y_{\mathrm{b}} > 0$. Shaded rectangles represent the total systematic uncertainty, while the vertical error bars represent the statistical uncertainty. The solid rectangle on the right-side of the plot represents the uncertainty on the T_{AB}.

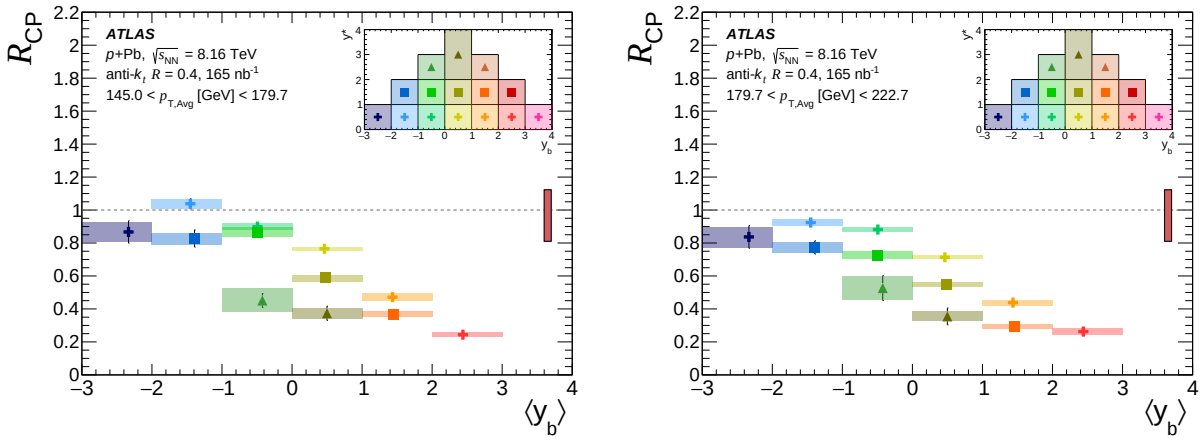

Figure 4.57: R_{CP} plotted as a function of the $\langle y_{\mathrm{b}} \rangle$ for different values of y^*, and 145 GeV $< p_{\mathrm{T,Avg}} <$ 179.7 GeV (left) and 179.7 GeV $< p_{\mathrm{T,Avg}} <$ 222.7 GeV (right). An inset legend is included, showing the (y_{b}, y^*) bins, and their corresponding markers. This representation is analogous to the one used to display the results as a function of approximated x_p and x_{Pb}, and allows for direct interpretation of the $\langle y_{\mathrm{b}} \rangle$ dependence in terms of the kinematics of the hard-scattering. The proton-going direction is defined by $y_{\mathrm{b}} > 0$. Shaded rectangles represent the total systematic uncertainty, while the vertical error bars represent the statistical uncertainty. The solid rectangle on the right-side of the plot represents the uncertainty on the T_{AB}.

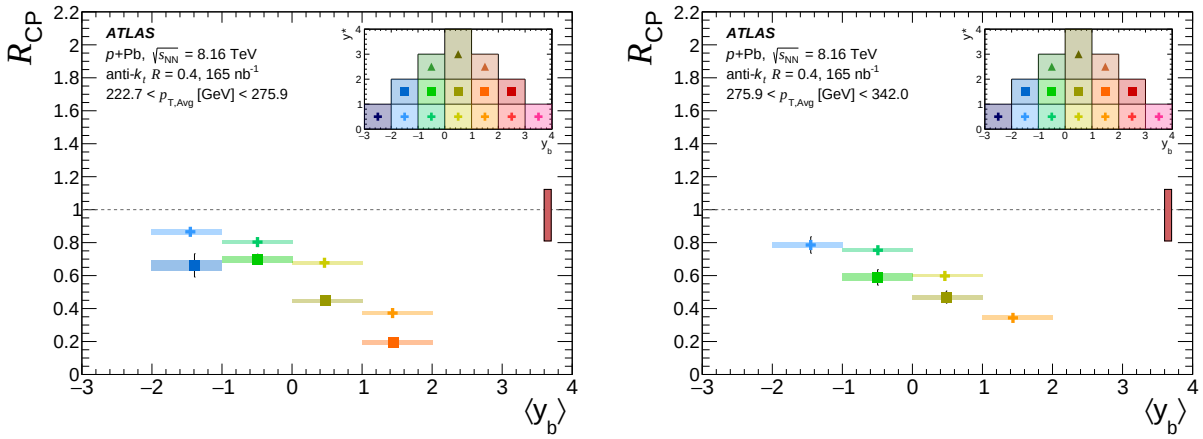

Figure 4.58: R_{CP} plotted as a function of the $\langle y_{\mathrm{b}} \rangle$ for different values of y^*, and 222.7 GeV $< p_{\mathrm{T,Avg}} <$ 275.9 GeV (left) and 275.9 GeV $< p_{\mathrm{T,Avg}} <$ 342 GeV (right). An inset legend is included, showing the (y_{b}, y^*) bins, and their corresponding markers. This representation is analogous to the one used to display the results as a function of approximated x_p and x_{Pb}, and allows for direct interpretation of the $\langle y_{\mathrm{b}} \rangle$ dependence in terms of the kinematics of the hard-scattering. The proton-going direction is defined by $y_{\mathrm{b}} > 0$. Shaded rectangles represent the total systematic uncertainty, while the vertical error bars represent the statistical uncertainty. The solid rectangle on the right-side of the plot represents the uncertainty on the T_{AB}.

4.8.6 Comparison to 5.02 TeV Results

As previously mentioned, ATLAS has published results for the p_{T} and rapidity dependence of inclusive jet production R_{CP} in p+Pb collisions at 5.02 TeV [152]. These results attracted considerable interest, and seeded a number of different models formulated to explain the observed centrality dependence of the jet production in p+Pb collisions, see for instance Refs. [154–156]. As explored in Section 2.2, thanks to complementary measurements like those carried out by ATLAS using dijets produced in pp collisions [157], the most plausible explanation for the observed R_{CP} suppression remains the one in terms of color transparency (CT) effects, described in Ref. [156].

By measuring only single jets in the final state, the 5.02 TeV p+Pb jet results did not provide access to the kinematics of the initial state. Conversely, a triple differential dijet measurement like the one presented in this thesis allows for direct characterization of the parton level kinematics of the initial state. It is therefore natural to ask whether the p+Pb R_{CP} results at 8.16 TeV can be mapped back to the 5.02 TeV results. In order to carry out such a comparison, the Feynman scaling variable [216], usually referred to as Feynman-x, or x_{F}, was used. Starting from the kinematics of the colliding partons, it can be expressed as

$$x_{\mathrm{F}} = x_p - x_{\mathrm{Pb}}, \tag{4.27}$$

where x_p and x_{Pb} are, in the case discussed in this thesis, given by Equations 4.3 and 4.4, respectively. The results previously shown in Figures 4.46, 4.47, and 4.48, where R_{CP} is plotted as a function of $p_{\mathrm{T,Avg}}$, were rescaled using the $\langle y_{\mathrm{b}} \rangle$ and $\langle y^* \rangle$ in a given (y_{b}, y^*) bin, and Equation 4.27. The results of this procedure are shown in Figure 4.59, where the x-axis is no longer plotted logarithmically, as the x_{F} distribution is defined between -1 and 1. A striking difference is observed between the R_{CP} for positive (x_p dominated) and negative (x_{Pb} dominated) x_{F} values. In collisions where the parton extracted from the proton carries most of the momentum fraction, the R_{CP} follows a very similar trend, regardless of y_{b} or y^*. Conversely, at negative values of x_{F}, where the parton extracted from the nucleus has the largest momentum fraction, the result seems to depend both on y_{b} and $p_{\mathrm{T,Avg}}$.

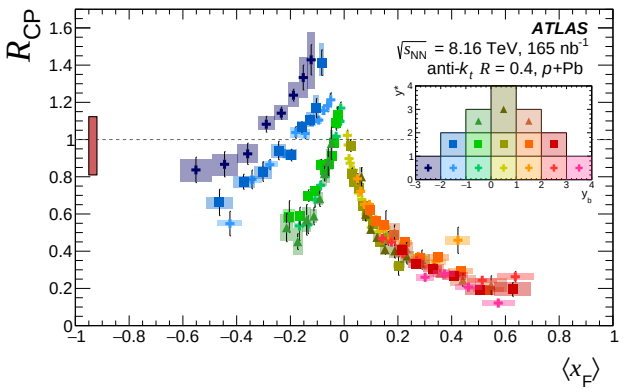

Figure 4.59: R_{CP} plotted as a function of approximated x_{F}, here indicated with $\langle x_{\mathrm{F}} \rangle$ and constructed using $\langle y_{\mathrm{b}} \rangle$ and $\langle y^* \rangle$. An inset legend is included, showing the (y_{b}, y^*) bins, and their corresponding markers. The proton-going direction is defined by $y_{\mathrm{b}} > 0$. Shaded rectangles represent the total systematic uncertainty, while the vertical error bars represent the statistical uncertainty. The solid rectangle on the left-side of the panel represents the uncertainty on the T_{AB}.

The Feynman scaling variable can also be defined as a property of the final state particle:

$$x_{\mathrm{F}} = \frac{2p_z}{\sqrt{s}} = \frac{2m_{\mathrm{T}} \times \sinh(\mathrm{y}^{\mathrm{CM}})}{\sqrt{s}} \simeq \frac{2p_{\mathrm{T}} \times \sinh(\mathrm{y}^{\mathrm{CM}})}{\sqrt{s}}, \tag{4.28}$$

where the final approximation was written recognizing that, for jets considered in this and the 5.02 TeV

analyses, it is possible to write $m_{\mathrm{T}} = \sqrt{m^2 + p_{\mathrm{T}}^2} \simeq p_{\mathrm{T}}$ with fairly good approximation.

Note that the 5.02 TeV results shown in Figure 2.16 are plotted as a function of $p_{\mathrm{T}} \times \cosh(\langle y^{\mathrm{CM}} \rangle)$. One can observe from Figure 4.60 that for positive values of x, $\cosh(x) \simeq \sinh(x)$, and for negative values of x, $\cosh(x) \simeq -\sinh(x)$. Therefore, if x_{F} scaling holds for the R_{CP}, the dijet results at positive values of x_{F} are expected to have a direct relation with the 5.02 TeV results at positive jet rapidity. On the other hand, the dependence of the 5.02 TeV jet results at negative values of rapidities can be directly mapped on the dijet results at negative x_{F} values if the abscissa sign is flipped (e.g. displaying them as a function of $-x_{\mathrm{F}}$). Once this operation is completed, a re-scaling of $\sqrt{s}/2$ (see Equation 4.28) is needed to achieve the full comparison.

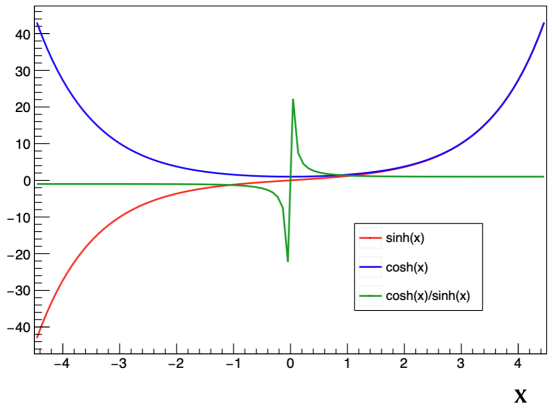

Figure 4.60: Demonstration of $\sinh(x)$ and $\cosh(x)$ functions in the abscissa range corresponding to ATLAS rapidity acceptance for jets.

The results of this exercise are shown in Figure 4.61, where the left and right panels show both the 5.02 TeV and 8.16 TeV R_{CP} results overlaid for positive and negative rapidity values, respectively. Qualitatively, a remarkable level of agreement is observed between the two measurements in the region where the major contribution to the kinematics is due to the parton extracted from the proton, corresponding to positive (di)jet rapidities and x_{F}. By looking at the left panel of Figure 4.50, one can see how these kinematic bins are associated to the proton valence region, where color fluctuation effects are supposed to be sizable due to the concentration of a considerable part of momentum on a single parton. In addition, the increasing suppression with x_p seems to corroborate this interpretation. Therefore, the agreement between the 5.02 TeV and 8.16 TeV results at positive values of x_{F} suggests that the underlying physics leading to the suppression of R_{CP} is the same for both 5.02 TeV and 8.16 TeV p+Pb collisions, and that it nicely scales with the Feynman variable. Conversely, if one looks at negative values of x_{F}, corresponding to kinematic bins where the initial momentum of the colliding particles is dominated by the Pb-originated parton, one can see how the agreement tends to progressively worsen towards backward rapidities. By looking at the right panel of Figure 4.50, one can see that the region where the agreement is worst corresponds to the valence region of x_{Pb}, where the R_{CP} results are the highest and tend to even exceed 1 in a kinematic region compatible with that of nuclear anti-shadowing [67]. Such an observation may suggest a relevance of nuclear effects in this kinematic regime. In addition, the x_p associated to these regions is definitively outside of the expected CT regime. It is also important to note that jets contributing to this kinematic region are typically nearer to the Pb-going side of the FCal, used to evaluate centrality. Therefore, a result of $R_{\mathrm{CP}} > 1$ may be interpreted in terms of a well-known pseudorapidity centrality bias [217, 218]. Note that this bias reduces with increasing gap between the range used for the centrality estimator and that used for the physics measurement. Therefore, no correction is applied in this analysis since the bias is expected to have marginal effect on the strong R_{CP} suppression observed at forward rapidities.

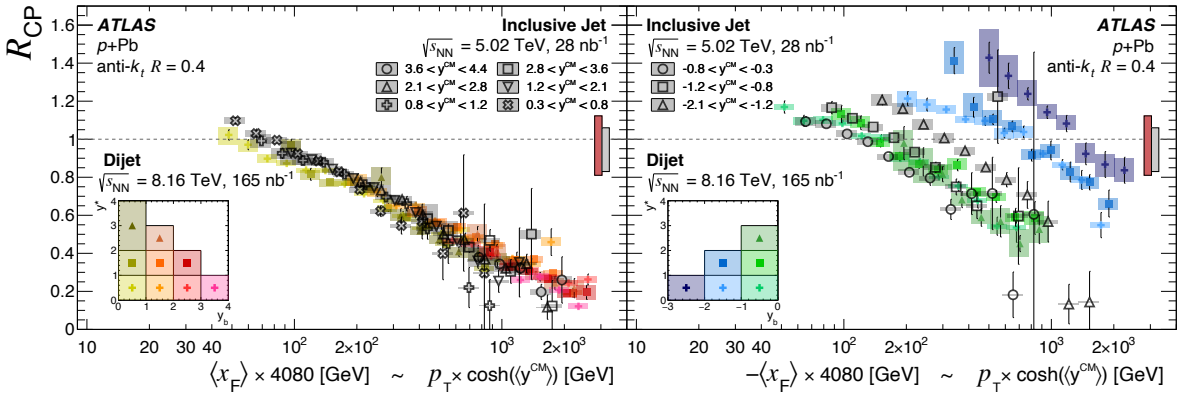

Figure 4.61: Dijet R_{CP} results from this Letter compared with inclusive jet R_{CP} at 5.02 TeV measured by ATLAS [152]. The dijet results are denoted by full markers and are reported as a function of $\pm\langle x_{\mathrm{F}} \rangle \times$ 4080 GeV, for positive (+, left panel) and negative (−, right panel) y_{b} (y^{CM}) results, respectively. An inset legend is included, showing the (y_{b}, y^*) bins, and their corresponding markers. The inclusive jet results are displayed as a function of $p_{\mathrm{T}} \times \cosh(\langle y^{\mathrm{CM}} \rangle)$ and use open markers. Shaded rectangles represent the total systematic uncertainty, while the vertical error bars represent the statistical uncertainty. The uncertainties on the T_{AB} on the dijet (inclusive jet) results are reported using the left (right) solid rectangle on the right side of each panel. The 5.02 TeV data for $-0.3 < y^{\mathrm{CM}} < 0.3$ was omitted since it belongs to the transition region between the two panels.

Chapter 5

Summary

This thesis presents a measurement of the centrality dependence of the triple-differential dijet yield using 165 nb^{-1} of p+Pb data collected at $\sqrt{s_{\text{NN}}} = 8.16$ TeV by ATLAS in 2016. The yields are measured in different centrality intervals as a function of the average transverse momentum of the jet pair, and the boost and half rapidity separation of the dijet system. The dijet $p_{\text{T,Avg}}$ spans 40 to 1000 GeV, while y_{b} and y^* are measured from -3.0 to 4.0 and 0.0 to 4.0, respectively. The event centrality is characterized by the total transverse energy measured in the Pb-going calorimeter near to the beam axis. A central-to-peripheral ratio of the dijet yields is then constructed, taking into account geometrical scaling, and the results are presented as a function of variables that approximate the kinematics of the initial hard parton-parton scattering process. Previous jet measurements in p+Pb collisions at 5.02 TeV, carrying out similar investigations, did not have full access to the kinematics of the initial state [152], or were not differential enough to do so [84], making this the first analysis to provide access to the centrality dependence of dijets as a function of the hard-scattering kinematics in p+Pb collisions. The measurement presented in this thesis, unfolded over a broad kinematic range, covering from the valence region down to $x_p \sim 10^{-3}$ and $x_{\text{Pb}} \sim 4 \cdot 10^{-4}$, provides an unprecedented input to advancing our understanding of p+A interactions.

The R_{CP} shows a scaling with the Bjorken-x of the parton originating from the proton, x_p, while no such trend is observed as a function of x_{Pb}. The results at 8.16 TeV are compared to a previous, less differential, analysis at 5.02 TeV by using the Feynman variable x_{F}. A remarkable level of agreement is observed in the valence dominance region of the proton, where color transparency effects are predicted to be significant. These results represent a unique input to further understand initial-state x_p-dependent color fluctuation effects in p+A collisions, where small proton configurations are characterized by a reduced interaction strength that results in less soft proton-nucleus collisions and, therefore, a biased centrality. The results obtained from the two datasets start to diverge when approaching the kinematic region where the momentum exchange is dominated by the parton originating from the Pb nucleus. This observation may suggest a relevant energy dependence of nuclear effects in this kinematic regime, and further highlights the importance of this measurement in improving our understanding of additional initial-state effects beyond color transparency in p+A collisions.

A universal understanding of color transparency requires detailed studies of these effects in lepton-nucleon interactions, where they are expected to manifest as an enhancement of so-called nuclear transparency. The future Electron-Ion Collider at Brookhaven National Lab will offer unparalleled opportunities to carry out these measurements and further advance the global understanding of color transparency effects.

References

[1] ATLAS Collaboration, *Observation of a new particle in the search for the Standard Model Higgs boson with the ATLAS detector at the LHC*, Phys. Lett. B **716** (2012) 1, arXiv: 1207.7214 [hep-ex] (cit. on p. 1).

[2] CMS Collaboration,
Observation of a new boson at a mass of 125 GeV with the CMS experiment at the LHC,
Phys. Lett. B **716** (2012) 30, arXiv: 1207.7235 [hep-ex] (cit. on p. 1).

[3] W. Commons,
File:Standard Model of Elementary Particles.svg — Wikimedia Commons, the free media repository,
[Online; accessed 17-January-2022], 2021,
URL: https://commons.wikimedia.org/w/index.php?title=File:Standard_Model_of_Elementary_Particles.svg&oldid=617661156 (cit. on p. 2).

[4] M. Planck, *Über eine Verbesserung der Wienschen Spektralgleichung. (German) [On an Improvement of Wien's Equation for the Spectrum]*, German, Verhandl. Dtsch. phys. Ges. **2** (1900) 202,
ISSN: 0372-5448 (cit. on p. 2).

[5] M. Planck, *Zur Theorie des Gesetzes der Energieverteilung im Normalspektrum. (German) [On the Theory of Distribution of Energy in the Normal Spectrum]*, German,
Verhandl. Dtsch. phys. Ges. **2** (1900) 237, ISSN: 0372-5448 (cit. on p. 2).

[6] P. Lenard, *Ueber die lichtelektrische Wirkung*, Annalen der Physik **313** (1902) 149 (cit. on p. 2).

[7] A. Einstein,
Über einen die Erzeugung und Verwandlung des Lichtes betreffenden heuristischen Gesichtspunkt. (German) [On a Heuristic Point of View Concerning the Production and Transformation of Light],
Annalen der Physik **322** (1905) 132 (cit. on p. 2).

[8] A. Einstein, *Die Plancksche Theorie der Strahlung und die Theorie der spezifischen Wärme. (German) [Planck's theory of radiation and the theory of specific heat]*,
Ann. Phys. (Berlin) **327** (1907) 180, ISSN: 0003-3804 (print), 1521-3889 (electronic) (cit. on p. 2).

[9] A. H. Compton, *A Quantum Theory of the Scattering of X-rays by Light Elements*,
Phys. Rev. **21** (5 1923) 483, URL: https://link.aps.org/doi/10.1103/PhysRev.21.483
(cit. on p. 2).

[10] E. Schrödinger, *An Undulatory Theory of the Mechanics of Atoms and Molecules*,
Phys. Rev. **28** (6 1926) 1049, URL: https://link.aps.org/doi/10.1103/PhysRev.28.1049
(cit. on p. 2).

[11] W. Heisenberg,
Physikalische Prinzipien der Quantentheorie. (German) [The Physical Principles of Quantum Theory],
Leipzig: Hirzel, 1930 (cit. on p. 2).

[12] R. P. Feynman, *Space - time approach to quantum electrodynamics*,
Phys. Rev. **76** (1949) 769, ed. by L. M. Brown (cit. on p. 3).

[13] P. A. M. Dirac, *The quantum theory of the electron*, Proc. Roy. Soc. Lond. A **117** (1928) 610
(cit. on p. 3).

[14] S. Tomonaga, *On a relativistically invariant formulation of the quantum theory of wave fields*,
Prog. Theor. Phys. **1** (1946) 27 (cit. on p. 3).

[15] J. S. Schwinger, *On Quantum electrodynamics and the magnetic moment of the electron*,
Phys. Rev. **73** (1948) 416 (cit. on p. 3).

[16] D. J. Griffiths, *Introduction to Elementary Particles*, United States: John Wiley & Sons, 1987,
ISBN: 0-471-60386-4 (cit. on pp. 3, 4, 6).

[17] M. Thomson, *Modern Particle Physics*, Cambridge University Press, 2013 (cit. on pp. 3, 7).

[18] S. Weinberg, *A Model of Leptons*, Phys. Rev. Lett. **19** (21 1967) 1264,
URL: https://link.aps.org/doi/10.1103/PhysRevLett.19.1264 (cit. on p. 4).

[19] S. L. Glashow, *Partial-symmetries of weak interactions*, Nuclear Physics **22** (1961) 579,
ISSN: 0029-5582 (cit. on p. 4).

[20] A. Salam, *Weak and Electromagnetic Interactions*, Conf. Proc. C **680519** (1968) 367 (cit. on p. 4).

[21] G. 't Hooft and M. Veltman, *Regularization and renormalization of gauge fields*,
Nuclear Physics B **44** (1972) 189, ISSN: 0550-3213 (cit. on p. 4).

[22] M. Gell-Mann, *A Schematic Model of Baryons and Mesons*, Phys. Lett. **8** (1964) 214
(cit. on pp. 4, 22).

[23] G. Zweig, *An SU_3 model for strong interaction symmetry and its breaking; Version 2*, (1964),
URL: https://cds.cern.ch/record/570209 (cit. on pp. 4, 22).

[24] E. D. Bloom et al., *High-Energy Inelastic e p Scattering at 6-Degrees and 10-Degrees*,
Phys. Rev. Lett. **23** (1969) 930 (cit. on pp. 4, 6).

[25] M. Breidenbach et al., *Observed behavior of highly inelastic electron-proton scattering*,
Phys. Rev. Lett. **23** (1969) 935 (cit. on pp. 4, 6).

[26] E. Rutherford, *The scattering of alpha and beta particles by matter and the structure of the atom*,
Phil. Mag. Ser. 6 **21** (1911) 669 (cit. on p. 5).

[27] J. D. Bjorken, *Asymptotic Sum Rules at Infinite Momentum*, Phys. Rev. **179** (5 1969) 1547,
URL: https://link.aps.org/doi/10.1103/PhysRev.179.1547 (cit. on p. 5).

[28] C. G. Callan and D. J. Gross,
High-Energy Electroproduction and the Constitution of the Electric Current,
Phys. Rev. Lett. **22** (4 1969) 156, URL: https://link.aps.org/doi/10.1103/PhysRevLett.22.156
(cit. on p. 5).

[29] J. B. Kogut and L. Susskind, *The Parton picture of elementary particles*, Phys. Rept. **8** (1973) 75
(cit. on p. 5).

[30] W. Bartel et al.,
Observation of Planar Three Jet Events in e+ e- Annihilation and Evidence for Gluon Bremsstrahlung,
Phys. Lett. B **91** (1980) 142 (cit. on p. 5).

[31] D. P. Barber et al.,
Discovery of Three Jet Events and a Test of Quantum Chromodynamics at PETRA Energies,
Phys. Rev. Lett. **43** (1979) 830 (cit. on p. 5).

[32] C. Berger et al., *Evidence for Gluon Bremsstrahlung in e+ e- Annihilations at High-Energies*,
Phys. Lett. B **86** (1979) 418 (cit. on p. 5).

[33] R. Brandelik et al., *Evidence for Planar Events in e+ e- Annihilation at High-Energies*,
Phys. Lett. B **86** (1979) 243 (cit. on p. 5).

[34] A. Bodek et al., *Experimental Studies of the Neutron and Proton Electromagnetic Structure Functions*,
Phys. Rev. D **20** (1979) 1471 (cit. on p. 6).

[35] J. Schwinger, *On Gauge Invariance and Vacuum Polarization*, Phys. Rev. **82** (5 1951) 664,
URL: https://link.aps.org/doi/10.1103/PhysRev.82.664 (cit. on p. 6).

[36] P. D. Group and R. L. Workman, *Review of Particle Physics*,
Progress of Theoretical and Experimental Physics **2022** (2022) 083C01, ISSN: 2050-3911,
URL: https://doi.org/10.1093/ptep/ptac097 (cit. on pp. 6, 35).

[37] D. J. Gross and F. Wilczek, *Ultraviolet Behavior of Non-Abelian Gauge Theories*,
Phys. Rev. Lett. **30** (26 1973) 1343,
URL: https://link.aps.org/doi/10.1103/PhysRevLett.30.1343 (cit. on p. 7).

[38] B. Andersson, G. Gustafson, G. Ingelman, and T. Sjöstrand,
Parton fragmentation and string dynamics, Phys. Rept. **97** (1983) 31 (cit. on p. 7).

[39] J. C. Collins, D. E. Soper, and G. F. Sterman, *Factorization of Hard Processes in QCD*,
Adv. Ser. Direct. High Energy Phys. **5** (1989) 1, arXiv: hep-ph/0409313 (cit. on p. 7).

[40] G.-Y. Qin and X.-N. Wang, *Jet quenching in high-energy heavy-ion collisions*,
Int. J. Mod. Phys. E **24** (2015) 1530014, ed. by X.-N. Wang, arXiv: 1511.00790 [hep-ph]
(cit. on pp. 8, 15).

[41] R. Atkin, *Review of jet reconstruction algorithms*,
Journal of Physics: Conference Series **645** (2015) 012008,
URL: https://dx.doi.org/10.1088/1742-6596/645/1/012008 (cit. on p. 10).

[42] UA1 Collaboration, *Hadronic jet production at the CERN proton-antiproton collider*,
Physics Letters B **132** (1983) 214, ISSN: 0370-2693 (cit. on p. 10).

[43] G. C. Blazey et al., "Run II jet physics",
Physics at Run II: QCD and Weak Boson Physics Workshop: Final General Meeting, 2000 47,
arXiv: hep-ex/0005012 (cit. on p. 10).

[44] G. P. Salam and G. Soyez, *A Practical Seedless Infrared-Safe Cone jet algorithm*,
JHEP **05** (2007) 086, arXiv: 0704.0292 [hep-ph] (cit. on p. 10).

[45] S. Catani, Y. L. Dokshitzer, M. H. Seymour, and B. R. Webber,
Longitudinally invariant K_t clustering algorithms for hadron hadron collisions,
Nucl. Phys. B **406** (1993) 187 (cit. on p. 11).

[46] Y. L. Dokshitzer, G. D. Leder, S. Moretti, and B. R. Webber, *Better jet clustering algorithms*, JHEP **08** (1997) 001, arXiv: hep-ph/9707323 (cit. on p. 11).

[47] M. Cacciari, G. P. Salam, and G. Soyez, *The anti-k_t jet clustering algorithm*, JHEP **04** (2008) 063, arXiv: 0802.1189 [hep-ph] (cit. on pp. 11, 43).

[48] M. Cacciari, G. P. Salam, and G. Soyez, *FastJet user manual*, Eur. Phys. J. C **72** (2012) 1896, arXiv: 1111.6097 [hep-ph] (cit. on p. 11).

[49] A. Accardi et al.,
Electron Ion Collider: The Next QCD Frontier: Understanding the glue that binds us all,
Eur. Phys. J. A **52** (2016) 268, ed. by A. Deshpande, Z. E. Meziani, and J. W. Qiu,
arXiv: 1212.1701 [nucl-ex] (cit. on p. 12).

[50] H. Abramowicz and A. Caldwell, *HERA collider physics*, Rev. Mod. Phys. **71** (1999) 1275,
arXiv: hep-ex/9903037 (cit. on p. 12).

[51] K. Kutak and S. Sapeta,
Gluon saturation in dijet production in p-Pb collisions at Large Hadron Collider,
Phys. Rev. D **86** (2012) 094043, arXiv: 1205.5035 [hep-ph] (cit. on p. 12).

[52] A. H. Mueller and J.-w. Qiu, *Gluon Recombination and Shadowing at Small Values of x*,
Nucl. Phys. B **268** (1986) 427 (cit. on p. 12).

[53] J. L. Albacete and C. Marquet,
Gluon saturation and initial conditions for relativistic heavy ion collisions,
Prog. Part. Nucl. Phys. **76** (2014) 1, arXiv: 1401.4866 [hep-ph] (cit. on p. 12).

[54] H. Abramowicz et al., *Combination of measurements of inclusive deep inelastic $e^{\pm}p$ scattering cross sections and QCD analysis of HERA data*, Eur. Phys. J. C **75** (2015) 580,
arXiv: 1506.06042 [hep-ex] (cit. on p. 13).

[55] *Review of Particle Physics*, Phys. Rev. D **98** (3 2018) 030001,
URL: https://link.aps.org/doi/10.1103/PhysRevD.98.030001 (cit. on p. 13).

[56] G. Altarelli and G. Parisi, *Asymptotic Freedom in Parton Language*, Nucl. Phys. B **126** (1977) 298
(cit. on p. 13).

[57] Y. L. Dokshitzer, *Calculation of the Structure Functions for Deep Inelastic Scattering and e+ e- Annihilation by Perturbation Theory in Quantum Chromodynamics.*, Sov. Phys. JETP **46** (1977) 641
(cit. on p. 13).

[58] V. N. Gribov and L. N. Lipatov, *Deep inelastic e p scattering in perturbation theory*,
Sov. J. Nucl. Phys. **15** (1972) 438 (cit. on p. 13).

[59] I. I. Balitsky and L. N. Lipatov, *The Pomeranchuk Singularity in Quantum Chromodynamics*,
Sov. J. Nucl. Phys. **28** (1978) 822 (cit. on p. 13).

[60] E. A. Kuraev, L. N. Lipatov, and V. S. Fadin,
The Pomeranchuk Singularity in Nonabelian Gauge Theories, Sov. Phys. JETP **45** (1977) 199
(cit. on p. 13).

[61] G. Aad et al., *Measurement of the inclusive jet cross-section in proton-proton collisions at $\sqrt{s} = 7$ TeV using 4.5 fb^{-1} of data with the ATLAS detector*,
JHEP **02** (2015) 153, [Erratum: JHEP 09, 141 (2015)], arXiv: 1410.8857 [hep-ex] (cit. on p. 13).

[62] K. J. Eskola, P. Paakkinen, H. Paukkunen, and C. A. Salgado,
EPPS21: a global QCD analysis of nuclear PDFs, Eur. Phys. J. C **82** (2022) 413,
arXiv: 2112.12462 [hep-ph] (cit. on p. 14).

[63] EMC Collaboration, *The ratio of the nucleon structure functions F2N for iron and deuterium*,
Physics Letters B **123** (1983) 275, ISSN: 0370-2693,
URL: https://www.sciencedirect.com/science/article/pii/0370269383904379
(cit. on pp. 14, 15).

[64] K. J. Eskola, P. Paakkinen, H. Paukkunen, and C. A. Salgado,
EPPS16: Nuclear parton distributions with LHC data, Eur. Phys. J. C **77** (2017) 163,
arXiv: 1612.05741 [hep-ph] (cit. on pp. 14, 24).

[65] N. Armesto, *Nuclear shadowing*, J. Phys. G **32** (2006) R367, arXiv: hep-ph/0604108 (cit. on p. 15).

[66] J. Qiu, *Nuclear shadowing at small values of x*, Nuclear Physics B **291** (1987) 746, ISSN: 0550-3213,
URL: https://www.sciencedirect.com/science/article/pii/0550321387904949 (cit. on p. 15).

[67] S. J. Brodsky and H. J. Lu, *Shadowing and antishadowing of nuclear structure functions*,
Phys. Rev. Lett. **64** (12 1990) 1342 (cit. on pp. 15, 110).

[68] O. Hen, E. Piasetzky, and L. B. Weinstein,
New data strengthen the connection between Short Range Correlations and the EMC effect,
Phys. Rev. C **85** (2012) 047301, arXiv: 1202.3452 [nucl-ex] (cit. on p. 15).

[69] A. Bodek and J. L. Ritchie,
Fermi-motion effects in deep-inelastic lepton scattering from nuclear targets,
Phys. Rev. D **23** (5 1981) 1070, URL: https://link.aps.org/doi/10.1103/PhysRevD.23.1070
(cit. on p. 15).

[70] J. D. Bjorken, *Energy Loss of Energetic Partons in Quark - Gluon Plasma: Possible Extinction of High p(t) Jets in Hadron - Hadron Collisions*, (1982) (cit. on p. 15).

[71] R. Aaij et al., *Centrality determination in heavy-ion collisions with the LHCb detector*,
Journal of Instrumentation **17** (2022) P05009 (cit. on p. 16).

[72] M. L. Miller, K. Reygers, S. J. Sanders, and P. Steinberg,
Glauber modeling in high energy nuclear collisions, Ann. Rev. Nucl. Part. Sci. **57** (2007) 205,
arXiv: nucl-ex/0701025 (cit. on pp. 16, 18).

[73] ATLAS Collaboration, *Charged hadron spectra and dijet p_T correlations measured in Xe+Xe collisions at $\sqrt{s_{NN}} = 5.44$ TeV with the ATLAS detector*, ATLAS-CONF-2018-007, 2018,
URL: https://cds.cern.ch/record/2318588 (cit. on p. 16).

[74] I. Angeli and K. Marinova, *Table of experimental nuclear ground state charge radii: An update*,
Atomic Data and Nuclear Data Tables **99** (2013) 69, ISSN: 0092-640X,
URL: https://www.sciencedirect.com/science/article/pii/S0092640X12000265
(cit. on p. 16).

[75] B. Alver and G. Roland, *Collision geometry fluctuations and triangular flow in heavy-ion collisions*,
Phys. Rev. C **81** (2010) 054905, [Erratum: Phys.Rev.C 82, 039903 (2010)],
arXiv: 1003.0194 [nucl-th] (cit. on p. 17).

[76] M. Aaboud et al., *Measurement of jet p_{T} correlations in Pb+Pb and pp collisions at $\sqrt{s_{\mathrm{NN}}} = 2.76$ TeV with the ATLAS detector*, Phys. Lett. B **774** (2017) 379, arXiv: 1706.09363 [hep-ex] (cit. on pp. 17, 18).

[77] ATLAS Collaboration,
Measurements of the suppression and correlations of dijets in Pb+Pb collisions at $\sqrt{s_{NN}} = 5.02$ TeV, (2022), arXiv: 2205.00682 [nucl-ex] (cit. on p. 18).

[78] *Dijet imbalance measurements in* Au + Au *and pp collisions at $\sqrt{s_{NN}} = 200$ GeV at STAR*, Phys. Rev. Lett. **119** (6 2017) 062301,
URL: https://link.aps.org/doi/10.1103/PhysRevLett.119.062301 (cit. on p. 18).

[79] *Jet radius dependence of dijet momentum balance in Pb+Pb collisions at 5.02 TeV with the ATLAS detector*, All figures including auxiliary figures are available at https://atlas.web.cern.ch/Atlas/GROUPS/PHYSICS/CONFNOTES/ATLAS-CONF-2023-060, 2023, URL: https://cds.cern.ch/record/2871730 (cit. on p. 18).

[80] ATLAS Collaboration, *Measurements of the Nuclear Modification Factor for Jets in Pb+Pb Collisions at $\sqrt{s_{NN}} = 2.76$ TeV with the ATLAS Detector*, Phys. Rev. Lett. **114** (2015) 072302, arXiv: 1411.2357 [hep-ex] (cit. on p. 18).

[81] J. Adam et al., *Measurement of jet suppression in central Pb-Pb collisions at $\sqrt{s_{\mathrm{NN}}} = 2.76$ TeV*, Phys. Lett. B **746** (2015) 1, arXiv: 1502.01689 [nucl-ex] (cit. on p. 18).

[82] ATLAS Collaboration, *Measurement of the nuclear modification factor for inclusive jets in Pb+Pb collisions at $\sqrt{s_{NN}} = 5.02$ TeV with the ATLAS detector*, Phys. Lett. B **790** (2019) 108, arXiv: 1805.05635 [hep-ex] (cit. on p. 19).

[83] ATLAS Collaboration,
Strong constraints on jet quenching in centrality-dependent p+Pb collisions at 5.02 TeV from ATLAS, (2022), arXiv: 2206.01138 [nucl-ex] (cit. on pp. 18, 27).

[84] CMS Collaboration, *Studies of dijet transverse momentum balance and pseudorapidity distributions in pPb collisions at $\sqrt{s_{NN}} = 5.02$ TeV*, Eur. Phys. J. C **74** (2014) 2951, arXiv: 1401.4433 [hep-ex] (cit. on pp. 18, 29, 33, 34, 106, 112).

[85] ATLAS Collaboration, *Two-particle azimuthal correlations in photonuclear ultraperipheral Pb+Pb collisions at 5.02 TeV with ATLAS*, Phys. Rev. C **104** (2021) 014903, arXiv: 2101.10771 [hep-ex] (cit. on p. 19).

[86] A. M. Poskanzer and S. A. Voloshin,
Methods for analyzing anisotropic flow in relativistic nuclear collisions, Phys. Rev. C **58** (1998) 1671, arXiv: nucl-ex/9805001 (cit. on p. 19).

[87] ATLAS Collaboration, *Measurements of azimuthal anisotropies of jet production in Pb+Pb collisions at $\sqrt{s_{NN}} = 5.02$ TeV with the ATLAS detector*, Phys. Rev. C **105** (2021) 064903, arXiv: 2111.06606 [nucl-ex] (cit. on pp. 19, 20).

[88] J. Adams et al., *Azimuthal anisotropy and correlations at large transverse momenta in p+p and Au+Au collisions at s(NN)**(1/2) = 200-GeV*, Phys. Rev. Lett. **93** (2004) 252301, arXiv: nucl-ex/0407007 (cit. on p. 19).

[89] ATLAS Collaboration, *Measurement of flow harmonics with multi-particle cumulants in Pb+Pb collisions at $\sqrt{s_{NN}} = 2.76$ TeV with the ATLAS detector*, Eur. Phys. J. C **74** (2014) 3157, arXiv: 1408.4342 [hep-ex] (cit. on p. 19).

[90] S. Voloshin and Y. Zhang, *Flow study in relativistic nuclear collisions by Fourier expansion of Azimuthal particle distributions*, Z. Phys. C **70** (1996) 665, arXiv: hep-ph/9407282 (cit. on pp. 19, 22).

[91] M. Gyulassy and L. McLerran, *New forms of QCD matter discovered at RHIC*, Nucl. Phys. A **750** (2005) 30, ed. by D. Rischke and G. Levin, arXiv: nucl-th/0405013 (cit. on p. 19).

[92] I. Arsene et al., *Quark gluon plasma and color glass condensate at RHIC? The Perspective from the BRAHMS experiment*, Nucl. Phys. A **757** (2005) 1, arXiv: nucl-ex/0410020 (cit. on p. 19).

[93] M. Connors, C. Nattrass, R. Reed, and S. Salur, *Jet measurements in heavy ion physics*, Rev. Mod. Phys. **90** (2018) 025005, arXiv: 1705.01974 [nucl-ex] (cit. on p. 20).

[94] ATLAS Collaboration, *Prompt and non-prompt J/ψ elliptic flow in Pb+Pb collisions at $\sqrt{s_{NN}} = 5.02$ TeV with the ATLAS detector*, Eur. Phys. J. C **78** (2018) 784, arXiv: 1807.05198 [hep-ex] (cit. on p. 20).

[95] ATLAS Collaboration, *Measurement of the centrality and pseudorapidity dependence of the integrated elliptic flow in lead–lead collisions at $\sqrt{s_{NN}} = 2.76$ TeV with the ATLAS detector*, Eur. Phys. J. C **74** (2014) 2982, arXiv: 1405.3936 [hep-ex] (cit. on p. 20).

[96] ATLAS Collaboration, *Measurement of the Azimuthal Angle Dependence of Inclusive Jet Yields in Pb+Pb Collisions at $\sqrt{s_{NN}} = 2.76$ TeV with the ATLAS detector*, Phys. Rev. Lett. **111** (2013) 152301, arXiv: 1306.6469 [hep-ex] (cit. on p. 20).

[97] CMS Collaboration, *Azimuthal anisotropy of charged particles with transverse momentum up to 100 GeV/c in PbPb collisions at $\sqrt{s_{NN}} = 5.02$ TeV*, Phys. Lett. B **776** (2018) 195, arXiv: 1702.00630 [hep-ex] (cit. on p. 20).

[98] C. A. Salgado et al., *Proton-Nucleus Collisions at the LHC: Scientific Opportunities and Requirements*, J. Phys. G **39** (2012) 015010, arXiv: 1105.3919 [hep-ph] (cit. on pp. 21, 48).

[99] J. L. Albacete et al., *Predictions for Cold Nuclear Matter Effects in p+Pb Collisions at $\sqrt{s_{NN}} = 8.16$ TeV*, Nucl. Phys. A **972** (2018) 18, arXiv: 1707.09973 [hep-ph] (cit. on p. 21).

[100] P. Abbon et al., *The COMPASS experiment at CERN*, Nucl. Instrum. Meth. A **577** (2007) 455, arXiv: hep-ex/0703049 (cit. on p. 21).

[101] K. Ackerstaff et al., *The HERMES spectrometer*, Nucl. Instrum. Meth. A **417** (1998) 230, arXiv: hep-ex/9806008 (cit. on p. 21).

[102] J. C. Collins and M. J. Perry, *Superdense Matter: Neutrons or Asymptotically Free Quarks?*, Phys. Rev. Lett. **34** (21 1975) 1353, URL: https://link.aps.org/doi/10.1103/PhysRevLett.34.1353 (cit. on p. 21).

[103] N. Cabibbo and G. Parisi, *Exponential Hadronic Spectrum and Quark Liberation*, Phys. Lett. B **59** (1975) 67 (cit. on p. 21).

[104] E. V. Shuryak, *Theory of Hadronic Plasma*, Sov. Phys. JETP **47** (1978) 212 (cit. on p. 21).

[105] CMS Collaboration, *Constraining Gluon Distributions in Nuclei Using Dijets in Proton–Proton and Proton–Lead Collisions at* $\sqrt{s_{NN}} = 5.02$ *TeV*, Phys. Rev. Lett. **121** (2018) 062002, arXiv: 1805.04736 [hep-ex] (cit. on pp. 21, 29).

[106] CMS Collaboration, *Observation of nuclear modifications in* $W^{\pm}$ *boson production in pPb collisions at* $\sqrt{s_{NN}} = 8.16$ *TeV*, Phys. Lett. B **800** (2020) 135048, arXiv: 1905.01486 [hep-ex] (cit. on pp. 21, 25).

[107] LHCb Collaboration, *Study of prompt* D^0 *meson production in pPb collisions at* $\sqrt{s_{NN}} = 5$ *TeV*, JHEP **10** (2017) 090, arXiv: 1707.02750 [hep-ex] (cit. on pp. 21, 23, 27).

[108] ATLAS Collaboration, *Observation of Associated Near-Side and Away-Side Long-Range Correlations in* $\sqrt{s_{NN}} = 5.02$ *TeV Proton–Lead Collisions with the ATLAS Detector*, Phys. Rev. Lett. **110** (2013) 182302, arXiv: 1212.5198 [hep-ex] (cit. on p. 22).

[109] ATLAS Collaboration, *Measurement with the ATLAS detector of multi-particle azimuthal correlations in p+Pb collisions at* $\sqrt{s_{NN}} = 5.02$ *TeV*, Phys. Lett. B **725** (2013) 60, arXiv: 1303.2084 [hep-ex] (cit. on p. 22).

[110] ATLAS Collaboration, *Measurement of long-range pseudorapidity correlations and azimuthal harmonics in* $\sqrt{s_{NN}} = 5.02$ *TeV proton–lead collisions with the ATLAS detector*, Phys. Rev. C **90** (2014) 044906, arXiv: 1409.1792 [hep-ex] (cit. on p. 22).

[111] ATLAS Collaboration, *Transverse momentum and process dependent azimuthal anisotropies in* $\sqrt{s_{NN}} = 8.16$ *TeV p+Pb collisions with the ATLAS detector*, Eur. Phys. J. C **80** (2020) 73, arXiv: 1910.13978 [hep-ex] (cit. on p. 22).

[112] CMS Collaboration, *Observation of long-range, near-side angular correlations in pPb collisions at the LHC*, Phys. Lett. B **718** (2013) 795, arXiv: 1210.5482 [nucl-ex] (cit. on p. 22).

[113] CMS Collaboration, *Multiplicity and transverse momentum dependence of two- and four-particle correlations in pPb and PbPb collisions*, Phys. Lett. B **724** (2013) 213, arXiv: 1305.0609 [hep-ex] (cit. on p. 22).

[114] B. Abelev et al., *Long-range angular correlations on the near and away side in p-Pb collisions at* $\sqrt{s_{NN}} = 5.02$ *TeV*, Phys. Lett. B **719** (2013) 29, arXiv: 1212.2001 [nucl-ex] (cit. on p. 22).

[115] B. B. Abelev et al., *Long-range angular correlations of* π*, K and p in p-Pb collisions at* $\sqrt{s_{\mathrm{NN}}} = 5.02$ *TeV*, Phys. Lett. B **726** (2013) 164, arXiv: 1307.3237 [nucl-ex] (cit. on p. 22).

[116] J.-Y. Ollitrault, *Anisotropy as a signature of transverse collective flow*, Phys. Rev. D **46** (1 1992) 229, URL: https://link.aps.org/doi/10.1103/PhysRevD.46.229 (cit. on p. 22).

[117] ATLAS Collaboration, *Measurement of the azimuthal anisotropy of charged particles produced in* $\sqrt{s_{NN}} = 5.02$ *TeV Pb+Pb collisions with the ATLAS detector*, Eur. Phys. J. C **78** (2018) 997, arXiv: 1808.03951 [hep-ex] (cit. on pp. 22, 43).

[118] N. Brambilla et al., *Heavy Quarkonium: Progress, Puzzles, and Opportunities*, Eur. Phys. J. C **71** (2011) 1534, arXiv: 1010.5827 [hep-ph] (cit. on p. 22).

[119] J. E. Augustin et al., *Discovery of a Narrow Resonance in e^+e^- Annihilation*, Phys. Rev. Lett. **33** (1974) 1406 (cit. on p. 22).

[120] J. J. Aubert et al., *Experimental Observation of a Heavy Particle J*, Phys. Rev. Lett. **33** (1974) 1404 (cit. on p. 22).

[121] F. Gelis, E. Iancu, J. Jalilian-Marian, and R. Venugopalan, *The Color Glass Condensate*, Ann. Rev. Nucl. Part. Sci. **60** (2010) 463, arXiv: 1002.0333 [hep-ph] (cit. on p. 23).

[122] D. Kharzeev and K. Tuchin, *Signatures of the color glass condensate in J/psi production off nuclear targets*, Nucl. Phys. A **770** (2006) 40, arXiv: hep-ph/0510358 (cit. on p. 23).

[123] B. B. Abelev et al., *J/ψ production and nuclear effects in p-Pb collisions at $\sqrt{S_{NN}} = 5.02$ TeV*, JHEP **02** (2014) 073, arXiv: 1308.6726 [nucl-ex] (cit. on p. 23).

[124] H. Fujii, F. Gelis, and R. Venugopalan, *Quark pair production in high energy pA collisions: General features*, Nucl. Phys. A **780** (2006) 146, arXiv: hep-ph/0603099 (cit. on p. 23).

[125] F. Arleo and S. Peigne, *Heavy-quarkonium suppression in p-A collisions from parton energy loss in cold QCD matter*, JHEP **03** (2013) 122, arXiv: 1212.0434 [hep-ph] (cit. on p. 23).

[126] F. Bechtel and P. Schleper, *The Underlying Event in Proton-Proton Collisions*, [Online; accessed 27-October-2023], 2009, URL: https://www.researchgate.net/figure/Drell-Yan-process-a-quark-of-one-hadron-and-an-antiquark-of-another-hadron-annihilate_fig1_254469235 (cit. on p. 24).

[127] S. D. Drell and T.-M. Yan, *Massive Lepton Pair Production in Hadron-Hadron Collisions at High-Energies*, Phys. Rev. Lett. **25** (1970) 316, [Erratum: Phys.Rev.Lett. 25, 902 (1970)] (cit. on p. 24).

[128] CMS Collaboration, *Study of Drell–Yan dimuon production in proton–lead collisions at $\sqrt{s_{NN}} = 8.16$ TeV*, JHEP **05** (2021) 182, arXiv: 2102.13648 [hep-ex] (cit. on p. 24).

[129] S. Dulat et al., *New parton distribution functions from a global analysis of quantum chromodynamics*, Phys. Rev. D **93** (2016) 033006, arXiv: 1506.07443 [hep-ph] (cit. on p. 24).

[130] CMS Collaboration, *Measurement of isolated photon production in pp and PbPb collisions at $\sqrt{s_{NN}} = 2.76$ TeV*, Phys. Lett. B **710** (2012) 256, arXiv: 1201.3093 [hep-ex] (cit. on p. 25).

[131] ATLAS Collaboration, *Z boson production in Pb+Pb collisions at $\sqrt{s_{NN}}$= 5.02 TeV measured by the ATLAS experiment*, Phys. Lett. B **802** (2020) 135262, arXiv: 1910.13396 [hep-ex] (cit. on p. 25).

[132] ATLAS Collaboration, *Measurement of $W^\pm$ boson production in Pb+Pb collisions at $\sqrt{s_{NN}} = 5.02$ TeV with the ATLAS detector*, Eur. Phys. J. C **79** (2019) 935, arXiv: 1907.10414 [hep-ex] (cit. on p. 25).

[133] ATLAS Collaboration,
Z boson production in $p+Pb$ collisions at $\sqrt{s_{NN}} = 5.02$ TeV measured with the ATLAS detector,
Phys. Rev. C **92** (2015) 044915, arXiv: 1507.06232 [hep-ex] (cit. on pp. 25, 26).

[134] ATLAS Collaboration, *Measurement of $W \to \mu\nu$ production in p+Pb collisions at $\sqrt{s_{NN}} = 5.02$ TeV with the ATLAS Detector at the LHC*, ATLAS-CONF-2015-056, 2015,
URL: https://cds.cern.ch/record/2055677 (cit. on pp. 25, 26).

[135] H. Paukkunen and C. A. Salgado,
Constraints for the nuclear parton distributions from Z and W production at the LHC,
JHEP **03** (2011) 071, arXiv: 1010.5392 [hep-ph] (cit. on p. 25).

[136] CMS Collaboration, *Study of W boson production in pPb collisions at $\sqrt{s_{NN}}$ 5.02 TeV*,
Phys. Lett. B **750** (2015) 565, arXiv: 1503.05825 [hep-ex] (cit. on p. 25).

[137] CMS Collaboration, *Study of Z boson production in pPb collisions at $\sqrt{s_{NN}} = 5.02$ TeV*,
Phys. Lett. B **759** (2016) 36, arXiv: 1512.06461 [hep-ex] (cit. on p. 25).

[138] J. Adam et al., *W and Z boson production in p-Pb collisions at $\sqrt{s_{\mathrm{NN}}} = 5.02$ TeV*,
JHEP **02** (2017) 077, arXiv: 1611.03002 [nucl-ex] (cit. on p. 25).

[139] S. Acharya et al.,
Z-boson production in p-Pb collisions at $\sqrt{s_{\mathrm{NN}}} = 8.16$ TeV and Pb-Pb collisions at $\sqrt{s_{\mathrm{NN}}} = 5.02$ TeV,
JHEP **09** (2020) 076, arXiv: 2005.11126 [nucl-ex] (cit. on p. 25).

[140] I. Helenius, K. J. Eskola, and H. Paukkunen, *Probing the small-x nuclear gluon distributions with isolated photons at forward rapidities in p+Pb collisions at the LHC*, JHEP **09** (2014) 138,
arXiv: 1406.1689 [hep-ph] (cit. on p. 25).

[141] Z.-B. Kang, I. Vitev, and H. Xing,
Effects of cold nuclear matter energy loss on inclusive jet production in $p + A$ collisions at energies available at the BNL Relativistic Heavy Ion Collider and the CERN Large Hadron Collider,
Phys. Rev. C **92** (5 2015) 054911, URL: https://link.aps.org/doi/10.1103/PhysRevC.92.054911
(cit. on p. 25).

[142] ATLAS Collaboration,
Measurement of prompt photon production in $\sqrt{s_{NN}} = 8.16$ TeV p+Pb collisions with ATLAS,
Phys. Lett. B **796** (2019) 230, arXiv: 1903.02209 [hep-ex] (cit. on pp. 25, 26).

[143] R. A. Khalek,
Impact of LHC dijet production in pp and pPb collisions on the nNNPDF2.0 nuclear PDFs,
SciPost Phys. Proc. (2022) 135 (cit. on p. 27).

[144] K. J. Eskola, P. Paakkinen, and H. Paukkunen, *Non-quadratic improved Hessian PDF reweighting and application to CMS dijet measurements at 5.02 TeV*, Eur. Phys. J. C **79** (2019) 511,
arXiv: 1903.09832 [hep-ph] (cit. on p. 27).

[145] K. J. Eskola, I. Helenius, P. Paakkinen, and H. Paukkunen,
A QCD analysis of LHCb D-meson data in p+Pb collisions, JHEP **05** (2020) 37,
arXiv: 1906.02512 [hep-ph] (cit. on p. 27).

[146] H. Paukkunen, "Status of nuclear PDFs after the first LHC p–Pb run", *Proceedings, The 26th International Conference on Ultra-relativistic Nucleus-Nucleus Collisions: Quark Matter 2017 (QM 2017)* (Chicago, Illinois, USA, Sept. 5–11, 2017) 241, arXiv: 1704.04036 [hep-ph] (cit. on p. 27).

[147] J.-P. Blaizot, *High gluon densities in heavy ion collisions*, Rept. Prog. Phys. **80** (2017) 032301, arXiv: 1607.04448 [hep-ph] (cit. on p. 27).

[148] D. Kharzeev, E. Levin, and L. McLerran, *Jet azimuthal correlations and parton saturation in the color glass condensate*, Nucl. Phys. A **748** (2005) 627, arXiv: hep-ph/0403271 (cit. on p. 27).

[149] ATLAS Collaboration, *Dijet azimuthal correlations and conditional yields in pp and p + Pb collisions at $\sqrt{s_{NN}} = 5.02$ TeV with the ATLAS detector*, Phys. Rev. C **100** (2019) 034903, arXiv: 1901.10440 [hep-ex] (cit. on p. 29).

[150] A. van Hameren, P. Kotko, K. Kutak, C. Marquet, and S. Sapeta, *Saturation effects in forward-forward dijet production in p+Pb collisions*, Phys. Rev. D **89** (2014) 094014, arXiv: 1402.5065 [hep-ph] (cit. on p. 29).

[151] ALICE Collaboration, *Measurement of charged jet production cross sections and nuclear modification in p-Pb collisions at $\sqrt{s_{NN}} = 5.02$ TeV*, Phys. Lett. B **749** (2015) 68, arXiv: 1503.00681 [nucl-ex] (cit. on p. 29).

[152] ATLAS Collaboration, *Centrality and rapidity dependence of inclusive jet production in $\sqrt{s_{NN}} = 5.02$ TeV proton-lead collisions with the ATLAS detector*, Phys. Lett. B **748** (2015) 392, arXiv: 1412.4092 [hep-ex] (cit. on pp. 29–33, 37, 47, 74, 88, 109, 111, 112).

[153] PHENIX Collaboration, *Centrality-dependent modification of jet-production rates in deuteron-gold collisions at $\sqrt{s_{NN}} = 200$ GeV*, Phys. Rev. Lett. **116** (2016) 122301, arXiv: 1509.04657 [nucl-ex] (cit. on pp. 29–31, 33).

[154] A. Bzdak, V. Skokov, and S. Bathe, *Centrality dependence of high energy jets in p+Pb collisions at energies available at the CERN Large Hadron Collider*, Phys. Rev. C **93** (2016) 044901, arXiv: 1408.3156 [hep-ph] (cit. on pp. 31, 32, 109).

[155] N. Armesto, D. C. Gülhan, and J. G. Milhano, *Kinematic bias on centrality selection of jet events in pPb collisions at the LHC*, Phys. Lett. B **747** (2015) 441, arXiv: 1502.02986 [hep-ph] (cit. on pp. 31, 32, 109).

[156] M. Alvioli, L. Frankfurt, D. Perepelitsa, and M. Strikman, *Global analysis of color fluctuation effects in proton– and deuteron–nucleus collisions at RHIC and the LHC*, Phys. Rev. D **98** (2018) 071502, arXiv: 1709.04993 [hep-ph] (cit. on pp. 31, 33, 37, 47, 52, 109).

[157] ATLAS Collaboration, *Measurement of the dependence of transverse energy production at large pseudorapidity on the hard-scattering kinematics of proton–proton collisions at $\sqrt{s} = 2.76$ TeV with ATLAS*, Phys. Lett. B **756** (2016) 10, arXiv: 1512.00197 [hep-ex] (cit. on pp. 32, 33, 109).

[158] I. Helenius, K. J. Eskola, H. Honkanen, and C. A. Salgado, *Impact-Parameter Dependent Nuclear Parton Distribution Functions: EPS09s and EKS98s and Their Applications in Nuclear Hard Processes*, JHEP **07** (2012) 073, arXiv: 1205.5359 [hep-ph] (cit. on p. 33).

[159] S. J. Brodsky, "Testing Quantum Chromodynamics",
Proceedings, XIII International Symposium on Multiparticle Dynamics
(Volendam, the Netherlands, June 6–11, 1982) 963 (cit. on p. 34).

[160] S. J. Brodsky and A. H. Mueller, *Using Nuclei to Probe Hadronization in QCD*,
Phys. Lett. B **206** (1988) 685 (cit. on p. 34).

[161] G. Bertsch, S. J. Brodsky, A. S. Goldhaber, and J. G. Gunion,
Diffractive Excitation in Quantum Chromodynamics, Phys. Rev. Lett. **47** (1981) 297 (cit. on p. 34).

[162] L. Frankfurt, G. A. Miller, and M. Strikman,
Coherent nuclear diffractive production of mini - jets: Illuminating color transparency,
Phys. Lett. B **304** (1993) 1, arXiv: hep-ph/9305228 (cit. on p. 34).

[163] L. L. Frankfurt, G. A. Miller, and M. Strikman,
The Geometrical color optics of coherent high-energy processes,
Ann. Rev. Nucl. Part. Sci. **44** (1994) 501, arXiv: hep-ph/9407274 (cit. on pp. 34, 37).

[164] L. L. Nemenov, *Superpenetrability of Ultrarelativistic Positronium*, Yad. Fiz. **34** (1981) 1306
(cit. on p. 34).

[165] V. L. Lyuboshitz and M. I. Podgoretskii,
Passage of ultrarelativistic positronium atoms through matter,
Sov. Phys. - JETP (Engl. Transl.); (United States) **54** (1981) (cit. on p. 34).

[166] D. Perkins, *Ionization at the origin of electron Pairs, and the lifetime of the neutral pion*,
The London, Edinburgh, and Dublin Philosophical Magazine and Journal of Science **46** (1955) 1146
(cit. on p. 35).

[167] G. Baym, "Color Transparency and Cross-Section Fluctuations in Hadronic Collisions",
Advances in Nuclear Physics, ed. by J. W. Negele and E. Vogt, Boston, MA: Springer US, 1996 101,
ISBN: 978-0-306-47065-3 (cit. on p. 35).

[168] S. Klein, *Suppression of Bremsstrahlung and pair production due to environmental factors*,
Rev. Mod. Phys. **71** (1999) 1501, arXiv: hep-ph/9802442 (cit. on p. 35).

[169] *Observation of Color-Transparency in Diffractive Dissociation of Pions*,
Phys. Rev. Lett. **86** (21 2001) 4773 (cit. on pp. 36, 37).

[170] A. Airapetian et al., *The Q**2 dependence of nuclear transparency for exclusive rho0 production*,
Phys. Rev. Lett. **90** (2003) 052501, arXiv: hep-ex/0209072 (cit. on p. 36).

[171] K. Gallmeister, M. Kaskulov, and U. Mosel, *Color transparency in hadronic attenuation of ρ^0 mesons*,
Phys. Rev. C **83** (2011) 015201, arXiv: 1007.1141 [hep-ph] (cit. on p. 36).

[172] G. A. Miller and M. Strikman, *Color Transparency at COMPASS energies*,
Phys. Rev. C **82** (2010) 025205, arXiv: 1005.0663 [nucl-th] (cit. on p. 36).

[173] A. Accardi et al.,
Electron Ion Collider: The Next QCD Frontier: Understanding the glue that binds us all,
Eur. Phys. J. A **52** (2016) 268, ed. by A. Deshpande, Z. E. Meziani, and J. W. Qiu,
arXiv: 1212.1701 [nucl-ex] (cit. on p. 36).

[174] S. J. Brodsky and G. F. de Teramond, *Onset of Color Transparency in Holographic Light-Front QCD*,
MDPI Physics **4** (2022) 633, arXiv: 2202.13283 [hep-ph] (cit. on p. 36).

[175] M. Alvioli, L. Frankfurt, V. Guzey, and M. Strikman,
Revealing "flickering" of the interaction strength in pA collisions at the CERN LHC,
Phys. Rev. C **90** (3 2014) 034914 (cit. on p. 37).

[176] ATLAS Collaboration, *The ATLAS Experiment at the CERN Large Hadron Collider*,
JINST **3** (2008) S08003 (cit. on pp. 40–42).

[177] ATLAS Collaboration, *ATLAS Insertable B-Layer: Technical Design Report*,
ATLAS-TDR-19; CERN-LHCC-2010-013, 2010, URL: https://cds.cern.ch/record/1291633
(cit. on p. 40), Addendum: ATLAS-TDR-19-ADD-1; CERN-LHCC-2012-009, 2012, URL:
https://cds.cern.ch/record/1451888.

[178] ATLAS Collaboration, *Production and integration of the ATLAS Insertable B-Layer*,
JINST **13** (2018) T05008, arXiv: 1803.00844 [physics.ins-det] (cit. on p. 40).

[179] R. Wigmans, *Calorimetry: Energy Measurement in Particle Physics*, Oxford University Press, 2017,
ISBN: 9780198786351 (cit. on p. 41).

[180] ATLAS Collaboration,
Jet energy scale and its uncertainty for jets reconstructed using the ATLAS heavy ion jet algorithm,
ATLAS-CONF-2015-016, 2015, URL: https://cds.cern.ch/record/2008677 (cit. on p. 43).

[181] J. A. Hanks et al., *Method for separating jets and the underlying event in heavy ion collisions at the BNL Relativistic Heavy Ion Collider*, Phys. Rev. C **86** (2 2012) 024908,
URL: https://link.aps.org/doi/10.1103/PhysRevC.86.024908 (cit. on p. 43).

[182] T. T. Rinn, A. M. Sickles, and P. A. Steinberg,
Measurement of Dijet Asymmetry in Pb+Pb and p p collisions at 5.02 TeV, tech. rep., CERN, 2020,
URL: https://cds.cern.ch/record/2711618 (cit. on p. 43).

[183] M. Rybar, W. Zou, B. Cole, M. Krivos, and M. Spousta,
Measurement of large-R jets and their substructure in Pb+Pb collisions, tech. rep., CERN, 2019,
URL: https://cds.cern.ch/record/2688696 (cit. on p. 43).

[184] ATLAS Collaboration,
Jet energy measurement with the ATLAS detector in proton–proton collisions at $\sqrt{s} = 7$ *TeV*,
Eur. Phys. J. C **73** (2013) 2304, arXiv: 1112.6426 [hep-ex] (cit. on p. 46).

[185] M. Krivos, M. Rybar, and M. Spousta,
Numerical inversion and cross-calibration for heavy-ion jet collections in 2017 pp and 2018 Pb+Pb,
tech. rep., CERN, 2020, URL: https://cds.cern.ch/record/2706256 (cit. on p. 46).

[186] T. Kosek et al., *Numerical inversion for calibration of Heavy-ion jets*, tech. rep., CERN, 2014,
URL: https://cds.cern.ch/record/1742072 (cit. on p. 46).

[187] J. Ouellette, *Calibration of Heavy Ion Jets in 2016 8.16 TeV p+Pb Collisions*, tech. rep.,
CERN, 2019, URL: https://cds.cern.ch/record/2655891 (cit. on p. 46).

[188] A. Cukierman and B. Nachman, *Mathematical Properties of Numerical Inversion for Jet Calibrations*,
Nucl. Instrum. Meth. A **858** (2017) 1, arXiv: 1609.05195 [physics.data-an] (cit. on p. 46).

[189] *Measurement of the centrality dependence of the dijet yield in p+Pb collisions at* $\sqrt{s_{\mathrm{NN}}} = 8.16$ *TeV with the ATLAS detector*, tech. rep., CERN, 2023, URL: https://cds.cern.ch/record/2854842
(cit. on p. 48).

[190] W. T. Giele, E. W. N. Glover, and D. A. Kosower,
Two-Jet Differential Cross Section at $O(\alpha_s^3)$ in Hadron Collisions, Phys. Rev. Lett. **73** (15 1994) 2019,
URL: https://link.aps.org/doi/10.1103/PhysRevLett.73.2019 (cit. on p. 50).

[191] D. Perepelitsa, B. Cole, and P. Steinberg,
Centrality Determination in the 2012 and 2013 p+Pb data in ATLAS, tech. rep., CERN, 2013,
URL: https://cds.cern.ch/record/1545591 (cit. on p. 52).

[192] D. V. Perepelitsa and P. A. Steinberg, *Calculation of centrality bias factors in p+A collisions based on a positive correlation of hard process yields with underlying event activity*, (2014),
arXiv: 1412.0976 [nucl-ex] (cit. on pp. 52, 76).

[193] K. K. Hill and D. Perepelitsa, *Centrality Calibration in 8.16 TeV p+Pb Collisions*, tech. rep.,
CERN, 2018, URL: https://cds.cern.ch/record/2301540 (cit. on pp. 56, 77–79, 81, 82, 91).

[194] *LAr HEC Q3 impact on 2016 p+Pb data, JIRA ticket*,
URL:https://its.cern.ch/jira/browse/ATLHI-100 (cit. on p. 58).

[195] T. Sjöstrand et al., *An introduction to PYTHIA 8.2*, Comput. Phys. Commun. **191** (2015) 159,
arXiv: 1410.3012 [hep-ph] (cit. on p. 60).

[196] R. D. Ball et al., *Parton distributions with LHC data*, Nuclear Physics B **867** (2013) 244,
ISSN: 0550-3213,
URL: https://www.sciencedirect.com/science/article/pii/S0550321312005500
(cit. on p. 60).

[197] S. Agostinelli et al., *Geant4—a simulation toolkit*,
Nuclear Instruments and Methods in Physics Research Section A: Accelerators, Spectrometers, Detectors and Associated Equipment **506** (2003) 250, ISSN: 0168-9002,
URL: https://www.sciencedirect.com/science/article/pii/S0168900203013688
(cit. on p. 60).

[198] *HIJetValTools GitLab page*,
URL:https://gitlab.cern.ch/atlas-physics/hi/jets/HIJetValTools (cit. on p. 62).

[199] *HIJetValTools-w-pPb GitLab page*,
URL:https://gitlab.cern.ch/rlongo/hi-jet-val-tools-w-p-pb (cit. on p. 62).

[200] ATLAS Collaboration, *Jet energy measurement and its systematic uncertainty in proton-proton collisions at $\sqrt{s} = 7$ TeV with the ATLAS detector*, Eur. Phys. J. C **75** (2015) 17,
arXiv: 1406.0076 [hep-ex] (cit. on p. 64).

[201] S. Baker et al., *Measurement of inclusive jet and dijet cross sections in proton-proton collisions at 7 TeV centre-of-mass energy with the ATLAS detector (Supporting Documentation)*, tech. rep.,
This is the supporting documentation for ATLAS-COM-CONF-2011-052:
http://cdsweb.cern.ch/record/1333967: CERN, 2011, URL: https://cds.cern.ch/record/1328678
(cit. on pp. 64, 65).

[202] ATLAS Collaboration, *Jet energy scale measurements and their systematic uncertainties in proton–proton collisions at $\sqrt{s} = 13$ TeV with the ATLAS detector*, Phys. Rev. D **96** (2017) 072002,
arXiv: 1703.09665 [hep-ex] (cit. on p. 64).

[203] *Recommended triggers in 2016 p+Pb runs*, URL:https://twiki.cern.ch/twiki/bin/view/AtlasProtected/TrigHIRecommendedTriggers2016 (cit. on p. 66).

[204] *ATLAS Luminosity Calculator*, URL:https://atlas-lumicalc.cern.ch (cit. on p. 67).

[205] T. Carli and T. Mkrtchyan, *ATLAS jet Trigger Performance in Run-2*, (2019), URL: https://cds.cern.ch/record/2704391 (cit. on p. 68).

[206] K. K. Hill, J. L. Nagle, Q. Hu, D. Perepelitsa, and J. Ouellette, *Transverse momentum and process dependent azimuthal anisotropies in $\sqrt{s_{NN}} = 8.16$ TeV p+Pb collisions with ATLAS*, tech. rep., CERN, 2019, URL: https://cds.cern.ch/record/2673781 (cit. on pp. 74, 76).

[207] V. Lendermann et al., *Combining Triggers in HEP Data Analysis*, Nucl. Instrum. Meth. A **604** (2009) 707, arXiv: 0901.4118 [hep-ex] (cit. on p. 75).

[208] *Weighted averages and their uncertainties*, URL:http://seismo.berkeley.edu/~kirchner/Toolkits/Toolkit_12.pdf (cit. on p. 81).

[209] G. D'Agostini, *A multidimensional unfolding method based on Bayes' theorem*, Nucl. Instrum. Meth. A **362** (1995) 487, ISSN: 0168-9002 (cit. on pp. 81, 83).

[210] T. Adye, "Unfolding algorithms and tests using RooUnfold", *Proceedings, 2011 Workshop on Statistical Issues Related to Discovery Claims in Search Experiments and Unfolding (PHYSTAT 2011)* (CERN, Geneva, Switzerland, Jan. 17–20, 2011) 313, arXiv: 1105.1160 [physics.data-an] (cit. on p. 81).

[211] ATLAS Collaboration, *Evaluating statistical uncertainties and correlations using the bootstrap method*, ATL-PHYS-PUB-2021-011, 2021, URL: https://cds.cern.ch/record/2759945 (cit. on p. 86).

[212] *EM+JES calibration and cross calibration recommendations for p+Pb @ 8.16 TeV*, URL: https://twiki.cern.ch/twiki/bin/view/AtlasProtected/HeavyIonpPbrel21 (cit. on p. 87).

[213] *Small-R (R=0.4) jet energy scale and jet energy resolution uncertainties for full run 2 analyses (release 21)*, URL: https://twiki.cern.ch/twiki/bin/viewauth/AtlasProtected/JetUncertaintiesRel21Summer2018SmallR (cit. on p. 87).

[214] *JES uncertainty for HI jets in Run2 data in rel 21*, URL: https://twiki.cern.ch/twiki/bin/view/AtlasProtected/UJES20172018 (cit. on p. 87).

[215] *JER uncertainty for HI jets in Run2 data in rel 21*, URL: https://twiki.cern.ch/twiki/bin/view/AtlasProtected/UJER20172018 (cit. on p. 88).

[216] R. P. Feynman, *Very High-Energy Collisions of Hadrons*, Phys. Rev. Lett. **23** (1969) 1415 (cit. on p. 109).

[217] ALICE Collaboration, *Centrality dependence of particle production in p-Pb collisions at $\sqrt{s_{NN}} = 5.02$ TeV*, Phys. Rev. C **91** (2015) 064905, arXiv: 1412.6828 [nucl-ex] (cit. on p. 110).

[218] ATLAS Collaboration, *Measurement of the centrality dependence of the charged-particle pseudorapidity distribution in proton–lead collisions at $\sqrt{s_{NN}} = 5.02$ TeV with the ATLAS detector*, Eur. Phys. J. C **76** (2016) 199, arXiv: 1508.00848 [hep-ex] (cit. on p. 110).

Appendix A

Unfolding Procedure Response Matrices

A.1 Response Matrices for R_{CP} Measurement

p+Pb (Period B) 0–10% Centrality

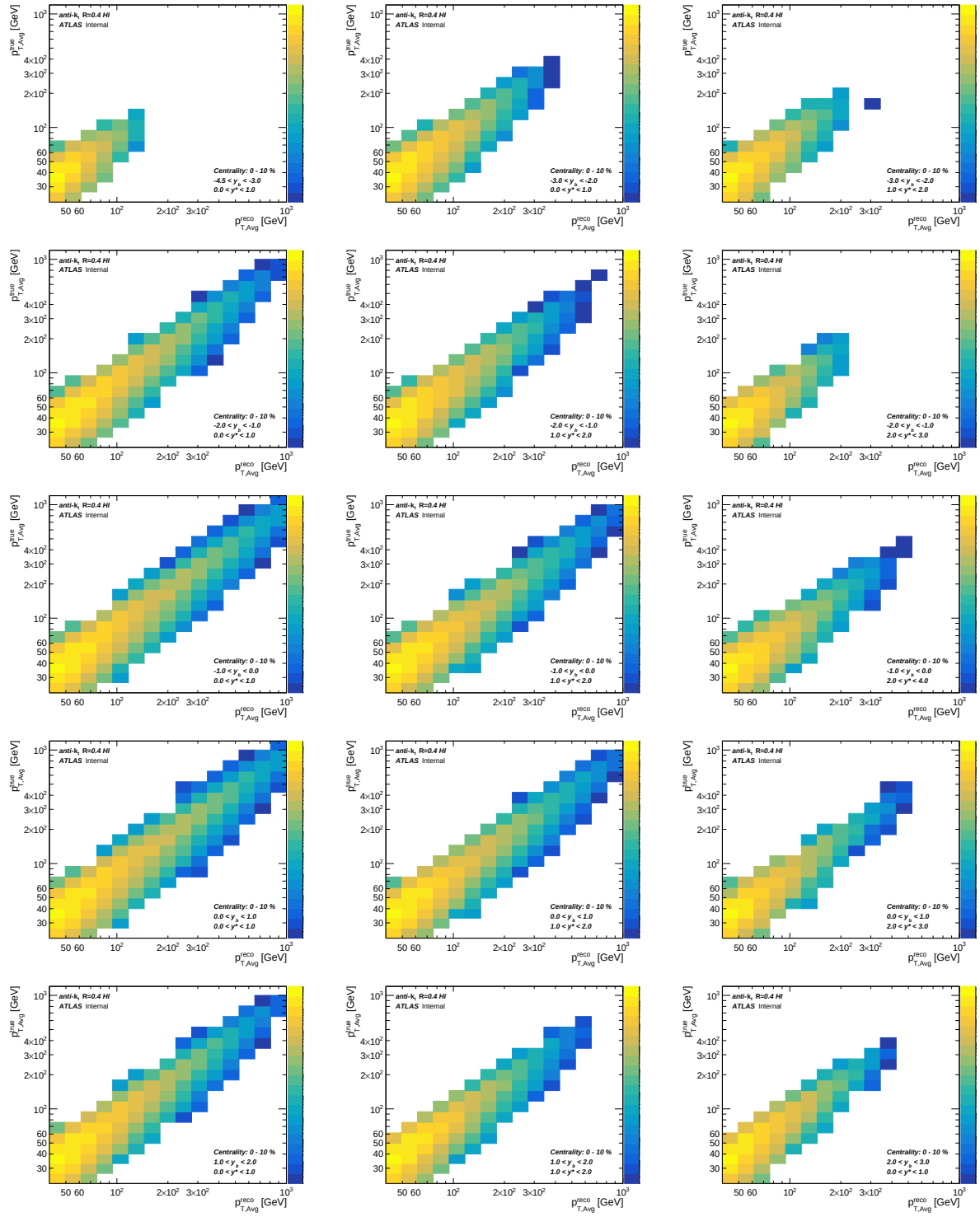

Figure A.1: Response matrices for p+Pb 0–10% unfolding.

p+Pb (Period B) 60–90%Centrality

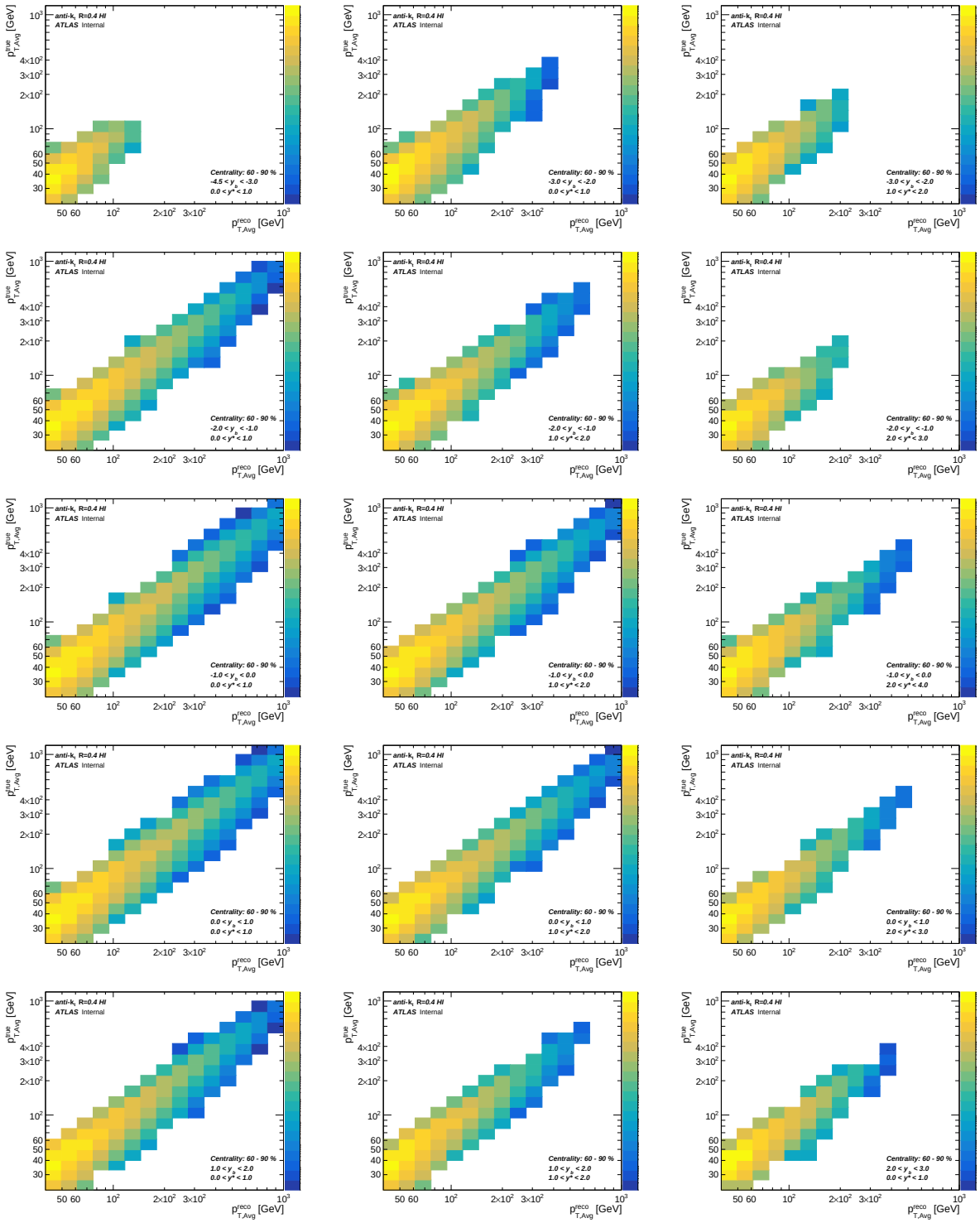

Figure A.2: Response matrices for p+Pb 60–90% unfolding.

Pb+p (Period C) 0–10% Centrality

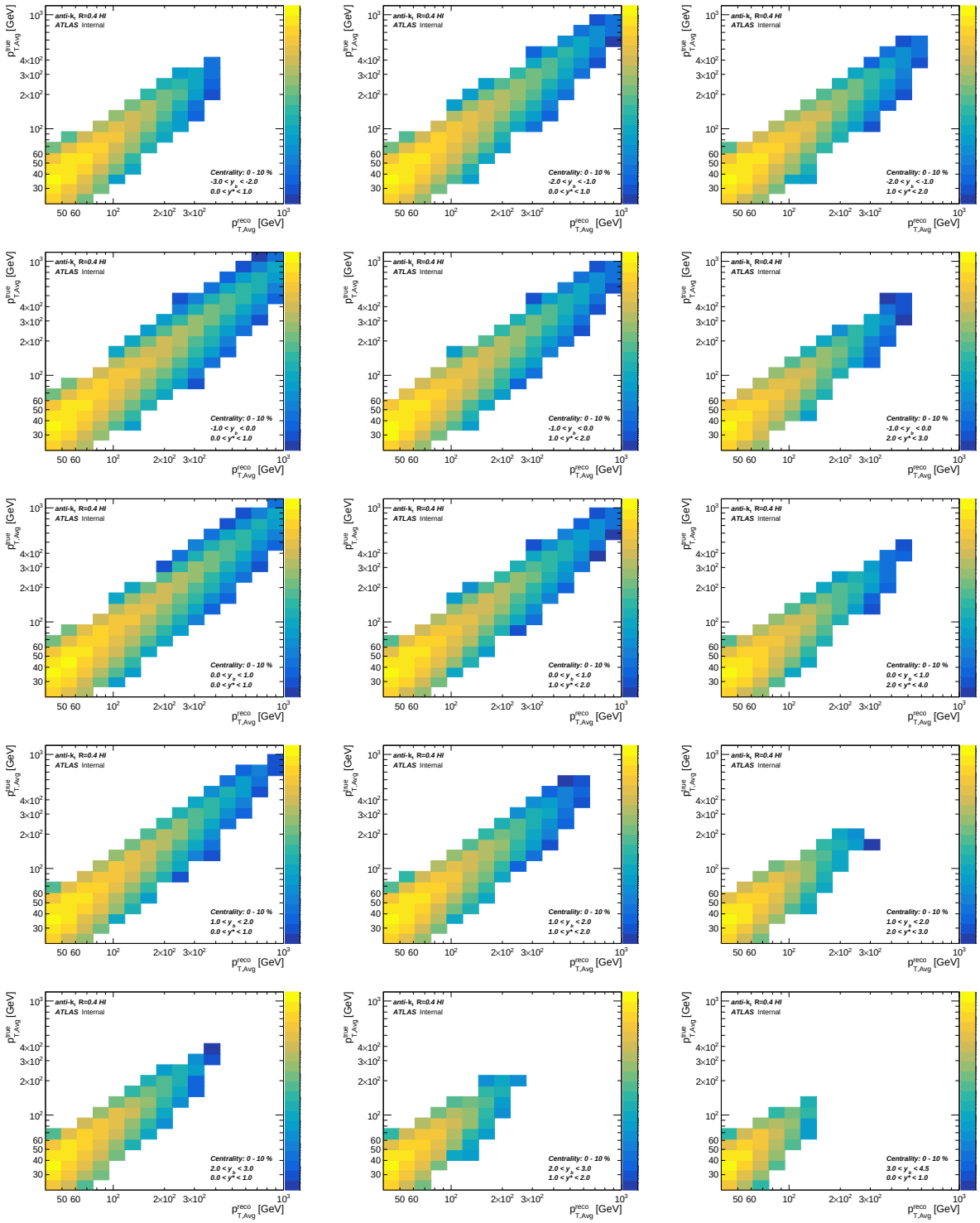

Figure A.3: Response matrices for Pb+p 0–10% centrality unfolding.

Pb+p (Period C) 60–90% Centrality

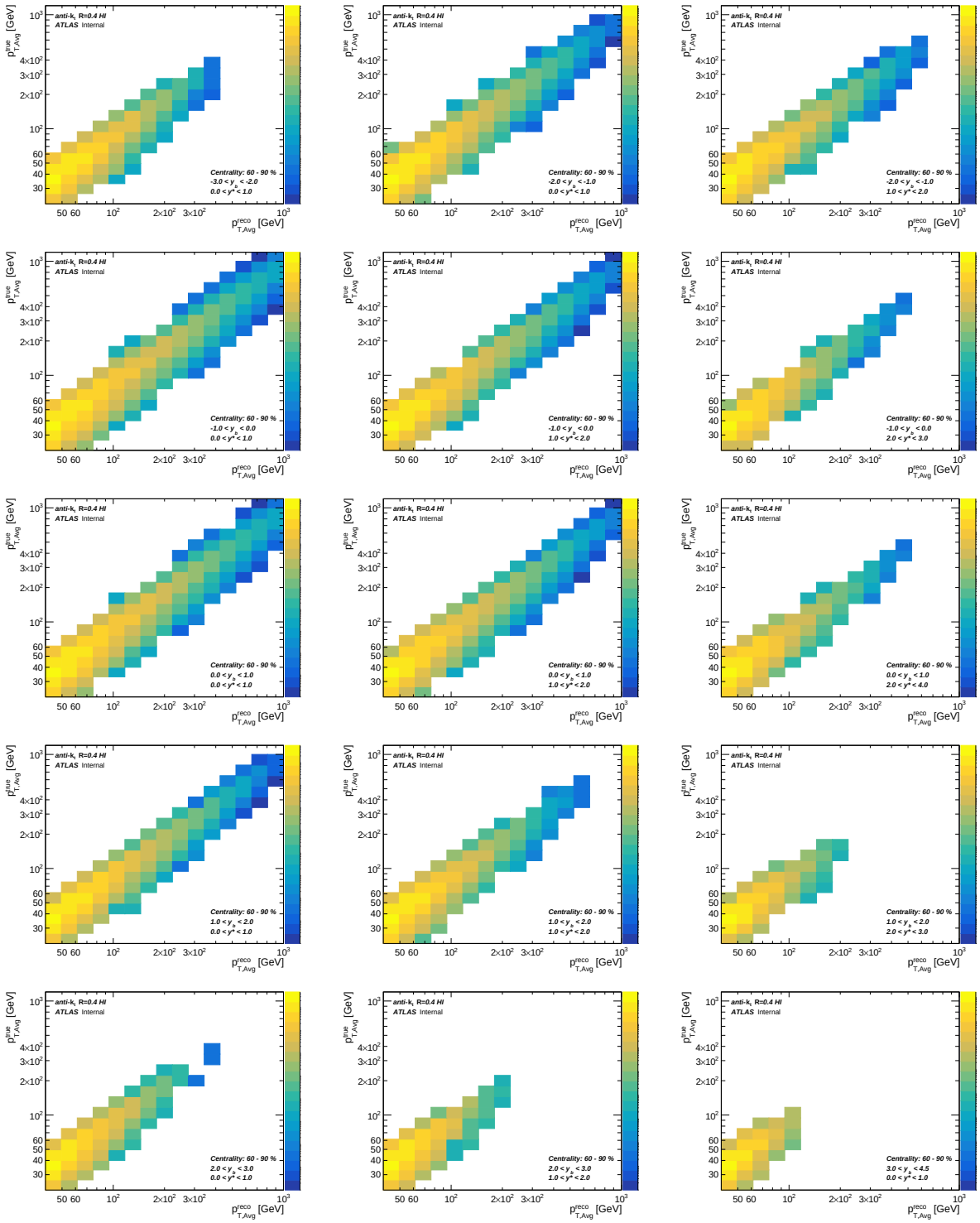

Figure A.4: Response matrices for Pb+p 60–90% centrality unfolding.

A.2 Normalized Response Matrices for R_{CP} Measurement

p+Pb (Period B) 0-10% Centrality

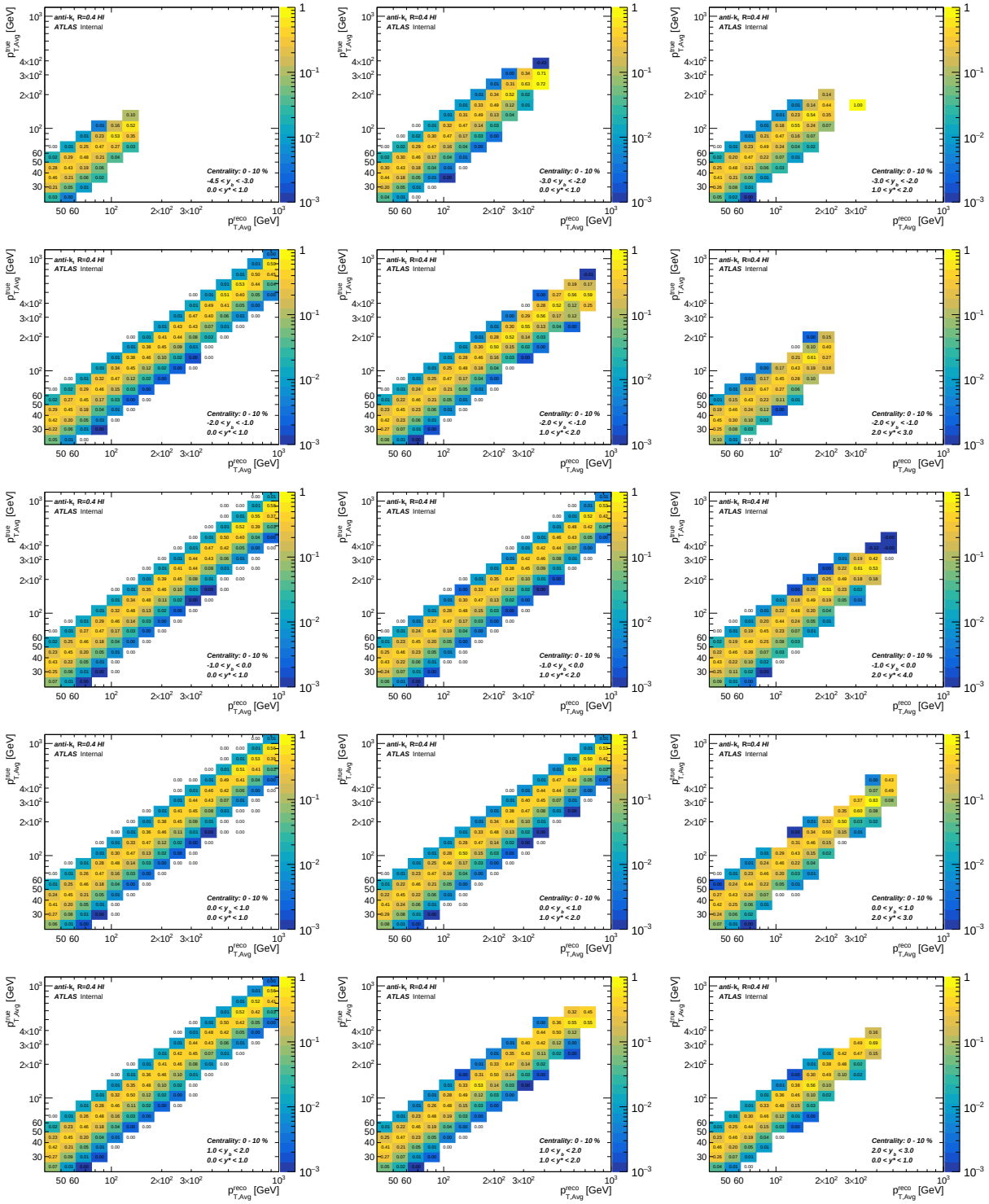

Figure A.5: Response matrices for p+Pb unfolding. The matrices are normalized such that each reconstructed bin (column) is normalized to unity.

p+Pb (Period B) 60-90% Centrality

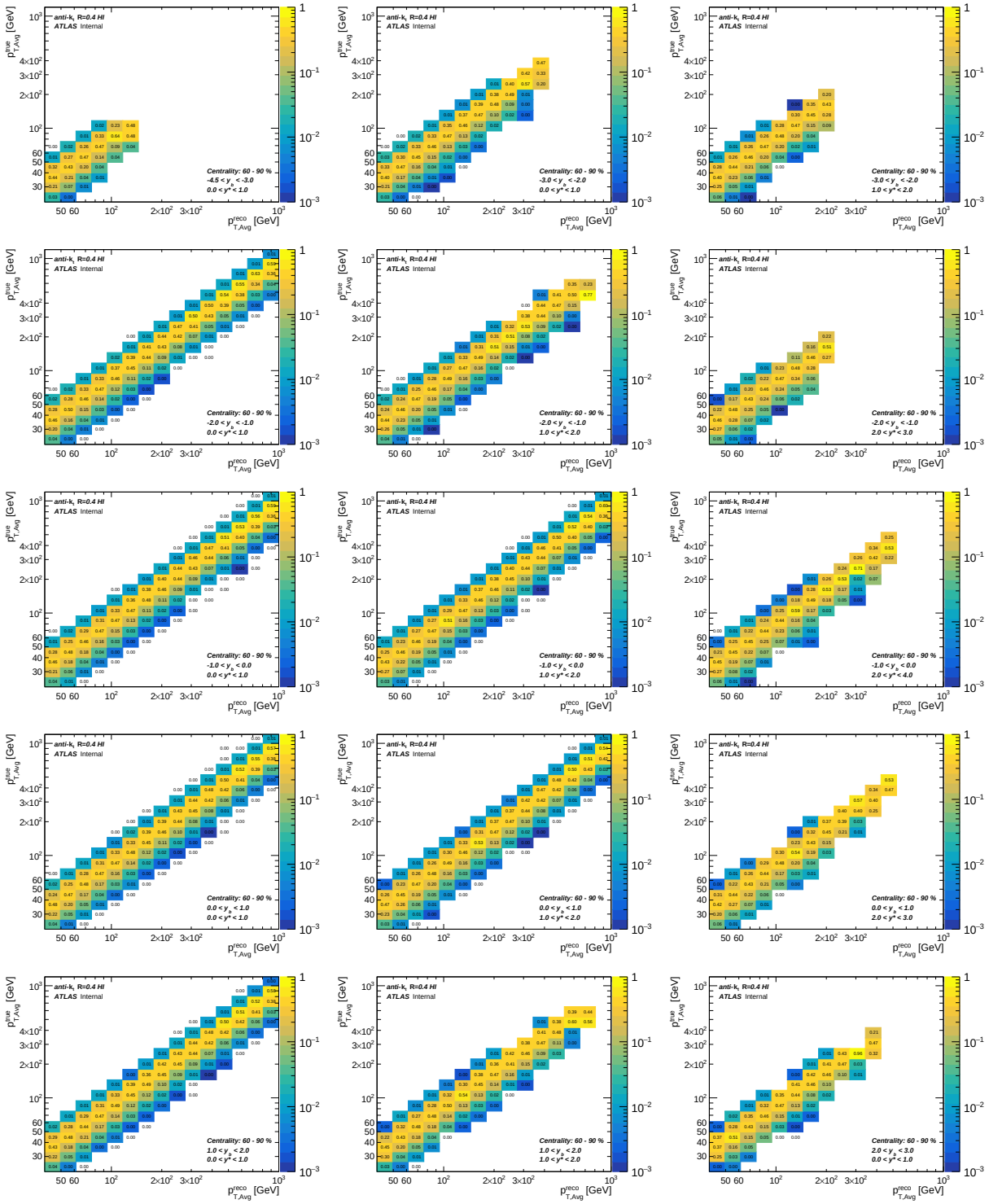

Figure A.6: Response matrices for p+Pb unfolding. The matrices are normalized such that each reconstructed bin (column) is normalized to unity.

Pb+p (Period C) 0-10% Centrality

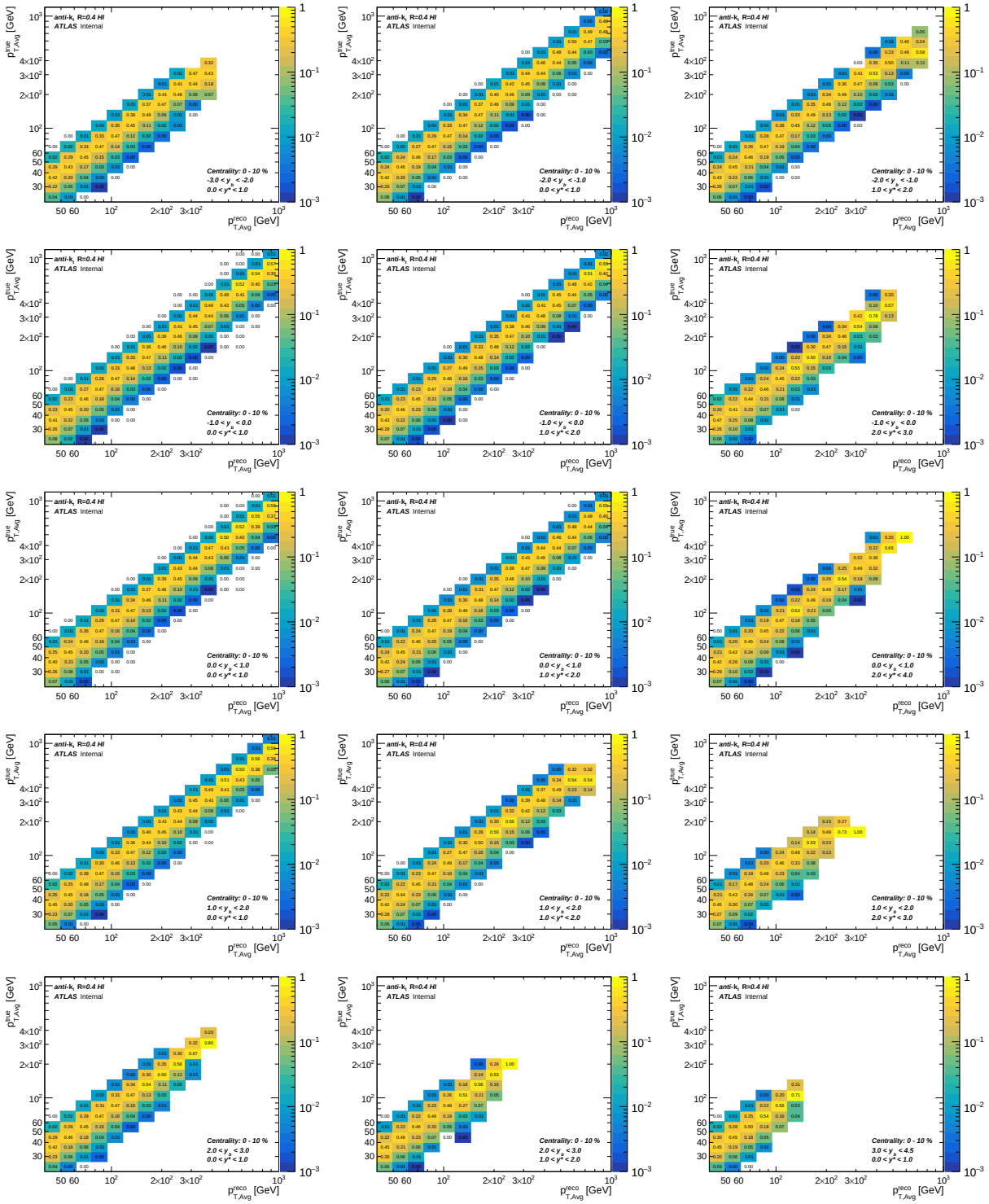

Figure A.7: Response matrices for Pb+p unfolding. The matrices are normalized such that each reconstructed bin (column) is normalized to unity.

Pb+p (Period C) 60-90% Centrality

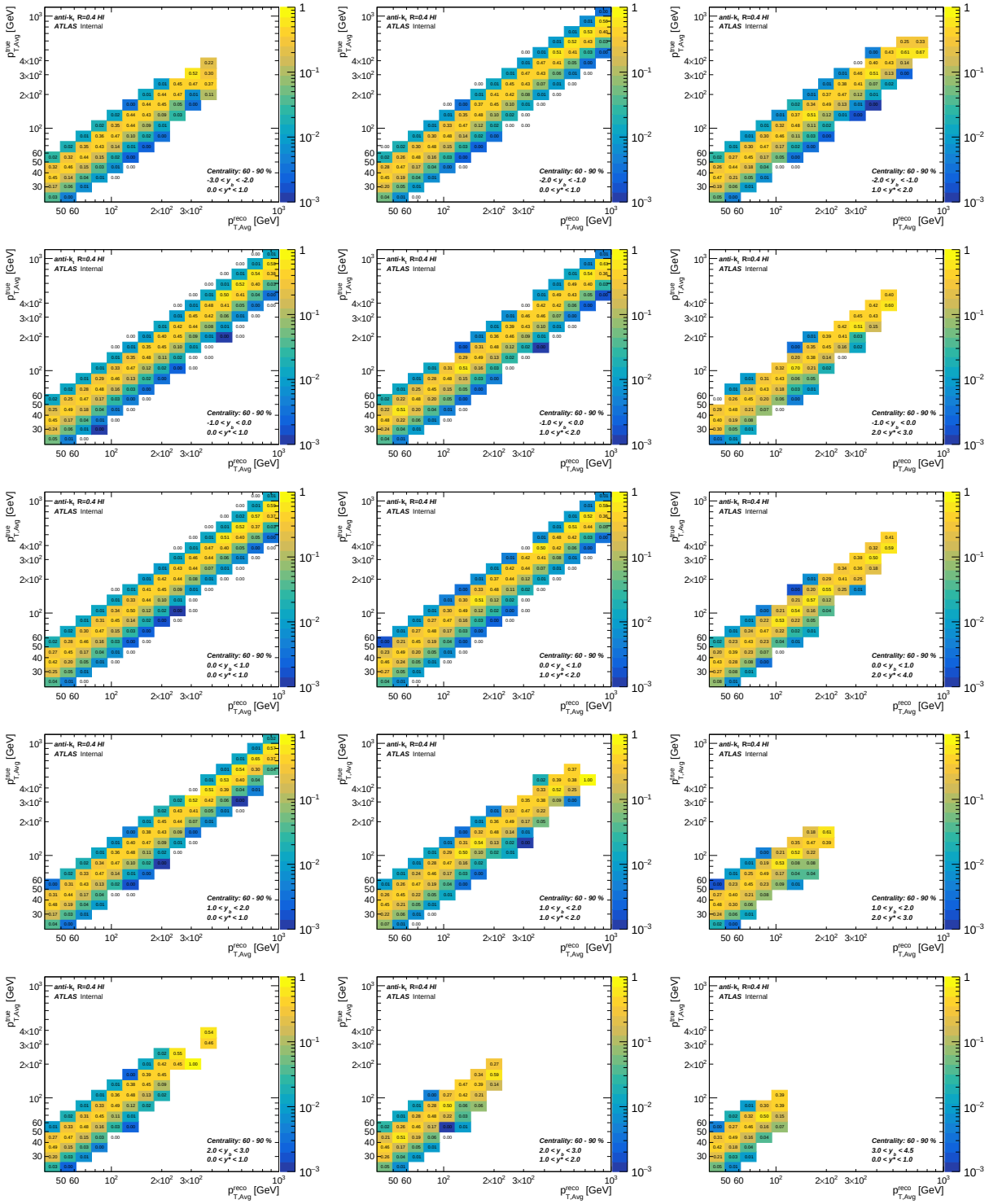

Figure A.8: Response matrices for Pb+p unfolding. The matrices are normalized such that each reconstructed bin (column) is normalized to unity.